An advanced stopped-flow reactor for the study of olefin polymerization

Yashmin Rafante Blazzio

Numéro d'ordre : 2020LYSE1079

THESE de DOCTORAT DE L'UNIVERSITE DE LYON

opérée au sein de

l'Université Claude Bernard Lyon 1

Ecole Doctorale 206

Ecole Doctorale de Chimie

Spécialité de doctorat : Polyolefins Reaction Engineering

Discipline : Chemical Engineering

Soutenu publiquement le 15/05/2020, par :

Yashmin Rafante Blazzio

An advanced stopped-flow reactor for the study of olefin polymerization

Devant le jury composé de :

Fongarland, Pascal	Directeur et Professeur – Laboratoire LGPC, Université Lyon 1	Président
Sheibat-Othman, Nida	Directrice de Recherches – Laboratoire LAGEP, Université Lyon 1	Co-directrice
Paulik, Christian	Head of Institute CTOM – University Johannes Kepler - Linz, Austria	Rapporteur
Julcour, Carine	Directrice de Recherches – Laboratoire de Génie Chimique Toulouse	Rapporteur
Tioni, Estevan	PhD – Process Engineer at Processium	Examinateur
McKenna, Timothy F.L.	Directeur du Laboratoire C2P2, Université Lyon 1	Directeur de thèse

UNIVERSITE CLAUDE BERNARD - LYON 1

Président de l'Université	M. le Professeur Frédéric FLEURY
Président du Conseil Académique	M. le Professeur Hamda BEN HADID
Vice-président du Conseil d'Administration	M. le Professeur Didier REVEL
Vice-président du Conseil Formation et Vie Universitaire	M. le Professeur Philippe CHEVALIER
Vice-président de la Commission Recherche	M. Fabrice VALLÉE
Directrice Générale des Services	Mme Dominique MARCHAND

COMPOSANTES SANTE

Faculté de Médecine Lyon Est – Claude Bernard	Directeur : M. le Professeur G.RODE
Faculté de Médecine et de Maïeutique Lyon Sud – Charles Mérieux	Directeur : Mme la Professeure C. BURILLON
Faculté d'Odontologie	Directeur : M. le Professeur D. BOURGEOIS
Institut des Sciences Pharmaceutiques et Biologiques	Directeur : Mme la Professeure C. VINCIGUERRA
Institut des Sciences et Techniques de la Réadaptation	Directeur : M. X. PERROT
Département de formation et Centre de Recherche en Biologie Humaine	Directeur : Mme la Professeure A-M. SCHOTT

COMPOSANTES ET DEPARTEMENTS DE SCIENCES ET TECHNOLOGIE

Faculté des Sciences et Technologies	Directeur : M. F. DE MARCHI
Département Biologie	Directeur : M. le Professeur F. THEVENARD
Département Chimie Biochimie	Directeur : Mme C. FELIX
Département GEP	Directeur : M. Hassan HAMMOURI
Département Informatique	Directeur : M. le Professeur S. AKKOUCHE
Département Mathématiques	Directeur : M. le Professeur G. TOMANOV
Département Mécanique	Directeur : M. le Professeur H. BEN HADID
Département Physique	Directeur : M. le Professeur J-C PLENET
UFR Sciences et Techniques des Activités Physiques et Sportives	Directeur : M. Y.VANPOULLE
Observatoire des Sciences de l'Univers de Lyon	Directeur : M. B. GUIDERDONI
Polytech Lyon	Directeur : M. le Professeur E.PERRIN
Ecole Supérieure de Chimie Physique Electronique	Directeur : M. G. PIGNAULT
Institut Universitaire de Technologie de Lyon 1	Directeur : M. le Professeur C. VITON
Ecole Supérieure du Professorat et de l'Education	Directeur : M. le Professeur A. MOUGNIOTTE
Institut de Science Financière et d'Assurances	Directeur : M. N. LEBOISNE

Abstract

Given the undeniable relevance of polyolefin production, it is of great interest to understand the key phenomena determining the quality of the polymerization process. Industrial scale polymerization reactions could be metaphorically compared to the launching of a space rocket, in which the success of the entire process is highly dependent on the mastery of the initial moments. This so-called 'nascent phase' of the polymerization (10^{-1} to 10^{2} s) is crucial in ensuring a satisfactory operation and properties of the final polymer. It is then that the catalyst activation takes place, the particle morphology is defined and the system is in its highest potential for mass transfer and heat transfer limitations.

Studying such short time-frames is challenging for a number of reasons (that we will see throughout this work) and requires specially adapted tools. Previous works from our research group have shown how the stopped-flow technique is a promising method to study aspects related to heat transfer and morphology evolution at early stages in gas-phase. It is mainly for this reason that the focus of the current project was on the improvement of such tools. The novel reactor developed in this work was especially designed to tackle some of the limitations encountered with the previous versions, mainly aspects related to poor heat evacuation, lack of robustness and imprecision in experimental measurements.

The first part of this PhD describes all steps taken until successful optimization of the hardware component of the novel stopped-flow reactor. The new set-up was a product of our innovative approach towards the reactor geometry (annular) and the tailored execution from a specialized engineering firm. Several improvements were achieved, such as the optimization of the reactor dimensions, the automated control of all functions and a wider range of operation conditions. Moreover, the capacity was highly improved by the possibility of injecting several gases simultaneously, as well as components that are liquid at room temperature. The new tool allows to perform polymerization reactions as short as 3s in gas phase, in reaction conditions that are representative of heat and mass transfer phenomena present in industrial scales.

In the second part of this work, we have developed a software component for the novel reactor, which consisted of a reactor model and state-observer. This tool was developed to estimate the dynamic polymerization rates from the temperature measurements and overcome the one-point character of such experiments (which provide no real information on the catalyst kinetics). For this purpose, a simplified one-dimensional model at the macromolecular level was developed and validated with experimental data.

At last, with hardware and software components at hand, we have demonstrated the usefulness of the new tool in specific case studies with different silica supported metallocene catalysts. In the first case study, we evaluated the impact of the pore structure of the support on the catalyst kinetics, polymer properties and particle morphology at short reaction times. On the second case study, we investigated the effect of various experimental conditions (reaction time, comonomer and hydrogen content) on the behavior of two different catalyst families. From both studies, the estimated reaction rates at early stages (<90s) reflected those observed in standard conditions (60 min). Moreover, the microscopy observations indicated that the catalyst surface seems to be inactive and polymer is being produced from the particle core. At last, we demonstrated how the new reactor set-up is a flexible and robust tool that can be used in the rapid evaluation of catalyst performance.

“If you’re gonna try, go all the way. Otherwise, don’t even start.”
Charles Bukowski

Acknowledgements

This PhD thesis is the result of a joint effort with numerous people, to whom I hereby wish to pay my special regards.

Firstly, I would like to express my sincere gratitude to my advisor Timothy F. L. McKenna for the trust and continuous support throughout these few years. Thank you for considering me suitable for this project, for giving me the chance to learn about polyolefins and meet people from all over the world. For your immense knowledge, your patience, the numerous motivational speeches and enormous working freedom you entrusted me: thank you! Your guidance, honest feedback and wise advice have helped me grow, trust myself and learn to ask better questions. It will be difficult to find a better boss.

Secondly, a sincere thank you to my co-advisor Nida Sheibat-Othman, for your essential participation in the modelling approach followed in my project. Thank you for sharing your expertise, for the long hours spent refining the model, for your dedication, your friendliness and generous spirit. I could not have done it without you.

I gratefully acknowledge the collaboration with INEOS, for the funding of my PhD project and for the presence in all steps of the way. I cannot thank you enough for this opportunity and the trust you placed in me. Thank you, Layane Deghedi, for your kind words of encouragement and attentive involvement, especially during the process of writing my thesis. Thank you, Serge Bettonville, for your curiosity and genuine interest in my advances. Thank you; Isabelle Cermelli, Gaëlle Pannier and Jean-Louis Chamayou for joining in and contributing to my project and meetings.

Thank you, Yves Ramjoie, for shedding some light on my dilemmas over R&D. If not for you, I might have not had the courage to take on this project and could have missed on the adventure.

Thank you, Innoue-San; from AGC Si-tech, for giving me the opportunity to learn about silica, catalyst synthesis and for sharing your stories from around the globe.

I want to acknowledge the competence and hard work of the ILS team, in Berlin. Thank you, Anton Nagy; your energy and vision are inspiring to me. Thank you, Helge Berger and Yannick Bofah, for your tireless dedication in building this remarkable piece of equipment. To you and the remaining ILS team: thank you for sharing your expertise and welcoming me with such friendliness during my visits to Berlin. *Danke sehr!*

As for the C2P2 team, I feel lucky to have worked in such a vibrant and welcoming environment. Thank you for the good times, for the informal blasts (mainly the Flan) and for making it an environment that encourages growth.

First and foremost, to Sébastien Norsic: what would we do without you? Thank you for sharing your knowledge, for teaching me to build things; to be patient and, most importantly: that it is never worth crying over the reactor. You are an exceptional person and I am lucky to have had your backup all along the way. *Cette victoire est aussi à toi, merci pour tout.*

Thank you, Nathalie Jouglard, who is the sunshine of the C2P2. Nathalie, *ma poule*, thank you for always making life easier, for being so bright and cheerful, for truly caring for us. *Ces années sont passées si vite et tu vas me manquer!*

Thank you, Christophe Boisson, for your interest and contribution to this project. On many occasions, you helped me by sharing your immense knowledge on chemistry and catalyst synthesis. Thank you, Manel Taam, for the invaluable technical support with the SEC; for your patience, your kindness and for bringing beauty wherever you go. Thank you, Franck Collas and Olivier Boyron, for your friendliness and indispensable help with the DSC and ATG. Thank you, Pierre-Yves Dugas, for the technical help with the microscopy and for sharing some good times - mainly involving French cheese.

To the LCOMS team, with whom I had the chance to work almost 1/3 of the time. Thank you, Kai Szeto, for all your help in the lab and vacuum lines. Thank you, Mostafa Taoufik, for being a part of my project, for your words of encouragement and your insights on catalyst behavior. To Vittoria Chiari, who walked the path with me. Thank you for being my friend and INEOS companion, for all our discussions on life, for your generosity and for opening your home to me.

Thank you, Frederic Bourgain, for your indispensable help in building the reactor prototypes, always with a smile. Thank you, Gérard Privat, for all the crucial technical support and for getting the lab ready in time for me to finish this project. *Merci pour l'amitié!*

Thank you to the office companions, who changed over the years and each contributed to a safe and pleasant workspace. Arthur, Aurélien, Magali, Bárbara, Fabiana, Cédric, Fabricio, Felipe, James, Juliette, Lionel, Niyi and Roberta. I feel lucky to have worked besides you. Fabiana Andrade, my very first friend in Lyon. Thank you for your friendship, your big heart and even bigger smile. *Obrigada pelas aventuras.* Lionel Bosco, you told me once that the PhD is an emotional rollercoaster. I thought of this advice several times, *merci*! Aurélien Bethegnies, *mon copain d'abord*, thank you for the shared good times, talks and french songs. James Delorme, thank you for your generosity and the good laughs in the office. Roberta Lopes, thank you for being such a pleasant person to be around, for your high spirits and for keeping my plants alive on several occasions. To Fabricio Machado, thank you for your guidance when pointing the way to the C2P2 lab, this story started with you.

A special thank you to the *Tim-team* (baptized by Sébastien), also called 'the cool kids of the lab' by some. Our multicultural group became my little family. Thank you, Aarón Cancelas, for passing me the torch of the stopped-flow reactor. You were right: at the end, things are not as complicated as they seem. To the Chinese spy, Yue Yu, for all your help in the lab and with the turbosphere, for our talks over coffee and for introducing me to real Chinese food. To Estela Gelinski, for your friendship, support and for sharing with me your vast knowledge on statistics. To Niyi Ishola, for all your help in the lab and for teaching me about DOE. *No wahala*, all is well. To Amel Ben Mrad, for all the good times we shared, for being my conference companion and sometimes (rarely) dancing until 3 AM. To Felipe Morais Bolner, my pupil and intern. Thank you for giving your sweat and soul to this project, for your dedication and friendship. One broken reactor, yes; but good results and great memories nonetheless. *Vai dar tudo certo.* To Igor Stefanichen, for all the talks of encouragement, figs and artichokes. To Thaissa Chaparro, for your friendship and for sharing the love for baby pineapples. To Abdulrahman Albeladi, for all the great talks. I'm happy to have you as a friend. To Anderson Medeiros (and Gigi, Thor and Maïté), for being a friendly shoulder during this scientific journey. *Brasilia é um ovo.* To Arne Wolpers*, mein einziger deutscher Freund*, thank you for your friendship and for letting me practice!

To Bárbara Rezende Lara. First an office neighbor, then a great friend. Thank you for all the laughs, for teaching me so much and for the spectacular hugs. To Rita Ferreira Alves, not only one of the most intelligent persons I know, but also my friendship soulmate. Thank you for your kindness, your generosity, your strength and for making the journey more colorful. You are a role model for me.

Thank you to all the friends who became my family in Lyon. In picnics, celebrations, birthdays... you made this city home! In particular, to Astrid Cordier, I'm grateful we shared this journey. Thank you for your kindness and your zest for life. *Aussi, merci pour la courge!* Priscilla Arnould, thank you for your support throughout this time and all our talks in the lab. To Edgar Spinoza, thank you for your friendship, for our great talks, shared picnics, and for your uplifting view of life. *Eres muy especial!*

Now, to my non-C2P2 family.

To Gilbert Audiffren, who provided me my home in Lyon. Thank you for trusting me, for being so caring and welcoming me into your family. To Antonin Vilpoix, my guitar teacher and friend. Thank you for all the great talks, for sharing your passion for music and encouraging my busking project. *Tu m'inspires à être meilleur!*

To my best friends, Gabriela Cunha and Julia Galvez. Your love and support know no distance or time zone. Thank you for being my chosen family, my backup squad, my perfect triad. *Migz 4-ever.*

To the girls from the book club in Lyon (Bárbara, Érika, Sara e Rita), thank you for your friendship and the strength we built together*. Sorte a minha de ter vocês.*

To Cédric Ysacco, my rock and partner in crime. Stars aligned to have you placed right there as my office neighbor. Thank you for caring so well for me, for fishing me out of my impostor syndrome and for always reminding me that I can do anything I set my mind to. *Je t'aime.* I extend a heartfelt thank you to your family (Sylvie, Hubert, Bob, Alice, Lucas, bientôt Carla, Jean-Claude, Chantal) who welcomed me hearts open and became my French family.

Finally, to my family, words are not enough to express my gratitude. To my sister, Roberta, for always having my back; encouraging my wild ideas and sharing so many adventures with me. To my brother, Rodrigo, for reminding me that we all have our own path and time. To my parents, Ney and Beatriz, who never spared their energy in encouraging me to go further. *Obrigada, Mãe*, for always bringing me back to Earth in our daily updates over the phone. *Obrigada, Pai,* for always encouraging me to listen to my heart. Thank you both for celebrating all my victories as your own, for being so present despite the ocean between us. Thank you for nurturing my projects, for traveling the world with me and for being such unconditionally loving parents. Thank you, the Blazzio team, I am lucky to have this crazy family of ours and I love you with all my heart.

Table of contents

Chapter 1: Literature Review

1. Introduction to polyolefins 17
   1.1. Manufacturing Processes 19
      1.1.1. High Pressure (Free Radical Polymerization) 19
      1.1.2. Low Pressure (Catalytic Polymerization) 20
   1.2. Heterogeneous Polymerization Catalysts 22
      1.2.1. Phillips (or Chromium) catalysts 22
      1.2.2. Ziegler-Natta catalysts 23
      1.2.3. Metallocene catalysts 25
   1.3. Conclusion 28
2. Polymer particle growth: Heat and Mass transfer at early stages 29
   2.1. Particle morphology and fragmentation 29
   2.2. Single Particle Models (SPM) 32
   2.3. Conclusion 35
3. Studying early stages of the polymerization 36
   3.1. Introduction to experimental studies at early stages 36
   3.2. The stopped-flow technique 39
      3.2.1. Stopped-flow reactors for slurry phase polymerization 39
      3.2.2. Stopped-flow reactors for gas phase polymerization 42
   3.3. Conclusion 46
4. Overall Conclusions 47
5. References 49

Chapter 2: A novel stopped-flow reactor for gas phase polymerization: towards the ideal set-up

1. Introduction 60

2. Experimental approach 61
   2.1. Full-time polymerization reactor 61
      2.1.1. Polymerization procedure 61

3. Existing stopped-flow reactor (SF1) 63
   3.1. Advantages and limitations of the existing set-up 63
   3.2. Experimental section 63
      3.2.1. Materials 64
      3.2.2. Reactor description and polymerization procedure 64
   3.3. Heat evacuation assessment 67
      3.3.1. Conclusion 70
   3.4. Hardware evaluation 70
      3.4.1. Conclusion 72
   3.5. Conclusions on assessment of reactor SF1 72

4. Stopped-flow reactor prototype (SF 2) 74
   4.1. Introduction 74
   4.2. Experimental section 75
      4.2.1. Materials 75
      4.2.2. Reactor description 76
      4.2.3. Polymerization procedure 77
      4.2.4. Estimating the particle temperature 78
   4.3. Heat evacuation assessment 78
      4.3.1. Improved temperature gradients with ZN catalyst 79
      4.3.2. Impact of seedbed on polymerization yield 80
      4.3.3. Conclusion 82
   4.4. Hardware inertness assessment 82
      4.4.1. Improving inertness by reactor conditioning with alkyl agents 83
      4.4.2. Conclusion 83
   4.5. Hardware thermal response assessment 84
      4.5.1. Conclusion 85
   4.6. Conclusions on assessment of reactor SF 2 86

5. Novel professionally engineered stopped-flow reactor (SF N) 88
   5.1. Introduction 88
   5.2. Reactor description 89
   5.3. Experimental section 93
      5.3.1. Materials 93
      5.3.2. Polymerization procedure 93

5.3.3. Reactor conditioning 94
5.4. Hardware thermal response assessment 95
5.4.1. Improved control of reaction conditions 95
5.4.2. Conclusion 97
5.5. Hardware inertness assessment 97
5.5.1. Demonstration of hardware inertness with highly sensitive CGC catalyst 97
5.5.2. Conclusion 98
5.6. Conclusions on assessment of reactor SF N 99
6. Chapter conclusions 100
7. References 102

Chapter 3: Development of software component for novel stopped-flow reactor

1. Introduction: why implement a software component? 107
2. Set-up description 108
2.1. Materials and operating procedure 108
2.2. Interpreting experimental results 109
2.3. Conclusion 110
3. Development of reactor model 111
3.1. Reaction rate and simplifying assumptions at the particle level 112
3.1.1. Monomer concentration in the particles 112
3.2. Energy Balances 113
3.2.1. Three phases in reaction zone 115
3.2.2. Two phases in reaction zone 116
3.3. Heat transfer correlations 117
3.3.1. Heat transfer coefficient between gas and particle 117
3.3.2. Heat transfer coefficient at the reactor wall 118
3.4. Conclusion 119
4. Validating the reactor model 120
4.1. Model programming 120
4.2. Simulation results 120
4.2.1. Three phases in reaction zone 120
4.2.2. Two phases in reaction zone 121
4.2.3. Conclusion 122
4.3. Sensitivity analysis 123
4.3.1. Superficial temperature of reactor wall (T_{wall}) 123
4.3.2. Catalyst particle heat transfer coefficient (h_{cat}) 124
4.3.3. Diameter of catalyst particles 124

4.3.4. Conclusion 125
4.4. Conclusions on model validation 126
5. Development of a High-Gain Observer 126
5.1. Introduction 127
5.2. The novel reactor as a Calorimeter 128
5.3. Implementing a High-Gain Observer 128
5.3.1. Heat balance and reaction rate 129
5.4. Validating the High-Gain Observer 129
5.5. Sensitivity analysis 130
5.5.1. Effect of tuning parameter 131
5.6. Conclusion 132
6. Chapter conclusions 133
7. Nomenclature 134
8. References 137

Chapter 4: Case studies: start-up behavior of supported catalysts in varying compositions of gas phase feed

1. Introduction 141
2. Impact of support structure on the behavior of classic metallocene catalysts 142
2.1. Experimental Section 142
2.1.1. Materials 142
2.1.2. Polymerization procedure 143
2.1.3. Catalyst synthesis procedure 144
2.1.4. Silica and catalysts characterization 145
2.2. Results and discussion 147
2.2.1. Catalyst kinetics 148
2.2.2. Reaction rates at early stages 150
2.2.3. Polymer properties 151
2.2.4. Particle morphology 152
2.3. Conclusion 156
3. Comparing 2 families of metallocene catalysts at different gas-feed compositions 158
3.1. Experimental Section 158
3.1.1. Materials 158
3.1.2. Polymerization procedures 158
3.1.3. Design of Experiments (DOE) 159
3.2. Variability assessment for catalysts in this study 160

3.2.1. Results 161
3.2.2. Conclusion 162
3.3. Results and discussion 163
3.3.1. Catalyst kinetics 163
3.3.2. Reaction rates at early stages 166
3.3.3. Polymer thermal properties 167
3.3.4. Molecular weight 173
3.3.5. Particle morphology 174
3.4. Conclusion 181
4. Chapter conclusions 183
5. References 185

Chapter 5: Conclusions and perspectives

1. Conclusions 189
2. Perspectives 193
3. References 194

Appendix section

Appendix 1: Experimental Section 203
Appendix 2: Reactor model sensitivity analysis 215
Appendix 3: List of Experiments 221

Chapter 1

Literature Review

Chapter 1: Content

1. Introduction to polyolefins 17
   1.1. Manufacturing Processes 19
      1.1.1. High Pressure (Free Radical Polymerization) 19
      1.1.2. Low Pressure (Catalytic Polymerization) 20
   1.2. Heterogeneous Polymerization Catalysts 22
      1.2.1. Phillips (or Chromium) catalysts 22
      1.2.2. Ziegler-Natta catalysts 23
      1.2.3. Metallocene catalysts 25
   1.3. Conclusion 28
2. Polymer particle growth: Heat and Mass transfer at early stages 29
   2.1. Particle morphology and fragmentation 29
   2.2. Single Particle Models (SPM) 32
   2.3. Conclusion 35
3. Studying early stages of the polymerization 36
   3.1. Introduction to experimental studies at early stages 36
   3.2. The stopped-flow technique 39
      3.2.1. Stopped-flow reactors for slurry phase polymerization 39
      3.2.2. Stopped-flow reactors for gas phase polymerization 42
   3.3. Conclusion 46
4. Overall Conclusions 47
5. References 49

1. Introduction to polyolefins

The term “polyolefins” is a generic name that includes all polymers of lighter α-olefins (such as ethylene and propylene) and their copolymers with varying fractions of higher α-olefins (most commonly 1-butene, 1-hexene, and 1-octene).

They are an integral part of our daily lives. From familiar items such as food packaging, containers, bottles, toys, adhesives and house appliances to high performance applications such as engineering plastics, construction pipes, automotive parts, medical applications and prosthetic implants; polyolefins present an immense range of applications. Besides their great versatility, polyolefins are highly durable materials, resisting damage by water, air, grease and most cleaning solvents. They are light materials, easy to manipulate into different shapes, yet resistant enough to be transported without damage. Finally, these polymers are cost effective materials, produced from relatively inexpensive natural gas, and despite the vast array of remarkable applications, polyolefins are very simple molecules formed of monomers, themselves composed only of carbon and hydrogen atoms.

These factors (chemical simplicity, large applicability, low cost) make polyolefins extremely useful and economically attractive, leading to production volumes in the order of 150 million tons (in 2015)[1–3], about half the global polymer production.

Despite having the same chemical structure, different polymers present very different physical properties. The properties of the final material are defined by how the monomer molecules (ethylene, propylene and higher α-olefins comonomers) are bound to the polymer chain. A given range of specific properties is achieved by manipulating the production conditions, which are a combination of the process in place, the reactor configuration and the chosen catalyst. These aspects will be further discussed in the following sections covering manufacturing processes and polymerization catalysts.

Polyolefins can be split into two main types of polymer resins: Polyethylene (PE) and Polypropylene (PP), accounting for different grades (compositions, copolymers) for each of them.

Polypropylene resins

Polypropylene resins represent close to one third of the global polyolefin production. Given the asymmetric character of the propylene monomer, the stereochemical configuration – the orientation of the pendant methyl group – of polypropylene plays a significant role in the final properties of the polymer. The most commonly found stereochemical configurations for propylene are shown in Figure 1: isotactic, syndiotactic and atactic propylene. In the isotactic configuration, the methyl groups are positioned on the same side of the chain backbone. In the syndiotactic configuration, the methyl groups are placed on alternating sides of the long chain. Finally, in the atactic configuration, the methyl groups are placed randomly across the backbone chain.

Atactic polypropylene is an amorphous polymer and, therefore, not commercially attractive. Isotactic and syndiotactic polypropylene are both semicrystalline polymers with a high melting temperature. Out of the three, the isotactic configuration is commercially preferred due to its efficient and inexpensive production with Ziegler-Natta and, to a lesser extent, with metallocene catalysts.

The production of polypropylene resins is out of the scope of the current project and the reader can find more information in a wide range of available sources, such as the review article from Maddah. [4]

While the focus of this work is polyethylene, it should be kept in mind that the tools and methodologies developed herein can also be applied to polypropylene.

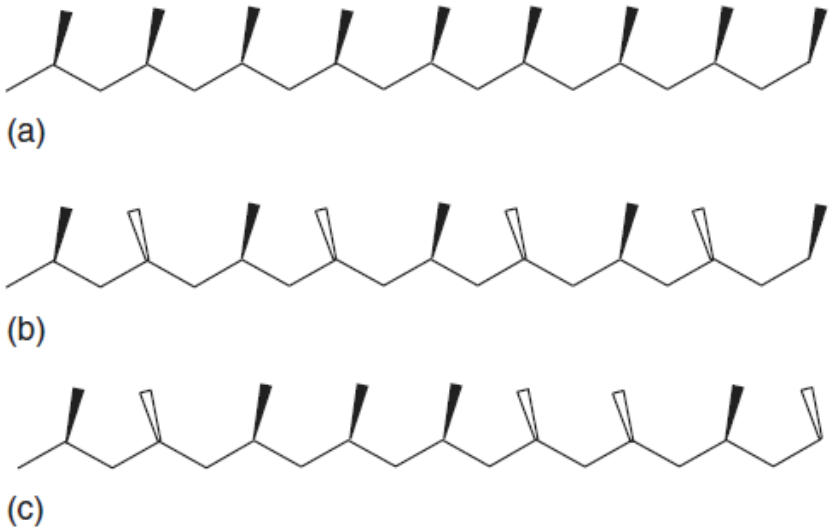

Figure 1: Main types of polypropylene resins: (a) isotactic, (b) syndiotactic, and (c) atactic. Reprinted with permission[5].

Polyethylene resins

Polyethylene is the polyolefin produced in largest volumes. [6] These resins are commonly divided into three main categories: low-density polyethylene (LDPE), linear low-density polyethylene (LLDPE) and high-density polyethylene (HDPE).

These categories are based on the characteristic density ranges for each polymer: typically on the order of 0.915–0.940 $g.cm^{-3}$ for LDPE, 0.915–0.94 $g.cm^{-3}$ for LLDPE and 0.941–0.970 $g.cm^{-3}$ for HDPE, although these limits can somewhat differ according to the source. Occasionally, polyethylene resins with densities ranging between 0.926-0.940 are also referred to as medium density (MDPE). HDPE with average molecular weight of several millions is referred to as Ultrahigh Molecular Weight Polyethylene (UHMWPE). Polyethylene with densities lower than 0.915 $g.cm^{-3}$ are occasionally referred to as ultra-low-density polyethylene (ULDPE) or very-low-density polyethylene (VLDPE); which are actually considered as polyethylene wax. [5]

Nonetheless, while density values are commonly used to classify polyethylene resins, they provide little to no information on the complex microstructure of the polymer. The microstructural characteristics are better described by their chain structure and chemical composition distribution (CCD). The chain structure of commonly found polyethylene resins is represented in Figure 2.

LDPE is made via free radical polymerization at pressures from 1200-3500 bars and at temperatures on the order of 250°C, leading to microstructures that are very different from those of HDPE and LLDPE, which are produced via catalyzed processes. LDPE contains short-chain branches (SCB) and long-chain branches (LCB) produced by different radical transfer steps, while polyethylene made using coordination catalysts generally contains only SCBs created by copolymerizing ethylene with short chain α-olefins.

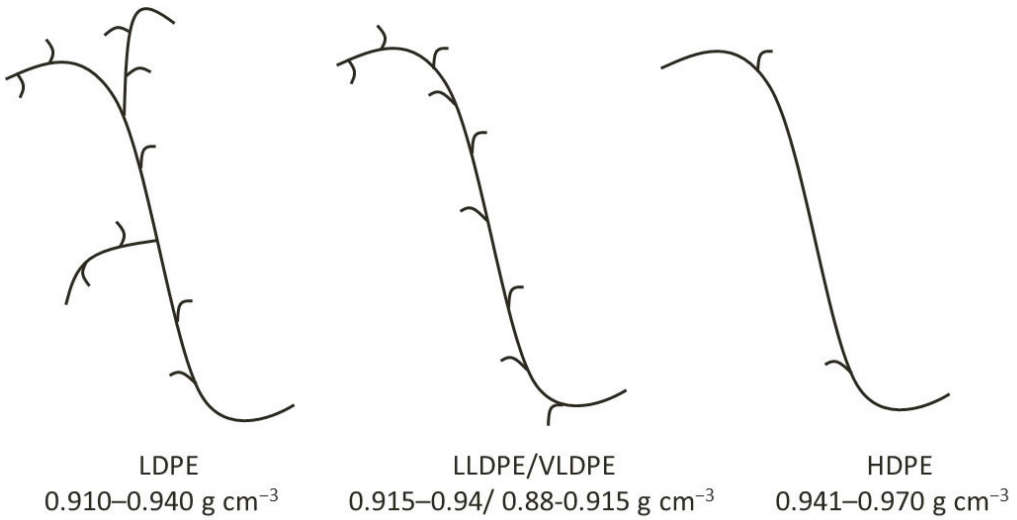

Figure 2: Polyethylene (PE) classification according to branching and density

1.1. Manufacturing Processes

In order to cover the market demand for a high variety of polyolefin products, a broad range of polymerization conditions is applied, each of them adapted to cover a specific need of polymer grade range and market necessity. The polymerization reactors, processes and catalysts are closely linked and will be determining for the properties of the final polymer (MWD, CCD and branching distributions).

When designing and controlling polymerization processes, several factors are considered, such as the residence time distributions (RTD) of a particular reactor, the ease in recovering the polymer formed while maintaining its properties intact and, most importantly, the effective heat removal from the reactor. Since olefin polymerization reactions are highly exothermic, effective and sufficient removal of heat from the reactor plays a crucial role in the choice of processes and reactors. Given the enthalpy of polymerization reactions (3600 $kJkg^{-1}$ for polyethylene, 2400 $kJkg^{-1}$ for polypropylene), heat removal is especially critical in polyethylene processes. When heat removal is not effective, the formation of hot spots in the reactor can lead to polymer melting and particle agglomeration. The formation of lumps can cause issues related to product transportation or blockage of the reactor outlet.

In a general manner, polyolefin production is carried out in solution, slurry or gas-phase reactors. A thorough discussion on the processes described hereafter can be found in the work of Soares and McKenna[7].

1.1.1. *High Pressure (Free Radical Polymerization)*

This type of process, *the first used* and perhaps most simple to implement, is carried out in tubular or autoclave reactors, in solution processes where catalyst and reactants are in the same phase. Temperatures range from 150 to 350 °C and pressures between 1200 and 3500 bar.

Free radical polymerization is used to produce LDPE, which contains the highest content of long and short chain branching of polyethylene resins. The high level of chain branching achieved with this process (therefore polymers with lower melting temperatures, 105-115 °C) leads to products that are

highly processable and moldable into different shapes. Examples of LDPE products include: plastic bags, soft packaging, containers, dispensing bottles, computer components.

The reactors used in this process count with short residence times that allow for rapid and low cost grade changes. The manufacturing by free radical polymerization is, nonetheless, out of the scope of the current project and the reader can find more information in a wide range of available sources, such as the review article from Bisht et Chatterjee. [8]

1.1.2. *Low Pressure (Catalytic Polymerization)*

The development of coordination catalysts marked the 1950's with the discovery of Ziegler–Natta and Phillips catalysts, leading to intense and continuous scientific research that led to several process improvements overtime.[1] As new systems were discovered and processes refined, the range of possibilities for producing polyolefins continued to grow, each catalyst family and process adequate for a different application.[5,9]

In low pressure processes (low with respect to the pressures used in the earlier LDPE processes), polymers are produced under mild conditions through catalytic polymerization. These processes account for about 80% [10] of the world production of polyethylene resins. Low pressure polymerization processes are energy efficient and easy to implement, thanks to the discovery of highly active catalysts.[1] Catalytic polymerization can be carried out in solution, slurry and gas-phase processes.

Solution

In solution polymerization processes, the unsupported (molecular) catalyst and polymer are soluble in the liquid reaction medium.

Homogeneous catalysts such as vanadium-based Ziegler–Natta, metallocene or constrained geometry (CGC) catalysts are employed in solution processes. Since all reactants are in the same phase, no mass transfer resistance is encountered. High temperatures are maintained to keep the polymer in the solution (140-250°C), which leads to very rapid polymerizations and reduced residence times (1-20 minutes). High temperatures also lead to polymers with lower molar masses.

Autoclaves and, more recently, tubular loop reactors are used in solution processes with reactor volumes ranging from 3 to 15m^3. Examples of polymers produced in solution process: PE grades (usually with 1-octene as comonomer) with soluble metalocene and ZN catalysts, ethylene-propylene-diene (EPDM) rubbers with Vanadium ZN or Titanium post-metallocene catalysts.[7]

Slurry

In slurry processes, heterogeneous (supported) catalysts are dispersed in a chosen diluent and the reactor operates in two (liquid/solid) or three (liquid/solid/gas) phases.

In diluent slurry processes for the production of HDPE and MDPE, linear alkanes are frequently used as inert diluents, such as: supercritical propane, subcritical isobutene and n-hexane. In bulk slurry processes for the production of polypropylene, liquid propylene is used both as a diluent and monomer. Given the reactants are not in the same phase, mass transfer resistance are possible and

solubility limitations for hydrogen and comonomers reduce the range of applicability in slurry processes.[7]

Loop reactors are the most common type of reactor used in slurry processes. Autoclave reactors are also used, although less frequently than in the past as loop reactors offer far better heat transfer conditions, and thus higher space time yields. In flashing units, the produced polymer is separated from the diluents, which are then recycled into the process cycle. Reaction temperatures lie between 75 and 100 °C and pressures vary between 8 and 65 bar, according to the reactor and diluent in case. The type and number of reactors applied impact the residence times, usually between 45 minutes and 5 hours. Process technology for slurry processes include those developed by, for instance, Chevron Phillips (CP Chem), Mitsui, LyondeBasell, Borealis and INEOS. The Phillips loop reactors from CP Chem is the most used for producing PE.[11]

While solution and slurry processes are commercially important, the focus of the current work is gas phase polymerization using supported catalysts. The remainder of the discussion in this, and subsequent chapters will focus on issues related to gas phase polymerization of ethylene on supported catalysts.

Gas-Phase

Gas phase processes were the last to be developed, but now account for nearly 75% of the global production for LLDPE and 25 % of the HDPE, in 2011. [12] This process offers an advantage to the use of liquid solvents (hydrocarbon diluents) employed in solution and slurry, besides providing an easier recovery of the produced polymer since the monomer is in the gas phase.

Given that there are no solubility limitations for hydrogen and comonomers in the gas phase, polymers with higher comonomer contents (α-olefin fraction) and Melt Flow Index (MFI) can be obtained. The MFI refers to the amount of polymer than can flow through a standard capillary in 10 minutes under the influence of a weight placed on top of the sample, and indicates the ease of flow and processability of a given thermoplastic polymer. [13]

Nevertheless, heat removal in gas-phase reactors is more critical than in solution and slurry, given the poor heat transfer properties of the gaseous medium. Overheating in the reactor can compromise the quality of the produced polymer as several properties (e.g. molecular weight, chemical composition and catalyst kinetic behavior) are dependent on the reaction temperature. Besides, particle softening and agglomeration can cause operational problems such as formation of sheets in the reactor walls, resulting in ineffective operation of reactor components, such as the fluidization bed. [7,14,15]

To avoid such issues, several steps are commonly taken to enhance the heat removal of gas-phase reactors, such as incorporating gas-phase components with high heat capacities (e.g. propane). [12] Further heat removal can be achieved through the latent heat of vaporization in what is referred to as condensed mode operation, where small amounts of condensable materials are injected in the reactor. Frequently used condensable materials are monomers (for propylene), comonomers such as 1-butene or 1-hexene (for LLDPE), or inert alkanes such as isobutane or isopentane (for PE).[14,16,17]

Gas-phase reactors are divided into Fluidized Bed Reactors (FBR) and stirred bed reactors (further subdivided into horizontal or vertical reactors).[7] In FBRs, a flow of monomer and inert gases at high superficial velocities (0.5-1 ms^{-1}) is used to fluidize the polymer.[14] The high relative gas-particle

velocities reached in FBRs make these the reactor with best heat removal capacity amongst the gas-phase reactors. This accounts for the fact that, with the exception of the new Hyperzone process for HDPE which uses a multizone recirculating reactor, virtually all gas phase PE processes use a FBR.[7,14]

Operating temperatures range from 70 to 110 °C, and pressures typically from 20 to 25 bar.[7] Reactor volumes lie between 50 and 150 m^3, with particle residence times of 1.5 to 3 hours. The two most widely licensed technologies for gas-phase processes that use FBRs are theUnipol PE from Univation Technologies[18] producing about 48 million tons per year (mTA) and the Innovene G from INEOS Technologies[19], with 5-8 mTA. Other processes include the Spherilene process from LyondellBasell, and the Evolue process from Mitsui.[7]

1.2. Heterogeneous Polymerization Catalysts

In the scope of the current work, heterogeneous catalysts refer to catalysts that have been chemically or physically fixated onto a solid organic or inorganic support.

The history of polyolefins is a success which was made possible by the discovery and design of catalysts that allow one to effectively control the microstructure and properties of the final polymer. The main types of catalysts used in olefin polymerization are Ziegler-Natta catalysts, Phillips (or Chromium) catalysts, Metallocene catalysts and late transition metal catalysts. [1,20] These are all called coordination catalysts, given that the monomer coordinates with the transition metal in the catalyst active site before inserting in the polymer chain. Since the monomer insertion happens in the transition metal-carbon bond, the nature of the active sites will determine the polymer chain formation. [20,21]

This coordination step is responsible for the different properties of the final material and provides a different kind of control of the polymer microstructure than in free radical polymerization. Since each catalyst provides a specific electronic and steric environment for the monomer insertion, important polymerization parameters will be affected with variations in this step, such as propagation and chain transfer rates, comonomer insertion ratios, stereoselectivity, and regioselectivity of the formed polymer.

Since each catalyst possesses specific features, it is useful to provide a brief overlook of their properties and commercial applicability. A thorough introduction to the catalysts described hereafter can be found in the work of Soares and McKenna. [20]

1.2.1. *Phillips (or Chromium) catalysts*

Phillips catalysts were discovered in 1951, marking the first major revolution in the field of olefin catalytic polymerization. [1]

In general, Phillips catalysts are prepared by the impregnation of chromium compounds (E.g. CrO_3) onto silica (SiO_2), followed by high temperature (200-900 ◦C) calcination under vacuum. [20]

Unlike Ziegler-Natta catalysts (which need a cocatalyst for catalyst activation), here the activation is due to the thermal effect of the calcination that aids the attachment of the Cr species on to the surface silanol groups of the silica. The thermal treatment applied during the activation step will affect the catalyst activity and properties of the final polymer, such as the MWD and the formation of long-chain

branches (LCB). For these catalysts, the MWD is dependent on the preparation of the catalysts, and on the porosity and pore volume of the support, whereas hydrogen has little effect on chain transfers. Concerning the activity of Phillips catalysts, long induction periods are often observed before the polymerization takes place.

These catalysts are not used to produce LLDPE, given their low incorporation of higher α-olefins. Nevertheless, they are a favorite when it comes to HDPE, controlling about 40% of the market production for this resin. Produced polymers possess broad MWD indicating the presence of different active sites.

Nonetheless, Phillips catalysts are not in the scope of this project, which is focused on the behavior of heterogeneous Ziegler-Natta and metallocene catalysts in gas-phase conditions.

1.2.2. *Ziegler-Natta catalysts*

The discoveries of Ziegler's organometallic catalysts and Natta's application to the stereoselective propylene polymerization were the second major breakthrough that revolutionized the plastic industry and initiated a wave of remarkable advances in polyolefin technology.[1,22] For their contribution, they were awarded the Nobel Prize in Chemistry in 1963.

In a broad definition, Ziegler-Natta catalysts are formed by salts (ionic assemblies) of a transition metal from groups IV-VII with metal alkyls from groups I-III.

The metal alkyls are known as *cocatalysts* or activators, as they are required to *activate* the catalyst in a two-step process of alkylation followed by reduction of the metal center. In the activation mechanism initially proposed by Cossee, [21,23] the monomer coordinates to the vacant site in the metal. This coordination step activates the C-C double bond that inserts into the Ti-C bond, resulting in augmentation of the polymer chain by one unit. After the insertion step, the metal vacant site becomes available for another insertion step and the polymer chain progressively grows.

In fact, the transition metal salts are accurately referred to as *precatalysts* prior to activation by a *cocatalyst*, since the metal alkyls are necessary to create the metal-carbon bond where monomer will insert. The most widely used cocatalysts are alkyl aluminum compounds, such as: trimethyl aluminum (TMA), Triisobutylaluminium (TiBA), triethyl aluminum (TEA) and diethyl aluminum chloride (DEAC). [20] The most used formulation for Ziegler-Natta catalysts is $TiCl_4$ with an activating alkyl aluminum compound (mainly TEA). Ziegler-Natta catalysts exist in homogeneous and heterogeneous forms. Nevertheless, focus here will be given to the heterogeneous form, since it is more widely used in the industry for the production of LLDPE and HDPE.

For more than 60 years after their discovery, Ziegler–Natta catalysts have been the focus of continuous research, and the many innovations over time are generally divided into catalyst generations. Classifications vary between four of five generations, according to the author.

According to Soares and McKenna[20], the first generation entails the use of crystallite $TiCl_3$ activated with DEAC. Important aspects of this stage of development are that most potential active sites in the crystallite catalyst were not promptly accessed by the monomer, leading to low polymer production activities. Moreover, costly post reactor purification steps such as the removal of atactic polypropylene and catalyst residue deashing were needed to obtain satisfactory products.

The second generation counted with the addition of electron donors (Lewis bases such as ethers and esters) to $TiCl_3$ as a means of increasing catalyst activity and stereoselectivity (for PP).

The third generation was marked by the discovery of $MgCl_2$ as an ideal support for $TiCl_3$ due to its high specific surface area and compatibility with active titanium species. These features improved the accessibility of the monomer to the active sites and resulted in high performance heterogeneous catalysts and polymers with controlled morphology. [24] Together with the use of internal donors (added during the catalyst preparation) and external donors (added to the polymerization reactor), the third generation catalysts jointly eliminated the issue of post-reactor purification steps and improved catalyst activity and stereoselectivity.

Finally, the fourth generation entails the development of larger catalysts with precisely controlled morphology that eliminated the need for polymer pelletization.

Ziegler-Natta catalysts are often referred to as multi-site catalysts because the metal active sites can be sterically and electronically influenced by their surroundings. Such slight variations in the active site behavior are reflected in the monomer coordination-insertion step and, therefore, on the properties of the produced polymer. Figure 3 illustrates how this heterogeneity in the behavior of active sites can be remarked on the bimodal chemical composition distribution (CCD) of a LLDPE resin derived from heterogeneous Ziegler-Natta catalysts. [5,20,25]

The chemical composition distribution (CCD) describes the α-olefin distribution in the main polymer chain and relates to the density of the polymer and also, to a lower extent, to its molecular weight. Given the multi-site character of ZN catalysts, each site will react differently with the monomers, thus leading to polymer chains varying in their α-olefin content (thus SCBs) and molecular weight.

In Figure 3, the sharp crystallinity peak reflects low α-olefin incorporation, while the broad low-crystallinity peak translates a higher α-olefin fraction in the polymer chain. The incorporation of SCBs acts as irregularities in the polymer chain, leading to a decrease in the polymer density, crystallinity and melting temperature, therefore lowering the polymer crystallinity.

It is, then, not surprising, that different catalysts will lead to very different CCD profiles. Moreover, the CCD will be affected by the ethylene/α-olefin ratio in the monomer feed, the type of α-olefin used and the polymerization temperature applied in the production process.

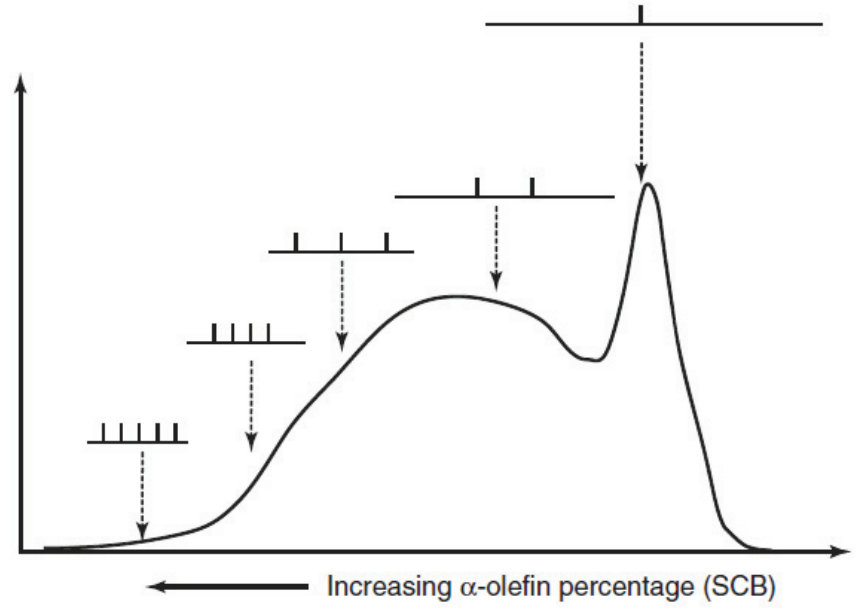

Figure 3: Generic CCD of an LLDPE resin derived from a heterogeneous ZN catalyst. Reprinted with permission.[5]

1.2.3. *Metallocene catalysts*

Metalocene catalysts, often called 'sandwich compounds', are organometallic compounds formed by a transition metal atom, usually of group IV, placed between two cyclopentadienyl or cyclopentadienyl-derivative rings – shown in Figure 4. The possibility of combining different ligands is essentially endless and will affect the catalyst behavior as the accessibility to the active sites is modified. The choice of metal atom will equally affect the catalyst behavior, with most common choices being Zr, Ti and Hf.

The sterically hindered configuration typical of metallocenes results (in theory) in only one type of active site, which is the main difference between metallocenes and Ziegler-Natta and Phillips catalysts, and why metallocenes are commonly referred to as single-site catalysts. The single-site character of metallocene catalysts leads to polymers with a narrow MWD and CCD profile. This unique characteristic is what makes metallocenes catalysts particularly attractive, due to the precise tailoring of polymer microstructures that their configurations allow. [20,22,24,26,27]

Metallocenes catalysts need an activator or cocatalyst (such as aluminum alkyls and ammonium borate) [28] to generate the Al^{-} Met^{+} ion pair vacancy on which the monomer will coordinate and allow chain growth through monomer insertion. Such cocatalysts are usually more expensive than the catalyst itself. [28] Metallocene catalysts only became a viable and attractive option for industrial purposes in the 1970s, after the discovery made by Kaminsky and Sinn of methylaluminoxane (MAO) as a catalyst activator and stabilizer. [1,26,29]

MAO is a product of the controlled hydrolysis of Trimethylaluminium (TMA) and exists in several grades, depending on the synthesis procedure. Despite the value of MAO in the metallocene industry, there is still debate on its chemical structure and several options have been proposed; such as linear, cyclic and cage structures. [29] Nevertheless, there is general consensus that MAO is a bulky molecule with molecular weights ranging between 700-18000 g/mol, [30,31] with several studies agreeing on a cage-like structure. [24,30,32]

While metallocene catalysts lead to polymers with extremely well controlled microstructures (narrow CCDs), this can often impair the processability of such polymers, especially at higher molecular weights. In polymers produced with ZN and Philips catalysts, the fraction of low molecular weight polymer in broader molecular weight distributions (MWDs) increases the shear thinning character of the polymer, which facilitates the polymer processing in common industrial extruders and blowers. This limitation in the processability of metallocene based polymers can be improved by introduction of LCBs in the polymer backbone through copolymerization reactions, significantly increasing the polymer melt elasticity.

Other approaches used in the industry include blending of polymers from different catalysts, combining different reactors and using catalysts with more than one active site (also called tandem catalysts). [20,25] Half-sandwich or Constrained Geometry Catalysts (CGC), represented in Figure 4-c, are an example of metallocenes with only one cyclopentadienyl ring. This family of metallocenes is known for their high α-olefin incorporation capacity due to easier accessibility of α-olefin comonomers to the active sites (achieved by the absence of the second Cp ring), as well other factors such as the electronic environment around the metal atom. As a consequence, long chain branches (LCBs) are formed from the copolymerization reaction, resulting in polymers with higher melt flow index (MFI) than those obtained with classic metallocene catalysts. [20,33]

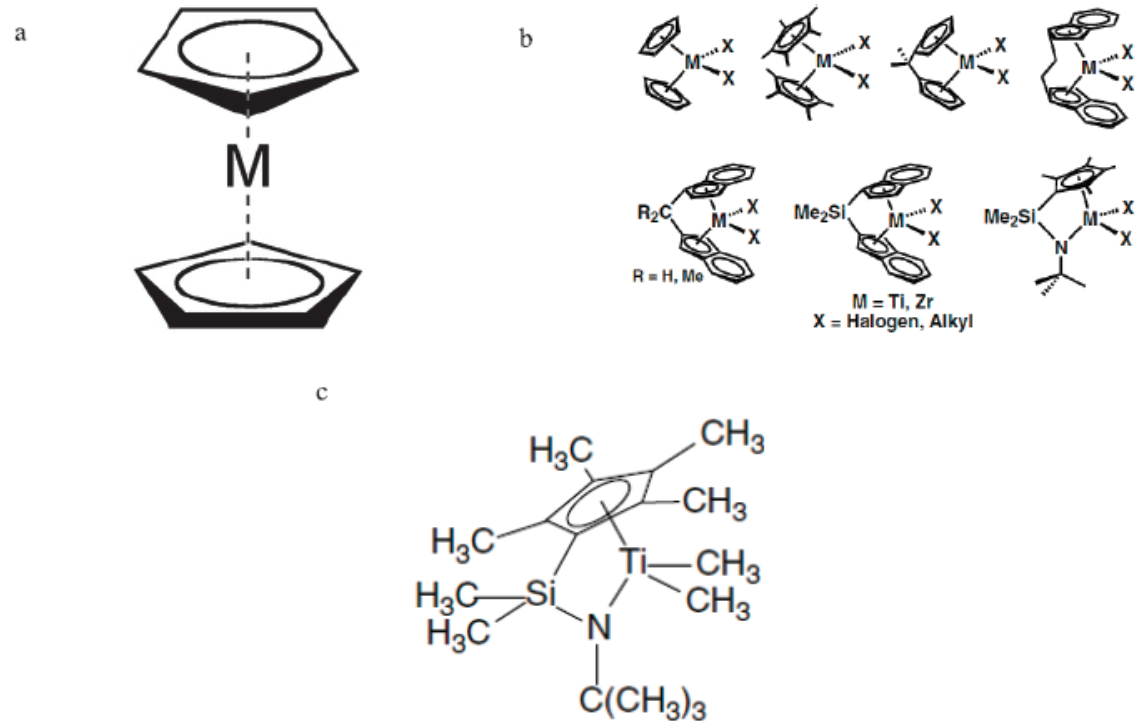

Figure 4: Representation of: a,b) metallocene catalysts and c) CGC. Reprinted with permission[11].

Metallocene catalysts can be used in their homogeneous form in solution processes, for which large ratios of aluminum to transition metal (at least 1000) are needed to obtain satisfactory catalyst activities, where an excess of MAO is required to shield adjacent active sites and prevent possible bimolecular deactivation reactions[20,34]. On the other hand, slurry and gas-phase processes require metallocene catalysts to be in their heterogeneous (supported) form.

The supporting of metallocene catalysts leads to several advantages in relation to the homogeneous catalyst, such as increased average molecular weight of the produced polymer, broader MWD allowing easier polymer processing ability, possibility of incorporating different catalysts to the same support to produce specific and tailored polymers.[20,34] Moreover, the needed aluminum to transition metal ratio is significantly reduced (at least 100) for heterogeneous metallocene catalysts, lowering the needed amount of the expensive MAO cocatalyst for slurry and gas-phase processes.

A commonly employed technique for the preparation of supported catalysts is the 'incipient wetness method', due to its simplicity in execution and reduced amount of solvent needed and byproducts produced. In this technique, the support is exposed in a controlled manner to a solution (ca. 100-150 % of the pore volume of the support) containing the active catalyst components. Capillary forces draw the solution into the pores, usually resulting in a homogeneous distribution of the active sites throughout the support particles. The solvent used to solubilize the active species is then removed through vacuum drying. [35–39] One approach to this technique is to first graft the alkyl aluminum (such as MAO) on the silica support and then introduce the metallocene over the modified support. This approach has been shown to shield the silica surface and avoid possible side reactions that could lead to catalyst deactivation or leaching from the support. [40–43] This two-step technique will be used, later in this study, for the synthesis of different supported metallocene catalysts.

Amongst the different materials commonly used as supports for heterogeneous catalysts (e.g. $MgCl_2$, clays, zeolites, γ-Al_2O_3*, silica), silica seems to be the most used in* the preparation of heterogeneous metallocene catalysts. Several aspects contribute to this preference, including the low cost of silica, ease of handling and the presence of hydroxyl groups throughout its structure that promptly react with metallocenes and cocatalysts. Physicochemical properties, such as the concentration of OH groups on the surface, can be easily tailored by thermal treatment. [44] Besides, the characteristic physical properties such as the particle size and pore structure particular to each type of silica play an important role in defining the catalyst behavior and allow a wide range of possible applications in catalyst synthesis.

A thorough discussion on more methods, supports and cocatalysts used for the preparation of heterogeneous catalysts can be found in the works of Bashir. [11]

The choice of material for supporting metallocenes will directly affect the behavior of the resulting catalyst and quality of the produced polymer. Besides, the physical properties of the support play a significant role on the growth and fragmentation of the growing particle, as will be discussed in more depth in the following sections.

1.3. Conclusion

Polyolefins are an integral part of our daily lives. The great economic attractiveness of such materials is due to their simplicity, low production cost and great versatility. Such a wide range of properties are achieved by different manufacturing processes and polymerization catalysts, each adapted to specific applications and commercial needs.

In the scope of the current project, we have introduced the several low-pressure processes (solution, slurry, gas-phase) and catalysts applied in the polyolefin production, with emphasis on polyethylene resins produced via low pressure polymerization processes. More precisely, our focus is on the use of heterogeneous Ziegler-Natta and metallocene catalysts in gas-phase processes, which cover an important portion of the global production of LLDPE and HDPE resins.

The fact of supporting a catalyst provides several economic advantages in relation to homogeneous catalysts. Nonetheless, it also adds complexities to the system, mainly related to the fragmentation step of the growing particle. Supporting a catalyst can lead to potential mass and heat transfer limitations, which are mostly related to the physical structure of the support particle, as will be viewed in more depth in the following sections.

2. Polymer particle growth: Heat and Mass transfer at early stages

As briefly introduced in the previous sections, heterogeneous catalysts cover about 70% of the world production of polyethylene resins. Using a catalyst in its heterogeneous form entails several advantages in relation to the unsupported counterpart, such as lowering the needed amounts of the costly cocatalyst and allowing for easier recovery of the produced polymer (in gas-phase), given that the support provides structure for the formation of solid polymer particles that are easier to handle.

Nonetheless, the act of anchoring the catalyst active sites on a solid support will affect the catalyst behavior and, therefore, the microstructure of the polymer. For the polymerization to happen, the monomer must reach the active sites, a process that is inherently more complex in heterogeneous systems and where issues related to heat and mass transfer limitations can arise. For instance, significant mass transfer limitations can lead to concentration gradients at the active sites, which can lead to inhomogeneous particle growth, impact the quality of the polymer and the functioning of the reactor. [45–47]

Moreover, significant heat transfer limitations can lead to overheating at the particle level, which can lead to catalyst deactivation, polymer melting, particle agglomeration and even reactor shut-down. Besides, given that several polymer properties (e.g. molecular weight, chemical composition) are temperature dependent, the quality of the final product can be compromised in case of overheating. [7,14,15]

As we can see, describing the particle growth in heterogeneous systems is a coupled mass and heat transfer problem and understanding the phenomena taking place during the polymerization is vital for ensuring satisfactory processes.

2.1. Particle morphology and fragmentation

When using heterogeneous catalysts, to reach the active sites, the monomer must be transported from the continuous phase in the reactor, through the external boundary layer around the particles, traverse the porosity of the solid support and, finally, through the internal boundary layer of forming polymer around the active sites. [45]

Moreover, the heat generated at the active sites must be evacuated in the opposite direction, so potential heat and mass transfer resistances (that could lead to catalyst deactivation, particle overheating, polymer melting and even reactor shut-down) accompany each of these steps. [47]

The potential internal and external mass and heat transfer resistances in a polymerizing particle are illustrated in Figure 5.

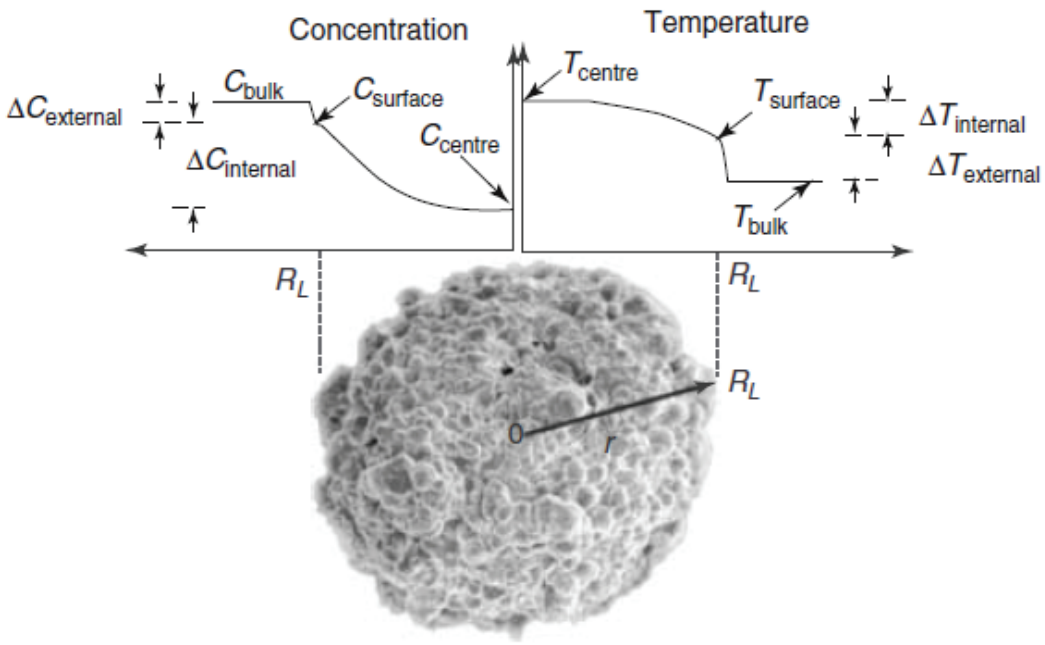

Figure 5: Potential temperature and concentration gradients in a heterogeneous system; reprinted with permission [45]

Once the reactive and inert species present in the continuous gas phase diffuse through the catalyst particle and to the active sites, the polymerization begins and the particle starts to grow.

The growth of the polymerizing particle happens in a complex process involving fragmentation and expansion in a series of mass transfer steps. The growing polymer gradually accumulates and fills the pores of the support, generating local stress build-up in the pores, which eventually leads to partial or total fragmentation of the inorganic support particle. The fragments of the original support remain bound by the polymer phase, transforming the particle into a continuous organic polymer phase in which the catalyst active sites are spread. [48–51]

The fragmentation step is essential for particle growth as it creates new void spaces that allow the monomer to continue diffusing to reach the active sites, thus leading to a cycle of particle growth by expansion.

If the fragmentation proceeds correctly and there is suitable balance between the mechanical strength of the particle and the rates of polymer production, one catalyst particle will transform into one polymer particle that can be up to 20 times larger than it was at the beginning. Ideally, the overall shape of the polymer particles (e.g. particle size distribution, overall particle shape) mimic those of the originating catalyst in what is called the *replication phenomenon*. [47]

Nonetheless, if the fragmentation process happens too quickly (e.g. if the support is too brittle or the polymerization rates are very high), the inorganic support might sinter into several small pieces before enough polymer has been formed to hold the fragments together and maintain the overall integrity of the growing particle. In this scenario, the resulting morphology might be compromised and there can be the formation of fine particles that can stick to the reactor walls and cause malfunction in various reactor systems. [15,47,48]

On the other hand, if the support is too firm or the stress produced by the polymer build-up is too little (low polymerization rates), the particle will not fragment, and the reaction will eventually be extinguished as the pores are filled with polymer and no more active sites become available. It becomes clear that the physical properties of the support, such as particle size and pore structure, play a role in the fragmentation step and correct catalyst activation. Indeed, previous studies have provided experimental evidence that bigger catalyst particles lead to more important mass transfer limitations. [11,52]

It is generally accepted that the risk of temperature gradients is most pronounced at early stages of the polymerization, when the ratio of the external surface of the growing particle is low compared to its volume – in other words, the capacity to evacuate heat is low compared to the amount of heat produced. Excessive temperature gradients at the particle level must be avoided particularly during the process of particle growth, as particle overheating can lead to issues such as polymer softening, particle agglomeration, clogging of the pores and catalyst deactivation. Besides, the properties of the polymer will certainly be affected as they are often temperature dependent. [46,47,53,54]

Moreover, if we consider the potential mass gradients depicted in Figure 5, it is reasonable to assume that longer diffusion paths for the monomer until reaching the active sites increase the chances of mass transfer limitations. Likewise, if the polymer being formed is hard or flexible, this is will certainly affect the monomer diffusion rates through the internal boundary layer. Therefore, the morphology of the growing catalyst/polymer particle and also the properties of the growing polymer will be influential in the particle growth process. [55]

It is clear that the process of particle growth and potential heat and mass transfer limitations will be critical for determining the properties and morphology of the final polymer. The polymer morphology evolution is, therefore, influenced by a number of factors that impact the particle fragmentation, including the catalyst physical structure, the rate of polymerization, the temperature at the particle level, as well as the physical properties of the growing polymer. As we can infer, good control of the fragmentation step during the nascent phase is key in ensuring what we consider to be satisfactory polymer morphology, meaning compact and well-defined particles that do not break into fine particles during the polymerization. [48]

A pre-polymerization step is frequently employed in order to avoid issues related to heat and mass transfer limitations in the begging of the reaction that can lead to uncontrolled particle fragmentation. This is done in a two-step process by starting the polymer production at mild reaction conditions (lower than usual pressures and temperatures) that prevent the particles to polymerize and fragment too quickly, thus ensuring proper morphology evolution. Once the risk of mass and heat transfer limitations has been eliminated (or reduced), the produced polymer is injected into the main reactor where the polymerization reaction continues in the standard conditions. Moreover, it has been shown that this pre-polymerization step also contributes to an increase in the catalyst activity. [47,48,56]

As we have seen in this brief presentation of the particle growth process, the fragmentation step is critical in the definition of the morphology and properties of the polymer. Additionally, several aspects are involved in ensuring a *controlled* fragmentation process, including the kinetics of the reaction, the morphology of the growing catalyst/polymer particle, the mechanical properties of the support and the conditions of heat evacuation from the reactor. At last, the fact that particle overheating and

potential mass transfer limitations are more pronounced at the reaction start contribute to the significance of the nascent phase to the whole polymerization process.

Understanding the reaction kinetics and particle growth has been focus of extensive research, mainly in the development of predictive models to provide insight on how the particles will behave in these critical early stages of the reaction. An overview of the main modeling approaches will be covered in the following section.

2.2. Single Particle Models (SPM)

As discussed thus far, the control over the polymer morphology and physical properties depends on a number of factors related to how the catalyst particle expands during the growth process, the conditions of heat evacuation as well as the physical properties of the growing polymer. Ultimately, the polymer properties are a function of the concentration and temperature profiles in the growing catalyst/polymer particles. It is then clear that understanding and predicting these phenomena is significant for industrial applications, as well as for the tailored design of new catalysts.

Significant efforts have been made on estimating the temperature and concentration gradients inside the particle, predicting how the fragmentation and morphology evolution take place, as well as the polymer properties, as described in the review article from McKenna and Soares. [48] Nonetheless, despite the advances in this area, one mathematical model that provides information on all the previous properties is still unavailable as it would be a very complex problem involving different length scales and a number of simplifying assumptions. A more realistic approach is the use of different single particle models (SPM) that focus on one or more of the aforementioned areas of interest and that are applicable to specific cases. Furthermore, such models can be categorized as polymer property and particle morphology models, according to their primary focus.

Particle morphology models, on the other hand, aim to describe the particle growth and fragmentation process at the nascent phase, which has been the focus of a number of works. [57–64] Nonetheless, such models require information on the material properties (such as evolving deformation and swelling parameters) that are not usually included in the performance single particle models. [48,55]

The fragmentation process is generally described by two descriptive modes. In the first, the support is said to fragment first at the larger macropores (which are more accessible to monomer) and progress to smaller pores as they become available. Other researchers propose a “layer-by-layer” or “onion-skin” fragmentation process, in which the polymer accumulation begins at the outer surface of the growing particle and proceeds to the center. [45,65] Nonetheless, there is still no consensus on the definitive mechanism for the fragmentation process, mainly due to the challenge of studying such phenomena experimentally, as will be reviewed in the following sections.

Polymer property single particle models are used to predict polymerization rates and some polymer properties such as MWD and CCD and the fragmentation process is usually assumed to be instantaneous. In general, polymer property single particle models consist of a set of mass and energy balances around a polymerizing particle, coupled with a reaction term. Although, prior to writing the mathematical problem, one must consider the initial morphology of the catalyst particle and how it will evolve as the reaction progresses. The particle morphology can then be assumed to be defined by two main particle growth model approaches, the MGM and PFM models illustrated in Figure 6.

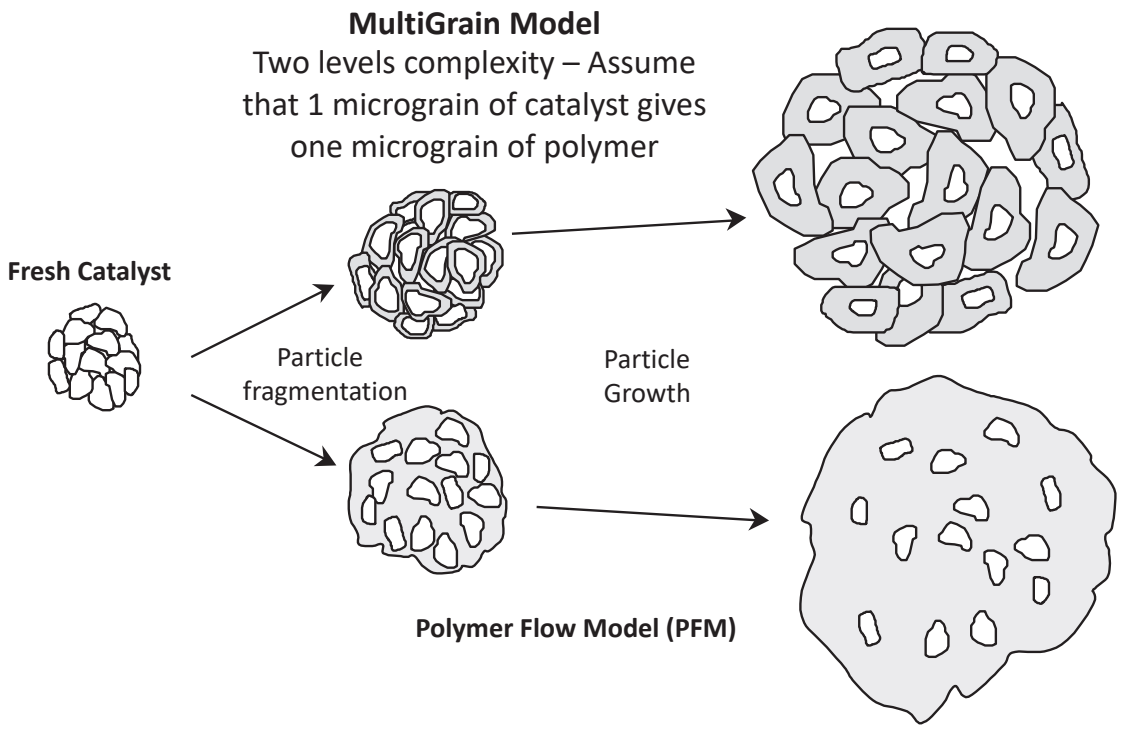

Figure 6: Commonly reported physical models for single particle growth [48]

The multigrain model was the first major effort in relating the particle morphology with the reaction mechanism. This model considers two levels of morphological organization including the macroparticle and microparticle. The growing polymer particle (or macroparticle) is assumed to be a cluster of micrograins, themselves consisting of catalyst fragments containing the active sites on the surface. The micrograins are assumed to be identical and organized in a perfectly homogeneous manner. The main assumption from the MGM model derives from SEM microscopy observations that confirm the presence of primary (macroparticle) and secondary (microparticle) morphological structures. [49–51,66–68]

Given the micrograins are assumed to be identical, they are equally exposed to the reaction monomer, so the polymerization rate becomes a function of the radial temperature and concentration gradients in the particle. In the scope of this work, our focus is on describing the phenomena taking place in the mesoscale level ($>10^{-3} – 10^{-2}$ m), where heat and mass transfer at the internal and external boundary layers are taken into account. The main limitation of the MGM model is the assumption that the internal structure of the polymer particle replicates that of the catalyst, which is not always true for heterogeneous catalysts. Besides, this model has extra levels of complexity which add very little to a mechanistic understanding of the particle growth and heat and mass transfer problem. For this reason, the polymer flow model (PFM) is often used as a simpler approach. [48]

The polymer flow model (PFM) is a simplified or pseudo-homogeneous approximation of the MGM model. Here, the polymerizing particle is assumed as a pseudo-homogeneous matrix where the growing polymer chains and catalyst fragments form a continuum. It is in this matrix that mass and heat diffusions take place. In the PFM model, the diffusion coefficient in the growing particle is used as an adjustable parameter that takes into account diffusion in the pore space and the polymer phase. Even though the PFM does not clearly describe the catalyst fragmentation and the heterogeneous character of the formed polymer particle, this model remains a valid choice for several applications and is

generally preferred due to its simplicity and the fact that it requires only the estimation of effective mass and heat transfer parameters of the polymer particle.

In all cases, the radial profile of monomer concentration in the growing particle can be described by the general diffusion-reaction equation in spherical coordinates:

$$\frac{\partial M_p}{\partial t} = D_{eff}\ \frac{1}{r^2}\frac{\partial}{\partial r}\left(r^2\frac{\partial M_p}{\partial r}\right) - R_p\ ; \tag{1}$$

With the following boundary conditions:

$$\frac{\partial M_p}{\partial r}(r = 0, t) = 0\ ; \tag{1a}$$

$$D_{eff}\frac{\partial M_p}{\partial r}(r = R, t) = k\left(M_b - M_p\right); \tag{1b}$$

And initial condition:

$$M_p(r, t = 0) = M_{p,0}\ ; \tag{1c}$$

Where M_p is the evolving concentration of monomer inside the particle, t is the polymerization time, r is the radial position in the particle, D_{eff} is the effective diffusion of monomer in the macroparticle and R_p is the polymerization rate. k is the mass transfer coefficient in the external film layer and M_b the bulk monomer concentration in the reactor. $M_{p,0}$ is the initial concentration of monomer in the particle. The value of R_p depends on the radial monomer concentration at the active sites.

Similarly, the temperature profiles are described as follows:

$$\rho_p C_p\frac{\partial T_p}{\partial t} = k_c\ \frac{1}{r^2}\frac{\partial}{\partial r}\left(r^2\frac{\partial T_p}{\partial r}\right) - \left(\Delta H_p\right)R_p\ ; \tag{2}$$

With the following boundary conditions:

$$\frac{\partial T_p}{\partial r}(r = 0, t) = 0\ ; \tag{2a}$$

$$k_c\frac{\partial T_p}{\partial r}(r = R, t) = h\left(T_b - T_p\right); \tag{2b}$$

And initial condition:

$$T_p(r, t = 0) = T_{p,0}\ ; \tag{2c}$$

Where ρ_p is the particle density, C_p is the heat capacity of the particle, T_p is the particle temperature, k_c is the particle effective thermal conductivity and ΔH_p is the heat of polymerization. h is the film convective heat transfer coefficient and T_b is the bulk temperature. $T_{p,0}$ is the initial particle temperature.

Both the MGM and PFM models have been applied to study mass and heat transfer limitations at the particle level. The MGM model has been widely used to study and predict mass and heat transfer resistances in slurry and gas phase polymerizations with different monomers and comonomers using supported Ziegler-Natta catalysts. [53,69–78]

A comprehensive work on modelling olefin polymerization at the meso-scale has been done by the research group of Ray et al. [53,54,72,74] One of the most significant conclusions from these works with the multigrain model were that mass and heat transfer resistances are more pronounced at the beginning of the polymerization reaction. [49,50] Kosek et al. observed similar results for the temperature gradient inside the particle, and extended their study to include dynamic changes in the catalyst activity.[79] The observations on particle overheating are in agreement with those achieved by Yiagopoulos et al.[80], who applied a PFM-based model including internal and external mass and heat transfer resistances. The authors observed that there can be considerable particle overheating at early stages of the reaction for highly active catalysts, which can be drastically reduced by implementing a pre-polymerization step.

2.3. Conclusion

The act of supporting the catalyst active sites onto a solid support provides advantages in relation to homogeneous catalysts, such as the need for less cocatalyst and ease in recovery of the produced polymer. Nonetheless, heterogeneous catalysts are inherently more complex than homogeneous systems, especially in terms of particle growth and possible transport limitations that accompany the fragmentation of the solid support. Concentration and temperature gradients can potentially exist in the internal and external boundary layers of the polymerizing particle and very few experimental settings are adapted to studying such phenomena in gas-phase conditions, as we will see in the following sections and throughout the current work.

Single particle models are often employed to understand and predict potential heat and mass transfer limitations, as well as to estimate polymerization rates and polymer microstructure. The most commonly used single particle models (PFM and MGM models) for olefin polymerization were introduced in the previous sections, highlighting the importance of the solid support on the fragmentation step, proper catalyst activation and overall good quality of the polymerization reaction.

Studies carried out applying the multigrain model have resulted in several insights concerning transport resistance in supported catalysts and, most importantly, that such effects are more pronounced at the beginning of the polymerization reaction. At last, the particle growth evolution is a sensitive process involving fragmentation and expansion, which are crucial for the polymerization process and quality of the final polymer. The physical properties of the catalyst support are critical in ensuring a satisfactory fragmentation step.

It should be evident from this short discussion that if we are to develop a mechanistic SPM, we need to be able to have more accurate information of what really occurs in the polymer particles, especially during the nascent polymerization step. Given the length and, in particular, time scales of the events involved here, it would be very useful to have tools that can allow us to experimentally explore these issues.

3. Studying early stages of the polymerization

As introduced in the previous sections, the development of particle morphology is usually dictated by the catalyst particle break-up process. Besides, modelling studies indicate that heat and mass transfer resistances are more pronounced at the early stages of the polymerization reaction. It is generally accepted that the quality of the reaction outcome is highly dependent on the development of the growing catalyst/polymer particle during the first seconds, or fractions of a second, depending on the catalyst being used.

Thus far, it is clear that, given the economic importance of the polyolefin market, understanding all steps of the polymerization process is of great interest; including the so-called nascent phase of the polymerization, which refers to the first fractions of a second up to a few tens of seconds of the reaction.

The nascent phase englobes very short time frames that might seem negligible in relation to the residence times applied in industrial conditions (10^{-1} seconds up to a couple of minutes). These moments are, nonetheless, critical in terms of ensuring proper catalyst activation, good development of the particle morphology and heat transfer limitations that could lead to reactor shut-down. The nascent phase of the polymerization is, therefore, crucial in ensuring the quality of the entire process.

3.1. Introduction to experimental studies at early stages

There has been a growing interest in the experimental study of the nascent phase of olefin polymerization over the past 20 years as its importance was recognized by the scientific community. Investigations on early stages of the polymerization can provide insights on aspects related to the evolution of catalyst kinetics, polymer properties and particle morphology, thus being valuable for the improvement of industrial processes and design of new catalysts.

Nevertheless, the main drawback to studying these early stages is the lack of properly adapted apparatus that allow to collect data in meaningful (industrially relevant) experimental conditions. Experimental studies at short reaction times and under industrially relevant conditions is definitely not an easy assignment.

Several aspects, theoretical and practical, contribute to the challenge of studying early stages experimentally:

- The short time scales that define particle morphology and polymer properties impose a challenge in ensuring stable experimental conditions;
- The rapidity of the corresponding changes, such as the particle fragmentation, are difficult to capture with precision;
- The high catalyst activities at the reaction start-up and the risk of particle overheating;
- The small length and time scales in play: catalyst supports of tenths of microns, pores of tenths of nanometers and fragmentation times of few seconds;
- The fact that the polymerization takes place at several bars in an oxygen-sensitive environment and is highly sensitive to other impurities such as humidity.

This is not to say that progress has not been made on the study of the nascent phase. Several techniques, briefly introduced in this section (more examples found in the works of Tioni and Mckenna et al.[46,81]), have been used as attempts to study different aspects of the early stages of olefin polymerization.

In the earliest attempt to study early stages, mercury porosimetry and nitrogen adsorption were applied to study fragmentation patterns on Phillips catalysts polymerized with ethylene. Different studies carried out in slurry (McDaniel et al.)[82] and gas phase (Weist et al.)[83] indicated similar trends, suggesting that the particle fragmentation initiated at the bigger pores of the silica support, a different behavior than the 'layer-by-layer' mechanism proposed by Chiovetta et al.[57,58] . Nonetheless, these studies were carried out under low conversion and mild reaction conditions, very different from those obtained in industrial scales.

Offline microscopy analysis (mainly SEM, TEM and EDX) is perhaps the simplest technique to study early stages, in which the polymerization reaction is interrupted after a short time and the structure of the recovered particles is observed. A number of groups used this technique to elucidate interesting phenomena. Fink et al.[84–88] observed an induction period of a few minutes for the activation of silica supported metallocene catalysts in slurry propylene polymerization. SEM analysis indicated the formation of a highly crystalline polymer layer, suggesting mass transfer limitations at the active sites (thus the observed induction period), that were overcome once the particle fragmentation was completed and more active sites became available. Nevertheless, despite the simplicity of microscopy analysis techniques, the experimental conditions used in the polymerization process are not always representative of industrial processes. For instance, if a highly active catalyst is employed, recovering low polymer yields requires very mild reaction conditions that can slow down the fragmentation process and morphology evolution.

Computer X-ray microtomography (CXRT) is a non-invasive technique that allows 3D observations of a solid structure by applying an X-ray beam and recording the photons that traversed the sample. This technique was first applied by Conner et al.[89–91] for systematically studying catalytic fragmentation. The authors studied HDPE polymers with yields between 11 and 200 g/g, deriving from silica-supported chromium catalysts. The obtained 3D topographies showed non-uniform distribution of fragments and void spaces within the particles, with larger fragments visible on the particle exterior for higher yields and bits of unfragmented support still visible for lower yields. The authors related this behavior to non-homogeneity of the active sites throughout the polymer phase, as well as the fact that the monomer transport length to reach the active sites is smaller than the particle diameter. This is a very promising technique if the analyzed polymers are obtained under controlled and representative conditions.

A similar technique called laser scanning confocal fluorescence microscopy was applied by Jang et al.[92] to study particle fragmentation of supported metallocene catalysts at varying reaction temperatures in ethylene slurry polymerization. This technique consists of incorporating a fluorescent dye in the catalyst support, which is then detected by moving laser scanning to generate a 3D image of the analyzed particle. This is a promising technique for obtaining a 3D distribution of the fragments at the interior of the particles, but one must make sure there are no interactions between the fluorescent dye and the active sites. Even if CXTR microtomography and confocal microscopy allow evaluating the particle morphology, these techniques provide no information on the evolution of the particle morphology or possible temperature gradients during the reaction.

Online techniques have also been applied to gain insight on the phenomena taking place during the polymerization reaction. The combination of micro reactors (with a transparent window) with video microscopy showed to be a useful technique for studying different aspects of gas phase polymerization reactions, such as measuring the catalyst activities without manipulating the particles. The group of Weickert was the first to apply this technique in industrially relevant conditions (up to 70°C and 35 bar) to study homo and co-polymerization reactions with ZN catalysts in gas phase.[93,94] The technology developed by Weickert was later adapted and used by Hamilton et al.[95] to study the behavior of active silica supported metallocene catalysts in gas phase ethylene and propylene polymerization at high temperatures and pressures (80-100°C, 21 bar). The authors observed two maximum activity peaks during the reactions, which they assigned active sites being exposed due to particle fragmentation. Nonetheless, this technique provided no information on the temperatures at the particle level.

Nonetheless, when combined with online Infrared measurements, video microscopy allows measuring both the reaction kinetics and temperature data. Using this approach in small gas-phase reactors, Hamilton et al. [95] observed that introducing particle clusters in the reactor led to higher temperature gradients than those observed in case of single particles. While this technique is useful in estimating the reaction rates of individual particles, the fact that the gas is stagnant exposes the particles to completely different heat transfer limitations than those expected in an industrial reactor.

At last, melt microscopy was applied to study internal aspects of the particles that were previously done only by SEM and EDX. Abboud et al.[96] used this technique to study the evolution of fragment size distribution and location with time. Polymers produced under mild conditions (50°C, 5 bar propylene) using different supported ZN and metallocene catalysts were melted at 170°C under a microscope. Following, the melting and crystallization phases were interpreted with a software. The authors observed that the fragment size and distribution was dependent on the catalyst support. Nevertheless, this technique provided no kinetic data, which made it difficult to correlate the morphological observations with the fragmentation process.

As we have seen, each of the aforementioned techniques is suited for a specific facet of the study of early stages, and they each present a number of limitations, mainly related to the use of mild reaction conditions that are not representative of the phenomena taking place in industrial scales.

These topics are discussed in more depth in a review article from our group, [46] in which it was clearly stated that if one wishes to preserve the *realistic* nature of the experiment, stopped flow reactors appear to be the practical and effective way to do so. It is, in large part, for this reason that the current thesis is focused on further developing and improving such tools.

3.2. The stopped-flow technique

Out of the several techniques employed to study different aspects of the nascent phase of the polymerization, the stopped-flow technique is the most promising if one wishes to preserve the *realistic* nature of the experiment, allowing conditions that are representative of industrial scales. [46]

At the risk of over-simplifying, the stopped-flow technique consists of rapidly mixing the reactant components so the reaction will take place in a well-defined environment for a specific time. Subsequently, the reaction is quickly and precisely quenched by changing the reaction environment. The ability to perform reactions in short and well-defined periods of time under meaningful reaction conditions makes the stopped-flow technique the most promising for studying nascent stages of olefin polymerization. [46,97]

The stopped-flow technique was first applied in the early 1940s for studying kinetics in fast enzyme reactions. [98,99] When used to investigate catalytic olefin polymerizations, the technique proved to be a powerful means for elucidating kinetic mechanisms and obtaining real-time information concerning active species, reaction intermediates and other kinetic parameters for heterogeneous [100–104] and homogeneous catalysts [105–107], as well as looking at the development of particle morphology. [108–110]

Given the physical constraints imposed by gas phase and slurry phase polymerizations, stopped-flow reactor configurations will be quite different than those observed in large scales. It is less challenging to control flows of small particles suspended in a liquid than those suspended in a gas, meaning that slurry phase stopped flow experiments can be carried out in either flow-through or fixed bed conditions. Nevertheless, as will be discussed in the following sections, the options for gas phase reactions are limited.

3.2.1. *Stopped-flow reactors for slurry phase polymerization*

An example of a stopped-flow set-up for solution and slurry reactions can be seen in Figure 7. Vessels A and B contain the polymerization reactants such as catalyst, co-catalyst and monomer. The polymerization reaction is initiated when the reactants come in contact (on the T mixer C). The reaction duration is determined by the length of the tube D and the pressure drop. The reaction will be instantly quenched when entering vessel E, where a suitable quenching agent is placed.

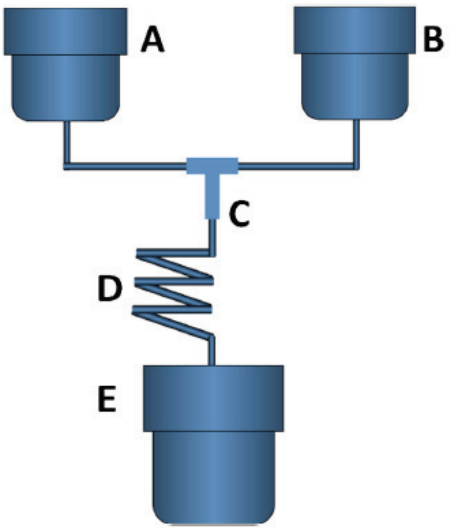

Figure 7: Schematic view of slurry phase stopped-flow reactor. Vessels A and B contain the reactants (catalyst, co-catalyst, monomer). Polymerization is initiated on the T mixer C, with reaction duration determined by the length of the tube D. The reaction is quenched when entering vessel E. Reprinted with permission. [46]

Most of the research conducted on nascent polymerization in solution and slurry phases has used the type of set-up described above, given the simplicity and effectiveness of this technique. As discussed in the following paragraphs, several works conducted with unsupported catalysts indicate that certain catalysts show an induction period during polymerization and also that only a small fraction of the catalyst actives sites are actually active for polymerization.

Keii et al. [111] pioneered in using the stopped-flow technique (Figure 7) in kinetics investigations using a supported Ziegler-Natta catalyst. Using a similar set-up, Kaminaka and Soga [112,113] investigated several aspects related to the kinetics of supported Ziegler-Natta, amongst them the nature of the active sites, determining true kinetics parameters, the effects of hydrogen and catalyst preparation.

The group of Fink et al. applied the stopped-flow technique coupled with C-NMR to elucidate mechanisms of monomer insertion in soluble Ziegler Natta catalysts as well as determination of kinetic parameters. These studies, in which polymerizations were carried out at about 220 K, showed that the slowest insertion step is the first monomer insertion. [114,115]

Studies on the activation of homogeneous metallocene catalysts (Cp_2TiCl_2-based precursor) with MAO in ethylene polymerization were carried out by Shiono et al. [105] using a similar apparatus described above. While working under mild conditions (20°C, 1 bar), they were able to demonstrate the presence of an induction period at short reaction times (30 ms) as well as a nonlinear increase of the polymer yield and number average molecular weight (Mn) at short reaction times. An induction period was also observed by Liu et al. [102,103], when performing solution co-polymerizations with 1-hexene in stopped-flow reactions.

Busico et al. [106] applied the stopped-flow technique to study kinetics at different temperatures with a homogeneous metallocene catalyst. They found that the concentration of active sites is significantly lower (5 to 25%) than the analytical Zr concentration in the catalyst. They also observed higher rates of chain propagation (*Rp*) than at experiments performed under *standard* conditions. Kinetic studies

conducted by Song et al. [107] with homogeneous metallocene catalysts also observed low fractions of active sites, as well as a non-linear dependence of yield with increasing reaction times.

Works conducted by Ranieri et al. [116] using the stopped-flow technique to study kinetic parameters of molecular catalyst and showed that only 25% of the catalyst sites were active in polymerization. The authors concluded that the stopped-flow technique is not adapted for the study of highly active catalysts, as quasi-living polymerization conditions cannot always be achieved, even with very mild experimental conditions. In addition, they found that variable pressure drops across the system during the polymerization also made it difficult to achieve short times accurately with the device that they were using.

Di Martino et al. [108,110,117] modified the set-up used by Keii et al. to increase the range of reaction conditions, allowing one to work up to 90°C and 20 bar. They also used a CO_2/heptane quenching solution that allowed one to recover the particles and study their morphology on the undamaged support. For the first time in the literature, the authors concomitantly followed the kinetic profiles of the catalyst as well as the evolution of the polymer properties with reaction time.

While working with supported ZN catalysts, Di Martino et al. [109,110,117] observed an unusual kinetic profile at short reaction times, with very high catalyst activities at early stages that rapidly decreased (after about 1s) to activity values obtained at *standard* reaction conditions (1L semi-batch reactors, longer reaction times). They attributed this behavior to the complex nature of the catalyst chemistry, and perhaps to the presence of 'one-off' active sites that polymerized rapidly but also deactivated rapidly.

A similar kinetic behavior was previously observed by Busico et al. [106] when working with homogeneous systems, which suggests that reaction rates could be more linked to the chemistry of the catalysts in hand than to physical factors such as mass and heat transfer limitations. Di Martino et al. [117] also studied the effect of pre-contacting the catalyst with its co-catalyst on the kinetic profiles and particle morphology. The authors were able to show the presence of uneven reaction rates when the catalyst is activated in situ, leading to undesirable particle morphologies (observed the particle shell expanding more than the core). On the other hand, satisfactory particle morphologies were obtained with pre-activated catalysts. This demonstrated the impact that heterogeneous site distributions can have on the resulting particle morphology. Another interesting observation from these authors was an increase of melting temperatures with reaction time (from 118 °C at 40 ms to 131 °C at 1 s), as well as low crystallinities (20% at 40 ms) that increased with reaction time. The authors attributed this behavior to the high reaction rates in the reaction start, which could lead to highly disordered chains, thus limiting the crystallization process. However, it is more likely (see below) that this is due to geometric constraints.

In a more recent study by Taniike et al. [118], the stopped-flow technique was used to follow the morphology development for supported ZN systems. By combining SEM, mercury porosimetry and BET analysis, the authors elucidated key aspects related to the particle fragmentation and filling of the particle pores by the forming polymer. The authors observed the macropore filling accompanied by decrease in pore diameter, thus concluding that macropores are the first to be filled by the growing polymer and, therefore, have a dominant role at early reaction stages.

A limitation found in most works in solution and slurry stopped-flow reactions was the use of quenching agents that disrupted or destroyed the particle support, thus disabling the possibility of following the morphology of the particles. In addition, with the exception of the work done in our lab by Di Martino et al., a limitation in a number of these studies is the fact that they were carried out under mild conditions (low pressures and temperatures). [109,110,117]

3.2.2. *Stopped-flow reactors for gas phase polymerization*

The main challenge in studying gas-phase polymerization reactions at early stages is to mimic the conditions found in industrial reactors and, in particular, the heat transfer conditions that are governed by the relative gas-particle velocities and can be strongly influenced by the composition of the gas phase. For that, it would be necessary to expose the catalyst particles to several different process gases, at moderate pressures and relative gas-particle velocities. Clearly, making a miniaturized fluidized bed reactor is neither practical nor representative of a larger scale device given the reaction hydrodynamics are scale-dependent.

One promising manner of applying the stopped-flow technique in gas phase polymerizations is to cause monomer to flow over a fixed bed of dispersant and catalyst for a defined amount of time, then abruptly stop the reactant flow and the instantaneously quench the reaction by changing the reaction environment by, for example, applying the flow of a quenching gas such as CO_2. While this is clearly not what happens in a lab or industrial scale reactor, the essential component of the experiment is to expose the particles to both reasonable reaction conditions *and* heat transfer conditions.

In a broad-spectrum description, at the single particle level, gas phase heat transfer is governed by the relative gas velocity *relative to the particles*. Therefore, using a fixed bed reactor that can expose the particles to the same range of relative velocities allows one to explore different conditions of heat transfer at temperatures and pressures representative of a full-scale production.

Polymer particles can be recovered with little effort and their morphology and properties can be investigated at early reaction stages. The gas phase stopped flow reactor also allows one to follow the evolution of the temperature in the reaction medium by applying a heat balance around the reactor, as proposed by Tioni et al. [119] This is particularly useful given the known heat transfer limitations for heterogeneous systems operated in gas-phase.

The first stopped-flow reactor adapted to gas-phase olefin polymerization was developed by Silva et al. in 2005.[120] The micro fixed-bed reactor developed by Silva et al., seen in Figure 8, proved to be a useful tool for studying morphology, fragmentation and reaction kinetics on supported catalysts for reaction durations as short as 100 ms. This set-up, however, did not allow for controlled flow rates and presented difficulties associated with back flow at low pressures and temperature gradients in the reaction bed. This eventually prompted a redesign of the reactor in the C2P2 lab by Olalla et al (2008)[121] with further improvements by Tioni et al. (2012). [97]

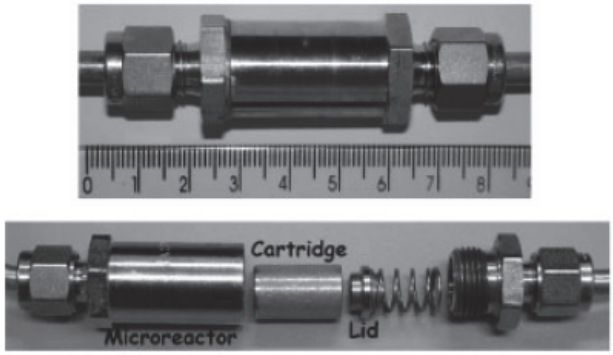

Figure 8: Fixed-bed micro reactor developed by Silva et al. Reprinted with permission.[120]

The reactor designed by Olalla et al.[121] and later optimized by Tioni et al.[97], seen in Figure 9, consisted of an improved configuration of the first version by Silva et al.[120], including solenoid valves for accurate feed rates, as well as a reduced aspect ratio (a cylinder of d=0.5 cm and L= 1 cm) that aimed to lower the temperature gradients in the reaction bed. The reactor consisted of a metal chamber closed with a fritted metal cartridge with thermocouples at the entry and exit of the reactor that allowed to measure the inlet and outlet gas temperatures.

The catalyst/dispersant mix was packed inside the cartridge and placed in the metal chamber. For the polymerization reaction, process gas was caused to flow through the bed under a specific set of conditions for a predetermined period of time. At the end of the specified time of polymerization a solenoid valve automatically switched from the reactive gases to CO_2, which rapidly poisoned the catalyst and quenched the reaction without destroying the particles. This allowed to obtain kinetic data by gravimetrically following the polymer production, as well as to obtain information on the polymer morphology and physical properties. However, in order to measure the polymerization rate as a function of time, it was necessary to perform one experiment per data point.

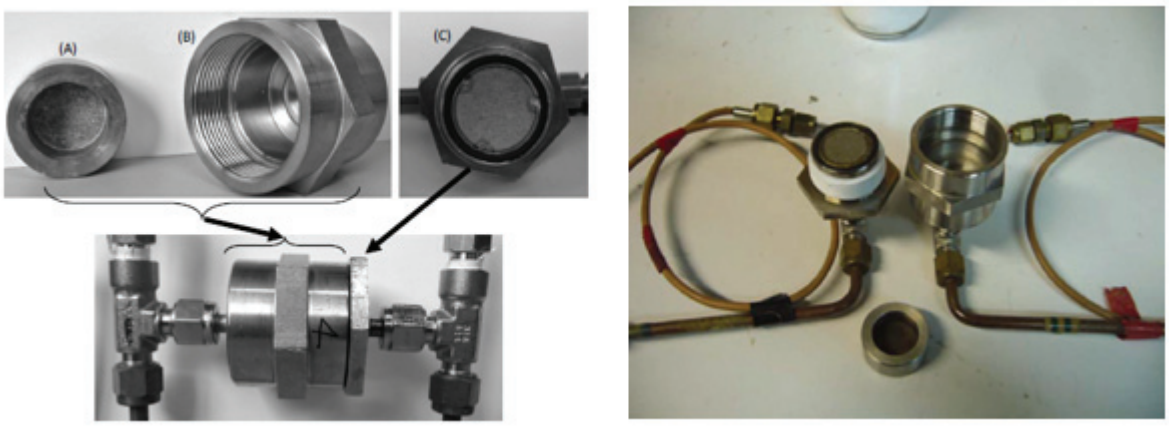

Figure 9: Stopped-flow reactor developed by Olalla et al. Reprinted with permission.[97]

In a subsequent study, Tioni et al. used the stopped-flow reactor to study the influence of various reaction conditions on the heat transfer regime at start up conditions. [46,119] Tioni et al. sought to find optimum reaction conditions in order to maximize the heat removal at the particle level. The authors concluded that a combination of factors should be applied to obtain optimum performance of the set-up and avoid thermal runway while producing enough polymer for analysis, including: increased

thermal conductivity of the gas feed obtained through different gas compositions, increased linear velocity of the gas phase and the properties of the seedbed particles (decreased particle size of the dispersant appeared to improve the heat-transfer coefficient from solid to gas, undoubtedly by increasing the conduction portion of the heat transfer). Details of the experiments can be found elsewhere. [81,97,119]

In addition to studying the influence of certain reaction parameters on heat transfer, Tioni et al. observed an effect of constrained crystal growth in the silica pores by following thermal properties of the polymers at increasing reaction times, leading to a suppression of the crystallization temperature. The authors used the notion of constraining porosity introduced by the research group of Woo et al.[122,123] The idea is that polymer formed in the pores that have not yet fragmented suffer a space confinement that affects the crystallization, limits crystal growth and reduces the crystallization and melting temperatures. As the polymerization progresses, more polymer grows free from this confined space until reaching temperature peaks that are characteristic of bulk polymer (or polymer formed after several minutes). The use of differential scanning calorimetry thus allowed to see the nano and meso pores of the silica 'disappear' as a function of time during the initial stages of reaction, thus providing a time frame for the particle fragmentation. While the results obtained by Tioni et al. [124] were for a single type of silica and one catalyst formulation, it would be interesting to use this type of analysis as one additional tool for understanding catalyst activation and morphology development.

Tioni et al. proposed a heat balance around the stopped-flow reactor using the inlet and outlet gas temperatures recorded during the experiment. This heat balance allowed the authors to calculate an upper estimate of the particle temperatures inside the reactor. [119] Regardless of the careful choice of reaction parameters to avoid thermal runway, Tioni et al. estimated that the particle temperatures could raise up to 20°C in the first few seconds of the reaction. Being able to estimate the particle temperature presented a significant advantage with respect to other online techniques (such as IR Microscopy) since it allowed one to study kinetics in realistic conditions with a reasonable approximation of the particle temperature rather than relying only on the gas temperature. [119] The heat balance described by Tioni et al. is described as follows.

By using the polymer yield (Y) and knowing the mass of catalyst used in the experiment (m_{cat}) and the enthalpy of polymerization ($-\Delta H_p$), one can calculate the amount of heat generated (Q_{gen}) during the reaction by equation (1-1).

$$Q_{gen} = Y m_{cat(-\Delta H_p)} \quad (1\text{-}1)$$

The total amount of energy transferred to the gas phase ($Q_{transfer}$) in time t is given by equation (1-2), with $\dot{q}$ the volumetric flow rate of the gas phase, ρ_g the density of the gas, $C_{p,g}$ the heat capacities of the solid and gas phases, $T_{g,out}$ and $T_{g,in}$ the recorded inlet and outlet experimental temperatures.

$$Q_{transfer} = \dot{q}\rho_g C_{p,g} \int_0^t (T_{g,out} - T_{g,in)dt} \quad (1\text{-}2)$$

If one neglects heat losses to the environment and to the reactor itself, the maximum amount of energy that is transferred to the solid phase *(salt, catalysts, polymer)*, Q_{solid}, is the difference between the heat generated during the reaction Q_{gen} and the heat removed by the gas phase $Q_{transfer}$, described in equation (1-3).

$$Q_{solid} = Q_{gen} - Q_{transfer} = m_{solid}\, C_{p,solid}(T_{solid} - T_0) \quad (1\text{-}3)$$

Here, T_0 is the initial temperature of the solid temperature (assumed to be the same as the initial temperature of the gas phase), m_{solid} is the mass of the bed (assumed to quickly reach uniform temperature) and $C_{p,solid}$ is the total heat capacity of the bed. Therefore, reaction (1-3) can be rearranged to provide an estimate of the average temperature of the solid particle in the reactor (assuming negligible temperature gradients in the particles[48]).

$$T_{solid} = T_0 + \frac{Q_{gen} - Q_{transfer}}{m_{solid}\, C_{p,solid}} \quad (1\text{-}4)$$

This provides us with as upper bound of the estimate of the particle temperatures, as heat absorption by the salt particles around the catalyst and by the metal frit were neglected, as well as any heat loss to the surroundings. Calculations showed that even under controlled heat transfer conditions, the particle temperature could increase by 15-20°C in 2 to 5 seconds, sometimes reaching values responsible for polymer melting. This implies that the assumptions made by Tioni at al. for the heat balance (such as uniform temperatures in the bed) were not necessarily valid.

A detailed modelling work on this set-up was carried-out by Browning et al.[125–127], in which a dynamic model of the stopped-flow reactor used by Tioni et al., represented in Figure 10, was developed and validated. The results obtained by Browning et al. allowed one to interpret the temperature rises observed experimentally and demonstrated that there was the possible existence of non-negligible temperature gradients inside the reactor despite its small volume.

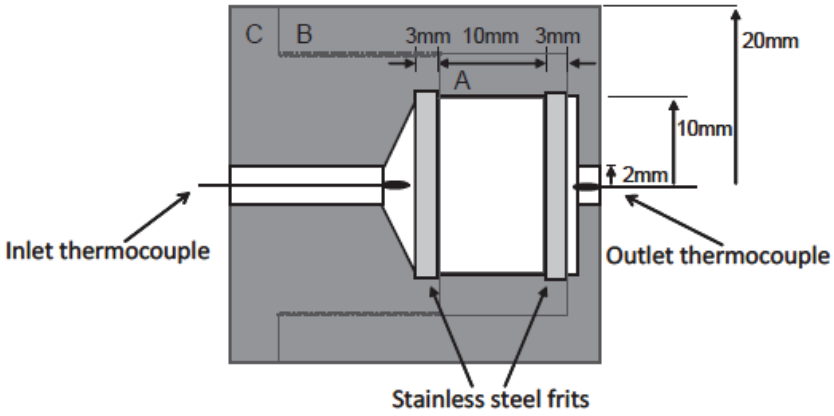

Figure 10: Section of the stopped-flow reactor used by Tioni et al. and modelled by Browning et al. Reprinted with permission.[126]

Simulations showed that temperature excursions exceeding the melting point of polyethylene were possible at early stages of the polymerization (2s), as shown in the modelling results shown in Figure 11, but not necessarily detected at the outlet. Browning et al. attributed this to the high heat capacity of the stainless steel frit at the reactor exit, which could partially absorb the energy produced at the reaction zone and, consequently, mask the effect of the sudden temperature rise of the reaction bed. Therefore, the temperatures measured experimentally at the reactor outlet didn't necessarily reflect temperatures inside the reactor.

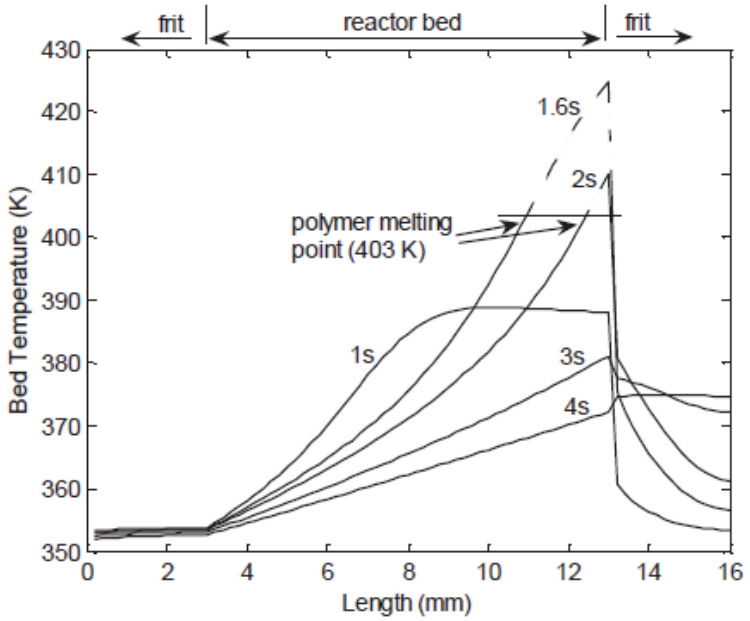

Figure 11: Calculated temperatures of gas and inert solid along the stopped-flow reactor at different reaction times, performed by Browning et al. Reprinted with permission.[126]

3.3. Conclusion

The early stages of the polymerization, also referred to as nascent phase, encompass the first fractions of a second up to a few tens of seconds of the polymerization reaction. The early stages are critical in ensuring the quality of the entire polymerization process, as it is then that the catalyst activation takes place, the particle morphology is defined and when heat transfer limitations are at their highest risk.

Collecting experimental data on the nascent phase of the polymerization is challenging for several reasons including the short time and physical scales at play, the rapidity of the corresponding changes, the high catalyst activities coupled with the risk of particle overheating, plus the fact that the polymerization takes place at several bars in an environment that is highly sensitive to oxygen and impurities.

Several experimental approaches have been applied to investigate different aspects of the nascent phase, but it appears that for gas phase polymerization the stopped-flow technique is the most promising in terms of preserving experimental conditions that are representative of industrial scales.

The stopped-flow technique in gas-phase conditions has been applied to investigate aspects related to heat transfer, particle fragmentation and morphology evolution. Studies from Tioni et al. provided insight on the evolution of the particle temperature inside the reactor, the peculiar crystallization behavior on inorganic supports and, finally, how thermal properties of the polymer could be used as ‘sensors’ for framing the particle fragmentation. Nonetheless, modelling studies carried out by Browning at al. demonstrated the possible existence of non-negligible temperature gradients inside the reactor, despite its small volume.

To the best of our knowledge, experimental studies on nascent polymerization in gas-phase have not been conducted elsewhere, so the only work discussed in the open literature was that presented above.

4. Overall Conclusions

In this literature review chapter, we have highlighted the crucial role that initial stages of the polymerization reaction have on the quality of the entire production process and properties of the final polymer.

Given the importance of polyolefins in the global market and in our daily lives, it is not an understatement to say that understanding all stages of the polymerization process is necessary in order to continue refining existing industrial processes and designing new catalysts.

In the scope of the current project, focus was given to low pressure polymerization processes with emphasis on polyethylene resins produced with heterogeneous Ziegler-Natta and metallocene catalysts in gas-phase processes.

As we have reviewed, heterogeneous catalysts offer several advantages in relation to their homogeneous counterparts, such as reduced needed amounts of the activating cocatalyst (which are often more expensive than the catalyst itself) and easier recovery of the produced polymer. Nonetheless, heterogeneous systems are accompanied by several complexities mainly related to the morphology development of the growing particles. The fact of supporting a catalyst, despite its advantages, increases risks related to mass and heat transfer limitations, which are mostly related to the physical structure of the support particle.

Several modelling efforts have been made to better understand such transport limitations, as well as to predict polymerization rates and microstructures of the final polymer. Single particle models, such as the commonly used Polymer Flow Model (PFM) and Multigrain Model (MGM) are often employed to describe the growth of the polymerizing particle and estimate potential temperature and concentration gradients. As seen throughout this chapter, the evolution of the particle growth is a delicate and complex process involving fragmentation and expansion, which are crucial for the entire course of the polymerization reaction. Moreover, the physical properties of the catalyst support are critical in ensuring a satisfactory fragmentation step, particle growth and good morphology development.

The very beginning of the polymerization reaction, also referred to the nascent phase, describes the first fractions of a second up to a few tens of seconds of the polymerization process. As several studies have pointed out, these early stages are crucial for the quality of the whole polymerization process. At the nascent phase, the catalyst activation takes place, as well as the definition of particle morphology. Moreover, heat transfer limitations are at their highest risk and there is the real risk of particle overheating which could lead to several complications such as polymer melting, particle agglomeration and reactor shut-down.

Studying these initial moments of the reaction is a challenging task given the short time and physical scales at play, the rapidity of the corresponding changes, the high catalyst activities coupled with the risk of particle overheating, plus the fact that the polymerization takes place at several bars in an oxygen sensitive environment that is highly sensitive to oxygen and impurities.

Several experimental approaches have been carried out to investigate different aspects of the nascent phase in homogeneous and heterogeneous systems. Nonetheless, the stopped-flow technique is the

most promising in terms of preserving experimental conditions that are representative of industrial scales.

The stopped-flow technique has been previously applied to investigate aspects related to heat transfer, particle fragmentation and morphology evolution in gas phase. However, as we have seen in the previous sections, options for studying early stages in gas-phase conditions are limited and the existing tools still encounter issues related to poor heat evacuation that are less than ideal if one wishes to evaluate the kinetic performance of heterogeneous catalysts under meaningful conditions.

Finally, we are convinced that there is room for improvement on the existing gas-phase stopped-flow reactors and it is, in in large part, for this reason that the current project is focused on further developing and improving such tools. In the scope of this project, we have pursued other alternatives to build the optimum tool for studying the nascent phase in gas-phase systems.

5. References

(1) Sauter, D. W.; Taoufik, M.; Boisson, C. Polyolefins, a Success Story. *Polymers* **2017**, *9* (6), 185. https://doi.org/10.3390/polym9060185.

(2) Al-Ali AlMa'adeed, M.; Krupa, I. Introduction. In *Polyolefin Compounds and Materials: Fundamentals and Industrial Applications*; Al-Ali AlMa'adeed, M., Krupa, I., Eds.; Springer Series on Polymer and Composite Materials; Springer International Publishing: Cham, 2016; pp 1–11. https://doi.org/10.1007/978-3-319-25982-6_1.

(3) Hutley, T. J.; Ouederni, M. Polyolefins—The History and Economic Impact. In *Polyolefin Compounds and Materials: Fundamentals and Industrial Applications*; Al-Ali AlMa'adeed, M., Krupa, I., Eds.; Springer Series on Polymer and Composite Materials; Springer International Publishing: Cham, 2016; pp 13–50. https://doi.org/10.1007/978-3-319-25982-6_2.

(4) Maddah, H. A. Polypropylene as a Promising Plastic: A Review. *Am. J. Polym. Sci.* **2016**, *6* (1), 1–11.

(5) Soares, J. B. P.; McKenna, T. F. L. Introduction to Polyolefins. In *Polyolefin Reaction Engineering*; John Wiley & Sons, Ltd, 2012; pp 1–13. https://doi.org/10.1002/9783527646944.ch1.

(6) Plastics https://polymerdatabase.com/polymer%20classes/Intro%20Plastics.html (accessed Apr 6, 2020).

(7) Soares, J. B. P.; L. McKenna, T. F. L. Polyolefin Reactors and Processes. In *Polyolefin Reaction Engineering*; John Wiley & Sons, Ltd, 2012; pp 87–129. https://doi.org/10.1002/9783527646944.ch4.

(8) Bisht, H. S.; Chatterjee, A. K. Living Free-Radical Polymerization—a Review. *J. Macromol. Sci. Part C* **2001**, *41* (3), 139–173. https://doi.org/10.1081/MC-100107774.

(9) Sinclair, K. B. Future Trends in Polyolefin Materials. *Macromol. Symp.* **2001**, *173* (1), 237–261. https://doi.org/10.1002/1521-3900(200108)173:1<237::AID-MASY237>3.0.CO;2-M.

(10) LDPE Production Capacity, Plants and Price. *Plastics Insight*.

(11) Bashir, M. A. Impact of Physical Properties of Silica on the Reaction Kinetics of Silica Supported Metallocenes and Polyethylene Morphology. phdthesis, Université de Lyon, 2016.

(12) Nexant. CHEMSYSTEMS PERP PROGRAM PERP 09/10-3, HDPE. 2011.

(13) D20 Committee. *Test Method for Melt Flow Rates of Thermoplastics by Extrusion Plastometer*; ASTM International. https://doi.org/10.1520/D1238-13.

(14) McKenna, T. F. L. Condensed Mode Cooling of Ethylene Polymerization in Fluidized Bed Reactors. *Macromol. React. Eng.* **2019**, *13* (2), 1800026. https://doi.org/10.1002/mren.201800026.

(15) Fischbuch, D. B.; Hagerty, R. O.; Hinds, S. C.; Holroyd, D. R.; Ng, A. V.; Singh, D. Low Molecular Weight Induced Condensing Agents. US7696289B2, April 13, 2010.

(16) Levine, I. E.; Folsom, L. T. Polymerization Process. US2484384A, October 11, 1949.

(17) Morita, Y.; Hayata, S.; Kato, A.; Nara, H.; Watanabe, T. Process for Multi-Step Gas-Phase Polymerization of Olefins. US4390669A, June 28, 1983.

(18) UNIPOL™ PE Process | Univation Technologies https://univation.dow.com/en-us/unipol/process (accessed Mar 26, 2020).

(19) Siberdt, F. INEOS Technologies - Innovene™ G & S Technologies. Recent Advances and Global Positioning.

(20) Soares, J. B. P.; McKenna, T. F. L. Polymerization Catalysis and Mechanism. In *Polyolefin Reaction Engineering*; John Wiley & Sons, Ltd, 2012; pp 53–86. https://doi.org/10.1002/9783527646944.ch3.

(21) Böhm, L. L. The Ethylene Polymerization with Ziegler Catalysts: Fifty Years after the Discovery. *Angew. Chem. Int. Ed.* **2003**, *42* (41), 5010–5030. https://doi.org/10.1002/anie.200300580.

(22) Mülhaupt, R. Catalytic Polymerization and Post Polymerization Catalysis Fifty Years After the Discovery of Ziegler's Catalysts. *Macromol. Chem. Phys.* **2003**, *204* (2), 289–327. https://doi.org/10.1002/macp.200290085.

(23) Cossee, P. Ziegler-Natta Catalysis I. Mechanism of Polymerization of a-Olefins with Ziegler-Natta Catalysts. *Journal of Catalysis, 1964. 3(1): p.80-88*.
(24) Soga, K.; Shiono, T. Ziegler-Natta Catalysts for Olefin Polymerizations. *Prog. Polym. Sci.* **1997**, *22* (7), 1503–1546. https://doi.org/10.1016/S0079-6700(97)00003-8.
(25) Bubeck, R. A. Structure–Property Relationships in Metallocene Polyethylenes. *Mater. Sci. Eng. R Rep.* **2002**, *39* (1), 1–28. https://doi.org/10.1016/S0927-796X(02)00074-8.
(26) Kaminsky, W. The Discovery of Metallocene Catalysts and Their Present State of the Art. *J. Polym. Sci. Part Polym. Chem.* **2004**, *42* (16), 3911–3921. https://doi.org/10.1002/pola.20292.
(27) Kaminsky, W.; Laban, A. Metallocene Catalysis. *Appl. Catal. Gen.* **2001**, *222* (1), 47–61. https://doi.org/10.1016/S0926-860X(01)00829-8.
(28) You-Xian Chen, E.; J. Marks, T. Cocatalysts for Metal-Catalyzed Olefin Polymerization: Activators, Activation Processes, and Structure−Activity Relationships | Chemical Reviews https://pubs-acs-org.docelec.univ-lyon1.fr/doi/full/10.1021/cr980462j (accessed Mar 17, 2020).
(29) Kaminsky, W. Discovery of Methylaluminoxane as Cocatalyst for Olefin Polymerization. *Macromolecules* **2012**, *45* (8), 3289–3297. https://doi.org/10.1021/ma202453u.
(30) Sinn, H. Proposals for Structure and Effect of Methylalumoxane Based on Mass Balances and Phase Separation Experiments. *Macromol. Symp.* **1995**, *97* (1), 27–52. https://doi.org/10.1002/masy.19950970105.
(31) Babushkin, D. E.; Brintzinger, H.-H. Activation of Dimethyl Zirconocene by Methylaluminoxane (MAO)Size Estimate for Me-MAO- Anions by Pulsed Field-Gradient NMR. *J. Am. Chem. Soc.* **2002**, *124* (43), 12869–12873. https://doi.org/10.1021/ja020646m.
(32) Koide, Y.; Bott, S. G.; Barron, A. R. Alumoxanes as Cocatalysts in the Palladium-Catalyzed Copolymerization of Carbon Monoxide and Ethylene: Genesis of a Structure−Activity Relationship. *Organometallics* **1996**, *15* (9), 2213–2226. https://doi.org/10.1021/om9508492.
(33) Wang, W.; Yan, D.; Charpentier, P. A.; Zhu, S.; Hamielec, A. E.; Sayer, B. G. Long Chain Branching in Ethylene Polymerization Using Constrained Geometry Metallocene Catalyst. *Macromol. Chem. Phys.* **1998**, *199* (11), 2409–2416. https://doi.org/10.1002/(SICI)1521-3935(19981101)199:11<2409::AID-MACP2409>3.0.CO;2-A.
(34) Hamielec, A. E.; Soares, J. B. P. Polymerization Reaction Engineering — Metallocene Catalysts. *Prog. Polym. Sci.* **1996**, *21* (4), 651–706. https://doi.org/10.1016/0079-6700(96)00001-9.
(35) Severn, J. R. Methylaluminoxane (MAO), Silica and a Complex: The “Holy Trinity” of Supported Single-Site Catalyst. In *Tailor-Made Polymers*; John Wiley & Sons, Ltd, 2008; pp 95–138. https://doi.org/10.1002/9783527621668.ch4.
(36) Kamfjord, T.; Wester, T. S.; Rytter, E. Supported Metallocene Catalysts Prepared by Impregnation of MAO Modified Silica by a Metallocene/Monomer Solution. *Macromol. Rapid Commun.* **1998**, *19* (10), 505–509. https://doi.org/10.1002/(SICI)1521-3927(19981001)19:10<505::AID-MARC505>3.0.CO;2-Q.
(37) Rytter, E.; Ott, M. Supported Metallocene Catalysts Prepared by Impregnation of Silica with Metallocene/Aluminoxane/1-Hexene Solutions. *Macromol. Rapid Commun.* **2001**, *22* (17), 1427–1431. https://doi.org/10.1002/1521-3927(20011101)22:17<1427::AID-MARC1427>3.0.CO;2-1.
(38) Moroz, B. L.; Semikolenova, N. V.; Nosov, A. V.; Zakharov, V. A.; Nagy, S.; O’Reilly, N. J. Silica-Supported Zirconocene Catalysts: Preparation, Characterization and Activity in Ethylene Polymerization. *J. Mol. Catal. Chem.* **1998**, *130* (1), 121–129. https://doi.org/10.1016/S1381-1169(97)00206-9.
(39) Bingel, C.; Goeres, M.; Fraaije, V.; Winter, A. Supported Catalyst System, Method for the Production and Use Thereof in Olefin Polymerization. US6444606B1, September 3, 2002.
(40) Santos, J. H. Z. dos; Dorneles, S.; Stedile, F. C.; Dupont, J.; Forte, M. M. de C.; Baumvol, I. J. R. Silica Supported Zirconocenes and Al-Based Cocatalysts: Surface Metal Loading and Catalytic Activity. *Macromol. Chem. Phys.* **1997**, *198* (11), 3529–3537. https://doi.org/10.1002/macp.1997.021981117.

(41) Semikolenova, N. V.; Zakharov, V. A. On the Interaction of Supported Zirconocene Catalysts with Alkylaluminium Co-Catalysts. *Macromol. Chem. Phys.* **1997**, *198* (9), 2889–2897. https://doi.org/10.1002/macp.1997.021980918.
(42) Chien, J. C. W. Supported Metallocene Polymerization Catalysis. *Top. Catal.* **1999**, *7* (1), 23–36. https://doi.org/10.1023/A:1019111700284.
(43) Ernst, E.; Reussner, J.; Neissl, W. Catalyst Supports, Supported Metallocene Catalysts and Their Use for the Preparation of Polyolefins. US5910463A, June 8, 1999.
(44) Bashir, M. A.; Vancompernolle, T.; Gauvin, R. M.; Delevoye, L.; Merle, N.; Monteil, V.; Taoufik, M.; McKenna, T. F. L.; Boisson, C. Silica/MAO/(n-BuCp)2ZrCl2 Catalyst: Effect of Support Dehydroxylation Temperature on the Grafting of MAO and Ethylene Polymerization. *Catal. Sci. Technol.* **2016**, *6* (9), 2962–2974. https://doi.org/10.1039/C5CY01285F.
(45) Soares, J. B. P.; McKenna, T. F. L. Particle Growth and Single Particle Modeling. In *Polyolefin Reaction Engineering*; John Wiley & Sons, Ltd, 2012; pp 271–309. https://doi.org/10.1002/9783527646944.ch7.
(46) McKenna, T. F. L.; Tioni, E.; Ranieri, M. M.; Alizadeh, A.; Boisson, C.; Monteil, V. Catalytic Olefin Polymerisation at Short Times: Studies Using Specially Adapted Reactors. *Can. J. Chem. Eng.* **2013**, *91* (4), 669–686. https://doi.org/10.1002/cjce.21684.
(47) McKenna, T. F. L.; Martino, A. D.; Weickert, G.; Soares, J. B. P. Particle Growth During the Polymerisation of Olefins on Supported Catalysts, 1 – Nascent Polymer Structures. *Macromol. React. Eng.* **2010**, *4* (1), 40–64. https://doi.org/10.1002/mren.200900025.
(48) McKenna, T. F.; Soares, J. B. P. Single Particle Modelling for Olefin Polymerization on Supported Catalysts: A Review and Proposals for Future Developments. *Chem. Eng. Sci.* **2001**, *56* (13), 3931–3949. https://doi.org/10.1016/S0009-2509(01)00069-0.
(49) Noristi, L.; Marchetti, E.; Baruzzi, G.; Sgarzi, P. Investigation on the Particle Growth Mechanism in Propylene Polymerization with MgCl2-Supported Ziegler–Natta Catalysts. *J. Polym. Sci. Part Polym. Chem.* **1994**, *32* (16), 3047–3059. https://doi.org/10.1002/pola.1994.080321606.
(50) Hock, C. W. How Ticl3 Catalysts Control the Texture of As-Polymerized Polypropylene. *J. Polym. Sci. [A1]* **1966**, *4* (12), 3055–3064. https://doi.org/10.1002/pol.1966.150041212.
(51) Kakugo, M.; Sadatoshi, H.; Sakai, J.; Yokoyama, M. Growth of Polypropylene Particles in Heterogeneous Ziegler-Natta Polymerization.
(52) Bashir, M. A.; Monteil, V.; Boisson, C.; McKenna, T. F. L. Experimental Proof of the Existence of Mass-Transfer Resistance during Early Stages of Ethylene Polymerization with Silica Supported Metallocene/MAO Catalysts. *AIChE J.* **2017**, *63* (10), 4476–4490. https://doi.org/10.1002/aic.15806.
(53) Floyd, S.; Choi, K. Y.; Taylor, T. W.; Ray, W. H. Polymerization of Olefins through Heterogeneous Catalysis. III. Polymer Particle Modelling with an Analysis of Intraparticle Heat and Mass Transfer Effects. *J. Appl. Polym. Sci.* **1986**, *32* (1), 2935–2960. https://doi.org/10.1002/app.1986.070320108.
(54) Floyd, S.; Choi, K. Y.; Taylor, T. W.; Ray, W. H. Polymerization of Olefines through Heterogeneous Catalysis IV. Modeling of Heat and Mass Transfer Resistance in the Polymer Particle Boundary Layer. *J. Appl. Polym. Sci.* **1986**, *31* (7), 2231–2265. https://doi.org/10.1002/app.1986.070310724.
(55) Alizadeh, A.; McKenna, T. F. L. Particle Growth during the Polymerization of Olefins on Supported Catalysts. Part 2: Current Experimental Understanding and Modeling Progresses on Particle Fragmentation, Growth, and Morphology Development. *Macromol. React. Eng.* **2018**, *12* (1), 1700027. https://doi.org/10.1002/mren.201700027.
(56) Soares, J. B. P.; Hamielec, A. E. Effect of Hydrogen and of Catalyst Prepolymerization with Propylene on the Polymerization Kinetics of Ethylene with a Non-Supported Heterogeneous Ziegler-Natta Catalyst. *Polymer* **1996**, *37* (20), 4599–4605. https://doi.org/10.1016/0032-3861(96)00285-6.

(57) Ferrero, M. A.; Chiovetta, M. G. Catalyst Fragmentation during Propylene Polymerization: Part I. The Effects of Grain Size and Structure. *Polym. Eng. Sci.* **1987**, *27* (19), 1436–1447. https://doi.org/10.1002/pen.760271903.
(58) Ferrero, M. A.; Chiovetta, M. G. Catalyst Fragmentation during Propylene Polymerization: Part II. Microparticle Diffusion and Reaction Effects. *Polym. Eng. Sci.* **1987**, *27* (19), 1448–1460. https://doi.org/10.1002/pen.760271904.
(59) Ferrero, M. A.; Chiovetta, M. G. Catalyst Fragmentation during Propylene Polymerization. III: Bulk Polymerization Process Simulation. *Polym. Eng. Sci.* **1991**, *31* (12), 886–903. https://doi.org/10.1002/pen.760311208.
(60) Ferrero, M. A.; Chiovetta, M. G. Effects of Catalyst Fragmentation during Propylene Polymerization. IV: Comparison between Gas Phase and Bulk Polymerization Processes. *Polym. Eng. Sci.* **1991**, *31* (12), 904–911. https://doi.org/10.1002/pen.760311209.
(61) Estenoz, D. A.; Chiovetta, M. G. A Structural Model for the Catalytic Polymerization of Ethylene Using Chromium Catalysts. Part I: Description and Solution. *Polym. Eng. Sci.* **1996**, *36* (17), 2208–2228. https://doi.org/10.1002/pen.10618.
(62) Estenoz, D. A.; Chiovetta, M. G. A Structural Model for the Catalytic Polymerization of Ethylene Using Chromium Catalysts. Part II: Thermal Effects. *Polym. Eng. Sci.* **1996**, *36* (17), 2229–2240. https://doi.org/10.1002/pen.10619.
(63) Estenoz, D. A.; Chiovetta, M. G. Olefin Polymerization Using Supported Metallocene Catalysts: Process Representation Scheme and Mathematical Model. *J. Appl. Polym. Sci.* **2001**, *81* (2), 285–311. https://doi.org/10.1002/app.1440.
(64) Fisch, A. G.; dos Santos, J. H. Z.; Secchi, A. R.; Cardozo, N. S. M. Heterogeneous Catalysts for Olefin Polymerization: Mathematical Model for Catalyst Particle Fragmentation. *Ind. Eng. Chem. Res.* **2015**, *54* (48), 11997–12010. https://doi.org/10.1021/acs.iecr.5b03740.
(65) Horáčková, B.; Grof, Z.; Kosek, J. Dynamics of Fragmentation of Catalyst Carriers in Catalytic Polymerization of Olefins. *Chem. Eng. Sci.* **2007**, *62* (18), 5264–5270. https://doi.org/10.1016/j.ces.2007.03.022.
(66) Buls, V. W.; Higgins, T. L. A Particle Growth Theory for Heterogeneous Ziegler Polymerization. *J. Polym. Sci. [A1]* **1970**, *8* (5), 1037–1053. https://doi.org/10.1002/pol.1970.150080502.
(67) Kakugo, M.; Sadatoshi, H.; Yokoyama, M.; Kojima, K. Transmission Electron Microscopic Observation of Nascent Polypropylene Particles Using a New Staining Method.
(68) Grof, Z.; Kosek, J.; Marek, M. Principles of the Morphogenesis of Polyolefin Particles. *Ind. Eng. Chem. Res.* **2005**, *44* (8), 2389–2404. https://doi.org/10.1021/ie049106j.
(69) Nagel, E. J.; Kirillov, V. A.; W. Harmon, R. Prediction of Molecular Weight Distributions for High-Density Polyolefins.
(70) Floyd, S.; Heiskanen, T.; Taylor, T. W.; Mann, G. E.; Ray, W. H. Polymerization of Olefins through Heterogeneous Catalysis. VI. Effect of Particle Heat and Mass Transfer on Polymerization Behavior and Polymer Properties. *J. Appl. Polym. Sci.* **1987**, *33* (4), 1021–1065. https://doi.org/10.1002/app.1987.070330402.
(71) Floyd, S.; Hutchinson, R. A.; Ray, W. H. Polymerization of Olefins through Heterogeneous Catalysis—V. Gas-Liquid Mass Transfer Limitations in Liquid Slurry Reactors. *J. Appl. Polym. Sci.* **1986**, *32* (6), 5451–5479. https://doi.org/10.1002/app.1986.070320617.
(72) Hutchinson, R. A.; Chen, C. M.; Ray, W. H. Polymerization of Olefins through Heterogeneous Catalysis X: Modeling of Particle Growth and Morphology. *J. Appl. Polym. Sci.* **1992**, *44* (8), 1389–1414. https://doi.org/10.1002/app.1992.070440811.
(73) Hutchinson, R. A.; Ray, W. H. Polymerization of Olefins through Heterogeneous Catalysis. VII. Particle Ignition and Extinction Phenomena. *J. Appl. Polym. Sci.* **1987**, *34* (2), 657–676. https://doi.org/10.1002/app.1987.070340220.
(74) Hutchinson, R. A.; Ray, W. H. Polymerization of Olefins through Heterogeneous Catalysis. VIII. Monomer Sorption Effects. *J. Appl. Polym. Sci. 41* (1–2), 51–81. https://doi.org/10.1002/app.1990.070410106.

(75) Hutchinson, R. A.; Ray, W. H. Polymerization of Olefins through Heterogeneous Catalysis. IX. Experimental Study of Propylene Polymerization over a High Activity MgCl2-Supported Ti Catalyst. *J. Appl. Polym. Sci.* **1991**, *43* (7), 1271–1285. https://doi.org/10.1002/app.1991.070430708.
(76) Debling, J. A.; Ray, W. H. Heat and Mass Transfer Effects in Multistage Polymerization Processes: Impact Polypropylene.
(77) Han-Adebekun, G. C.; Hamba, M.; Ray, W. H. Kinetic Study of Gas Phase Olefin Polymerization with a TiCl4/MgCl2 Catalyst I. Effect of Polymerization Conditions. *J. Polym. Sci. Part Polym. Chem.* **1997**, *35* (10), 2063–2074. https://doi.org/10.1002/(SICI)1099-0518(19970730)35:10<2063::AID-POLA22>3.0.CO;2-D.
(78) Hamba, M.; Han-Adebekun, G. C.; Ray, W. H. Kinetic Study of Gas Phase Olefin Polymerization with a TiCl4/MgCl2 Catalyst. II. Kinetic Parameter Estimation and Model Building. *J. Polym. Sci. Part Polym. Chem.* **1997**, *35* (10), 2075–2096. https://doi.org/10.1002/(SICI)1099-0518(19970730)35:10<2075::AID-POLA23>3.0.CO;2-C.
(79) Kosek, J.; Grof, Z.; ák, A.; Štěpánek, F.; Marek, M. Dynamics of Particle Growth and Overheating in Gas-Phase Polymerization Reactors. *Chem. Eng. Sci.* **2001**, *56* (13), 3951–3977. https://doi.org/10.1016/S0009-2509(01)00070-7.
(80) Yiagopoulos, A.; Yiannoulakis, H.; Dimos, V.; Kiparissides, C. Heat and Mass Transfer Phenomena during the Early Growth of a Catalyst Particle in Gas-Phase Olefin Polymerization: The Effect of Prepolymerization Temperature and Time. *Chem. Eng. Sci.* **2001**, *56* (13), 3979–3995. https://doi.org/10.1016/S0009-2509(01)00071-9.
(81) Phd thesis Tioni final - document https://tel.archives-ouvertes.fr/tel-01416887/document (accessed Jan 16, 2017).
(82) McDaniel, M. P. Fracturing Silica-Based Catalysts during Ethylene Polymerization. *J. Polym. Sci. Polym. Chem. Ed.* **1981**, *19* (8), 1967–1976. https://doi.org/10.1002/pol.1981.170190809.
(83) Weist, E. L.; Ali, A. H.; Naik, B. G.; Conner, W. C. Morphological study of supported chromium polymerization catalysts. 2. Initial stages of polymerization https://pubs.acs.org/doi/pdf/10.1021/ma00198a009 (accessed Mar 28, 2020). https://doi.org/10.1021/ma00198a009.
(84) Steinmetz, B.; Tesche, B.; Przybyla, C.; Zechlin, J.; Fink, G. Polypropylene Growth on Silica-Supported Metallocene Catalysts: A Microscopic Study to Explain Kinetic Behavior Especially in Early Polymerization Stages. *Acta Polym.* **1997**, *48* (9), 392–399. https://doi.org/10.1002/actp.1997.010480907.
(85) Fink, G.; Steinmetz, B.; Zechlin, J.; Przybyla, C.; Tesche, B. Propene Polymerization with Silica-Supported Metallocene/MAO Catalysts. *Chem. Rev.* **2000**, *100* (4), 1377–1390. https://doi.org/10.1021/cr9804689.
(86) Fink, G.; Tesche, B.; Korber, F.; Knoke, S. The Particle-Forming Process of SiO2-Supported Metallocene Catalysts. *Macromol. Symp.* **2001**, *173* (1), 77–88. https://doi.org/10.1002/1521-3900(200108)173:1<77::AID-MASY77>3.0.CO;2-1.
(87) Knoke, S.; Korber, F.; Fink, G.; Tesche, B. Early Stages of Propylene Bulk Phase Polymerization with Supported Metallocene Catalysts. *Macromol. Chem. Phys.* **2003**, *204* (4), 607–617. https://doi.org/10.1002/macp.200390028.
(88) Knoke, S.; Ferrari, D.; Tesche, B.; Fink, G. Microkinetic Videomicroscopic Analysis of Olefin Polymerization with a Supported Metallocene Catalyst. *Angew. Chem. Int. Ed.* **2003**, *42* (41), 5090–5093. https://doi.org/10.1002/anie.200351582.
(89) Conner, W. C.; Webb, S. W.; Spanne, P.; Jones, K. W. Use of x-ray microscopy and synchrotron microtomography to characterize polyethylene polymerization particles https://pubs.acs.org/doi/pdf/10.1021/ma00224a002 (accessed Mar 28, 2020). https://doi.org/10.1021/ma00224a002.
(90) Jones, K. W.; Spanne, P.; Webb, S. W.; Conner, W. C.; Beyerlein, R. A.; Reagan, W. J.; Dautzenberg, F. M. Catalyst Analysis Using Synchrotron X-Ray Microscopy. *Nucl. Instrum.*

Methods Phys. Res. Sect. B Beam Interact. Mater. At. **1991**, *56–57*, 427–432. https://doi.org/10.1016/0168-583X(91)96063-Q.
(91) Ferrero, M. A.; Sommer, R.; Spanne, P.; Jones, K. W.; Conner, W. C. X-Ray Microtomography Studies of Nascent Polyolefin Particles Polymerized over Magnesium Chloride-Supported Catalysts. *J. Polym. Sci. Part Polym. Chem.* **1993**, *31* (10), 2507–2512. https://doi.org/10.1002/pola.1993.080311011.
(92) Jang, Y.-J.; Bieber, K.; Naundorf, C.; Nenov, N.; Klapper, M.; Müllen, K.; Ferrari, D.; Knoke, S.; Fink, G. Optical Methods to Study the Behaviour of Supported Metallocene Catalysts during Olefin Polymerisation. *E-Polym.* **2005**, *5* (1). https://doi.org/10.1515/epoly.2005.5.1.132.
(93) Pater, J. T. M.; Weickert, G.; van Swaaij, W. P. M. New Method for Online Observation of Growing Polyolefin Particles https://www.ingentaconnect.com/content/scs/chimia/2001/00000055/00000003/art00029 (accessed Mar 28, 2020).
(94) Pater, J. T. M.; Weickert, G.; van Swaaij, W. P. M. Optical and Infrared Imaging of Growing Polyolefin Particles. *AIChE J.* **2003**, *49* (2), 450–464. https://doi.org/10.1002/aic.690490215.
(95) Hamilton, P.; Hill, D. R.; Luss, D. Optical and Infrared Study of Individual Reacting Metallocene Catalyst Particles.
(96) Abboud, M.; Denifl, P.; Reichert, K.-H. Fragmentation of Ziegler-Natta Catalyst Particles During Propylene Polymerization. *Macromol. Mater. Eng.* **2005**, *290* (6), 558–564. https://doi.org/10.1002/mame.200500049.
(97) Tioni, E.; Spitz, R.; Broyer, J. P.; Monteil, V.; McKenna, T. Packed-Bed Reactor for Short Time Gas Phase Olefin Polymerization: Heat Transfer Study and Reactor Optimization. *AIChE J.* **2012**, *58* (1), 256–267. https://doi.org/10.1002/aic.12576.
(98) Chance, B. The Accelerated Flow Method for Rapid Reactions. *J. Frankl. Inst.* **1940**, *229* (6), 737–766. https://doi.org/10.1016/S0016-0032(40)90963-2.
(99) Gomez-Hens, A.; Perez-Bendito, D. The Stopped-Flow Technique in Analytical Chemistry. *Anal. Chim. Acta* **1991**, *242*, 147–177. https://doi.org/10.1016/0003-2670(91)87060-K.
(100) Mori, H.; Terano, M. Stopped-Flow Techniques in Olefin Polymerization. *Trends Polym. Sci.* **1997**, *10* (5), 314–321.
(101) Mori, H.; Yamahiro, M.; Prokhorov, V. V.; Nitta, K.; Terano, M. High-Pressure Stopped-Flow Polymerization for Polypropene-Block-Poly(Ethene-Co-Propene) Having Controlled Molecular Weight: Synthesis and Characterization. *Macromolecules* **1999**, *32* (19), 6008–6018. https://doi.org/10.1021/ma981862b.
(102) Liu, B.; Matsuoka, H.; Terano, M. Stopped-Flow Techniques in Ziegler Catalysis. *Macromol. Rapid Commun.* **2001**, *22* (1), 1–24. https://doi.org/10.1002/1521-3927(20010101)22:1<1::AID-MARC1>3.0.CO;2-T.
(103) Liu, Z.; Somsook, E.; White, C. B.; Rosaaen, K. A.; Landis, C. R. Kinetics of Initiation, Propagation, and Termination for the [Rac-(C2H4(1-Indenyl)2)ZrMe][MeB(C6F5)3]-Catalyzed Polymerization of 1-Hexene. *J. Am. Chem. Soc.* **2001**, *123* (45), 11193–11207. https://doi.org/10.1021/ja016072n.
(104) Liu, Z.; Somsook, E.; Landis, C. R. A 2H-Labeling Scheme for Active-Site Counts in Metallocene-Catalyzed Alkene Polymerization. *J. Am. Chem. Soc.* **2001**, *123* (12), 2915–2916. https://doi.org/10.1021/ja0055918.
(105) Shiono, T.; Ohgizawa, M.; Soga, K. Reaction of the Ti-Polyethylene Bond with Carbon Monoxide over the Bis(Cyclopentadienyl)Titanium Dichloride-Methylaluminoxane Catalyst System. *Polymer* **1994**, *35* (1), 187–192. https://doi.org/10.1016/0032-3861(94)90070-1.
(106) Busico, V.; Cipullo, R.; Esposito, V. Stopped-Flow Polymerizations of Ethene and Propene in the Presence of the Catalyst System Rac-Me2Si(2-Methyl-4-Phenyl-1-Indenyl)2ZrCl2/Methylaluminoxane. *Macromol. Rapid Commun.* **1999**, *20* (3), 116–121. https://doi.org/10.1002/(SICI)1521-3927(19990301)20:3<116::AID-MARC116>3.0.CO;2-A.

(107) Song, F.; Cannon, R. D.; Bochmann, M. Zirconocene-Catalyzed Propene Polymerization: A Quenched-Flow Kinetic Study. *J. Am. Chem. Soc.* **2003**, *125* (25), 7641–7653. https://doi.org/10.1021/ja029150v.
(108) Martino, A. D.; Broyer, J. P.; Spitz, R.; Weickert, G.; McKenna, T. F. A Rapid Quenched-Flow Device for the Characterisation of the Nascent Polymerisation of Ethylene under Industrial Conditions. *Macromol. Rapid Commun.* **2005**, *26* (4), 215–220. https://doi.org/10.1002/marc.200400530.
(109) Martino, A. D.; Weickert, G.; McKenna, T. F. L. Contributions to the Experimental Investigation of the Nascent Polymerisation of Ethylene on Supported Catalysts, 1. *Macromol. React. Eng.* **2007**, *1* (1), 165–184. https://doi.org/10.1002/mren.200600013.
(110) Di Martino, A.; Broyer, J.-P.; Schweich, D.; de Bellefon, C.; Weickert, G.; McKenna, T. F. L. Design and Implementation of a Novel Quench Flow Reactor for the Study of Nascent Olefin Polymerisation. *Macromol. React. Eng.* **2007**, *1* (2), 284–294. https://doi.org/10.1002/mren.200600038.
(111) Keii, T.; Terano, M.; Kimura, K.; Ishii, K. A Kinetic Argument for a Quasi-Living Polymerization of Propene with a MgCl2-Supported Catalyst. *Makromol. Chem. Rapid Commun.* **1987**, *8* (11), 583–587. https://doi.org/10.1002/marc.1987.030081113.
(112) Kaminaka, M.; Soga, K. Polymerization of Propene with the Catalyst Systems Composed of Al2O3- or MgCl2-Supported Et[IndH4]2ZrCl2 and AlR3 (R = CH3, C2H5). *Makromol. Chem. Rapid Commun.* **1991**, *12* (6), 367–372. https://doi.org/10.1002/marc.1991.030120611.
(113) Kaminaka, M.; Soga, K. Polymerization of Propene with Catalyst Systems Composed of Al2O3 or MgCl2-Supported Zirconocene and Al(CH3)3. *Polymer* **1992**, *33* (5), 1105–1107. https://doi.org/10.1016/0032-3861(92)90031-Q.
(114) Fink, G.; Fenzl, W.; Mynott, R. Ethylene Insertion with Soluble Ziegler Catalysts: Direct Insight into the Reaction Using Enriched 13C2 H4 and 13C NMR Spectroscopy II. The System Cp2TiMeCl/AlMeCl2/13C2H4. *Z. Für Naturforschung B* **2014**, *40* (2), 158–166. https://doi.org/10.1515/znb-1985-0204.
(115) Fink, G.; Rottler, R.; Schnell, D.; Zoller, W. Elementary Steps in Ziegler-Natta Catalysis. *J. Appl. Polym. Sci.* **1976**, *20* (10), 2779–2790. https://doi.org/10.1002/app.1976.070201012.
(116) Ranieri, M. M. Measuring on Main Kinetic Parameters of Molecular Catalyst for Olefin Polymerization Using High-Pressure-Type Quenched Flow Reactor. 2011.
(117) Martino, A. D.; Weickert, G.; McKenna, T. F. L. Contributions to the Experimental Investigation of the Nascent Polymerisation of Ethylene on Supported Catalysts, 2. *Macromol. React. Eng.* **2007**, *1* (2), 229–242. https://doi.org/10.1002/mren.200600018.
(118) Taniike, T.; Thang, V. Q.; Binh, N. T.; Hiraoka, Y.; Uozumi, T.; Terano, M. Initial Particle Morphology Development in Ziegler-Natta Propylene Polymerization Tracked with Stopped-Flow Technique. *Macromol. Chem. Phys.* **2011**, *212* (7), 723–729. https://doi.org/10.1002/macp.201000598.
(119) Tioni, E.; Broyer, J. P.; Monteil, V.; McKenna, T. Influence of Reaction Conditions on Catalyst Behavior during the Early Stages of Gas Phase Ethylene Homo- and Copolymerization. *Ind. Eng. Chem. Res.* **2012**, *51* (45), 14673–14684. https://doi.org/10.1021/ie301682u.
(120) Silva, F. M.; Broyer, J. P.; Novat, C.; Lima, E. L.; Pinto, J. C.; McKenna, T. F. Investigation of Catalyst Fragmentation in Gas-Phase Olefin Polymerisation: A Novel Short Stop Reactor. *Macromol. Rapid Commun.* **2005**, *26* (23), 1846–1853. https://doi.org/10.1002/marc.200500576.
(121) Olalla, B.; Broyer, J.-P.; McKenna, T. F. L. Heat Transfer and Nascent Polymerisation of Olefins on Supported Catalysts. *Macromol. Symp.* **2008**, *271* (1), 1–7. https://doi.org/10.1002/masy.200851101.
(122) Woo, E.; Huh, J.; Jeong, Y. G.; Shin, K. From Homogeneous to Heterogeneous Nucleation of Chain Molecules under Nanoscopic Cylindrical Confinement. *Phys. Rev. Lett.* **2007**, *98* (13), 136103. https://doi.org/10.1103/PhysRevLett.98.136103.

(123) Shin, K.; Woo, E.; Jeong, Y. G.; Kim, C.; Huh, J.; Kim, K.-W. Crystalline Structures, Melting, and Crystallization of Linear Polyethylene in Cylindrical Nanopores. *Macromolecules* **2007**, *40* (18), 6617–6623. https://doi.org/10.1021/ma070994e.
(124) Tioni, E.; Monteil, V.; McKenna, T. Morphological Interpretation of the Evolution of the Thermal Properties of Polyethylene during the Fragmentation of Silica Supported Metallocene Catalysts. *Macromolecules* **2013**, *46* (2), 335–343. https://doi.org/10.1021/ma302150v.
(125) Browning, B.; Pitault, I.; Sheibat-Othman, N.; Tioni, E.; Monteil, V.; McKenna, T. F. L. Dynamic Modelling of a Stopped Flow Fixed Bed Reactor for Gas Phase Olefin Polymerisation. *Chem. Eng. J.* **2012**, *207–208*, 635–644. https://doi.org/10.1016/j.cej.2012.07.027.
(126) Browning, B. Dynamic modelling of a fixed bed reactor - PhD Thesis https://tel.archives-ouvertes.fr/tel-01175971/document (accessed Dec 1, 2016).
(127) Browning, B.; Sheibat-Othman, N.; Pitault, I.; McKenna, T. F. L. A 2-D Observer to Estimate the Reaction Rate in a Stopped Flow Fixed Bed Reactor for Gas Phase Olefin Polymerization. *AIChE J.* **2014**, *60* (10), 3511–3523. https://doi.org/10.1002/aic.14538.

Chapter 2

A novel stopped-flow reactor for gas phase polymerization: towards the ideal set-up

Chapter 2: Content

1. Introduction 60

2. Experimental approach 61

2.1. Full-time polymerization reactor 61

2.1.1. Polymerization procedure 61

3. Existing stopped-flow reactor (SF1) 63

3.1. Advantages and limitations of the existing set-up 63

3.2. Experimental section 63

3.2.1. Materials 64

3.2.2. Reactor description and polymerization procedure 64

3.3. Heat evacuation assessment 67

3.3.1. Conclusion 70

3.4. Hardware evaluation 70

3.4.1. Conclusion 72

3.5. Conclusions on assessment of reactor SF1 72

4. Stopped-flow reactor prototype (SF 2) 74

4.1. Introduction 74

4.2. Experimental section 75

4.2.1. Materials 75

4.2.2. Reactor description 76

4.2.3. Polymerization procedure 77

4.2.4. Estimating the particle temperature 78

4.3. Heat evacuation assessment 78

4.3.1. Improved temperature gradients with ZN catalyst 79

4.3.2. Impact of seedbed on polymerization yield 80

4.3.3. Conclusion 82

4.4. Hardware inertness assessment 82

4.4.1. Improving inertness by reactor conditioning with alkyl agents 83

4.4.2. Conclusion 83

4.5. Hardware thermal response assessment 84

4.5.1. Conclusion 85

4.6. Conclusions on assessment of reactor SF 2 86

5. Novel professionally engineered stopped-flow reactor (SF N) 88

5.1. Introduction 88

5.2. Reactor description 89

5.3. Experimental section 93

5.3.1. Materials 93

5.3.2. Polymerization procedure 93

5.3.3. Reactor conditioning 94

5.4. Hardware thermal response assessment 95

5.4.1. Improved control of reaction conditions....95
5.4.2. Conclusion....97
5.5. Hardware inertness assessment....97
5.5.1. Demonstration of hardware inertness with highly sensitive CGC catalyst....97
5.5.2. Conclusion....98
5.6. Conclusions on assessment of reactor SF N....99
6. Chapter conclusions....100
7. References....102

1. Introduction

As discussed in Chapter 1, the heterogeneous catalysts used industrially have both complex chemical and physical structures that play important roles in the polymerization process, especially in regards as to how the catalyst activation will take place. The physical nature of the supported catalyst will have a direct impact on the fragmentation step and, therefore, the growth of the polymer particle, the evolution of its morphology, and, in the case where overheating is a problem, on the deactivation of the catalyst.

It is widely accepted that the early stages of the polymerization, a time frame we are arbitrarily defining as ranging from seconds to a couple of minutes, are crucial in ensuring the quality of the entire process. This so called nascent phase is particularly difficult to study for several reasons,[1,2] many of them discussed in chapter 1. Besides the aspects related to the chemical reaction, a great part of the challenge lies in the lack of especially adapted tools that allow to study early stages, particularly for gas phase.

As discussed in chapter 1, the stopped-flow technology seems the most promising technique for studying early stages. [1] Previous works have shown the potential of this tool for studying the impact of reaction conditions on heat transfer and provided insights on particle fragmentation in gas-phase.[1,3–5]

However, as will be discussed in this chapter, the version of the gas phase stopped flow reactor present in the laboratory had significant limitations; limitations that we will discuss as we move through the chapter. Improving such tools is the main focus of this project.

The main objective of this PhD project was to design, build and test an optimized tool that can be used to study gas phase polymerization reactions at early stages under controlled and meaningful reaction conditions, and that provides the user with a maximum amount of information on how the polymerization unfolds. This was carried out by the development of an improved stopped-flow reactor tool that included both a hardware and a software component.

The development of the hardware component included improvements to the previously existing set-up and operation protocol, leading to the conception of a reactor prototype that was constructed and tested in our lab. Finally, an optimized stopped-flow reactor that fulfilled our initial criteria was designed in collaboration with an engineering company specialized in the construction of made-to-measure laboratory equipment for chemistry R&D. In this chapter, the reader will find all stages involved towards obtaining the hardware component of the novel stopped-flow reactor set-up. The software component consisted of the mathematical description of the novel stopped-flow reactor, in which heat and mass exchanges were taken into account to build a mathematical tool for predicting polymerization rates from the experimental data (temperature profiles). The development of the software component will be described in Chapter 3.

2. Experimental approach

Throughout this chapter, we have experimentally assessed the performance of different stopped-flow reactor set-ups. Our approach in evaluating the reactor performance consisted in following the performance of catalyzed reactions, as well as aspects unrelated to the polymerization.

The initial step in following the kinetic behavior of different catalysts was to test them in standard laboratory conditions in order to have a reference for the catalyst behavior in full-time polymerizations. The term 'full-time polymerization' is, in the scope of this work, refers to reaction times in which most (if not all) of the catalyst particles have had sufficient time to polymerize. Unless stated otherwise, all full-time polymerization tests had a duration of 60 minutes.

Next, catalysts were tested at short reaction times using the different stopped-flow reactors described in this work, for durations of 60 seconds or less. Moreover, the effect of hardware components unrelated to the polymerization reaction was assessed with cold tests carried out without catalysts, with the inert seedbed only (salt).

2.1. Full-time polymerization reactor

The full-time kinetic behavior of the catalysts used throughout this work was assessed using a semi-batch lab-scale reactor of 2.5 L capacity. This reactor is commonly referred to as *turbosphere* reactor due to its spherical shape and has been used in previous works from our group.[6–9]

2.1.1. *Polymerization procedure*

In Figure 1, the turbosphere reactor is represented as R-1. Ethylene (B-1 in the diagram) was purified prior to the reaction by columns C-1 of reduced BASF R3-16 catalyst (CuO supported on alumina), C-2 of molecular sieves (13X, 3A, Sigma-Aldrich), and column C-3 of Selexsorb COS (Alcoa), being later stored in a gas cylinder – denominated ballast, B-2.

Cylinders B-3 and B-4 were respectively hydrogen and propylene vessels and were not used for the current study, as well as liquid comonomer pump P-1 and the heat exchanger E-2. The vacuum pump is represented by VE-1; PT is the pressure transmitter; PI, pressure indicator; TIT, temperature transmitter and indicator; and TI, temperature indicator.

The system was previously cleaned with heptane and kept under isothermal conditions with vacuum/argon cycles to purge the reactor prior to the polymerization reaction. An injection cartridge containing catalyst and seedbed was prepared inside a Glove Box of Argon atmosphere. For the performed gas-phase polymerizations, 100 g of sodium chloride (NaCl) was used as seed bed, previously dried under vacuum at 400 °C for 4 hours.

Alkylated agents were injected in the reactor prior to catalyst insertion. Catalysts were introduced to the reactor through an injection cartridge under monomer pressure, which marked the beginning of the polymerization reaction. The mechanical agitation was kept constant during the reaction at 200 rpm.

A pressure reducer was used to maintain the pressure constant throughout the reaction. Continuous measurements of the monomer pressure in the ballast were interpreted using the SRK-EOS state

equation[10], to obtain a continuous productivity. Finally, the derivative of the pressure drop provided an estimate of the reaction rate.

The polymerization was quenched at the desired time by simultaneously venting the monomer and cooling the reactor to room temperature. The formed polymer was then washed in water to remove the NaCl seedbed and, finally, dried under vacuum at 70 °C for, at least, two hours.

Experimental conditions for the catalysts used in this chapter

For the Ziegler-Natta catalyst (ZN 1) used in this chapter, 10-15 mg catalyst were used and 1 mmol TEA (Triethylaluminium) was used as cocatalyst and scavenger for impurities. The reaction temperature was 70 °C and ethylene pressure kept constant at 7 barg.

For the classic metallocene catalysts (CpZ 1 and CpZ 2) used in this chapter, 50-100 mg catalyst were used and 0.8 mmol TiBA (Triisobutylaluminium) was used as scavenger for the reactor environment. The reaction temperature was 85 °C and ethylene pressure kept constant at 7 bar.

For the classic commercial CGC catalyst used in this chapter (CGC M), 100 mg catalyst were used and 0.8 mmol TiBA (Triisobutylaluminium) was used as scavenger for the reactor environment. The reaction temperature was 70 °C and ethylene pressure kept constant at 7.5 bar.

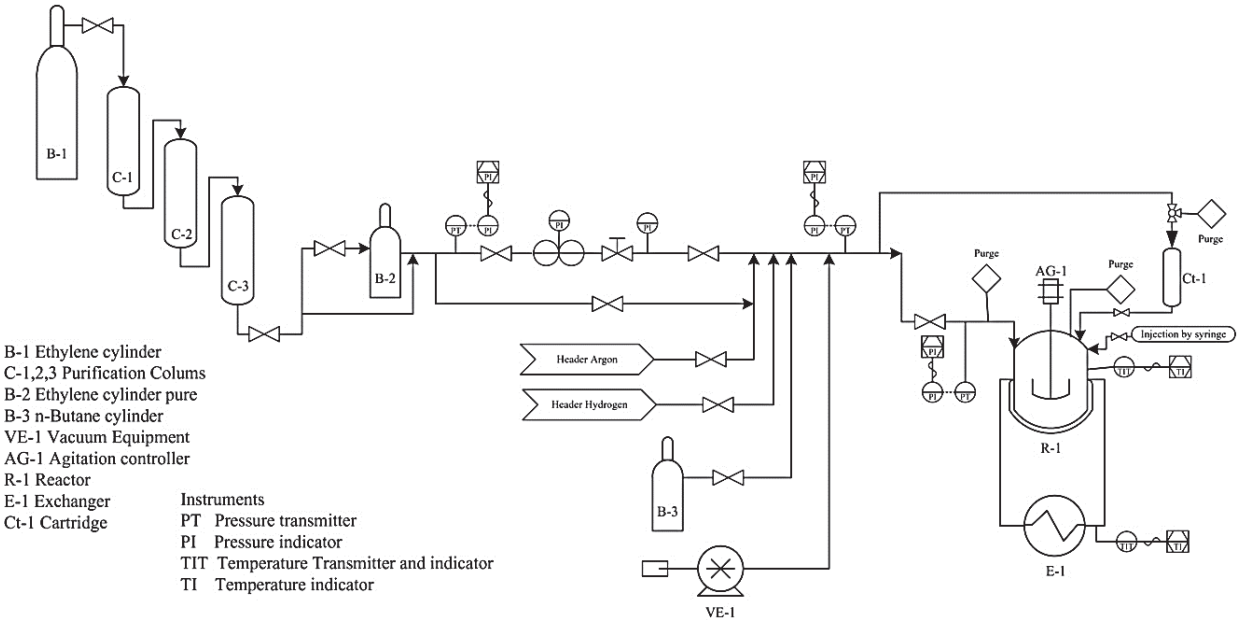

Figure 12: Turbosphere reactor experimental set-up and control system. Reprinted with permission.[8]

3. Existing stopped-flow reactor (SF1)

The existing stopped-flow set-up evaluated in this section was initially conceived by Ollala et al.[11] and further optimized and used by Tioni et al.[12] This set-up will be hereafter referred to as Stopped-Flow Reactor 1 (SF1).

The performance of this reactor set-up has been experimentally assessed, aiming to determine the key aspects of potential improvement.

3.1. Advantages and limitations of the existing set-up

The stopped-flow reactor described and assessed in this section was developed in our research group by conceived by Ollala et al.[11] and later optimized by Tioni et al.[12]. This set-up proved to be a valuable tool for investigating aspects related to heat transfer[3], reaction kinetics[4], morphology and particle fragmentation[5] in gas phase reactions as short as 100 ms, all in industrially realistic reaction conditions.

A simplified heat balance around the reactor, proposed by Tioni et al., allowed an upper estimate of the particle temperature inside the reactor.[1,4] This was a significant advance in terms of getting a realistic picture of the polymerization reaction in its earliest stages, given that previous studies relied only on the temperature of the gas. Moreover, studies carried out by Tioni et al. showed this tool could be used to follow the timeframe of particle fragmentation.[5] By following the evolution of polymer thermal properties with increasing reaction times, the authors showed that the fragmentation step in supported metallocene catalysts could take several tens of seconds to be completed.

Nevertheless, despite the advantages listed above, the geometry and conception of the SF 1 set-up limited the heat evacuation from the reaction zone, often observed as temperature spikes as high as 20°C. This also contributed to inhomogeneous polymer formation throughout the reaction bed.

As shown in the detailed modelling work of Browning et al.[13], the presence of a metal frit with a high heat capacity at the reactor exit absorbed a significant part of the heat of reaction. This meant that the recorded experimental temperatures did not reflect the real temperature of the reaction bed, which was detrimental to the correct interpretation of the reaction kinetics and estimation of kinetic parameters.

Moreover, Browning et al. implemented a 2-D observer to estimate the reaction rate from the experimental data. Nevertheless, the downside remained that the input data for the observer were the calculated temperatures from the model, given the limitation of the set-up in accurately detecting the temperatures in the reaction bed.[14]

3.2. Experimental section

Considering all the aforementioned aspects of the existing set-up (SF 1) and the objectives of the current project, our initial step towards improving the stopped-flow reactor set-up was to thoroughly evaluate the existing set-up, hereafter referred to as Stopped-flow reactor 1 (SF 1) and determine the main practical aspects to be improved.

Catalyst testing was first carried out in a ‘standard’ lab-scale semi-batch reactor as a reference of the catalyst behavior in full time polymerizations of 60 minutes duration. Next, catalysts were tested with

the Stopped-Flow reactor 1 (SF 1) at short reaction times of 60 seconds duration. The 60 second duration was chosen, at this point, as it includes the critical period of catalyst activation and potential overheating in the reaction bed.

Besides the pre-activation method described in the procedures section for the commercial Ziegler-Natta catalyst, we also explored the possibility of activating the catalyst in-situ by injecting a desired amount of TEA solution under argon flow directly over the reaction bed during the polymerization reaction, aiming to minimize the pre-contact time between the catalyst and cocatalyst.

Particle temperatures were calculated with the heat balance proposed by Tioni et al. and described in section 3.1.2. of Chapter 1.

Finally, several tests performed with no catalyst, hereby referred to as *cold* tests, to evaluate the impact of hardware components unrelated to the polymerization reaction.

3.2.1. *Materials*

For the assessment of the existing set-up (SF1), we have used a classic commercial Titanium Ziegler-Natta catalyst, hereafter referred to as ZN 1.

This catalyst was chosen for the high polymerization activities and fast activation observed at full-time polymerization tests.

According to the available published information on this set-up (SF 1), the main hardware limitation encountered were temperature excursions related to poor heat evacuation from the reactor. Therefore, a classic Ziegler-Natta catalyst seemed like an appropriate choice for the purpose of evaluating the heat evacuation in this set-up.

The performance of the SF 1 set-up was assessed in homopolymerization conditions with ethylene.

Triisobutylaluminum (TiBA) purchased from Witco GmbH was used as scavenger in a 1 M solution in dry heptane. Ethylene with 99.95% purity purchased from Air Liquide – France was used as monomer gas throughout this study.

3.2.2. *Reactor description and polymerization procedure*

The stopped-flow reactor 1 (SF 1), shown in Figures 2 to 4, consists of a fixed bed reactor in which the catalyst is dispersed in a salt bed, and the process gases pass through the bed for a predetermined duration. The reactor itself is composed of a circular stainless-steel cartridge with fritted base (20 mm diameter, 10 mm depth), which is placed into a stainless-steel chamber that is closed with a fritted metal filter.

The fritted metal filters present in the inlet and outlet of the reactor (3 mm thick with 13 µm pores) ensure the bed stability and prevent solid loss during the reaction. The system is equipped with 1 mm T-type thermocouples that measure the inlet and outlet gas temperatures (before the inlet frit and after the outlet frit), with information collection every 0.5 s. Additionally, the set-up is equipped with solenoid valves that allow an automated control of the gas injection, the degassing of the reactor and

injection of quenching gas. More details on the operation of this reactor set-up can be found in previous works [4,11,12]

The general mode of functioning consisted of filling the reactor chamber in a glove box with a mixture of inert seedbed (salt, in this case) and catalyst (1-15 wt% depending on reaction duration). The fine salt used in the experiments is prepared by re-precipitation in ethanol and citric acid and the protocol has been described elsewhere. [4,15] The metal cartridge is weighed before and after packing to obtain the amount of solid inserted.

The Ziegler-Natta catalyst is pre-activated in the glove box with a 1 M TEA solution in dry Heptane. The desired amount of the TEA solution is added to the salt/catalyst mixture, aiming for a specific Al/metal ratio. The mixture is vigorously agitated by hand, then dried under active vacuum for at least 15 minutes before inserting in the reactor.

The reactor system was attached to feed lines and plunged into a water bath set to the desired reaction temperature. Reactions with catalyst ZN 1 were carried out at 70 °C and 7 barg of Ethylene pressure. The gas liner velocities were calculated from the gas flowrates measured by a rotameter at the reactor exit.

The reactor was purged with argon during the heating step. The polymerization started when the solenoid valve was opened for monomer flow, set for a desired reaction time. The reactor was then rapidly degassed and a shot of carbon dioxide simultaneously quenched any remaining catalyst activity.

The polymerization yield was measured gravimetrically by weighing the cartridge bed before and after the reaction. The polymer was recovered by washing away the salt seedbed and dried under vacuum at 70°C for at least two hours.

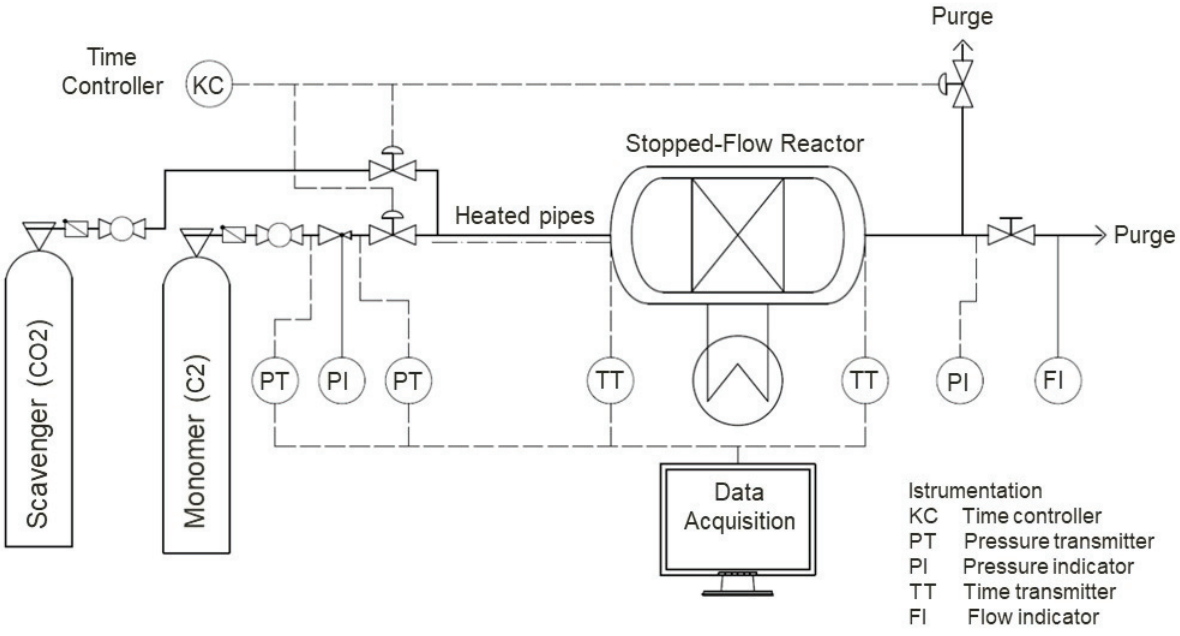

Figure 2: Stopped-flow Reactor 1 (SFR 1) experimental set-up and control system. Adapted from Cancelas et al.[16]

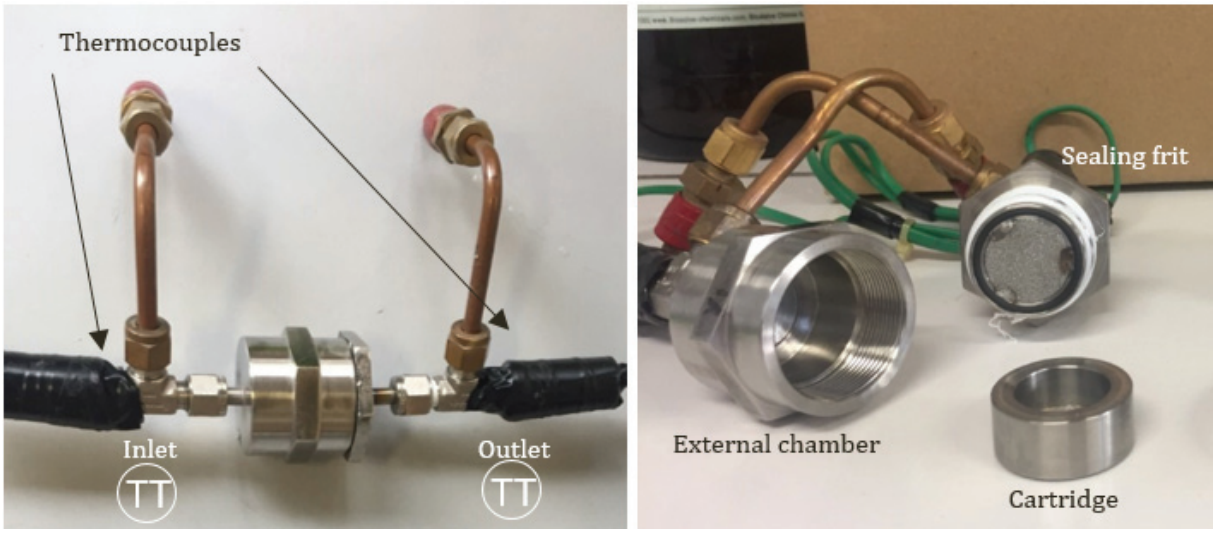

Figure 3: Stopped flow reactor 1 (SF 1), assembled (left) and disassembled (right).

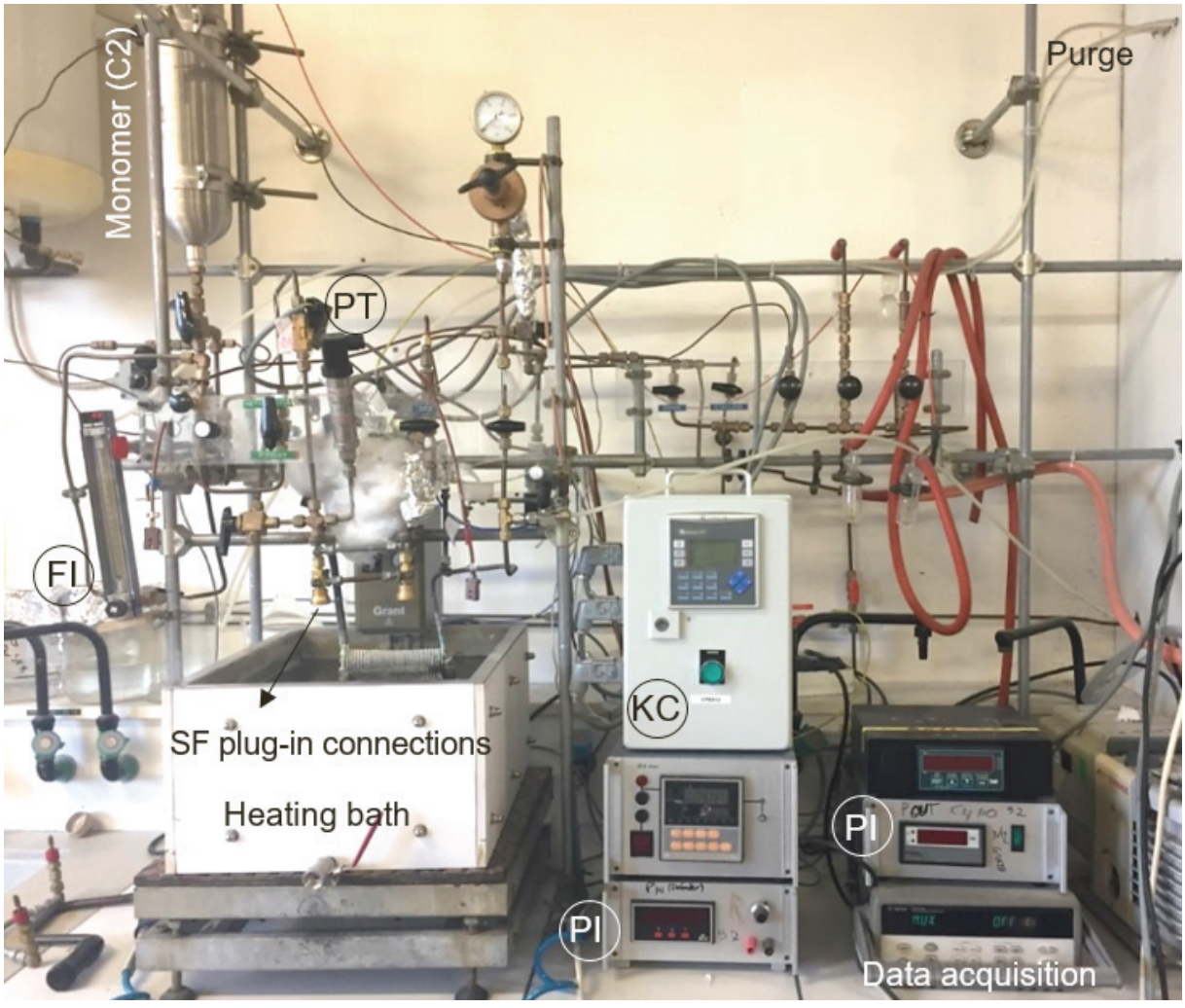

Figure 4: Stopped-flow Reactor 1 (SF 1) set-up in 2016, at the beginning of this project

3.3. Heat evacuation assessment

Full time polymerization kinetics obtained from standard polymerization tests of 60 minutes duration are seen in Figure 5. The activity profiles obtained in homopolymerizations with the commercial Ziegler-Natta ZN 1 were in agreement with previously observed tests under similar conditions.[8]

Short time polymerization results obtained with the Stopped Flow Reactor 1 (SF 1) using a commercial Ziegler-Natta catalyst (ZN 1) are seen in Table 1. The outlet temperature profiles recorded during the 60 second experiments are found in Figure 6 and the corresponding inlet temperature profiles are seen in Figure 7. The temperature profiles of the reaction performed with in-situ catalyst activation can be seen in Figure 8.

The obtained polymer yields are coherent with the catalyst activities obtained from the full-time polymerization assessment. Moreover, they are in agreement with previously observed studies carried out in our group at similar reaction conditions. [16] Nonetheless, as seen in Figure 6, all experiments led to very high temperature gradients with excursions as high as 40 °C.

From the results seen in Table 1, we noticed that, at comparable reaction conditions (experiments named ZN 1 #1 and #2), the obtained polymerization yields values were not reproducible. This fluctuation was reflected in the estimated particle temperatures, as well as on the recorded outlet temperature profiles seen in Figure 6. We related the lack of reproducibility to fluctuations in the gas flowrates, often observed during the experiments. We attributed this phenomenon to the reactor frits being partially clogged by remaining polyethylene and residual alkylated solutions built-up overtime.

Moreover, as observed for experiment named ZN 1 #3, the heat evacuation seems to be less effective at lower linear gas velocities. This effect was obviously expected and was reflected in the estimated particle temperatures (well over the polymer melting temperature) and the outlet temperature profile. This observation is in agreement with the studies previously carried out by Tioni et al. on the heat transfer conditions using this reaction set-up. [3,4]

Concerning the in-situ activation of the commercial Ziegler-Natta catalyst, we observed a noticeable increase in the produced polymer yield (Table 1), leading also to polymer melting, seen in Figure 9.

Nevertheless, activating in situ under a gas flow did not allow us to know the real Al/Ti ratio and the reaction bed. In addition, the direct injection of alkyl aluminum reagents in-line can lead to equipment shut-down due to clogging (formation of alumina). Despite the high observed polymer yield, the outlet temperatures are lower than those observed for the pre-activated ZN catalyst in the GB. We linked this behavior to the fact that the liquid TEA/Heptane solution was injected in the set-up directly through the reactor, not going through the heating coil in the water bath, an adaptation made to minimize the path of the liquid solution. In addition to the impact of the sensible heat of this second feed to the reactor, adding TEA and heptane also changes the heat capacity of the gas phase, causing it to absorb more of the heat of reaction that is the case for a dry feed.

A common observation in the performed tests was a significant temperature drop (2 to 6 °C) in the inlet gas temperatures. This behavior was later assessed in cold test experiments, discussed below.

Despite the satisfactory polymerization yields obtained, the reactions were often unsuccessful, with a high failure quota of about 70%, where no polymer was produced. We suspected the reactor quick

plug-in connections were a source of contamination by air. This hypothesis was assessed at the hardware evaluation.

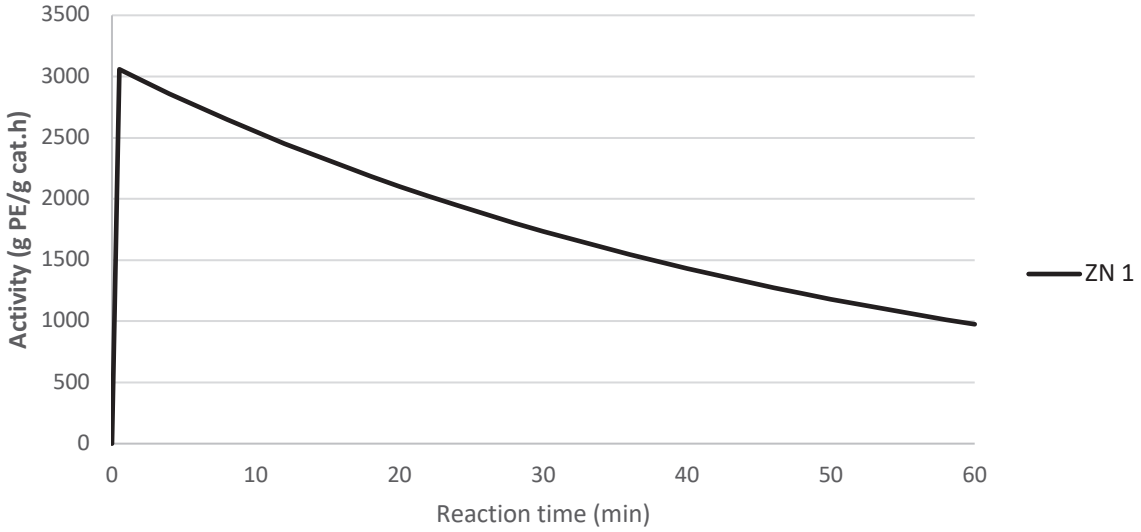

Figure 5: Full polymerization kinetics for 60 minute homopolymerization reactions with commercial Ziegler-Natta catalyst ZN 1. Conditions: 70 °C, 7 bar ethylene,

Catalyst used	Experiment #	Yield (g/g)	Gas linear vel. (cm/s)	Estimated Particle T (°C)
ZN 1	ZN 1 #1	9	18	145
	ZN 1 #2	5	18	73
	ZN 1 #3	12	4	209
	ZN 1 in-situ TEA	17	18	277

Tableau 1: Polymerization yields for 60 second homopolymerization reactions with ZN 1 catalyst, using the FR 1 reactor.

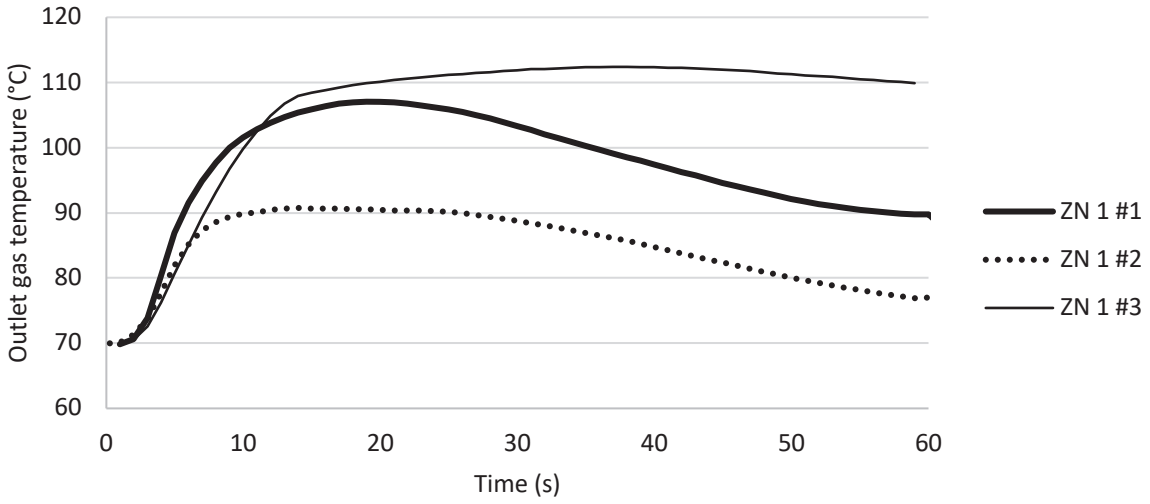

Figure 6: Recorded outlet temperature profiles 60 second experiments with ZN 1 catalyst. Reaction conditions described in Table 1.

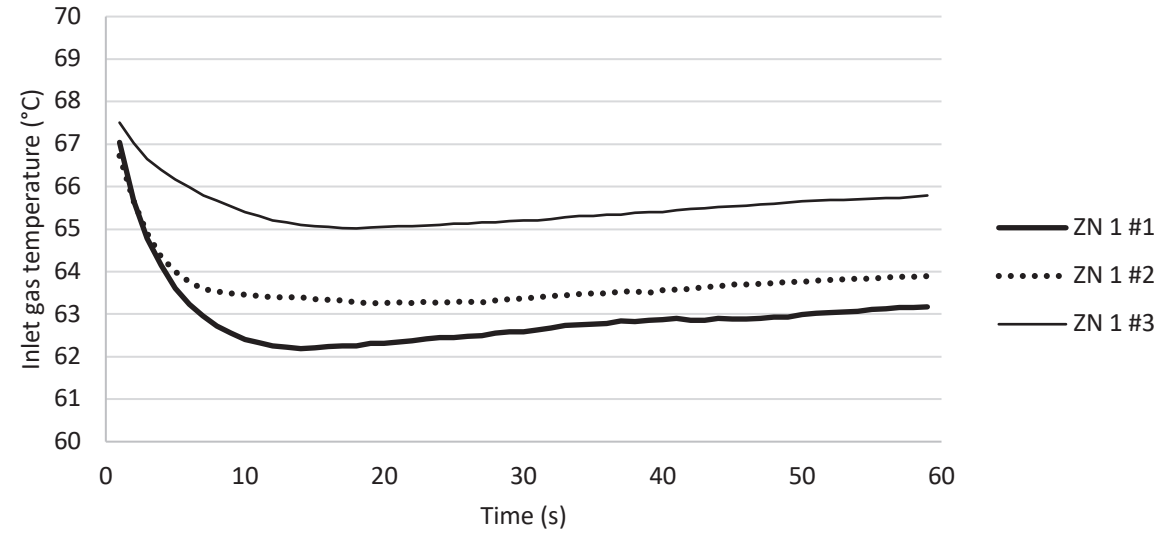

Figure 7: Recorded inlet temperature profiles 60 second experiments with ZN 1 catalyst. Reaction conditions described in Table 1.

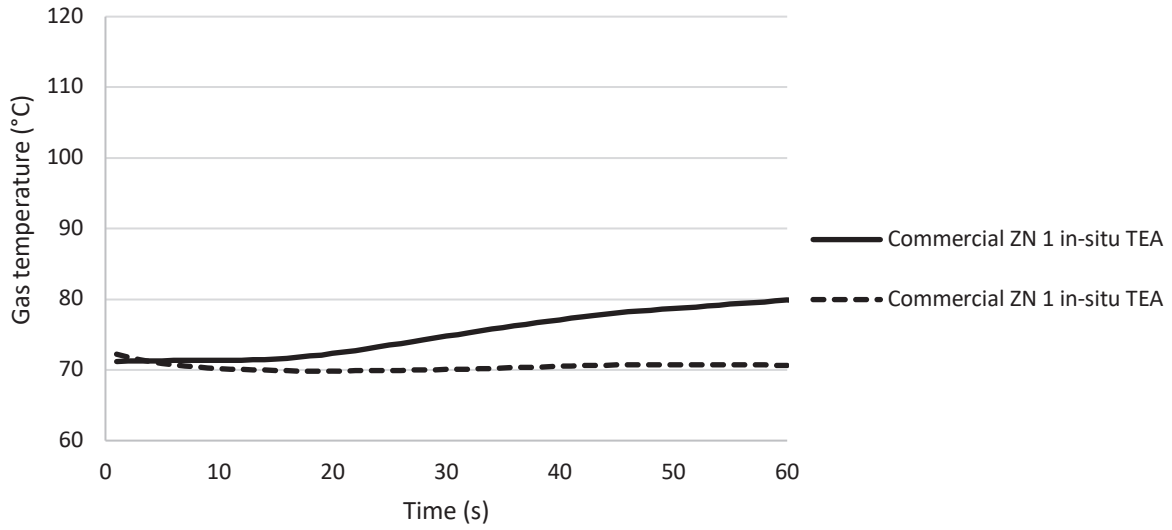

Figure 8: Inlet and Outlet temperature profiles recorded during the 60 second experiment, with commercial Ziegler-Natta activated in-situ, during the experiment

Figure 9: Polymer obtained from in-situ activation of commercial Ziegler-Natta catalyst. TEA injection over catalyst bed under Argon flow during polymerization reaction.

3.3.1. *Conclusion*

The obtained polymerization yields are satisfactory and in agreement with previous studies carried out at similar experimental conditions. Nonetheless, important temperature gradients (as high as 40 °C) were observed in homopolymerization conditions, seen in the outlet temperature profiles for the 60 second reactions performed with a classic Ziegler-Natta catalyst.

The polymerization yields were not reproducible for similar reaction conditions; an effect that was attributed to fluctuations in the gas flowrates caused by partial clogging o the reactor frit (perhaps by remaining polymer or residues from the alkylated agents). The lack of reproducibility was also reflected on the estimated particle temperatures, as well as on the outlet temperature profiles obtained experimentally. We observed that the heat evacuation is less effective at lower linear gas velocities, an observation that is in agreement with the previous studies carried out by Tioni et al. [3,4]

3.4. Hardware evaluation

Tests in this section were performed with no catalyst, hereafter referred to as *cold* tests. The reactor was filled only with the salt seedbed to evaluate the impact of hardware components unrelated to the polymerization reaction.

The influence of different flow velocities on the inlet gas temperature drop can be found in Figure 10. Clearly, higher gas flowrates lead to more significant heat loss, as heat exchange with the heating coil is reduced for higher flowrates. It seems reasonable to assume that this is linked to a limitation of the set-up, as heating of the gases through the heating coil inside the water bath does not suffice to keep temperatures constant.

We observed that heating the gas directly at the cylinder source led to no significant improvement on the inlet gas temperature drop, which can be seen in Figure 11. For these experiments, the monomer ballast was substituted by a heating ballast that allowed to set the desired temperature of the incoming gas. Equal temperatures were set for the heated ballast and the water bath.

Given the high experimental failure rate observed during polymerization tests, we added a bypass to allow purging the quick plug-in connections with argon, which were suspected to be a source of contamination by air. This modification of the set-up can be seen in Figure 12.

Nevertheless, the valves in the bypass added many moving parts to the system and were a significant source of leaks and contamination, besides making the system quite heavy and more difficult to handle in the glove box.

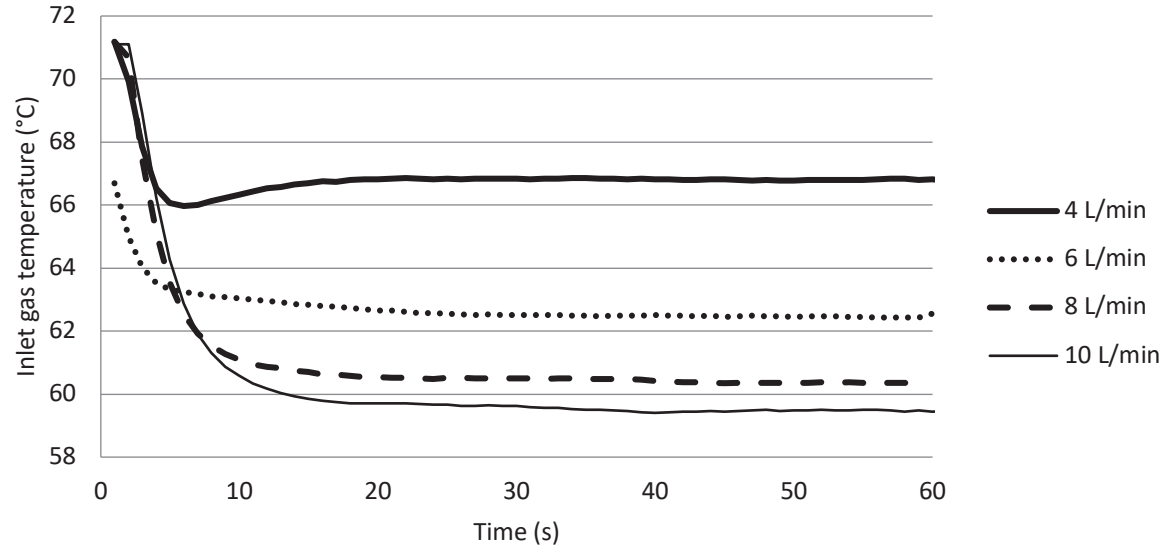

Figure 10: Influence of flow velocities on inlet gas temperature drop

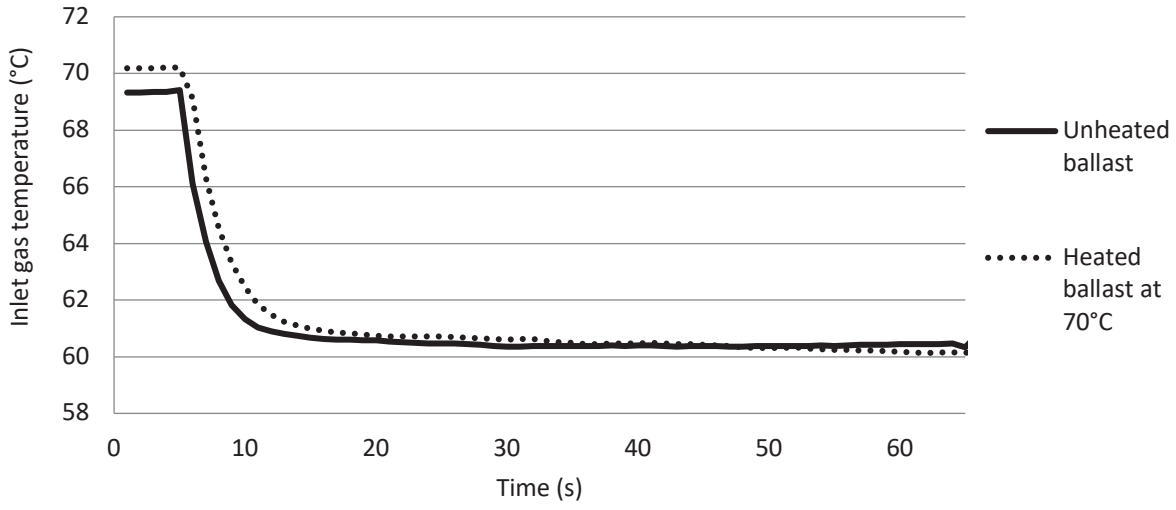

Figure 11: Influence of heating monomer cylinder on inlet gas temperature drop

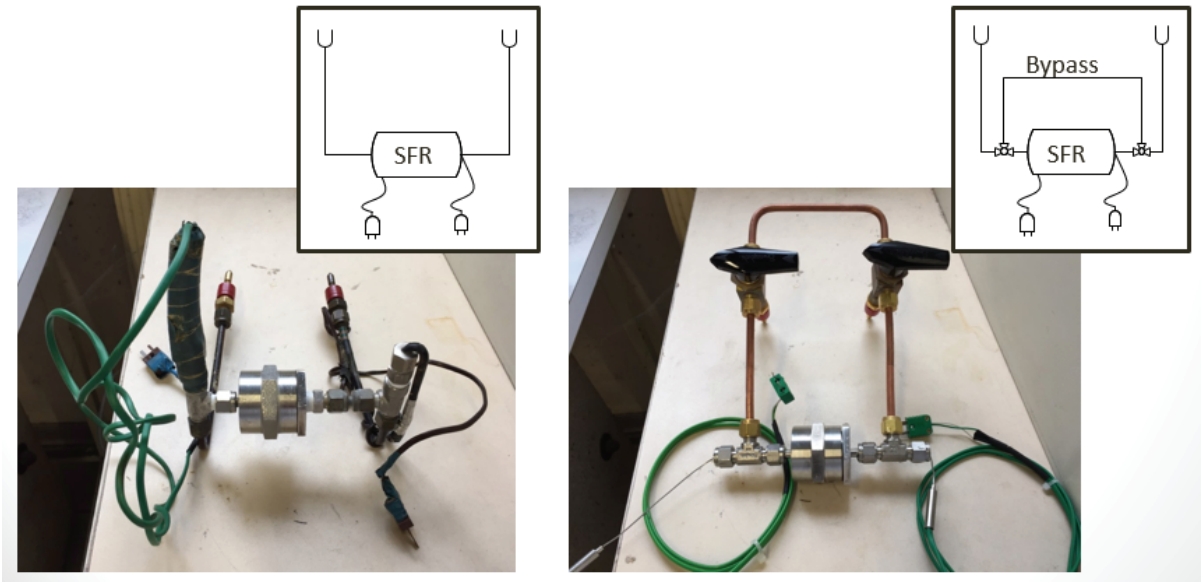

Figure 12: Stopped-flow Reactor 1 (SF 1) reactors and their representations. Before (left) and after (right) addition of by-pass for purging the plug-in connections.

3.4.1. *Conclusion*

The hardware evaluation was performed without catalysts in order to detect effects unrelated to the polymerization reaction.

By varying the flowrates of the monomer feed, we remarked significant drops of the inlet gas temperatures, which were more pronounced at higher gas flowrates. Heating the monomer ballast seemed to have little to no effect in reducing the temperature drop. This indicated a limitation of the set-up in effectively heating the inlet gas and keeping constant temperatures throughout the reaction.

A bypass route was added to the reactors, aiming to reduce possibilities of contamination by air. Nevertheless, this approach made the set-up more difficult to handle in the glovebox and the addition of moving parts increased the possibility of leaks during the reaction.

3.5. Conclusions on assessment of reactor SF1

The objective of this set of experiments was to determine the main sources of issues and aspects to be improved in the existing stopped flow reactor set-up (SF 1). Tests in homopolymerization with ethylene were performed with a commercial Ziegler-Natta catalyst (ZN 1).

When the experiments worked, we obtained satisfactory polymerization yields that were in agreement with previous studies. Nevertheless, the experiments had a high failure rate (about 70%), often caused by leaks in the system and catalyst contamination by oxygen or impurities. Moreover, significant temperature drops were observed on the inlet gas due to a limitation of the set-up in sufficiently heating the gas and keeping constant gas temperatures. This effect is detrimental to the precise kinetic evaluation of a given catalyst.

The main factor leading to experimental failure was catalyst contamination with oxygen through leaks in the set-up, an issue accentuated by the fact that the reactor had several moving parts and could not

be completely sealed in the glovebox, given the size of the reactor itself. We also observed irregular fluctuation of the gas flows, which were attributed to the reactor frits being partially clogged by remaining polyethylene and residual alkylated solutions built-up overtime.

The Stopped-Flow Reactor 1 (SF 1) was first build in 2009, and counted several interventions during the last decade, which made it challenging to track all modifications performed and the impact of each of them. In addition, the reactor lines were all in copper alloy, far from ideal to be placed in a water bath.

In spite of the satisfactory obtained polymer yields, the obtained polymer was often melted into a block, indicating the reaction zone reached temperatures beyond the polymer melting point. The high temperature gradients (often more than 30°C) observed were mainly linked to poor heat evacuation in the reactor due to its geometry and small volume. As observed by Tioni et al.[3,4,12] and mathematically described by Browning et al.,[13,17] the presence of a metal frit before the outlet thermocouple led to lower recorded outlet temperatures than those reached in the reaction zone. Besides, the small volume of the reaction bed limited the polymer production to few milligrams per experiment and the set-up allowed a limited possibility of reaction conditions, as the system was not adapted for injecting liquids in a controlled manner in the reaction zone. Therefore, performing co-polymerization reactions (e.g. with 1-hexene) or studies in condensed mode operation (e.g. with n-pentane) were not straightforward with this set-up.

From the practical analysis of the existing set-up for stopped-flowed gas-phase polymerizations, we concluded there was room for improvement of the set-up concerning its effectiveness in heat evacuation, experimental robustness, risk of sample contamination, ease of handling, larger capacity for polymer production and increased possibility of reaction conditions.

4. Stopped-flow reactor prototype (SF 2)

Based on careful analysis of the available tool (SF 1), we detected several aspects that could potentially be improved in order to perform short-time polymerization reactions in gas-phase under precisely controlled conditions.

Mainly, those aspects were: improvement of the heat evacuation in the reactor to avoid thermal runway and polymer melting, improvement in the reactor inertness in terms of preventing contamination by oxygen and water. Moreover, it would be helpful to allow larger capacity for polymer production and make the reactor easier to handle during preparations in the glovebox.

4.1. Introduction

We aimed to tackle some of the aforementioned limitations of the existing set-up (SF 1) with a new reactor geometry.

With focus on improving the heat evacuation on the reactor and eliminating any internal temperature gradients like those described by Browning et al. [13,17], we targeted to improve the gas distribution by changing its configuration from a “disc-shaped” bed to a longer one that allowed for a more homogenous gas flow through the entire bed.

This was accomplished by choosing an annular reactor design and incorporating a porous stainless-steel membrane as the inner cylinder of the annulus, through which the inlet gas will flow before reaching the catalyst particles. The catalyst/salt bed is placed in the outer space of the annulus, and the gas fed through the center.

Our aim was to reduce the gas pathway to the catalyst and, therefore, obtain a more homogeneous flow distribution with reduced possibility of temperature gradients inside the reactor, as shown in the work of Al-Juaied et al.[18] Moreover, several advantages have been claimed for the use of an annular geometry for the study of highly exothermic reactions, such as improved gas-flow patterns, low (or negligible) pressure drops, fast transport, and effective heat dissipation of the reaction heat, with comparison to standard fixed-bed reactors. [19–21] Besides, the choice of an annular geometry has been (experimentally and theoretically) shown to improve issues related to internal diffusion limitations in the works of Groppi et al.[21,22] The reactor prototype was named stopped-flow reactor 2 (SF 2) and its schematic view is found in Figure 13.

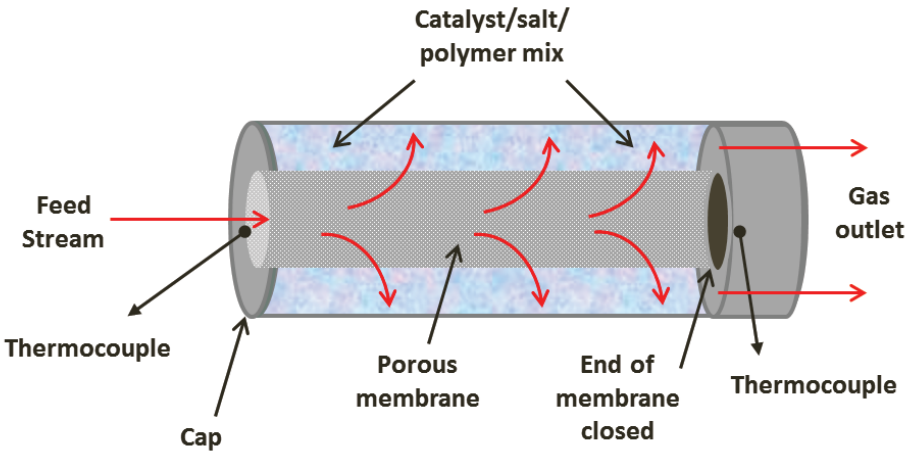

Figure 13: Schematic view of the stopped-flow reactor prototype (SF 2)

4.2. Experimental section

In order to evaluate the performance of the new reactor prototype (SFR 2), we initially assessed the heat evacuation with the new proposed reactor geometry. The assessment was carried out with a high activity Ziegler-Natta catalyst and a classic metallocene catalyst that is much more sensitive to reaction impurities.

At first, catalysts were tested in full-time polymerization conditions in the turbosphere semi-batch reactor in reactions of 60 minutes of duration. Next, catalysts were tested with the stopped-flow reactor prototype (SF 2) and evaluated in terms of polymerization yields and thermal properties of the obtained polymer through DSC analysis. Polymerization times varied between 5 and 60 seconds.

Following, the inertness of the reactor hardware was assessed with a classic metallocene catalyst very sensitive to impurities such as oxygen and water. Different purification measures in the system were assessed in order to define an optimal protocol for reactor conditioning, aiming to minimize the sources of contamination to the reaction medium.

Finally, we assessed the thermal response of the reactor prototype with a series of cold tests (performed with no catalyst) at varying pressures of the inlet gas.

4.2.1. *Materials*

The SF 2 reactor prototype was built with Swagelok 316 stainless-steel male and female VCR locks (Fitting 1/4 in), Swagelok Stainless Steel VCR 1/4 in. Tube Socket and porous frit by Stemm. The welding work was done by the CNRS research workshop at the Institute of research on catalysis and the environment (IRCE Lyon), located at University Claude Bernard Lyon 1 campus.

For the assessment of heat evacuation in the new reactor prototype (SF 2), we have used a classic Titanium Ziegler-Natta catalyst (ZN 1), given the high polymerization activities and fast activation obtained with this catalyst.

For the assessment of heat evacuation and hardware inertness in the new reactor prototype (SF 2), we have used a classic Zirconium metallocene catalyst, hereafter referred to as CpZ. Two different batches

of this catalyst were used in this study, referred to as CpZ 1 and CpZ 2. This catalyst was chosen for its high sensitivity to impurities.

Fine Glass wool from VWR, France was dried in an oven for at least 2 hours close to 100 °C.

Sylopol 948 silica grafted with TEA, hereby referred to as Si-TEA, kindly provided by INEOS – Lavera, France.

4.2.2. *Reactor description*

The new reactor prototype named stopped-flow reactor 2 (SF 2) was assembled using available marketed components, seen in Figure 14. The reactor prototype is shown in Figure 15.

In order to reduce the chance of contamination by air, the quick plug-in connections used in the previous version (SF 1) were removed and a three-way valve was added as a bypass to purge the reactor entry prior to the polymerization reaction. The reactor dimensions of the SF 2 are as follows:

- Diameter of external cylinder: 22 mm
- Outer diameter of porous membrane: 17 mm
- Pore diameter of membrane: 5 µm
- Reactor length: 11 cm

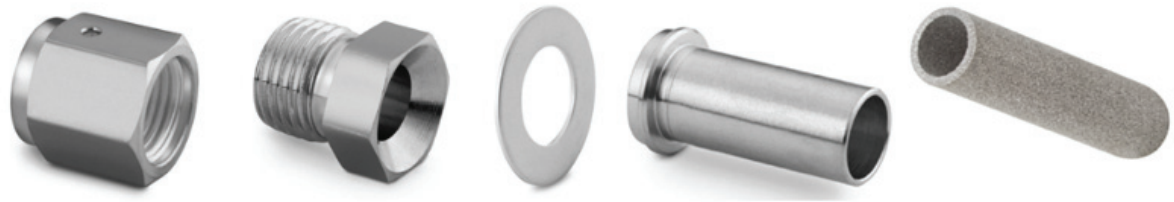

Figure 14: Commercial parts used in the construction of the SF2 reactor prototype

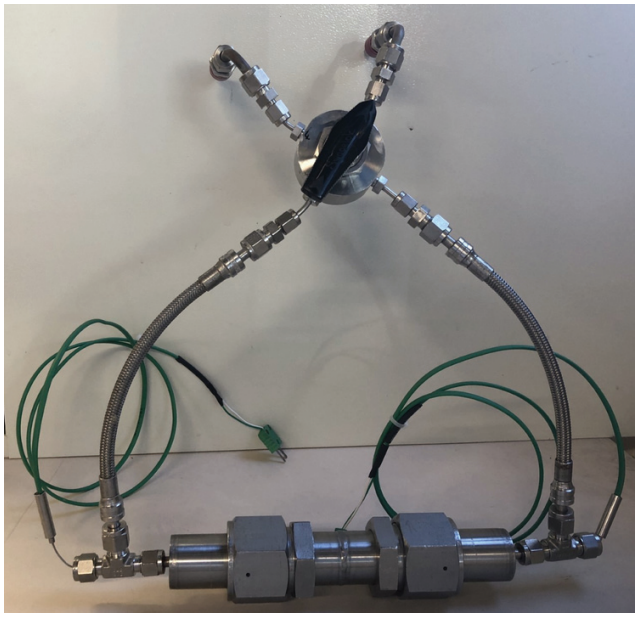

Figure 15: Stopped-flow reactor 2 (SF 2)

4.2.3. *Polymerization procedure*

Before each experiment, the reactor was dismantled, cleaned with heptane and kept in an oven (close to 100 °C) overnight.

Inside a glove box under argon atmosphere, a glass vial is filled with a mixture of an inert seedbed (NaCl) and the desired catalyst amount (1.5 to 2 wt%). Coarse NaCl salt consisting of single cubes of 250–500 µm were previously dried under vacuum for 6 hours at 400°C. The procedure for preparing fine NaCl salt with singe cubes of 5 µm has been described elsewhere. [4,15]

The Ziegler-Natta catalyst was pre-activated in the glovebox with a 1 M TEA solution in dry Heptane. The desired amount of the TEA solution is added to the salt/catalyst mixture, aiming for a specific Al/metal ratio. The mixture is vigorously agitated by hand, then dried under active vacuum for at least 15 minutes before inserting in the reactor.

The solid mixture was then inserted in the annular reactor gap with the aid of a funnel and a layer of glass wool (average of 1.5 g) was placed at the top to fill the void space in the reactor and keep the solid from being expelled by the incoming gas, as shown in Figure 16.

The solid content inserted in the reactor was gravimetrically determined by weighing the mixing container (vial) before and after filling the reactor with the solid. The reactor was manually closed with the outer lid and hermetically sealed upon exit of the glovebox.

The reactor and feed lines were plunged into a water bath to set the bed and feed temperatures. The reactor bypass isolated the reaction bed as the system was purged with Argon. The inlet and outlet gas temperatures were measured with two 1 mm T-type thermocouples placed on the entry and exit of the reactor. The polymerization occurred when a pulse of the monomer gas was fed to the reactor for a fixed time (possible range: 0.01 to 100 seconds). At the end of the pre-determined polymerization time, the reactor was simultaneously vented and fed with carbon dioxide, our quenching agent.

After the reaction, the polymer was recovered by washing away the salt seedbed. Finally, the recovered polymer was dried under vacuum at 70 °C for, at least, two hours.

Experimental conditions for the catalysts used in this section

For the Ziegler-Natta catalyst (ZN 1) used in this study, 35-40 mg catalyst were used and 1 mmol TEA was used as cocatalyst aiming for a ratio Al/Ti=60. The reaction temperature was 70 °C and ethylene pressure kept constant at 7 barg with gas velocity of 18 cm/s in average.

For the classic metallocene catalysts (CpZ 1 and CpZ 2) used in this study, 40-45 mg catalyst were used without addition of alkyl agents, unless states otherwise. The reaction temperature was 80 °C and ethylene pressure kept constant at 7 barg with gas velocity of 18 cm/s in average.

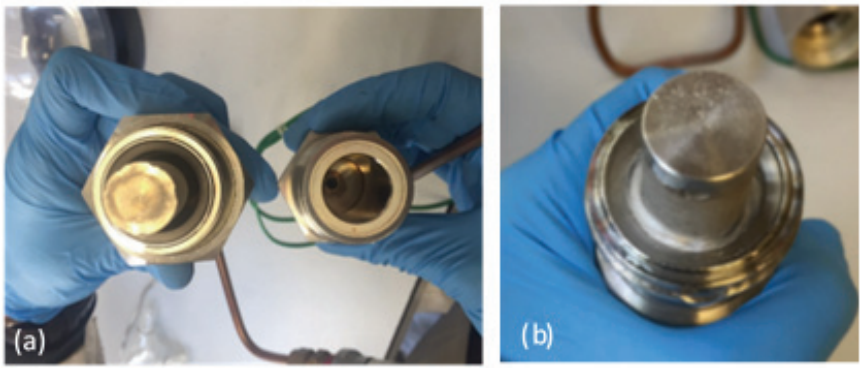

Figure 16: Open view of the stopped-flow reactor 2 (SFR 2): (a): before packing with solid mixture, (b): reactor after packing with catalyst and glass-wool

4.2.4. *Estimating the particle temperature*

When estimating the particle temperatures with this reactor (SF 2), we applied the simplified heat balance described in Chapter 1, section 3.1.2. The only difference were the terms included in the heat contribution term (mC_p), which are: the mass of solid (salt + catalyst) in the reactor and the addition of glass wool in the reaction bed (average 1.5 g). A more detailed model of this reactor was developed to estimate the particle temperatures and interpret the experimental data more accurately. The model will be described further in Chapter 3.

4.3. Heat evacuation assessment

The heat evacuation in the reactor prototype was initially assessed with a high activity Ziegler-Natta, the same catalyst used to assess the previous set-up (SF 1). Next, the impact of using coarse and fine salt as inert seedbed was assessed with a classic metallocene catalyst (CpZ 1).

The catalysts used in this section were initially tested in full-time polymerization conditions as a reference for the catalyst behavior at longer reaction times. Kinetic profiles were obtained with the turbosphere semi-batch reactor, with reaction conditions for each catalyst described in section 2.1.1. of this chapter. The activity polymerization profiles obtained for reactions of 60 minutes duration are seen in Figure 17.

Next, as described in the following sub-sections, catalysts were tested with the stopped-flow reactor prototype (SF 2) and evaluated in terms of polymerization yields, experimental temperature profiles and thermal properties of the obtained polymer through DSC analysis. Polymerization times varied between 5 and 60 seconds.

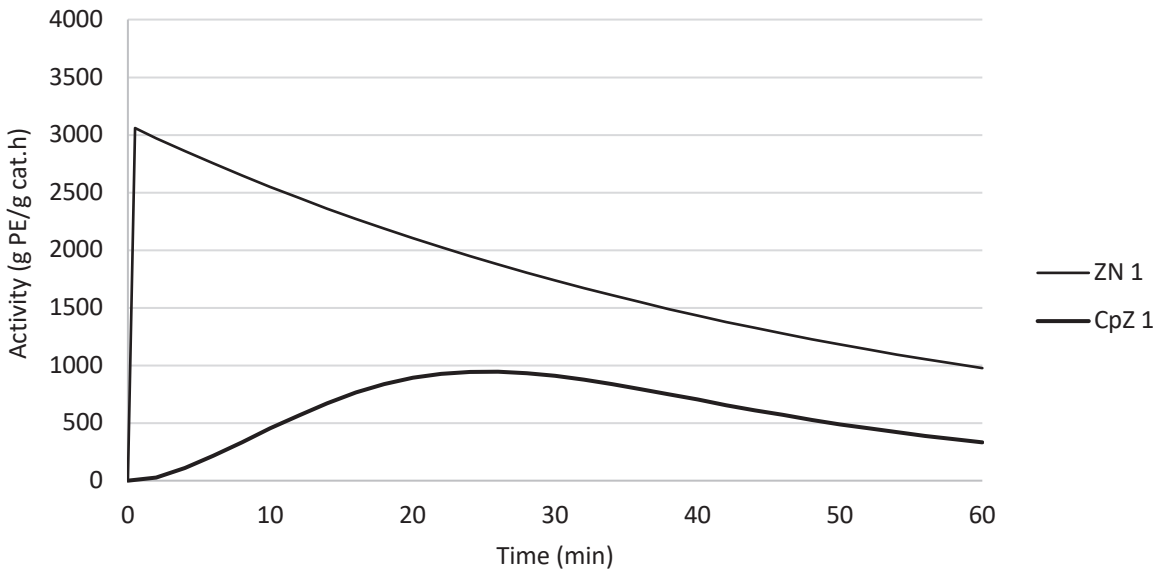

Figure 17: Full polymerization kinetics for 60 minute homopolymerization reactions with classic Ziegler-Natta and Metallocene catalysts used in this section

4.3.1. *Improved temperature gradients with ZN catalyst*

Results obtained using a commercial Ziegler-Natta catalyst are seen in Table 2. The obtained polymer yields have acceptable reproducibility (standard deviation of 0.87) and are in agreement with the values achieved using the previous reactor (SF 1) at similar experimental conditions. The obtained yields are also coherent with the catalyst activities obtained from the full-time polymerization assessment.

The polymers presented satisfactory thermal properties (crystallinity and melting temperatures) and the estimated particle temperatures are lower than the ones obtained with the previous reactor (SF 1) for similar polymer yields, which is an indication that the heat removal from the reactor has been improved.

Moreover, from the obtained outlet temperature profiles seen in Figure 18, we observed lower maximum temperatures than those obtained using the previous reactor (excursions for SF 1 were as high as 40 °C) for similar reaction conditions and comparable polymer yields. We observed some variation in the temperature profiles, which could be due to fluctuations of the initial reaction temperature, given the reactors are in a water bath exposed to room temperatures. Nevertheless, we consider these experiments to be satisfactorily reproducible.

Catalyst used	Experiment #	Yield (g/g)	Estimated Particle T (°C)	Tm (°C)	Crystallinity (%)
ZN 1	1	6,5	94	132	54
	2	8,3	98	131	52
	3	6,4	108	131	41

Tableau 2: Repeatability assessment with commercial Ziegler-Natta catalyst. Reactions of 60s duration, performed with 30-40 mg catalyst at 80°C activated with TEA at Al/Ti=60, 7 bars Ethylene with gas velocity of 18 cm/s in average

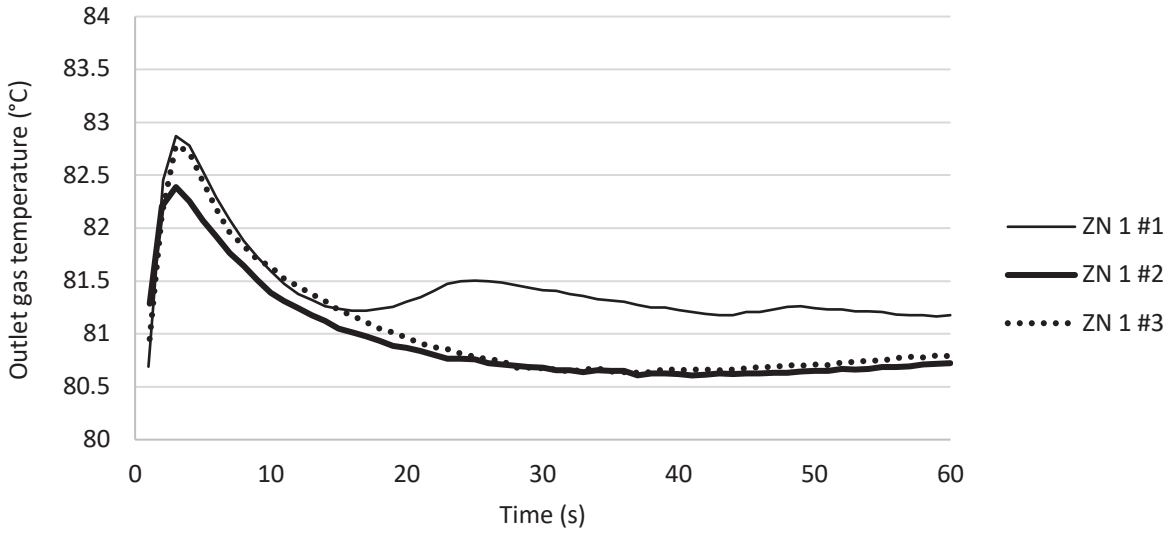

Figure 18: Outlet temperature profiles of 60 s polymerizations performed with Commercial ZN 1 using the SFR 2 reactor. Reaction conditions described in Table 2

4.3.2. *Impact of seedbed on polymerization yield*

Results from ethylene homopolymerization with a classic metallocene catalyst (CpZ 1) using coarse (450 µm crystals) and fine (5 µm crystals agglomerated into particles of average diameter of 50 µm) salt as inert seedbed at increasing reaction times are seen in Table 3.

From the plot in Figure 19, we observed a linear trend between the polymer yield and increasing reaction times, indicating coherence in the polymerization yield evolution with reaction time. Besides, we observed similar polymerization yields for both types of inert seedbed.

In the works of Tioni et al.[4], the authors observed that using fine salt particles improved the heat transfer from solid to gas in relation to using coarse salt. The increased heat-transfer coefficient led to lower temperature outruns and improved operational control when using finer particles. Given the heat transfer studies carried out by Tioni et al., this can be taken as another indication that heat removal has been improved with the new annular reactor geometry.

In Figure 20, DSC thermal analysis results for polymers obtained with coarse salt have been plotted, showing an evolution of the thermal properties for increasing polymerization times. We observed an increase of melting and crystallization temperature peaks with reaction time. A slight bimodality is observed at 5s of reaction, which then progresses to one defined peak. This behavior can be related to the increasing polymerization yields with reaction time and has been observed in previous studies. Although evaluating different time scales, this behavior is in accordance with similar effects observed by Tioni at al.[5] and Di Martino et al.[23] This could suggest that the polymerization is happening in a confined space, so full crystallization takes a certain amount of time to be completed.

C19alyst used	Reaction time (s)	Inert seedbed	PE Yield (g/g)	Tm (°C)	Crystallinity (%)
CpZ 1	20	Fine salt	1,2	130.3	23.3
	40		4,8	131.1	47.5
	60		7,3	131.0	49.8
	5	Coarse salt	0,9	130.5	26.6
	10		1,5	131.2	44.1
	20		2,8	131.8	43.1
	40		4,6	131.9	50.7
	60		8,2	131.5	43.7

Tableau 3: Impact of type of salt at increasing reaction times. Reactions performed with 60 mg catalyst at 80°C, 7 bars Ethylene with gas velocity of 18 cm/s in average.

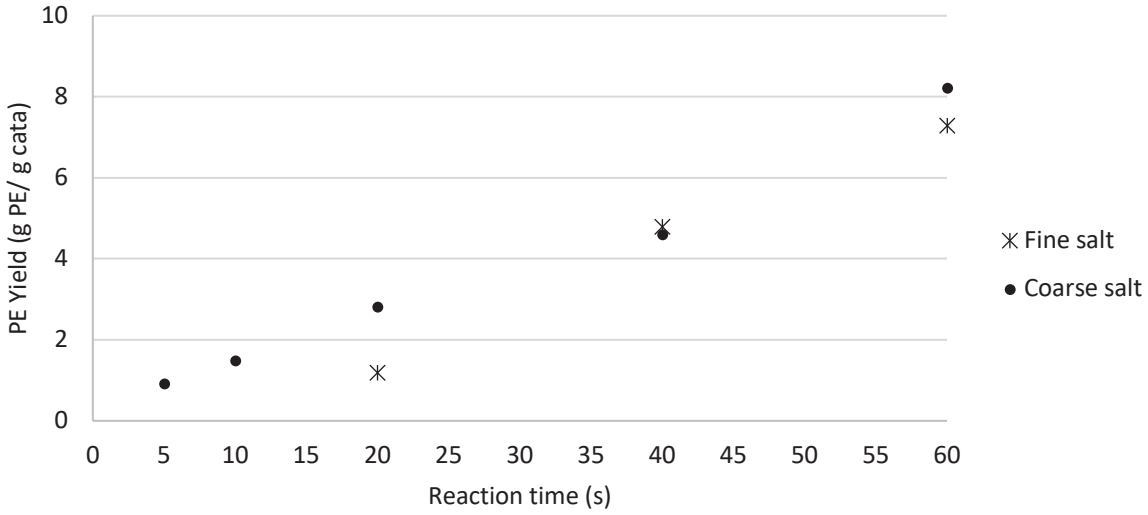

Figure 19: Evolution of yield with reaction time for experiments performed with fine and coarse salt. Conditions described in Table 3.

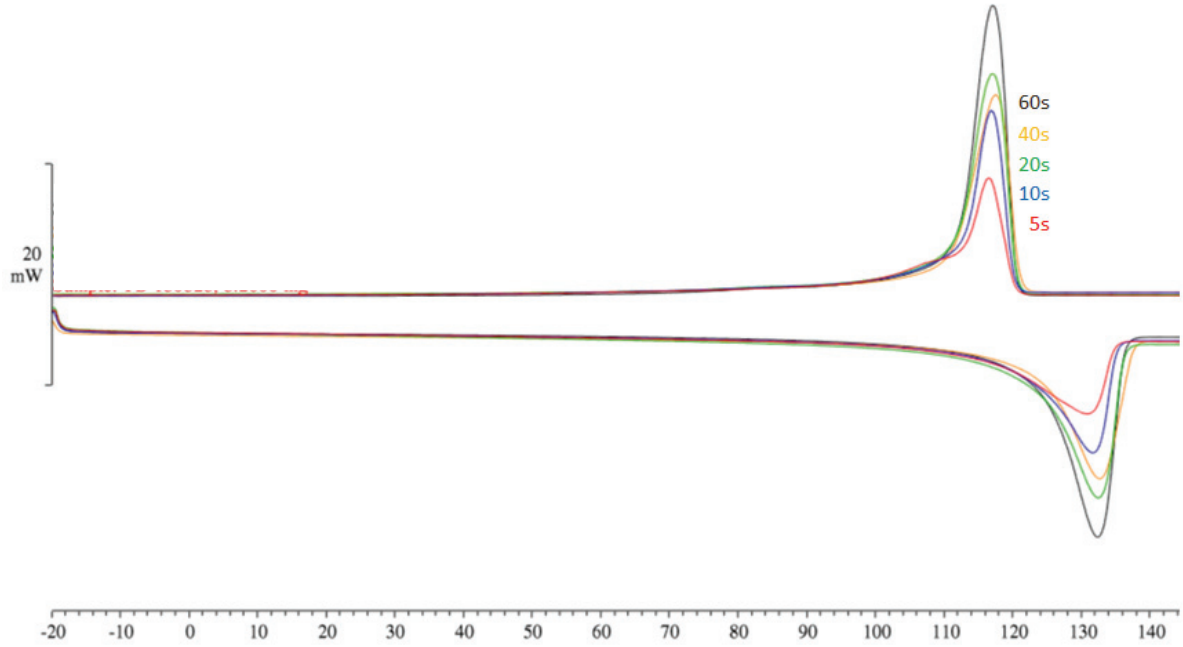

Figure 20: Evolution of the polymer thermal properties with reaction time, done with coarse salt and metallocene CpZ 1

4.3.3. *Conclusion*

The heat evacuation in the reactor prototype was assessed with a high activity Ziegler-Natta. Satisfactory repeatability of polymerization yields (with standard deviation of 0.87) and polymer thermal properties were obtained. The measured outlet temperature profiles showed lower maximum temperatures than those obtained using the previous reactor for similar reaction conditions and comparable polymerization yields. This indicated a considerable improvement of the heat evacuation in the reactor in relation to the previous reactor set-up (SF 1).

Next, the impact of different types of salt as seedbed on the polymerization yield and polymer properties was assessed with a classic metallocene catalyst (CpZ 1). Similar polymerization yields were obtained for both types of inert seedbed. Given the heat transfer studies carried out by Tioni et al.[4], this can be taken as another indication that heat removal has been improved with the new annular reactor geometry.

4.4. Hardware inertness assessment

The inertness of the reactor prototype (SF 2) was assessed in terms of preventing catalyst contamination by impurities such as oxygen and water. The assessment was done with a classic metallocene catalyst, due to the sensitivity of this catalyst to such impurities.

Different purification measures using alkylated agents as scavenger were added to the system in order to define an optimal protocol for reactor conditioning and minimize sources of contamination to the reaction medium.

4.4.1. *Improving inertness by reactor conditioning with alkyl agents*

Alkylated agents were used as scavengers for impurities. They were added to the system in different approaches in order to define an optimal protocol for reactor conditioning. The effect of each approach was assessed in terms of polymerization yields and thermal properties of the obtained polymer.

Short time polymerization tests in this section were obtained with the Stopped Flow Reactor 2. Results are seen in Table 4, in which purification measures were progressively added to the system, as follows:

1. Reaction bed composed of catalyst and fine salt;
2. Reaction bed composed of catalyst fine salt and 15 %wt silica grafted with TEA ;
3. Reaction bed composed of catalyst and fine salt. Addition of silica grafted with TEA cartridge in the ethylene (C2) feed line: Si-TEA cartridge.

We see from the polymerization yields and polymer thermal properties in table 4 that the purification measures seem to have a direct impact on the quality of the polymerization. This assessment indicated that the presence of impurities, mainly in the gas feed, was problematic for the catalyst activity. Therefore, we have hereafter conducted short-time polymerization reactions with a cartridge of inert support grafted with TEA as an added purification measure for the monomer gas.

The presence of impurities acts as poisons to the catalyst and this effect is particularly pronounced at the beginning of the polymerization reaction. At the reaction start, when catalysts are highly reactive and incorporate high amount of monomer, the amount of impurities present in the feed gas will be proportional.

Catalyst used	Purification measures	PE Yield (g/g)	Tm (°C)	Crystallinity (%)
CpZ 1	Catalyst + fine salt	1.2	--	--
	Catalyst + fine salt + Si-TEA	1.5	126.5	7.6
	Catalyst + fine salt + Si-TEA cartridge for C2	4.8	131.1	47.5

Tableau 4: Impact of incrementing purification measures. Reactions of 40 s duration, performed with 60 mg catalyst at 80°C, 7 bars Ethylene with gas velocity of 18 cm/s in average.

4.4.2. *Conclusion*

The inertness of the reactor prototype (SF 2) was assessed and improved by addition of alkylated agents to the reactor system. Out of the different purification measures tested, the most efficient in improving the polymerization yield and polymer properties was the addition of a cartridge filled with silica grafted with TEA (Si-TEA) in the monomer feed line.

Therefore, we incorporated the use of this cartridge with silica grafted with TEA in the reaction protocol for reaction conditioning.

4.5. Hardware thermal response assessment

The influence of increasing monomer pressure on the inlet and outlet gas temperature profiles can be seen in Figures 21 and 22, respectively. As observed, higher gas pressures led to more significant heat loss in the inlet gas temperatures, as seen in Figure 21. This is linked to inefficient gas heating of the set-up and is in agreement with what was observed in the previous set-up (SF 1).

In Figure 22, we observed temperature spikes at the first few seconds of reaction, which we linked to the effect of gas pressurization. This effect was previously observed for the previous set-up (SF 1) in the works of Tioni et al.[12] As seen in Figure 22, this effect is more pronounced as the pressure of the inlet gas increases. It is of no surprise that higher gas pressures lead to more significant temperature spikes due to the heat of gas compression. Nonetheless, given that the temperature gain is of the same order of magnitude as the temperature increase observed in some of the polymerization reactions at similar reaction conditions, this effect is not negligible.

To try to circumvent this effect, we pre-pressurized the reactor with an inert gas prior to ethylene injection, seen in Figure 23. The reactor was pressurized with Helium at 7 bar (0 to 60 s) and quickly manually switched to ethylene (60 to 120 s) at the beginning of the polymerization reaction. We noticed the temperature spike due to pressurization with Helium at the begging of the test. Nevertheless, when switching to ethylene at 60 s, we noticed that the temperature increase due to the heat of compression was successfully reduced when comparing to the same experiment performed without reactor pre-pressurization.

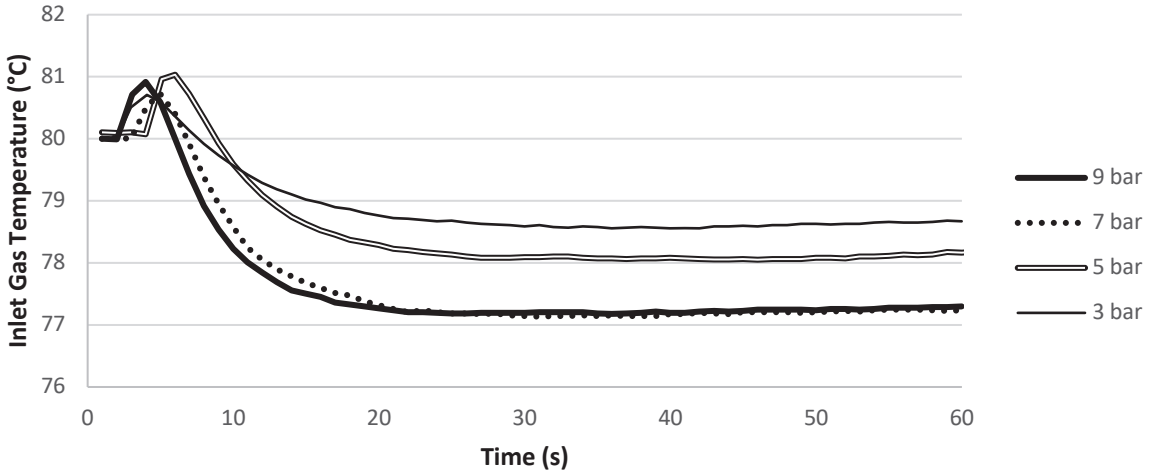

Figure 21: Effect of monomer pressure on inlet gas temperature drop

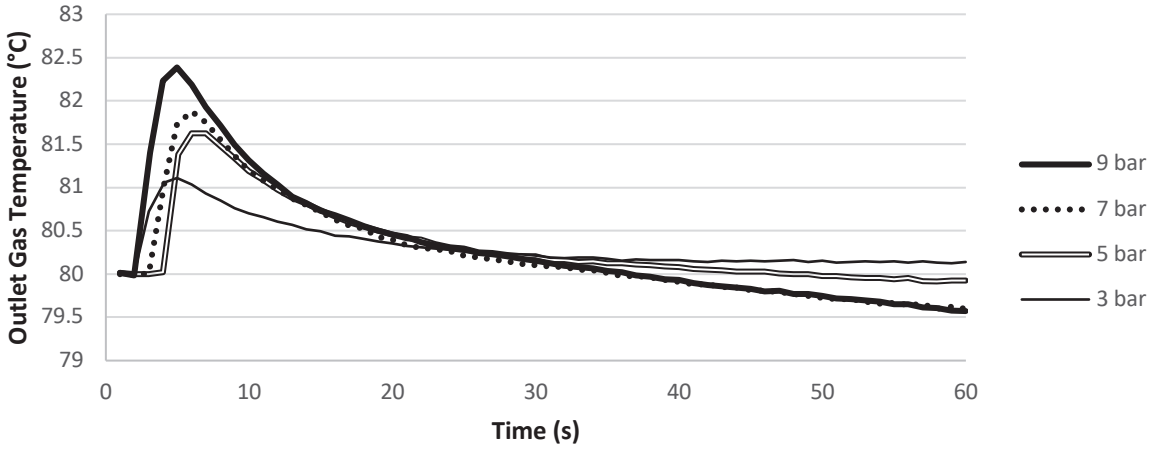

Figure 22: Effect of monomer pressure on outlet gas temperature profiles

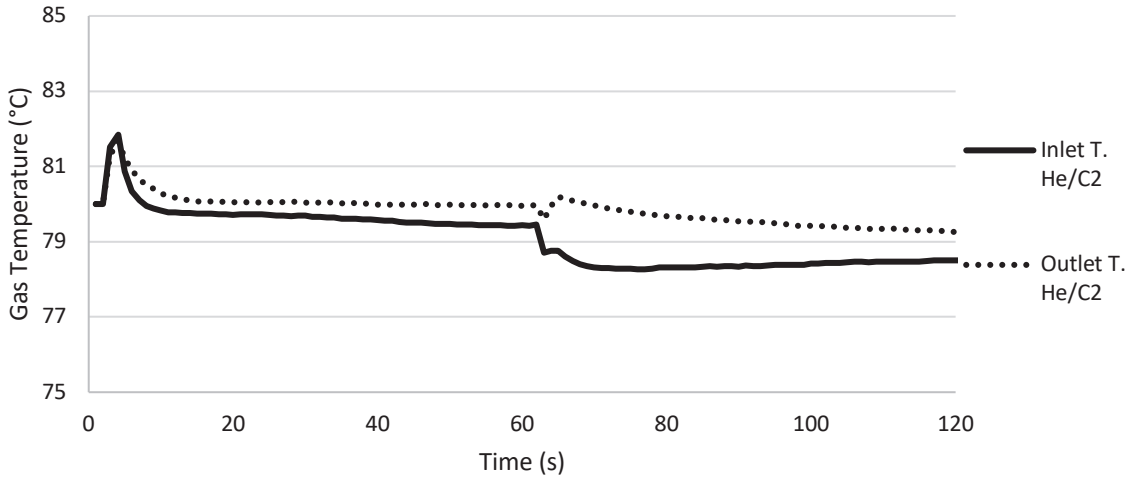

Figure 23: Effect of pressurizing the reactor before ethylene injection. 0-60 s: 7 bar of Helium, 60-120 s: 7 bar of ethylene.

4.5.1. *Conclusion*

Increased monomer pressure led to more pronounced heat loss, seen in the inlet gas temperature profiles. This effect was also observed in the previous set-up (SF 1) and was linked to inefficient gas heating of the set-up by the coils in the water bath.

Increased monomer pressure also led to more pronounced temperature peaks due to the heat released by the gas compression. Given the temperature gain was of the same order as the temperature increase observed in some of the polymerization reactions, the pressurization effect was not negligible. Pressurizing the reactor with an inert gas before the polymerization had a positive effect in the stability of the outlet temperature profiles, significantly reducing the temperature spikes due to gas pressurization.

4.6. Conclusions on assessment of reactor SF 2

We have proposed a new reactor geometry with aim to tackle some of the limitations detected with the existing set-up (SF 1), mainly the heat evacuation from the reactor. The reactor prototype, referred to as stopped-flow reactor 2 (SF 2) was built from available marketed parts and assessed in terms of heat evacuation, hardware inertness and thermal stability. The volume polymer volume capacity was doubled in the SF 2 reactor in relation to the previous SF 1 set-up, which is positive for the characterization analysis of the obtained polymer

From this series of experiments, we were able to conclude that several advances were gained with the new annular geometry of the new reactor prototype (SF 2) in relation to the previous set-up (SF 1).

From the heat evacuation assessment, several factors indicated that the evacuation from the reactor was improved in relation to the previous set-up (SF 1). Lower maximum outlet temperatures were observed for reaction conditions and polymerization yields comparable to those obtained with the previous set-up (SF 1). Likewise, estimated particle temperatures did not indicate temperature overshoots that reached polymer melting temperatures (> 120°C). Our main goal with the new prototype was to prevent the limitations observed in previous reactors (inaccurate temperatures measurements) and provide temperature reading that are as consistent as possible to the real temperatures inside the reaction bed. By using a layer of glass-wool (C_p=0.84 $J.g^{-1}K^{-1}$) instead of the metal frit (C_p =0.45 $J.g^{-1}K^{-1}$), we reduced the amount of heat that is absorbed from the reaction and thus improved the accuracy of the temperature measurements.

Moreover, similar polymerization yields were obtained when using coarse and fine salt as inert seedbed. Given the heat transfer studies carried out by Tioni et al.,[3,4] in which better heat evacuation was observed with finer particles in the previous set-up (SF 1), we interpreted the similar yields as an indication of improved heat removal with the new annular geometry.

With the assessment of hardware inertness, we gained some significant insight on the experimental protocol and purification measures to be taken to improve the reaction process. We concluded that using a Si-TEA cartridge for ethylene purification provided significant improvements in terms of reaction yield and polymer thermal properties. Finally, we observed that pressurizing the reactor with an inert gas prior do the monomer injection could significantly reduce the temperature increase due to gas compression at the initial moments of the reaction.

Nonetheless, despite the aforementioned improvements achieved with the reactor prototype, several limitations were still observed.

The set-up remained quite outdated and some of the issues observed with the first version (SF 1) were still encountered. We were often faced with reaction failure due to unknown factors, mostly contamination by air through leaks in the set-up, mostly due to many moving parts in the reactor conception. Besides, a limited possibility of reaction conditions was possible with this set-up, as it was not adapted for injecting liquids in the reaction zone. Therefore, performing co-polymerization reactions or studies in condensed mode operation were not straightforward with this set-up.

As in the previous set-up (SF 1), significant temperature drops were observed due to insufficient heating of the inlet gas. Finally, given its large dimensions, the reactor was not hermetically sealed when leaving the Glovebox, which meant a window was always open for oxygen contamination.

From the practical assessment of the Stopped-Flow reactor 2 (SF 2), we concluded the reactor has great potential for studying gas-phase short time reactions. Nevertheless, there was still room for improvement in the set-up in regards of its inertness, thermal stability, ease of handling, increasing the range of reaction conditions (e.g., performing co-polymerizations with liquid reagents), speeding up the assessment of reproducibility and reducing the risk of sample contamination.

5. Novel professionally engineered stopped-flow reactor (SF N)

From the assessment of the reactor prototype done in the previous sections, we concluded that the annular geometry provided significant improvements, mainly in terms of heat evacuation. Nevertheless, the main limitations of this set-up (insufficient heating of inlet gas, several moving parts leading to leaks and limited available reaction conditions) could not be solved with our available tools in the usual laboratory setting. As discussed in the introduction of this chapter, one of the objectives of the current project was the acquisition of an improved set-up, professionally tailored to our needs.

5.1. Introduction

At this point is has become clear that we have been able to identify the strengths and weaknesses of the "in-house" stopped-flow reactors. It is clear that this type of reactor is useful in understanding what happens during the initial moments of polymerization.

In the 15 years since Silva et al.[24] proposed the first gas phase stopped flow reactor, there have been feasible alternatives proposed in the open literature (whereas work has continued on slurry reactors which are easier to design). The strong points are that we are able to estimate particle temperatures during the nascent phase, able to recover the polymer particles to study their morphology and physical properties, and get, for the first time, a picture of how the first few seconds of a gas phase polymerization unfolds. However, we have also identified a number of short comings in the current chapter that need to be overcome if we are to develop a robust process tool. Perhaps the principal limitation to achieving this goal is the "do-it-yourself" nature of the experimental set-up. We have designed and tested different reactor concepts, and in this chapter have demonstrated that adapting the annular fixed bed approach allows us to overcome certain problems related to heat transfer and sample volumes. However is also clear that we need to move toward a professionally engineered reactor system to tackle the issues encountered with the Stopped-flow reactor 2 (SF 2), and to obtain a reactor set-up that would fulfill our end-goal: to perform gas-phase polymerizations at short reaction times with accurate control of reaction conditions, all while working in an inert environment. In addition, the ideal set-up should allow a wider range of experimental conditions, including the ability to inject different process gases, some of which are liquids at room temperature, in a user-friendly and efficient manner.

As the C2P2 has successfully worked with a firm called ILS (Integrated Lab Solutions), a specialized engineering firm based in Berlin, on previous projects, we decided to partner with them for the construction of the new improved set-up. Details on the novel reactor set-up, hereafter referred to as Novel stopped-flow reactor (SF N) are described in the following sections.

The engineering aspects of the novel reactor are discussed in the following paragraphs. A more detailed description of the steps followed from the purchase agreement to reactor delivery can be found in the Appendix 1 section.

5.2. Reactor description

The new reactors are based on the SF 2 prototype, but conceived to facilitate manipulation, to reduce the pressure drop during the reaction and allow sealing in the glovebox to minimize the risk of oxygen contamination. The dimensions of the new reactors were reduced to make it easier to manipulate them in the glove box, while keeping a similar reaction volume (6.5 cm^3) to the previous reactor prototype (SF 2) in order to ensure that sample volumes were sufficient to obtain enough polymer to do physical analyses, and to keep a 3 mm filling gap between the porous frit and outer cylinder so that generating the fixed bad was a feasible task. The reactor dimensions are as follows:

- Diameters of external cylinder: 16 mm
- Outer diameter of porous membrane: 10 mm
- Pore diameter of membrane: 5 µm
- Reactor length: 56 mm

In Figure 24, we find the concept and dimensions of the custom made reactors. The new reactors followed the same design of the previously tested prototypes (SF 2) (annular geometry and porous frits in the center) and the dimensions were reduced to facilitate handling and, most importantly, to allow sealing the reactor in the glove box. The reactor sealing in the novel set-up is ensured by the use of aluminum crimp caps with rubber septum.

Figure 25 shows a photo of the reactor parts (a), half assembled (b) and fully assembled (c).

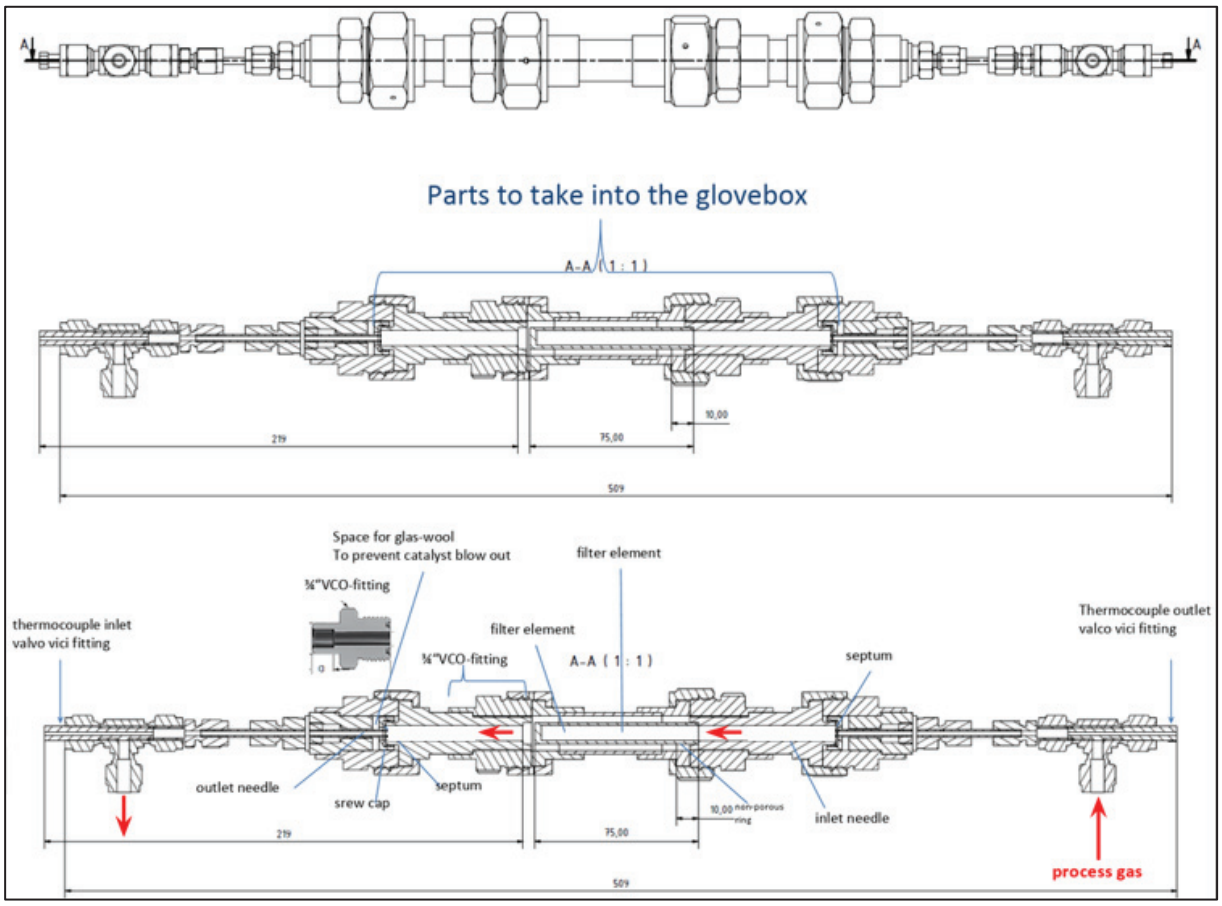

Figure 24: Reactor concept and dimensions (in mm).

Figure 25: Custom made reactor from the novel set-up, a) reactor parts b) half assembled reactor with crimp caps, c) fully assembled reactors

In Figure 26 we find the Piping and instrumentation diagram (P&ID) of the novel set-up. When zooming on different regions of the P&ID, in Figure 26, we find representations of the system feed, the reaction zone and the liquid injection system. In Figure 27 one can see a photograph of the finished system.

The improvements represented in this design include (numbers correspond to zones indicated in Figures 26 and 27):

1. Blue boxes: Multiple gas injection lines. The set-up allows feeding multiple gaseous components in the reactor, such as: Ethylene or Propylene (monomers), Hydrogen (chain transfer agent), Nitrogen (inert gas) and CO2 (quenching agent). There is no limit on which components can be used in this section as long as they are not liquids at room temperature. The system operates in pressures between 5 and 16 barg and allows gas velocities as high as 50 cm/s for reaction times as short as 3 seconds;

2. Red box: Liquid injection. One liquid component can be vaporized then injected into the reactors along with the gaseous components. The liquid vessel is previously filled in the glovebox with the desired liquid or mixture of liquids. The dosed liquids are evaporated in a three-valve evaporator (CEM) and the vapor is carried with the feed gases to the reaction zone;

3. Green Box: Oven with 3 reactors in parallel. The reaction zone consists of three custom-made reactors operated in parallel. The reactors are placed inside an electric heating chamber sealed to ensure good thermal control and equipped with gas detectors that abort the on-going reaction in case of gas leaks. A photograph of the oven with the 3 reactors in place can be seen in Figure 28.

In the novel set-up, Coriolis Mass-Flow Controllers from Bronkhorst were employed for monomer and liquid dosing instead of thermal mass flow controllers. This allows a better precision in the flow control and to use any liquid, gas or mixed components without the need of recalibration. Temperatures are recorded in intervals of 0.5 s by two 0.5 mm T-type thermocouples placed at the entry and exit of the reactors.

Mass Flow Meters from Bronkhorst control the gas flowrates with the following ranges:

- 43-2166 g/h for Ethylene or Propylene;
- 34-1700 NL/h for Nitrogen and CO2;
- 4.3-216.6 NL/h for Hydrogen;
- 18.6-930 g/h for the injection of liquids.

Moreover, all commands for the novel set-up are automated and controlled through a user-friendly interface. The novel set-up allows to automatically pressurize the reactors prior to the polymerization, in order to prevent a pressure drop when switching between gas feeds, as well as to avoid temperature spikes due to gas compression (as observed for set-ups SF 2 and SF 1).

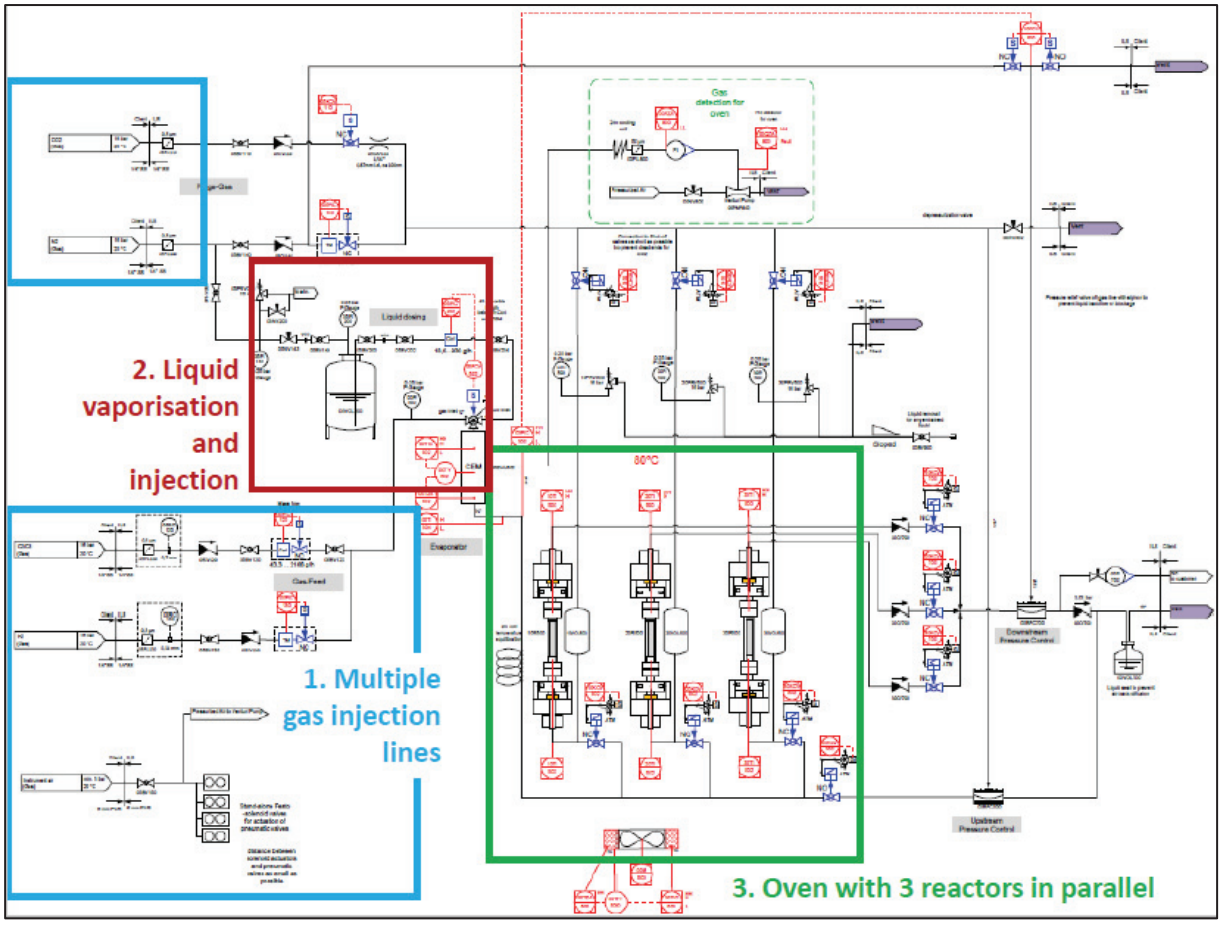

Figure 26: Piping and instrumentation diagram (P&ID) of the new 3 reactor design.

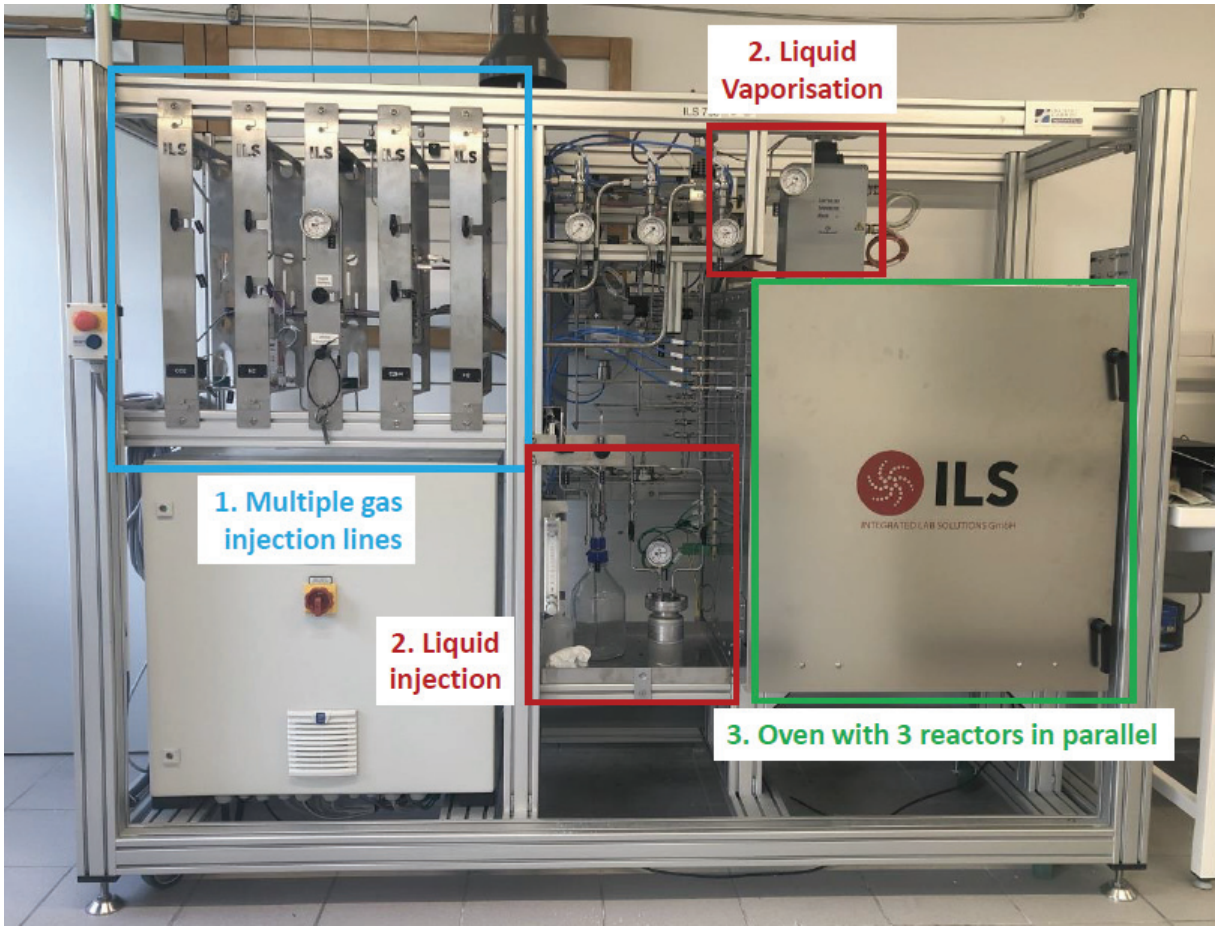

Figure 27: Novel stopped-flow reactor installed in our laboratory


Figure 28: Three reactors operated in parallel, plugged into the heating chamber

5.3. Experimental section

The novel stopped-flow reactor (SF N) was assessed in terms of its thermal response and hardware inertness.

The thermal response was evaluated in terms of sufficient heating of the monomer feed, as well maintenance of constant temperatures of the inlet gas throughout the reaction, an issue observed in both previously assessed stopped-flow reactors (SF 1 and SF 2).

5.3.1. *Materials*

A classic Zirconium metallocene catalyst, hereafter referred to as CpZ 2, was used for the assessment of the thermal stability in the novel reactor (SF N). The number in the catalyst name refers to the two different batches of the same catalyst that were used throughout this study. This catalyst was chosen for its sensitivity to impurities, as well as to compare the results obtained with the previous set-up (SF 2).

A commercial constrained geometry catalyst, hereafter referred to as GCG M was used for the assessment of the hardware inertness in the novel reactor set-up (SF N). This catalyst was chosen for its extremely high sensitivity to impurities (even higher than CpZ).

Balance from Mettler Toledo (model ME 2002) with 10 mg precision was used to follow the polymer production. Nitrogen gas with 99.999% purity purchased from Air Liquide France was used as inert gas in the short-time polymerization reactions for plugging in the reactors, purging the set-up and pressurizing the reactor before polymerization. The remainder of the materials are the same as those used in section 3.2.1. above.

5.3.2. *Polymerization procedure*

The reaction zone in the set-up contained three independent reactors operated in parallel inside the electric heating chamber, shown in Figure 28.

For each set of reactions, the reactors were previously cleaned with heptane and dried in an oven at 80 °C for at least 2 hours.

The catalysts are dispersed in an inert seedbed of fine NaCl (preparation described elsewhere) [4,15] in the annular space of the reactors, as was the case with the SF2 prototype. The catalyst amount was recorded and usually represented 2-5 wt% of the total weight of the bed.

The reactors were packed with the catalyst/inert mix inside a glove box under argon atmosphere. The lower and middle parts of the reactors were tightened and around 150 mg of glass wool (previously dried overnight in an oven at approximately 100 °C) was placed at the bottom of the reactor to facilitate product removal and reactor clean-up. The prepared mixture was then inserted in the annular gap and another layer of dry glass-wool (about 350 mg) was added to keep the mixture in place. The reactors were closed in the glovebox and sealed with rubber crimp caps (Fisher, 13 mm diameter, 2 mm thickness) to prevent air contamination.

The reactors were then plugged into the heating zone by piercing the crimp-caps under Nitrogen flow (200 NL/h, 1 bar) and we waited until thermal equilibrium was reached, which usually took about one hour. The gas flows, pressures and temperatures are collected automatically and recorded to the linked computer.

All steps of the polymerization process were automated. Prior to the polymerization (monomer injection), the reactors were pressurized with Nitrogen for 20 seconds. The polymerization took place as monomer was inserted at the set pressure and flowrates for the desired duration of the reaction. Following, the reaction was quenched by injection of a pulse of CO2 gas for 15 seconds. Finally, the reactors were purged with Nitrogen for another 15 s.

The polymer production was followed gravimetrically by weighing the reactors before and after the polymerization reaction in a balance from Mettler Toledo (model ME 2002) with 10 mg precision.

Experimental conditions for the catalyst used in this section

For the classic metallocene catalyst used in this section (CpZ 2), 30-50 mg catalyst were dispersed in fine NaCl seedbed. The reaction temperature was 84 °C and ethylene pressure kept constant at 7.5 barg with gas velocity of 50 cm/s.

For the commercial CGC catalyst used in this section (CGC M), 40-60 mg catalyst were dispersed in fine NaCl seedbed. The reaction temperature was 70 °C and ethylene pressure kept constant at 7.5 barg with gas velocity of 50 cm/s.

5.3.3. *Reactor conditioning*

The reactor conditioning was done by proper reactor sealing and by applying purification measures for the monomer gas, as concluded in the inertness assessment for the previous set up (SF 2).

The correct sealing of the reactors was assessed by shutting the reactors with the rubber septa (13 mm diameter, 2 mm rubber thickness) from Fisher Scientific. We pierced one of the sides and applied an Argon pressure (0.5 bar) while the other unpierced side was immersed in water. The fact no bubbling was observed from the sealed end indicates that the crimp caps seal the reactor satisfactorily.

In addition to passing the monomers over the purification columns used for all processes gases, a cartridge filled with 10 g of Alumina grafted with TEA was installed in the feed line as an additional purification measure for ethylene. Given the high gas flows (order of 1700 g/h) applied with the new set-up, we chose to graft TEA over Al_2O_3 pellets (0.1 mm diameter) instead of silica particles (40 µm diameter) in order to avoid the possibility that the finer silica particles could eventually blow into the reactor system. The procedure used for the grafting is described in the Appendix 1.

In order to determine when the Al-TEA cartridge was to be changed for a fresh batch, we carried out a reference test at the beginning of every week. From following the behavior of the chosen catalyst in the reference conditions, we then determined the purification cartridge was to be re-charged every 30 to 40 reaction runs.

5.4. Hardware thermal response assessment

The thermal response of the novel reactor assessed in polymerization reactions with a classic metallocene catalyst (CpZ 2).

The catalyst used in this section was first tested in full-time polymerization conditions as a reference for the catalyst behavior at longer reaction times. Tests were carried out with the turbosphere semi-batch reactor and reaction conditions are described in section 2.1.1. of this chapter. The activity polymerization profiles obtained for reactions of 60 minutes duration are seen in Figure 29.

Following, the thermal response of the novel reactor was evaluated with a classic metallocene catalyst (CpZ 2), also used in the assessment of the reactor prototype (SF 2).

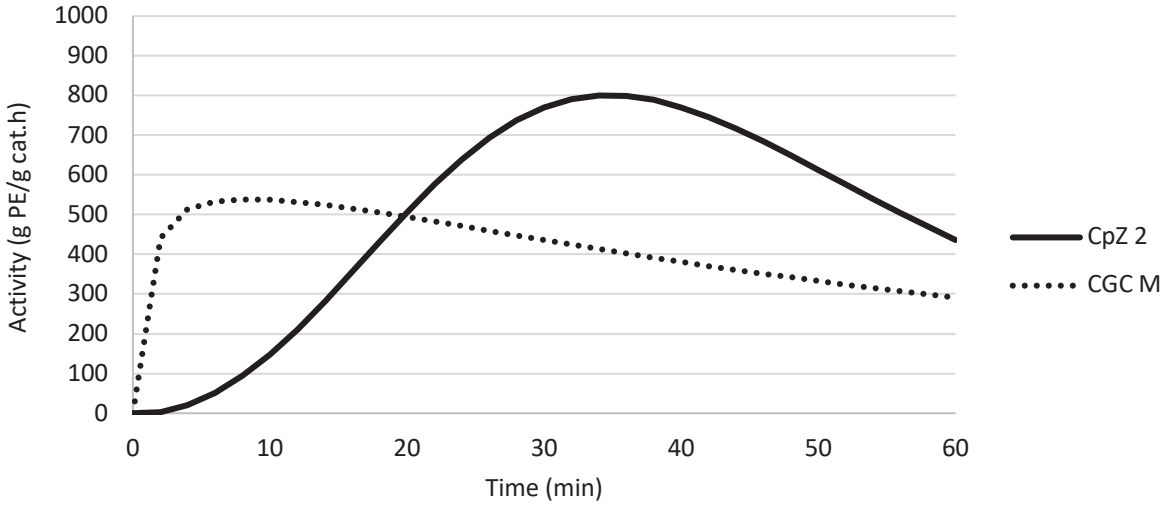

Figure 29: Full polymerization kinetics for 60 minute homopolymerization reaction with classic metallocene (CpZ 2) and CGC (CGC M) catalysts used in this section

5.4.1. *Improved control of reaction conditions*

The inlet and outlet temperature profiles obtained from a 60 second polymerization reaction with catalyst CpZ 2 are seen in Figure 30. The indicated numbers in the temperature profiles correspond to the different steps followed during the polymerization protocol, as follows:

Reaction conditions, polymerization yield polymer thermal properties are described in Table 5.

1. Reactor pressurization with Nitrogen (20s);
2. Polymerization reaction (60s);
3. Reaction degassing and quenching with CO2 (15s);
4. Purging of reactors with Nitrogen (15s).

The obtained polymerization yield and polymer properties are in agreement with those achieved with the previous set-up (SF 2) at comparable reaction conditions. From the temperature profiles in Figure 30, we observed that the inlet gas temperatures remained essentially constant throughout the reaction. The observed thermal stability was achieved by satisfactory heating of the reactors and feed gases in the sealed heating chamber. The gas flowrates and pressures recorded during the

polymerization are shown in Figure 31. We observed satisfactory stability for these parameters during the reaction.

Catalyst used	Reaction time (s)	Reaction T (°C)	Reaction P (bar)	C2 linear velocity (cm/s)	Yield (g/g)	Tm (°C)	Crystallinity (%)
CpZ 2	60	84	7.5	50	3.1	133,7	42,8

Tableau 5: Reaction conditions, yield and polymer properties for catalyst CpZ2 in homopolymerization conditions

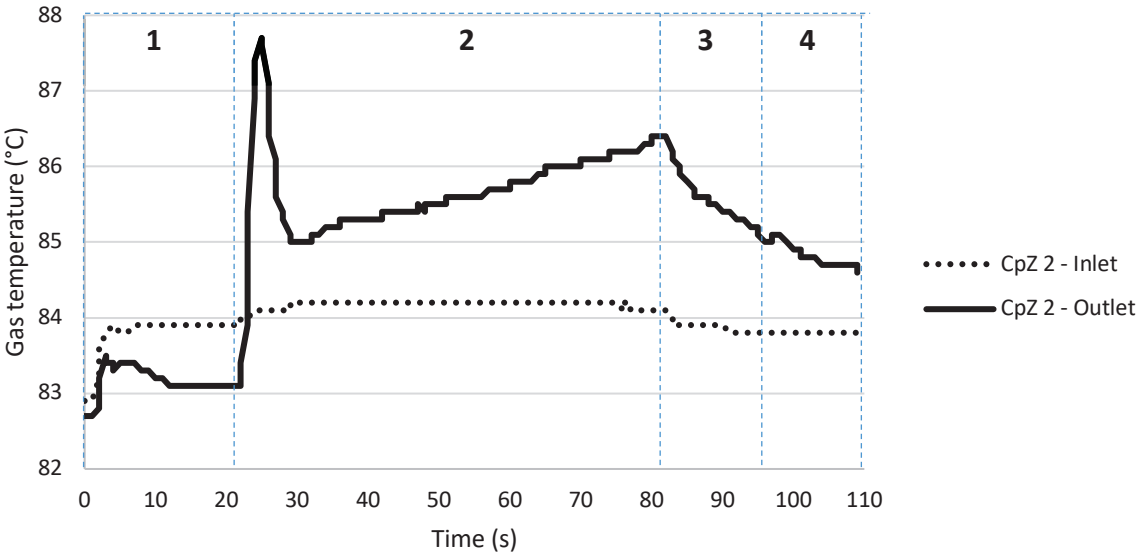

Figure 30: Inlet and outlet gas temperature profiles in all steps of the polymerization reaction: 1) reactor pressurization with N2 for 20s, 2) polymerization reaction for 60s, 3) reactor degassing and quenching with CO2 for 15s, 4) reactor purge with N2 for 15s

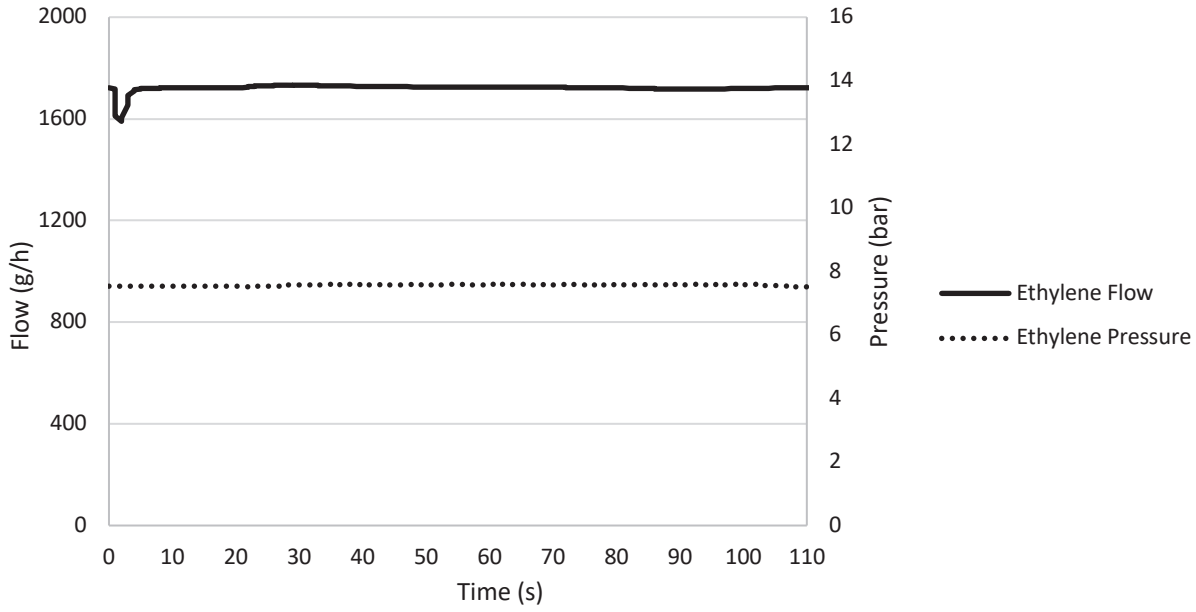

Figure 31: Ethylene gas flowrates and pressures in a 60 s experiment with the novel set-up

5.4.2. *Conclusion*

Several improvements related to the hardware operation and control of reaction conditions were observed with the novel set-up. The use of mass flow controllers for precise regulation of gas flowrates, coupled with the automatized control of the entire process let to extremely stable flowrates and reactor pressures throughout the polymerization reaction, as seen in Figure 31.

The issue of thermal response observed in the previous reactors (temperature drops for inlet gas during the reaction) was improved by use of a sealed electric heating chamber and reflected in the temperature inlet profile seen in Figure 30, with nearly constant inlet gas temperatures kept during the reaction.

Satisfactory polymerization yield was achieved for the classic metallocene catalyst CpZ 2. For tests performed with the novel reactor, we observed a temperature peak at the first seconds, which then decreased and continued to increase progressively (as the full-time polymerization kinetic curve would suggest). This behavior, only captured at very early stages, is perhaps due to an inhomogeneity in the size of the catalyst particles.

5.5. Hardware inertness assessment

The assessment of reactor inertness was done in homopolymerization conditions through catalyst tests performed with a commercial CGC metallocene catalyst (CGC M), known for its very high sensitivity to reaction impurities.

The catalyst was initially tested in full-time polymerization conditions as a reference for the catalyst behavior at longer reaction times. Kinetic profiles were obtained with the turbosphere semi-batch reactor, with reaction conditions described in section 2.1.1. of this chapter. The activity polymerization profiles obtained for the 60 minutes reaction with this catalyst is seen in Figure 29. Next, the CGC catalyst was tested with the novel stopped-flow reactor (SF N) and evaluated in terms of polymerization yields, experimental temperature profiles and thermal properties of the obtained polymer through DSC analysis in a 60 second reaction in homopolymerization conditions.

5.5.1. *Demonstration of hardware inertness with highly sensitive CGC catalyst*

The inlet and outlet temperature profiles obtained from a 60 second polymerization reaction with catalyst CGC M are seen in Figure 32. The indicated numbers in the temperature profiles correspond to the different steps followed during the polymerization protocol, as described in section 5.4.1.

Reaction conditions, polymerization yield polymer thermal properties are described in Table 6. The obtained polymerization yield is in agreement with those achieved in full-time polymerization conditions (higher than for the classic metallocene CpZ 2 assessed in the previous section). The thermal properties of the obtained polymer were considered satisfactory for a 60 second reaction.

From the temperature profiles in Figure 32, we observed that the inlet gas temperatures remained essentially constant throughout the reaction and the outlet temperatures gradually increase for the duration of the reaction, reflecting the catalyst kinetics. The interpretation of catalyst kinetics from the temperature profiles will be assessed in more depth in chapter 3, in which a software was developed for this purpose.

Catalyst used	Reaction time (s)	Reaction T (°C)	Reaction P (bar)	C2 linear velocity (cm/s)	Yield (g/g)	Tm (°C)	Crystallinity (%)
CpZ 2	60	70	7.5	50	5,0	133,5	37,3

Table 6: Reaction conditions, yield and polymer properties for catalyst CGC M in homopolymerization conditions

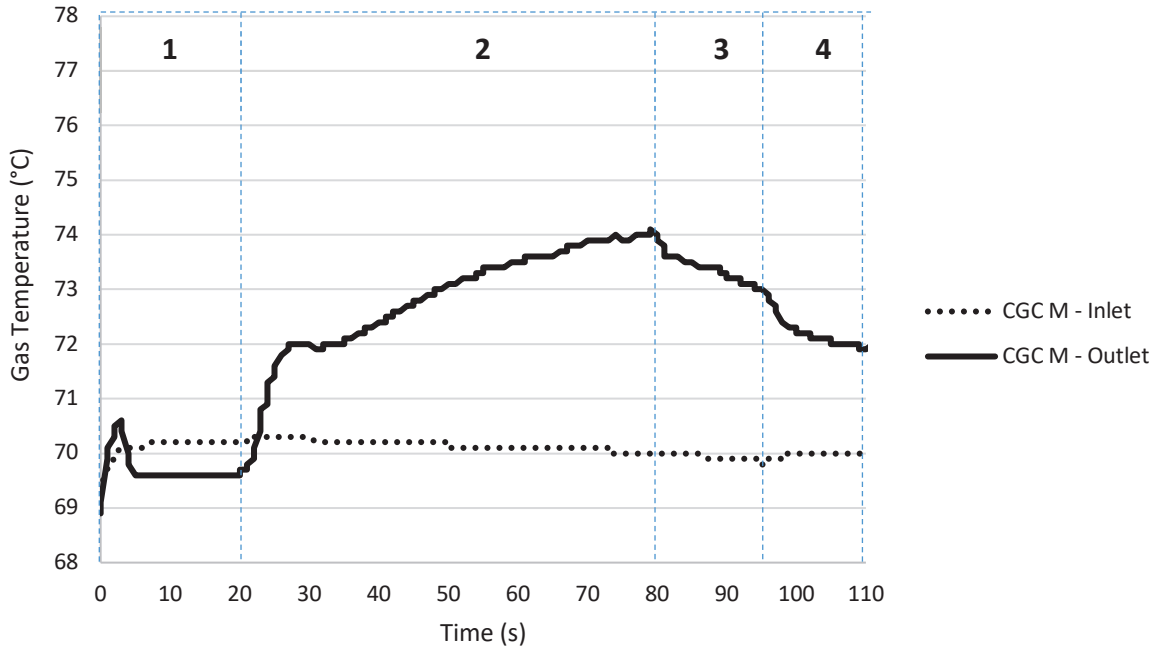

Figure 32: Inlet and outlet gas temperature profiles in all steps of the polymerization reaction: 1) reactor pressurization with N2 for 20s, 2) polymerization reaction for 60s, 3) reactor degassing and quenching with CO2 for 15s, 4) reactor purge with N2 for 15s

5.5.2. *Conclusion*

The inertness of the novel reactor was demonstrated through satisfactory polymerization yields obtained with the tested CGC metallocene catalyst. The obtained yield was coherent with the catalyst activity profiles at full-time polymerization conditions, which are higher than catalyst CpZ 2 in the initial moments of the reaction.

The novel set-up was engineered to target several issues related to hardware inertness observed in the previous set-ups (SF 1 and SF 2), mainly the fact that the previous reactors had several moving parts that increased the possibility of leaks. Moreover, the dimensions of the previous reactors did not allow for complete sealing inside the glove box, increasing the chance of catalyst contamination by oxygen.

In the novel set-up, the inertness was improved mainly through the custom-made reactors with adapted dimensions (that allow sealing inside the glovebox), and the use of crimp caps.

The acceptable yields and polymer properties obtained with the tested CGC catalyst (highly sensitive to impurities) demonstrated that we have achieved satisfactory inertness with the novel stopped-flow reactor (SF N).

5.6. Conclusions on assessment of reactor SF N

A novel stopped-flow reactor set-up incorporated the improvements demonstrated with SF 2, but was professionally engineered to tackle certain operation limitations faced with the previous versions of the SF reactors at the C2P2. The issues observed with the reactor prototype were mainly of structural character, including: challenges in inertness due to the reactor dimensions and presence of several moving parts, thermal instability due to insufficient gas heating, difficulty in handling inside the glovebox, as well as reaction conditions essentially limited to homopolymerization conditions.

All of these challenges were tackled during the development of the novel stopped-flow reactor set-up, which was professionally tailored to our needs resulting in a number of improvements with the new set-up.

Stable gas flowrates and pressures were achieved through the use of automated switch valves and mass flow controllers coupled with a full automatization of the polymerization process, controlled by a straight-forward user-friendly interface. Stable thermal conditions and efficient heating of the monomer feed were achieved by use of a sealed electric heating chamber. The thermal stability was observed in polymerization tests carried out with a classic metallocene catalyst, in which the inlet gas temperatures remain essentially constant throughout the reaction.

The reactor inertness was improved in relation to the previous reactors mainly through custom-made reactors with optimized dimensions that allowed sealing inside the glovebox, as well as easier handling during experimental preparations. Moreover, the reactor sealing with crimp caps prevented contamination during reactor plug-in. The improvements in inertness were demonstrated with satisfactory polymerization yields obtained with CGC metallocene, a catalyst highly sensitive to reaction impurities.

Finally, the novel set-up allowed a much wider choice of reaction conditions and range of operations, in particular with the ability to feed multiple gases independently, and to use liquid feeds. This was achieved due to the addition of an CEM evaporator, thus permitting the injection of vaporized liquids (such as liquid comonomers or inert alkanes) in the reaction zone and mass flow controllers allowing for gas linear velocities as high as 50 cm/s.

6. Chapter conclusions

This chapter describes the conclusion an essential milestone of the current project. We have successfully acquired, tested and validated a novel stopped-flow reactor set-up that fulfills our requirements for studying polymerization reactions at early stages under meaningful conditions representative of industrial scales.

We assessed the existing set-up, originally conceived by Olalla et al.[11] in 2008 (SF 1), and concluded this set-up presented limitations mainly related to poor heat evacuation from the reactor. Moreover, this reactor set-up was outdated, had a small polymer production capacity and the lack of experimental inertness led to frequent contamination by oxygen or impurities.

With an eye to improving aspects related to heat evacuation while simultaneously increasing the polymer production capacity, we proposed a new annular geometry to promote a more homogenous gas flow through the entire reaction bed. The reactor prototype, named stopped-flow reactor 2 (SF 2), was fabricated and tested in our lab facilities. With this set-up, we demonstrated that the annular geometry had a positive impact on the heat evacuation with much lower temperature gradients obtained in relation to the previous reactor as well as similar polymerization yields achieved with fine and coarse NaCl seedbeds. The reactor prototype provided insights on purification measures to be taken in order to optimize the experimental protocol, resulting in the addition of an alkylated support for purification of the monomer feed. Moreover, we concluded that pressurizing the reactor prior to the polymerization successfully avoided thermal instability caused by gas pressurization.

Nonetheless, the reactor prototype remained an outdated system and some limitations persisted. The inertness of this reactor was not optimal. The reactor was not easy to handle and, given its large dimensions, it was not sealed inside the glovebox, leaving room for catalyst contamination by oxygen. Finally, the heating coil in the water bath was not effective in sufficiently heating the monomer gas, resulting in significant temperature drops were observed during the experiments.

With the results of this analysis in hand, we contacted a partner that we have previously worked with in the laboratory on a different project to help us create a professionally engineered stopped-flow reactor that allowed us to use the concept of the improved reactor prototype (SF 2), and to overcome many of the physical limitations of our previous systems. The new reactor set-up, named novel stopped-flow reactor (SF N), was custom made by a specialized engineering firm (ILS, Berlin) to perform short polymerization experiments with precise control of the reaction conditions, all while ensuring an environment inert from oxygen, water and other impurities.

The issue of thermal response observed in the previous reactors (insufficient heating of the monomer through a coil in a water bath) was improved by use of a sealed electric heating chamber, which resulted in nearly constant inlet gas temperatures during the reaction. Besides, the use of automated switch valves and mass flow controllers coupled with a full automatization of the polymerization process allowed stable gas flowrates and pressures throughout the polymerization reaction.

At last, the inertness of the novel reactor was demonstrated through satisfactory polymerization yields obtained in homopolymerization conditions with a CGC metallocene catalyst known to be extremely sensitive to impurities in the reaction zone (such as oxygen and water). By reducing the number of moving parts and applying crimp caps to seal the reactors inside the glovebox, the risk of reaction

failure due to catalyst contamination was drastically reduced in relation to the previous reactors (SF 1 and SF 2).

The novel set-up allowed a much wider choice of reaction conditions, mainly due to the possibility of injecting vaporized liquids (such as liquid comonomers or inert alkanes) in the reaction zone, achieved by the addition of a CEM evaporator to the set-up. Moreover, the set-up allows a larger range of reaction operations (gas linear velocities as high as 50 cm/s) that are fully automated and controlled by a straight-forward user-friendly interface.

The novel stopped-flow reactor allows to perform gas-phase polymerization reactions as short as 3 seconds. The minimum reaction times achieved with this set-up are longer than those obtained with the reactor built by Olalla et al.[11] (SF 1), which were as low as 100 ms. Nevertheless, the time adjustment was a necessary trade-off in order to work under reaction conditions that allow to expose the catalyst and growing polymer particles to heat and mass transfers that are representative of those reached in industrial reactors.

In this chapter, we have completed the development of the hardware component of the novel stopped-flow reactor. As presented in the introduction of this chapter, the new set-up includes both a hardware and software component, which are to be used together in order to best extract and interpret the experimental data. The development of the software component, which consists of a mathematical model and state observer describing the reactor, will be subject of chapter 3.

7. References

(1) McKenna, T. F. L.; Tioni, E.; Ranieri, M. M.; Alizadeh, A.; Boisson, C.; Monteil, V. Catalytic Olefin Polymerisation at Short Times: Studies Using Specially Adapted Reactors. *Can. J. Chem. Eng.* **2013**, *91* (4), 669–686. https://doi.org/10.1002/cjce.21684.

(2) Soares, J. B. P.; McKenna, T. F. L. Polymerization Catalysis and Mechanism. In *Polyolefin Reaction Engineering*; John Wiley & Sons, Ltd, 2012; pp 53–86. https://doi.org/10.1002/9783527646944.ch3.

(3) Tioni, E.; Broyer, J. P.; Spitz, R.; Monteil, V.; McKenna, T. F. L. Heat Transfer in Gas Phase Olefin Polymerisation. *Macromol. Symp.* **2009**, *285* (1), 58–63. https://doi.org/10.1002/masy.200951108.

(4) Tioni, E.; Spitz, R.; Broyer, J. P.; Monteil, V.; McKenna, T. Packed-Bed Reactor for Short Time Gas Phase Olefin Polymerization: Heat Transfer Study and Reactor Optimization. *AIChE J.* **2012**, *58* (1), 256–267. https://doi.org/10.1002/aic.12576.

(5) Tioni, E.; Monteil, V.; McKenna, T. Morphological Interpretation of the Evolution of the Thermal Properties of Polyethylene during the Fragmentation of Silica Supported Metallocene Catalysts. *Macromolecules* **2013**, *46* (2), 335–343. https://doi.org/10.1021/ma302150v.

(6) Cancelas, A. J.; Monteil, V.; McKenna, T. F. L. Influence of Activation Conditions on the Gas Phase Polymerisation of Propylene. *Macromol. Symp.* **2016**, *360* (1), 133–141. https://doi.org/10.1002/masy.201500099.

(7) Bashir, M. A. Impact of Physical Properties of Silica on the Reaction Kinetics of Silica Supported Metallocenes and Polyethylene Morphology. phdthesis, Université de Lyon, 2016.

(8) Andrade, F. N.; McKenna, T. F. L. Condensed Mode Cooling for Ethylene Polymerization: Part IV. The Effect of Temperature in the Presence of Induced Condensing Agents. *Macromol. Chem. Phys.* **2017**, *218* (20), 1700248. https://doi.org/10.1002/macp.201700248.

(9) Andrade, F. N. de. Effect of Condensable Materials during the Gas Phase Polymerization of Ethylene on Supported Catalysts. phdthesis, Université de Lyon, 2019.

(10) Soave-Redlich-Kwong EOS (1972) | PNG 520: Phase Behavior of Natural Gas and Condensate Fluids https://www.e-education.psu.edu/png520/m10_p5.html (accessed May 16, 2018).

(11) Olalla, B.; Broyer, J.-P.; McKenna, T. F. L. Heat Transfer and Nascent Polymerisation of Olefins on Supported Catalysts. *Macromol. Symp.* **2008**, *271* (1), 1–7. https://doi.org/10.1002/masy.200851101.

(12) Phd thesis Tioni final - document https://tel.archives-ouvertes.fr/tel-01416887/document (accessed Jan 16, 2017).

(13) Browning, B.; Pitault, I.; Sheibat-Othman, N.; Tioni, E.; Monteil, V.; McKenna, T. F. L. Dynamic Modelling of a Stopped Flow Fixed Bed Reactor for Gas Phase Olefin Polymerisation. *Chem. Eng. J.* **2012**, *207–208*, 635–644. https://doi.org/10.1016/j.cej.2012.07.027.

(14) Browning, B.; Sheibat-Othman, N.; Pitault, I.; McKenna, T. F. L. A 2-D Observer to Estimate the Reaction Rate in a Stopped Flow Fixed Bed Reactor for Gas Phase Olefin Polymerization. *AIChE J.* **2014**, *60* (10), 3511–3523. https://doi.org/10.1002/aic.14538.

(15) Gaillard, C.; Despois, J. F.; Mortensen, A. Processing of NaCl Powders of Controlled Size and Shape for the Microstructural Tailoring of Aluminium Foams. *Mater. Sci. Eng. A* **2004**, *374* (1), 250–262. https://doi.org/10.1016/j.msea.2004.03.015.

(16) J. Cancelas, A.; Monteil, V.; L. McKenna, T. F. Impact of Catalyst Injection Conditions on the Gas Phase Polymerization of Propylene. *React. Chem. Eng.* **2017**, *2* (1), 75–87. https://doi.org/10.1039/C6RE00224B.

(17) Browning, B. Dynamic modelling of a fixed bed reactor - PhD Thesis https://tel.archives-ouvertes.fr/tel-01175971/document (accessed Dec 1, 2016).

(18) Al-Juaied, M. A.; Lafarga, D.; Varma, A. Ethylene Epoxidation in a Catalytic Packed-Bed Membrane Reactor: Experiments and Model. *Chem. Eng. Sci.* **2001**, *56* (2), 395–402. https://doi.org/10.1016/S0009-2509(00)00235-9.

(19) McCarty, J. G. Kinetics of PdO Combustion Catalysis. *Catal. Today* **1995**, *26* (3), 283–293. https://doi.org/10.1016/0920-5861(95)00150-7.
(20) Beretta, A.; Baiardi, P.; Prina, D.; Forzatti, P. Analysis of a Catalytic Annular Reactor for Very Short Contact Times. *Chem. Eng. Sci.* **1999**, *54* (6), 765–773. https://doi.org/10.1016/S0009-2509(98)00261-9.
(21) Groppi, G.; Ibashi, W.; Tronconi, E.; Forzatti, P. Structured Reactors for Kinetic Measurements in Catalytic Combustion. *Chem. Eng. J.* **2001**, *82* (1), 57–71. https://doi.org/10.1016/S1385-8947(00)00342-9.
(22) Groppi, G.; Ibashi, W.; Valentini, M.; Forzatti, P. High-Temperature Combustion of CH4 over PdO/Al2O3: Kinetic Measurements in a Structured Annular Reactor. *Chem. Eng. Sci.* **2001**, *56* (3), 831–839. https://doi.org/10.1016/S0009-2509(00)00295-5.
(23) Martino, A. D.; Weickert, G.; McKenna, T. F. L. Contributions to the Experimental Investigation of the Nascent Polymerisation of Ethylene on Supported Catalysts, 1. *Macromol. React. Eng.* **2007**, *1* (1), 165–184. https://doi.org/10.1002/mren.200600013.
(24) Silva, F. M.; Broyer, J. P.; Novat, C.; Lima, E. L.; Pinto, J. C.; McKenna, T. F. Investigation of Catalyst Fragmentation in Gas-Phase Olefin Polymerisation: A Novel Short Stop Reactor. *Macromol. Rapid Commun.* **2005**, *26* (23), 1846–1853. https://doi.org/10.1002/marc.200500576.
(25) Tioni, E.; Spitz, R.; Broyer, J. P.; Monteil, V.; McKenna, T. Packed-Bed Reactor for Short Time Gas Phase Olefin Polymerization: Heat Transfer Study and Reactor Optimization. *AIChE J.* **2012**, *58* (1), 256–267. https://doi.org/10.1002/aic.12576.

Chapter 3

Development of software component for novel stopped-flow reactor

Chapter 3: Content

1. Introduction: why implement a software component? 107

2. Set-up description 108
   2.1. Materials and operating procedure 108
   2.2. Interpreting experimental results 109
   2.3. Conclusion 110

3. Development of reactor model 111
   3.1. Reaction rate and simplifying assumptions at the particle level 112
      3.1.1. Monomer concentration in the particles 112
   3.2. Energy Balances 113
      3.2.1. Three phases in reaction zone 115
      3.2.2. Two phases in reaction zone 116
   3.3. Heat transfer correlations 117
      3.3.1. Heat transfer coefficient between gas and particle 117
      3.3.2. Heat transfer coefficient at the reactor wall 118
   3.4. Conclusion 119

4. Validating the reactor model 120
   4.1. Model programming 120
   4.2. Simulation results 120
      4.2.1. Three phases in reaction zone 120
      4.2.2. Two phases in reaction zone 121
      4.2.3. Conclusion 122
   4.3. Sensitivity analysis 123
      4.3.1. Superficial temperature of reactor wall (T_{wall}) 123
      4.3.2. Catalyst particle heat transfer coefficient (h_{cat}) 124
      4.3.3. Diameter of catalyst particles 124
      4.3.4. Conclusion 125
   4.4. Conclusions on model validation 126

5. Development of a High-Gain Observer 126
   5.1. Introduction 127
   5.2. The novel reactor as a Calorimeter 128
   5.3. Implementing a High-Gain Observer 128
      5.3.1. Heat balance and reaction rate 129
   5.4. Validating the High-Gain Observer 129
   5.5. Sensitivity analysis 130
      5.5.1. Effect of tuning parameter 131
   5.6. Conclusion 132

6. Chapter conclusions 133

7. Nomenclature 134

8. References 137

1. Introduction: why implement a software component?

The reactor presented in Chapter 2 was conceived to promote efficient heat removal from the particle, aiming to avoid thermal runway, polymer melting and particle agglomeration. In the previous chapter, we described the development of the hardware component: the novel stopped-flow reactor set-up, custom-made to study polymerization reactions at early stages under meaningful conditions. The final tool consists of both a hardware and a software component, to be used together in order to optimize the data extraction and interpretation of the experimental results.

The main purpose of the software component, at this point, is to use the recorded experimental data to predict polymerization rates and kinetic parameters, allowing to interpret the kinetic behavior of the catalyst under study.

Moreover, the estimation of polymerization rates is particularly useful for the current stopped-flow set-up given that the experiments provide *one-point* information on the polymer formation, with polymerization yields followed gravimetrically. Even if the recorded temperature profiles reflect the catalyst kinetics, they provide no insight on the evolution of the polymerization rates during the reaction.

The approach developed in the current work builds on previous studies carried out to describe the earlier version of the stopped-flow reactor [1,2] (referred to as SF 1 in this work). The modeling works of Browning et al. [3,4] resulted in a 2-D dynamic model of the tubular gas-phase stopped-flow reactor (SF 1). The model allowed the authors to predict the temperature runways observed experimentally and showed the presence of non-negligible temperature gradients inside the reactor, despite its small volume. The model was used to implement a 2-D observer to estimate the reaction rate from the experimental data, [5] but due to certain uncertainties in measuring the outlet temperatures accurately, the input data for the observer were the calculated temperatures from the model, not the experimental data. The end result was that the output from the observer was not a reliable picture of the rate of polymerization.

In the current project, the set-up to be modelled was optimized to prevent the limitations observed in previous reactors and provide temperature readings that are as consistent as possible to the real temperatures inside the reactor. As described in chapter 2, an annular geometry was implemented to allow more uniform flow distribution, reduce the possibility of temperature gradients inside the reactor and improve the evacuation of the heat of reaction.

In this chapter, the development of the software component has been described. This software consisted of the heat and mass balances that constitute the model for the reactor set-up, together with a High-Gain Observer, implemented to access the reaction rates from the experimental data.

2. Set-up description

The system to be modeled consisted of a laboratory scale reactor, named novel stopped-flow reactor (SF N), especially developed for short-time polymerization reactions in gas-phase reactions. A more detailed description of this set-up, including the P&ID and ranges of operation, can be found in chapter 2. The set-up allowed three stopped-flow reactors to be operated in parallel. The reactors fit into an electric heating chamber that sets the reaction temperature.

The diagram of the annular reactor with its dimensions can be seen in Figure 1.

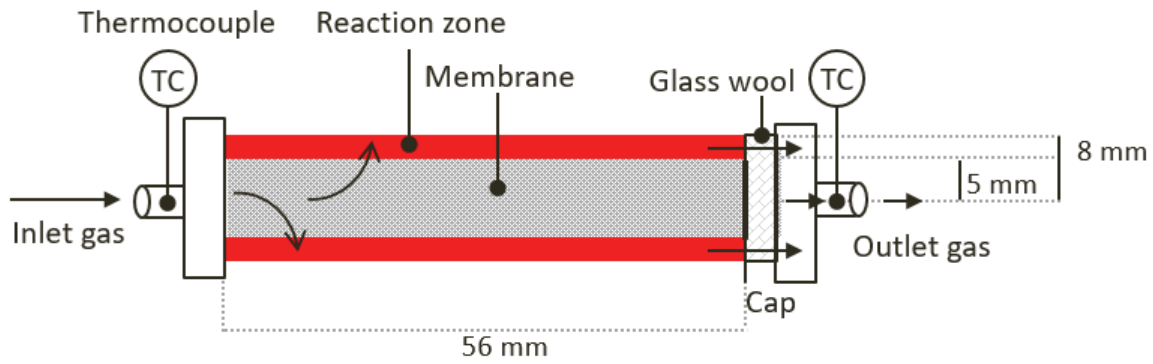

Figure 1: Diagram of annular reactor described in this work

2.1. Materials and operating procedure

As described in chapter 2, the system allows a wide range of operation conditions, such as injection of hydrogen and liquids in the feed stream. Nonetheless, in the model development phase, the reaction gas consists purely of ethylene in order to simplify the presentation and the kinetic model. Adapting the model for multiple gases should be straightforward.

A commercial constrained geometry catalyst (average particle diameter of 40 µm), hereafter referred to as CGC M, was used to validate the current reactor model and High-Gain Observer. Validations were done with a 60 seconds experiment carried out in homopolymerization conditions with Ethylene.

The reaction medium is composed of a solid mixture of catalyst and fine salt as inert seedbed (5 µm crystals agglomerated into particles of average diameter of 50 µm (prepared as described elsewhere)[2,6] to disperse the catalyst and increase the heat capacity of the bed. The catalyst represented 2-5 wt% of the total weight of the bed. The solid mixture is kept in place by a layer of dry glass wool (approximately 500 mg, on average). The reactors are packed inside a glove box under Argon atmosphere and contamination is prevented by use of rubber crimp caps.

The reactors are then plugged into the heating chamber under Nitrogen flow and the polymerization is launched once thermal equilibrium has been reached. Inert gas (Nitrogen in our case) is injected to pressurize the reactors before the polymerization, thus preventing compression heat effects when ethylene is injected as well as pressure drop when switching between gas feeds. Nitrogen gas with 99.999% purity from Air Liquide – France was used for plugging in the reactors and purging the system after the reaction was completed.

Ethylene with 99.95% purity from Air Liquide – France was used as monomer gas throughout this study. The gas was purified by flowing through tree purification columns. The first was filled with reduced BASF R3-16 catalyst (CuO supported on alumina), the second with molecular sieves (13X, 3A, Sigma-Aldrich), and finally a column of Selexsorb COS (Alcoa).

Carbon dioxide with 99.995% purity from Air Liquide – France was used to quench the catalyst activity, thus ending the polymerization reaction.

The polymerization yields were followed gravimetrically by weighing the reactors before and after the reaction in a balance from Mettler Toledo (model ME 2002), with 10 mg precision. We assumed the precision in yield measurement to be that of the balance (10 m).

2.2. Interpreting experimental results

For each experiment, the following data were recorded: the catalyst and inert masses, mass of glass wool, final polymer yields and the oven temperature. Other data is recorded every 0.5s for each experiment: reaction time, inlet gas mass flow rates and pressures, inlet and outlet gas temperatures.

The recorded temperature profiles for a typical experiment of 60 second duration is shown in Figure 2, in which all steps followed during the experimental protocol have been portrayed:

5. Reactor pressurization with Nitrogen (0 to 20s);
6. Polymerization reaction (60s);
7. Reaction degassing and quenching with CO2 (15s);
8. Purging of reactors with Nitrogen (15s).

We observed a peak in the measured outlet temperature at the start of each experiment, which was linked to the heat of compression as the reactor is suddenly pressurized with Nitrogen from the initial atmospheric pressure. As discussed in chapter 2, pressurizing the reactor prior to the polymerization prevented the heat of pressurization to be added to the heat of reaction, as well as avoiding pressure drops in the reactor when switching between gases.

We observed that, in all experiments, the inlet temperatures were approximately 2 °C higher than the outlet temperatures at the beginning of the experiment. This is counterintuitive, since both temperatures should be equal before the experiment starts. We attributed this effect to an artefact of the system. Given the mass of the reactor (weighing over 1.5 kg), it has a high thermal inertia and long times were needed to reach perfect thermal equilibrium (well over 2 hours). We therefore determined to launch the reactions once the inlet temperatures were stable to the set values. The catalysts used in this study were suited for working under slight temperature variations around the set-value, which is reached in about 1 hour. As discussed below, this variation was accounted for in the description of the heat balances by a correction term that added the difference between the two probes to the inlet temperature.

This 60 second experiment (Figure 2) was carried out with catalyst CGC M and will be used as reference for validating the current model. The applied experimental conditions were: 38 mg catalyst in 1.2 g fine NaCl seedbed, 500 mg glass wool, reaction temperature set to 70 °C, ethylene pressure of 7.5 barg with gas velocity of 50 cm/s.

As described a few paragraphs back, step 2 (depicted in Figure 2) is when ethylene is injected in the reactor and when the polymerization reaction takes place. As this is the only step of the experimental protocol in which heat is generated in the reactor, it is thus of interest to be modelled as it is the only phase that allows to predict the reaction rate. Note that part of the generated heat is evacuated in steps 3 and 4, but this amount is negligible due to the high ethylene flowrates applied (around 1700 g/h) in step 2.

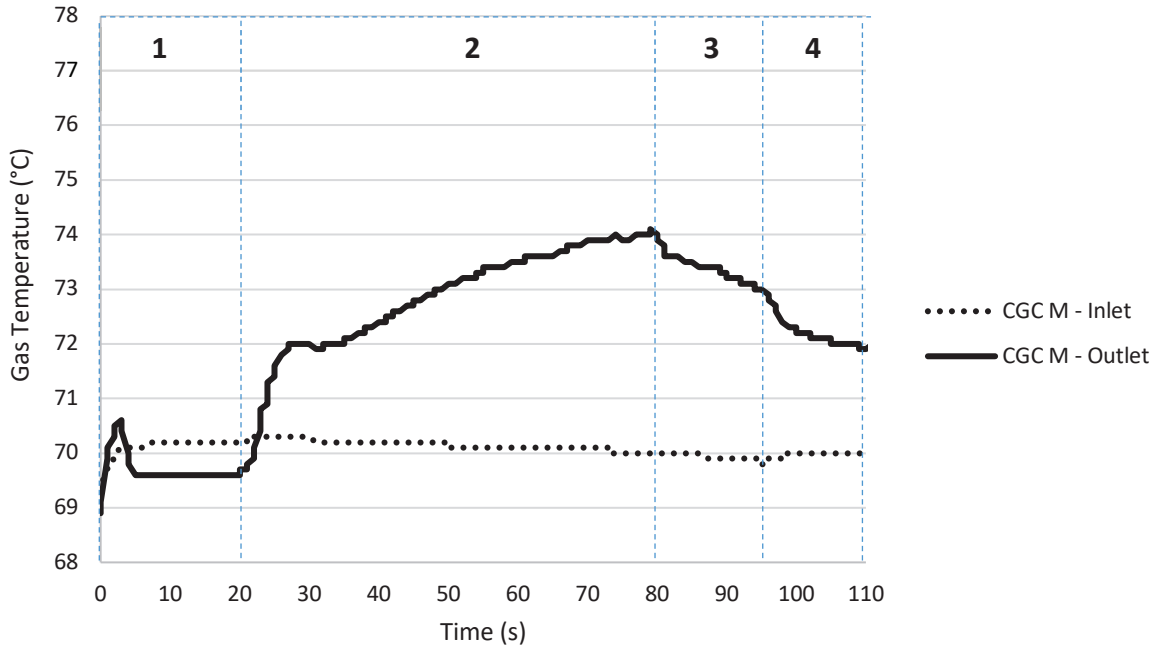

Figure 2: Inlet and outlet temperatures from a typical experiment with the novel stopped-flow reactor with catalyst CGC M

2.3. Conclusion

The stopped-flow reactor to be modelled (SF N) was presented. More details on the set-up construction and range of operations are found in chapter 2.

Known experimental data with the current set-up include the reaction duration, catalyst and inert masses, mass of glass wool, polymer yields (with 10 mg precision), inlet gas pressures and mass flowrates, inlet and outlet gas temperatures. The temperature of the heating chamber is known and considered constant throughout the reaction.

The observed experimental outlet temperatures, together with the high flowrates applied, suggest that the heat generated during the polymerization reaction is evacuated from the reactor mainly during the reaction step, which will be the step described in the current model and portrayed hereafter.

The following assumptions are made at this point: constant temperature of the heating chamber, as well as thermal equilibrium of the inlet gas phase. Unknown data include the temperature of the reactor stainless steel walls, which is to be included in the reactor model.

3. Development of reactor model

The principal objective of the model is to use it to link the changes in the inlet and outlet gas temperature to the rate of polymerization in the bed.

In order to write the detailed mass and energy balances on which this model will be based, we need to evaluate the transport processes taking place at different levels in the reactor.

A schematic view of the different components of a full reactor model is given in Figure 3. A full model would include a set of mass and energy balances around the reactor, any eventual radial and axial temperature and concentration gradients in the reactive particle bed (salt, catalyst, polymer), and ultimately any temperature and/or concentration gradients in the polymerizing particles themselves. This is a complex problem, and for reasons discussed in Chapter 1, it is not at all clear that an exact model of transport phenomena in the growing particles is a feasible (or even useful) thing to do in this context.

We will discuss the model construction and simplifying assumptions made in the rest of this section, before moving on to the validation in section 4.

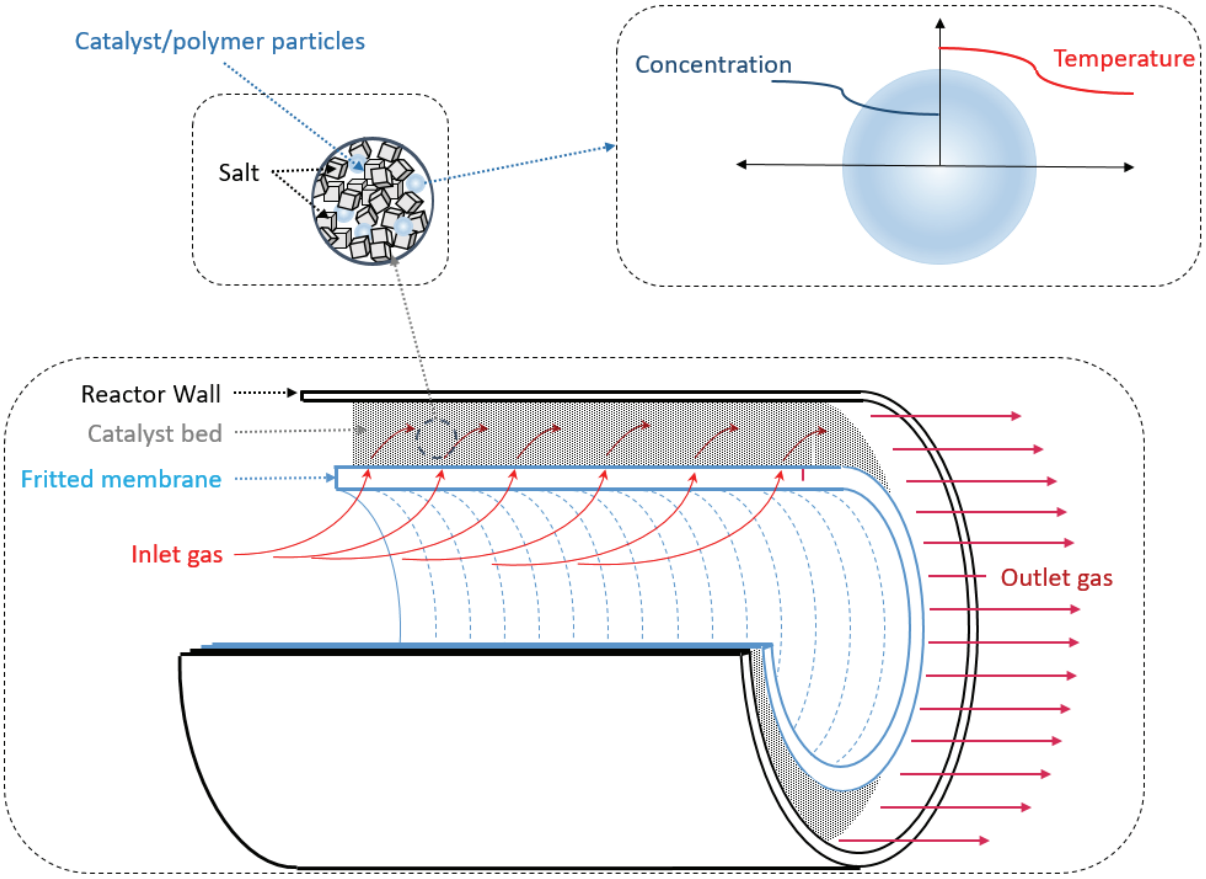

Figure 3: Levels of complexity to consider for the reactor model.

3.1. Reaction rate and simplifying assumptions at the particle level

In its simplest form, the rate of polymerization (R_{p}) can be represented by the propagation step for a first order reaction, [7] as follows:

$$R_p = k_{p0}\, C^* C_{C2,amorph} = k_{p0}\, e^{-\frac{Ea}{RT}} C^* C_{\mathrm{C2,amorph}} \tag{3-1}$$

Where k_{p0} is the pre-exponential propagation rate constant ($m^3.mol^{-1}.s^{-1}$) and C^* is the concentration of active sites of catalyst per unit volume of particle. Ultimately, C^* could include the total metal content of the catalyst (C_{Metal}) and the *active* fraction of active sites (ϕ_{active}). However, even if the metal content of the catalyst is known, it is almost impossible to accurately calculate the value of ϕ_{active}, so this factor was considered in a lumped factor (k_{p0}') together with the propagation reaction rate constant, such as:

$$k_{p0}' = k_{\mathrm{p0}} \phi_{\mathrm{active}} \tag{3-2}$$

So the reaction rate becomes:

$$R_p = k'_{p0} e^{-\frac{Ea}{RT}} C^* C_{\mathrm{C2,amorph}} \tag{3-3}$$

The reaction rate (R_{p}) can also be described in terms of the total heat produced by the reaction (Q_{r}), the reaction enthalpy (ΔH_r) and monomer molar mass (M_{w}). The reaction rate used in the model (and the reaction rate that we will estimate in real time using the state estimator described below) becomes:

$$R_p = k_{p0}' e^{-\frac{Ea}{RT}} C_{\mathrm{Metal}} C_{\mathrm{2,amorph}} = -\frac{Q_{\mathrm{r}}}{\Delta H_r M_{\mathrm{w}}} \tag{3-4}$$

It is also usually interesting to calculate the reaction rate per mass of catalyst ($R_{p,c}$):

$$R_{p,c} = \frac{Q_{\mathrm{r}}}{(-\Delta H_{\mathrm{r}}) m_{\mathrm{cat}}} \tag{3-5}$$

Where m_{cat} is the catalyst mass.

3.1.1. *Monomer concentration in the particles*

As previously discussed in chapter 1, it is possible that monomer gradients can form at the level of the individual particles, and that these gradients (like those for the temperature in the particle and boundary layer) are more significant at short times. However, our major current objective is to develop a software tool that allows us to estimate the rate of polymerization at each moment during the polymerization experiment rather than to delve into details such as internal concentration gradients. It is possible to use the information obtained based on the tool outlined below to do so in a separate step, but we do not need this information at the level at which we are aiming. Furthermore, based on an analysis by Floyd et al.[8], it is safe to neglect significant concentration gradients through the boundary layer under the flow conditions used in this experiment. For these reasons we will assume that the monomer concentration in the system is at equilibrium with the gas phase flowing through the reactor. [9]

Given the relatively short times and the fact that the gas is flowing continuously (i.e. the gas phase concentrations are always constant and conversion can be considered almost negligible), any errors caused with this assumption will be reflected in the estimated value for k_{p0}', and as we have discussed this lumped parameter contains many different contributions. Similarly, we will develop the model for homopolymerization in the current work. Again, this is a reasonable assumption for the same reasons. Even if we have 2 monomers in the gas phase, the overall gas phase consumption is extremely small and the outlet conversion extremely low. So once again, k_{p0}' is a lumped parameter. And again, we are most interested in extracting rate data rather than exact kinetic data, so assuming constant monomer concentration in the particles is not a poor hypothesis. We later used the estimated reaction rates from the high Gain Observer to calculate the monomer conversion, seen in the Appendix 2. We estimated ethylene conversions lower than 2%, which provides confidence in our assumption of constant monomer concentration in the reactor.

In order to validate the model, we will calculate the monomer concentration in the amorphous phase of the polymer using Henry's law, as described by Hutchinson et al.[10], with the Henry coefficient (k^*) as follows:

$$C_{2,\mathrm{amorph}} = 10^3 k^* P$$

$$\log k^* = -2.38 + 1.08\left(\frac{T_c}{T}\right)^2 \qquad (3\text{-}6)$$

Where P is the pressure in atm, $C_{2,\mathrm{amorph}}$ is the concentration of ethylene in the amorphous polymer (mol.m-^{3}), T_c is the critical temperature of ethylene and T is the gas phase temperature (named T_g in the three phases model, T_{inert} (gas and salt) in the two phases model, and T in the observer).

Therefore, the balance for the mass of accumulating polymer (m_{PE}) is:

$$\frac{dm_{PE}}{dt} = M_{\mathrm{w}} R_{\mathrm{p}} V = \frac{Q_{\mathrm{r}}}{(-\Delta H_{\mathrm{r}})} \qquad (3\text{-}7)$$

Where R_{p} is the reaction rate and V is the volume of the reaction zone.

3.2. Energy Balances

The structure of the reactor model will depend on what simplifying assumptions of heat transfer and mass transfer we can make.

At this point, we have assumed plug-flow conditions as the reactor length (56 mm) to particle diameter (average 0.040 mm) ratio is sufficiently large (well above the limit of 50)[11], so axial conduction (on the particle level) can be neglected. We have extended this assumption to neglect potential heat transfer gradients on the radius of the reactor, considering the monomer flowrates are substantially higher than the consumption rates and the improved heat dissipation provided by the annular geometry. This simplifying assumption is in agreement with the experimental and theoretical studies performed by Groppi et al.[12,13] with highly exothermic combustion reactions with an annular reactor. In all cases, describing the flow dynamics in more detail could be verified as an extension to the current project.

In terms of mass transfer, or at least the concentration of reactive species in the gas phase, it seems very reasonable to neglect concentration gradients. The residence time of the gas phase in the reactor

is a second or so at most, and fresh feed gas is constantly being fed along the entire length of the reactor through the fritted membrane. For these reasons, we will consider that the gas phase in the reactor has a uniform composition, equal to that of the feed gas. It should be pointed out that if this assumption works reasonably well for a full-scale fluidized bed reactor, with a per pass conversion of several mole percent, it should just as easily apply here.

Furthermore, given the high degree of dilution of the catalyst in the inert solid (2-5 wt%) and the high heat transfer coefficient of the fine NaCl seedbed (h_{salt} =2.9x10^3 W.m^{-2}.K^{-1}), it is reasonable to assume that temperature gradients between the inlet gas and inert solid are negligible. The calculation of h_{salt} is described later in this chapter, in section 3.3.1. We have verified this approach by modelling the reaction gas as a separate phase in the reactor, shown in the following sections.

Considering the glass wool used to keep the reacting solid in place and its inert nature, we have assumed that any temperature gradients between the glass wool and the gas phase leaving the reactor are also negligible. Therefore, the salt and the glass wool were jointly described in the reactor model as pseudo-homogeneous phase, hereafter referred to as the *inert* phase of the reaction zone.

Based on the aforementioned considerations (1-D model), we have applied the general convection-diffusion equation in cylindrical coordinates assuming no radial gradients, as follows:

$$\rho C_p \left(v_{\mathrm{z}} \frac{\partial T}{\partial z}\right) = k_{\mathrm{e,z}} \frac{\partial^2 T}{\partial z^2} - R_{\mathrm{p}} \Delta H_{\mathrm{r}} \tag{3-8}$$

$$\rho C_p \left(\frac{\partial T}{\partial t} + v_{\mathrm{z}} \frac{\partial T}{\partial z}\right) = k_{\mathrm{e,z}} \frac{\partial^2 T}{\partial z^2} + \frac{Q_{\mathrm{r}}}{V} \tag{3-9}$$

In which T is the gas temperature at time and axial coordinates (t, z), $\rho \mathrm{C_p}$ is the average volumetric heat capacity, $k_{\mathrm{e,z}}$ the effective thermal conductivity, ΔH_{r} the enthalpy of polymerization and Q_r the reaction heat.

With boundary conditions: z=0 and at z=L, are given by: $\frac{\partial T}{\partial z} = 0$

The supported catalysts used in this study are assumed to be spherical particles of known diameter (average 40 µm). The inert seedbed is formed of cubic NaCl crystals agglomerated into particles of 50 µm average diameter. [2,3]

The temperature of the external reactor wall was assumed equal to the set value of the heating chamber and constant throughout the experiment. The internal reactor wall, in contact with the reaction zone, can, in principle, exchange heat with the gas inside the reactor and we have approximated by $T_{\mathrm{w}} = (T_{\mathrm{oven}} + T_{\mathrm{g}})/2$. This assumption was made due to lack of experimental measures of the reactor wall. A more precise estimation could be achieved by a separate heat balance describing the reactor metal walls. We have estimated the heat transfer coefficient at the reactor wall in section 3.3.2.

The metal frit used to feed the monomer into the reaction zone and was not accounted for as a contributor to the total heat capacity of the reactor model. The feed gas is continually flowing through the frit and exchanging with it on the way into the reaction. We judged that the frit is likely at approximately the same temperature of the as the feed, and that it does not exchange significant amounts of heat with the gas phase or bed in the reactor for the relatively short duration of the

experiments. At last, the role of the metal frit in the reaction zone was assessed in a sensitivity analysis study, in section 4.3.

Note that these assumptions were all made to allow us to develop a reactor model and state estimator in a reasonable time frame. A sensitivity analysis will help us to identify any potential weakness in the model, and future work could certainly involve applying a more complete reactor model, relaxing several of the assumptions if need be. Given the time constraints associated with this work, we opted to use a simplified model based on reasonable assumptions to demonstrate the feasibility of the tool and approach.

3.2.1. *Three phases in reaction zone*

In this section, we have written the energy balances for the reactor accounting for three separate phases: the inert phase (salt and glass wool), the reacting phase (catalyst and polymer) and the gas phase.

By assuming the general convection-diffusion equation in cylindrical coordinates and neglecting radial temperature gradients in the reactor scale, the heat balances on a volume element of the bed is described for the three phases, subsequently in the matrix:

$$\begin{bmatrix} (mC_p)_{\mathrm{g}}\left(\frac{\partial T_{\mathrm{g}}}{\partial t}+v_{\mathrm{z}}\frac{\partial T_{\mathrm{g}}}{\partial z}\right) \\ (mC_p)_{\mathrm{s}}\left(\frac{\partial T_{\mathrm{s}}}{\partial z}\right) \\ (mC_p)_{\mathrm{r}}\left(\frac{\partial T_{\mathrm{r}}}{\partial z}\right) \end{bmatrix} = \begin{bmatrix} k_{\mathrm{e,z,g}}V_g\frac{\partial^2 T_{\mathrm{g}}}{\partial z^2} \\ k_{\mathrm{e,z,s}}V_s\frac{\partial^2 T_s}{\partial z^2} \\ k_{\mathrm{e,z,r}}V_r\frac{\partial^2 T_r}{\partial z^2} \end{bmatrix} + F_{\mathrm{g}}\rho_{\mathrm{g}}C_{\mathrm{pg}}\begin{bmatrix} \left(T_{\mathrm{g}}^{\mathrm{in}}-T_{\mathrm{g}}\right)+\left(T_{\mathrm{s}}-T_{\mathrm{g}}\right)+\left(T_{\mathrm{r}}-T_{\mathrm{g}}\right) \\ \left(T_{\mathrm{g}}-T_{\mathrm{s}}\right) \\ \left(T_{\mathrm{g}}-T_{\mathrm{r}}\right) \end{bmatrix} + \\ \begin{bmatrix} S_{\mathrm{r}}h_{\mathrm{r}}\left(T_{\mathrm{r}}-T_{\mathrm{g}}\right)+S_{\mathrm{s}}h_{\mathrm{s}}\left(T_{\mathrm{s}}-T_{\mathrm{g}}\right)+S_{\mathrm{w}}h_{\mathrm{w}}\left(T_{\mathrm{w}}-T_{\mathrm{g}}\right) \\ -S_{\mathrm{s}}h_{\mathrm{s}}\left(T_{\mathrm{s}}-T_{\mathrm{g}}\right) \\ -S_{\mathrm{r}}h_{\mathrm{r}}\left(T_{\mathrm{r}}-T_{\mathrm{g}}\right) \end{bmatrix} + \begin{bmatrix} 0 \\ 0 \\ Q_{\mathrm{r}} \end{bmatrix} \quad (3\text{-}10)$$

With the heat capacity terms for the different phases in the reaction zone are as follows:

Gas phase: $\left(MC_p\right)_g = V_g\rho_{\mathrm{g}}C_{p_{\mathrm{g}}}$ (3-11)

Inert phase: $\left(MC_p\right)_i = V_{\mathrm{s}}\rho_{\mathrm{s}}C_{p_{\mathrm{s}}} + m_{\mathrm{glassWool}}C_{p_{\mathrm{glassWool}}}$ (3-12)

Reacting phase: $\left(MC_p\right)_r = m_{\mathrm{PE}}C_{p_{\mathrm{PE}}} + m_{\mathrm{c}}C_{p_{\mathrm{c}}}$ (3-13)

The gas, salt and reacting volumes were calculated as follows:

V_{s}: The salt volume is constant overtime and known from the experimental preparation;

$V_{\mathrm{g}} = \varepsilon V_{\mathrm{bed}}$; (3-14)

V_{r}: The volume of the reactive phase (catalyst and polymer) it is obtained from the polymer mass balance in eq. (3-7).

ε is the volume fraction of gas in the reaction zone, calculated from: $\varepsilon = 1 - \frac{(V_{\mathrm{r}}+V_{\mathrm{s}})}{V}$ (3-15)

The volumetric flowrate(F_{g}) is calculated from the experimental flowrate ($F_{\mathrm{g,m}}$) and the gas density (ρ_{g}) from the ideal gas law ($\rho_{\mathrm{g}} = \frac{M_{\mathrm{w}}P}{RT}$): $F_{\mathrm{g}} = F_{g,m}/\rho_{\mathrm{g}}$. (3-16)

The linear velocity of the gas (v_{z}) is obtained from the volumetric flowrates: $v_{\mathrm{z}} = \frac{F_{\mathrm{g}}}{S_{\mathrm{r}}\varepsilon}$. (3-17)

The surface area of the polymer particles was calculated as:

$$S_{\mathrm{PE}} = 4\pi r_{\mathrm{PE}}^2 N_{\mathrm{c}} \quad (3\text{-}18)$$

Where N_{c} is the number of catalyst particles, and r_{PE} is the radius of polymer particles calculated based on the reaction rate as follows:

$$R_{p,c} = \left(\frac{3V_{\mathrm{PE}}}{4\pi N_{\mathrm{c}}}\right)^{1/3} \quad (3\text{-}19)$$

The surface of the inert (NaCl) is given by:

$$S_{\mathrm{s}} = 6d_s^2 N_s \quad (3\text{-}20)$$

Where d_s is the length of an edge of the salt cube.

The error bar for the produced polymer mass is determined by the precision of the balance used for following polymer production (10 mg).

3.2.2. *Two phases in reaction zone*

Here, we have written the energy balances for the reactor accounting for two phases in the reaction zone: the inert phase (salt, glass wool and gas) and the reacting phase (catalyst and polymer).

When considering the reaction zone as two components, the gas velocity term was excluded as the gas was jointly described with the inert components. The gas is in motion, but the salt particles and glass wool are not. Therefore, we excluded the convection term for the inert component. Besides, from a numerical analysis which can be seen in the Appendix 2, we concluded these terms to be negligible.

The heat balance based on the general convection-diffusion equation then becomes:

$$\begin{bmatrix} \left(mC_p\right)_{\mathrm{i}}\left(\frac{\partial T_{\mathrm{i}}}{\partial t}\right) \\ \left(mC_p\right)_{\mathrm{r}}\left(\frac{\partial T_{\mathrm{r}}}{\partial t}\right) \end{bmatrix} = \begin{bmatrix} k_{\mathrm{e,z,i}}V_i\frac{\partial^2 T_i}{\partial z^2} \\ k_{\mathrm{e,z,r}}V_r\frac{\partial^2 T_r}{\partial z^2} \end{bmatrix} + F_{\mathrm{g}}\rho_{\mathrm{g}}C_{\mathrm{pg}}\begin{bmatrix} \left(T_{\mathrm{g}}^{\mathrm{in}} - T_{\mathrm{i}}\right) + \left(T_{\mathrm{r}} - T_{\mathrm{i}}\right) \\ -\left(T_{\mathrm{r}} - T_{\mathrm{i}}\right) \end{bmatrix} + \begin{bmatrix} S_{\mathrm{r}}h_{\mathrm{r}}(T_{\mathrm{r}} - T_{\mathrm{i}}) + S_{\mathrm{w}}h_{\mathrm{w}}(T_{\mathrm{w}} - T_{\mathrm{i}}) \\ -S_{\mathrm{r}}h_{\mathrm{r}}(T_{\mathrm{r}} - T_{\mathrm{i}}) \end{bmatrix} + \begin{bmatrix} 0 \\ Q_{\mathrm{r}} \end{bmatrix} \quad (3\text{-}21)$$

With the heat capacity term of the different phases described as follows:

Inert phase: $\left(MC_p\right)_i = \varepsilon V\rho_{\mathrm{g}}C_{p_{\mathrm{g}}} + V_{\mathrm{s}}\rho_{\mathrm{s}}C_{p_{\mathrm{s}}} + m_{\mathrm{glassWool}}C_{p_{\mathrm{glassWool}}}$ (3-22)

Reacting phase: $\left(MC_p\right)_r = m_{\mathrm{PE}}C_{p_{\mathrm{PE}}} + m_{\mathrm{c}}C_{p_{\mathrm{c}}}$ (3-23)

And: $V_i = V_g + V_s$ (3-24)

3.3. Heat transfer correlations

The required heat coefficients were estimated using known correlations between the Nusselt number and Reynold particle number, reminded bellow: [14]

- Particle Reynolds : $Re = \frac{\rho_g v d_\mathrm{p}}{\mu_g}$ (3-25)
- Nusselt number for gas-particle heat transfer: $Nu = \frac{h_\mathrm{p} d_\mathrm{p}}{k_\mathrm{g}}$ (3-26)
- Prandtl number: $Pr = \frac{\mu_\mathrm{g} C_{p_g}}{k_\mathrm{g}}$ (3-27)
- Ranz-Marshall correlation: $Nu = \left(2 + 0.6\sqrt{Re}Pr^{1/3}\right)$ (3-28)
- By combining the 2 Nusselt correlations, we get $h_\mathrm{p} = \frac{k_\mathrm{g}}{d_\mathrm{p}}\left(2 + 0.6\sqrt{Re}Pr^{1/3}\right)$ (3-29)

The coefficients used throughout the model, together with their correlations, are found in Table 1. Details on the calculations are found in the following sections.

Parameter	Correlation	Calculated value [a]
Heat transfer coefficients:		
Catalyst particle	Kunii and Levenspiel [14]	h_p=3.13×10^3 W.m^{-2}.K^{-1}
NaCl particle	Kunii and Levenspiel [14]	h_s=2.78×10^3 W.m^{-2}.K^{-1}
Reactor internal wall	Specchia et al. [15]	h_w=1.99×10^3 W.m^{-2}.K^{-1} $(h_w)_t$ =791.13 W.m^{-2}.K^{-1} $(h_w)_0$ =1.197×10^3 W.m^{-2}.K^{-1}
Effective heat conductivity of the bed	Zehner and Schlünder[16]	0.0392 W.m^{-2}.K^{-1}
[a] at 70°C, gas composition: only ethylene and P=8.55 bar, F= 4.94×10^{-4} m3/s		

Tableau 1: Coefficients used in the model

3.3.1. *Heat transfer coefficient between gas and particle*

The heat transfer coefficient between particles and gas (h_p) was obtained from the following correlation proposed by *Kunii et Levenspiel (chapter 11, eq. 25).* [14]

$$h_\mathrm{p} = \frac{k_\mathrm{g}}{d_\mathrm{p}}\left(2 + 0.6\sqrt{Re}Pr^{1/3}\right) \quad (3\text{-}30)$$

Where k_g is the thermal conductivity of the monomer gas and d_p, the diameter of the corresponding particle, then leading to catalyst (h_r) and salt (h_s) particle heat transfer coefficients when the corresponding particle diameters are applied.

3.3.2. *Heat transfer coefficient at the reactor wall*

The heat transfer coefficient at the reactor internal-side wall (h_{w}) is calculated from a combination of both stagnant/conductive $(h_{\mathrm{w}})_0$ contribution and turbulent/convective $(\mathrm{h_w})_{\mathrm{t}}$ contributions, as elucidated by Specchia et al.[15], as follows:

$$h_{\mathrm{w}} = (h_{\mathrm{w}})_0 + (h_{\mathrm{w}})_{\mathrm{t}} \tag{3-31}$$

The stagnant contribution is obtained from relation (3-32), valid for low Reynolds number (between 10 and 1200). [15] The heat transfer resistance between the particles, the fluid and the wall is taken into account with the dimensionless number φ_{w}, calculated from equation (3-33). [15]

$$\frac{(h_{\mathrm{w}})_0 d_p}{k_g} = 2\varepsilon + \frac{\beta(1-\varepsilon)}{\gamma\frac{k_g}{k_s}+\varphi_{\mathrm{w}}} \tag{3-32}$$

$$\varphi_{\mathrm{w}} = 0.0024\left(\frac{d_R}{d_p}\right)^{1.58} \tag{3-33}$$

d_p is the particle diameter, where the salt diameter was used and d_R is the bed diameter ($d_{\mathrm{R}} = d_{\mathrm{R}}^{\mathrm{out}} - d_{\mathrm{R}}^{\mathrm{in}}$) and $\gamma = 2/3$ and β=1 in Kunii and Levenspiel. [14]

The turbulent contribution $(\mathrm{h_w})_{\mathrm{t}}$ is obtained from relation (3-34), valid for low Reynolds numbers (between 10 and 1200)[15]. The relation was solved for the diameter of the salt particles, given the high dilution of the catalyst particles in the inert seedbed.

$$(h_{\mathrm{w}})_{\mathrm{t}} = \frac{0.0835\, Re^{0.91} k_{\mathrm{g}}}{d_{\mathrm{p}}} \tag{3-34}$$

The superficial temperature of the reactor wall from the reactor side was approximated by:

$$T_{\mathrm{w}} = \frac{T_{\mathrm{oven}}+T_{\mathrm{g}}}{2} \tag{3-35}$$

3.4. Conclusion

A dynamic one-dimensional model was selected as an appropriate choice to describe the current set-up. Plug-flow was assumed and axial conduction was neglected, based on the high ratio between the reactor length and the particle diameter. Radial temperature gradients in the reactor were neglected based on the improved heat dissipation provided by the annular geometry, which has been observed experimentally in the current study (mainly discussed in chapter 2) and suggested in works of Groppi et al. with a similar set-up. [12,13]

After assessment of the transport limitations at the reaction zone, mass transfer limitations were neglected at the intra-particle level; given ethylene is the only monomer gas, so potential diffusive mechanisms were discarded - as described by Floyd et al. [17] In view of the high monomer flow rates compared to the consumption rates, the concentration of monomer can be assumed to be uniform in the bed and constant over time.

The reaction zone was assumed to be composed of three components (or phases). Catalyst and the growing polymer were considered as a pseudo-homogeneous phase, referred to as the reacting phase of the reaction zone. Likewise, the salt seedbed and glass wool were assumed to have the same temperatures, referred to as the inert phase of the reaction zone. Finally, the gas phase was considered separately as the third component of the reaction zone. This hypothesis for the number of phases in the reactor was assessed in the model validation, discussed later in this chapter.

The superficial temperature of the reactor wall was supposed to increase gradually when the inner gas temperature increases. Interactions of the metal frit with the reaction zone were neglected, given the direction of the inlet gas. These assumptions were later assessed in the sensitivity study.

The reaction rate was defined as a first order reaction and the monomer concentration in the reaction zone was assumed constant due to the high gas flow rates, small reaction volume and short reaction times. The monomer concentration was assumed constant in the reactor and was calculated using Henry's law. The polymerization rate was also defined in terms of the heat produced by the reaction (Q_{r}).

Intraparticle heat and mass transfer limitations were not included in the model at this stage as we focused mainly on the reactor and macroparticle scales in the scope of this project. Nonetheless, the particle growth model could be incorporated later.

4. Validating the reactor model

In this section, the developed reactor model was validated with experimental data obtained with the novel set-up. Simulation results were presented for both approaches in describing the reaction zone: three phases and two phases, respectively.

4.1. Model programming

The reactor was described in a one-dimensional model using the *pdepe*[18] solver function in MATLAB, which solves a system of parabolic and elliptic partial differential equations with spatial and time variables, in the following form:

$$c\left(x,t,u,\frac{\partial u}{\partial x}\right)\frac{\partial u}{\partial t}=x^{-m}\frac{\partial}{\partial x}\left(x^{m}f\left(x,t,u,\frac{\partial u}{\partial x}\right)\right)+s\left(x,t,u,\frac{\partial u}{\partial x}\right) \quad (3\text{-}36)$$

The scalar m reflects the geometry of the problem, which is cylindrical in our case (m=1). The discretization of space must be specified by the user prior to solving. For the current model, the reactor was described in 20 intervals of 2.8 mm length. The MATLAB function was applied to solve the energy balances described for the reaction zone. Finer meshing was also assessed and was found not necessary as the precision of simulation results was not improved.

4.2. Simulation results

In this section, we have evaluated the simulation results obtained for the reactor model initially for the system described by three phases in the reaction zone, then by two phases.

4.2.1. *Three phases in reaction zone*

The model assuming three phases (inert phase - salt and glass wool, the reacting phase - catalyst and polymer, and the gas phase) in the reaction zone was validated with a 60-second reaction with catalyst CGC M, in homopolymerization conditions with ethylene.

Temperature simulations of the three phases using a mean value of $k'_{p0}=130$ m^3 mol^{-1} s^{-1} are found in Figure 4-a, together with the experimental inlet and outlet temperatures. Figure 4-b shows the simulation results of the polymer mass formation overtime, together with the experimental result. This value of k'_{p0} was chosen in a way that the polymer mass at the end of the run corresponds exactly to the experimental mass.

The temperature profiles estimated from the model considering three phases in the reaction zone provide relatively good capturing of the average temperature values obtained experimentally, but did not reflect the nonlinear behavior of the system. This is reasonable, as we did not include a kinetic model that takes into account the activation and deactivation processes of the catalyst. In the sensitivity analysis, we have assessed the impact of imposing an activation period for the catalyst on the temperature predictions.

The predicted temperatures for the reacting phase (catalyst and polymer) only slightly exceed those of the gas and inert phases. We took this as an indication of good heat evacuation from the reactor.

The temperature predictions of the inert phase (salt and glass wool) seem to superpose with those of the gas phase. The very similar temperature profiles obtained for the two phase provides confidence in our assumption of describing the inert and gas phases in a lumped factor, and so reducing the model system to two phases.

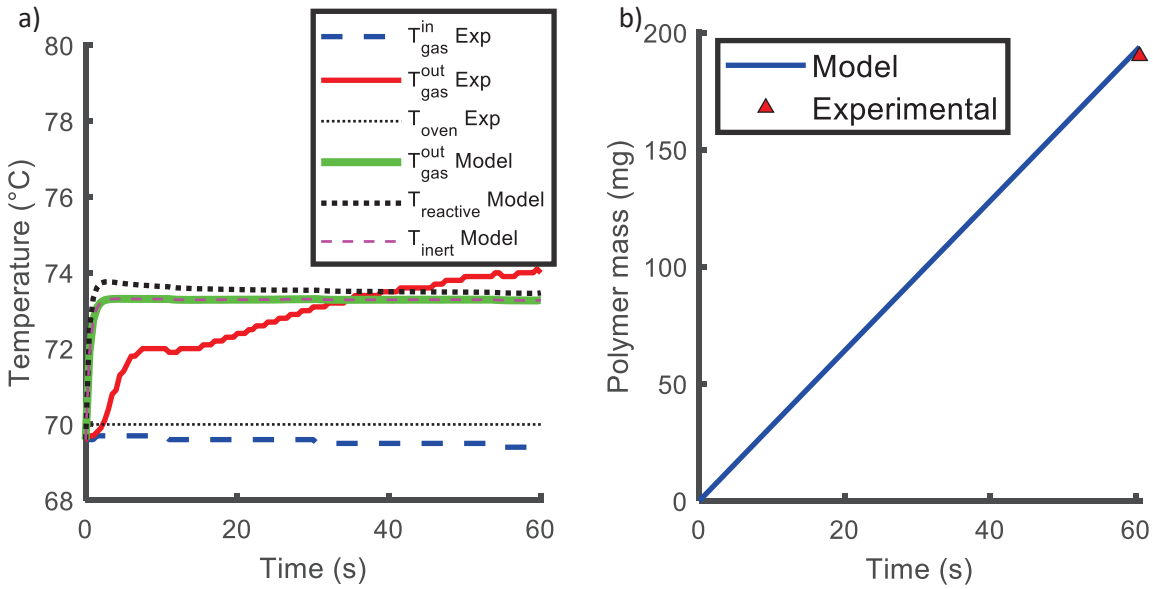

Figure 4: Simulation results for reactor model assuming three phases in reaction zone: a) estimated temperatures in reaction zone, b) estimated mass of produced polymer with reaction time

4.2.2. *Two phases in reaction zone*

The model assuming two phases in the reaction zone was validated with a 60-second reaction with catalyst CGC M, in hopolymerization conditions.

At this stage, the estimated phases were the inert phase (salt, glass wool and gas) and the reacting phase (catalyst and polymer).

Figure 5-a shows the estimated temperatures for the two phases, obtained with a mean value of $k'_{p0} = 130$ m^3 mol^{-1} s^{-1}, together with the experimental temperature profiles. Figure 5-b shows the estimated polymer production, together with the experimental value.

The temperature profiles predicted from the model assuming two phases in the reaction zone provided good fitting with the average temperature values obtained experimentally. As in the three phases model, due to the consideration of a constant reaction rate (not accounting for activation/deactivation), the predictions did not capture the nonlinear behavior of the reaction.

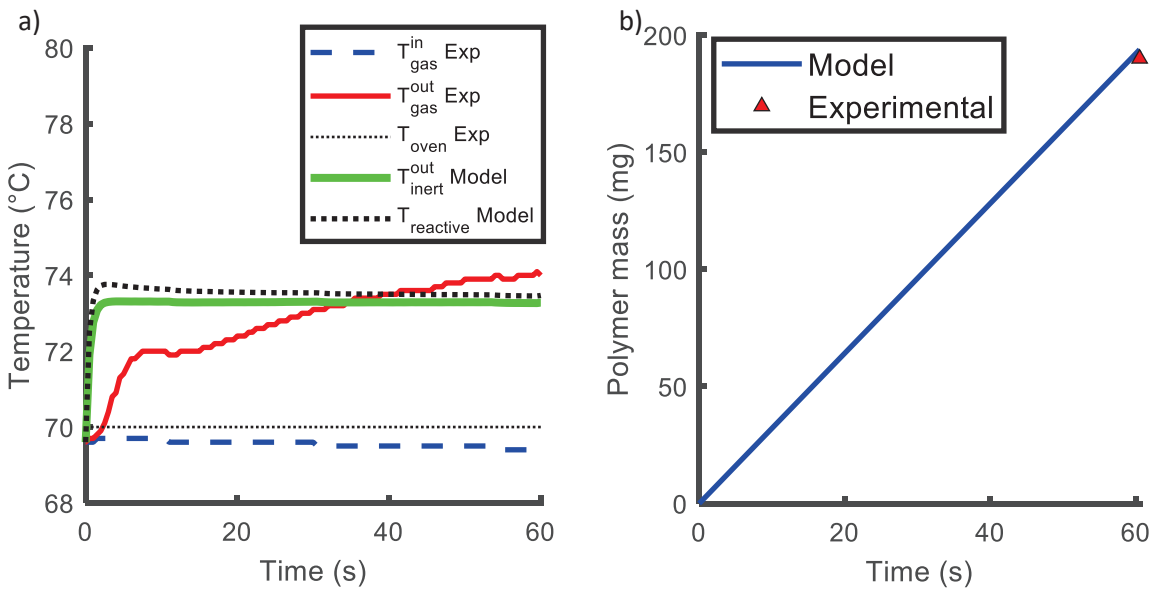

Figure 5: Simulation results for reactor model assuming three phases in reaction zone: a) estimated temperatures in reaction zone, b) estimated mass of produced polymer with reaction time

4.2.3. *Conclusion*

In this section, we have simulated the energy balances previously written, which included two approaches as to how to treat the reaction zone.

The initial approach was to model the reactor assuming three phases in the reaction zone, including the inert phase (salt and glass wool), the reacting phase (catalyst and polymer) and the gas phase.

Following, since the salt and gas temperatures were equal in the three-phase model, we assumed only two phases in the reaction zone, the inert and reacting phases. We considered that there were no temperature gradients between the inert phase and the gas phase, which were jointly described as 'inert phase'.

In both approaches, the predicted temperatures provided reasonable fits with the average values recorded experimentally, but do not reflect the nonlinear behavior of the catalysts.

Based on the obtained simulation results, we have validated the description of the reaction zone in two phases for the reactor model.

4.3. Sensitivity analysis

In this section, we have performed a sensitivity study on some of the parameters and assumptions used for the reactor model, in order to verify their impact on the model predictions.

The evaluated parameters were the heat transfer coefficients $(h_{\mathrm{w}}, h_{\mathrm{salt}}, h_{\mathrm{cat}})$, the superficial temperature of the wall and the values for axial thermal conductivities.

The evaluated assumptions for the model were the treatment of the metal frit and the activation period for the catalyst.

We have defined a variation margin for these terms, in order to observe their effect on the temperatures predicted by the model, as well as the sensitivity of the model in capturing variation in the parameters.

In the current section, we have presented the terms that we deemed to have a more important impact on the quality of the model. The effects of the remaining assessed factors were judged to have negligible impact on the quality of model predictions and can be found in the Appendix 2.

4.3.1. *Superficial temperature of reactor wall (T_{wall})*

In the development of the current model, we have assumed that the superficial reactor temperature wall is approximated by $T_{\mathrm{w}} = (T_{\mathrm{oven}} + T_{\mathrm{g}})/2$. This assumption was made due to lack of experimental measures of the reactor wall.

In the sensitivity analysis, we observed this assumption has a significant impact on the temperatures estimated by the model. Imposing $T_{\mathrm{w}} = T_{\mathrm{oven}}$ led to significant decrease of all predicted temperatures, as seen in Figure 6. However, it is logical to assume that the wall temperature (at least at the inner surface) will be influenced by the gas temperature inside the bed. Therefore, we keep our initial simplified approximation assumption.

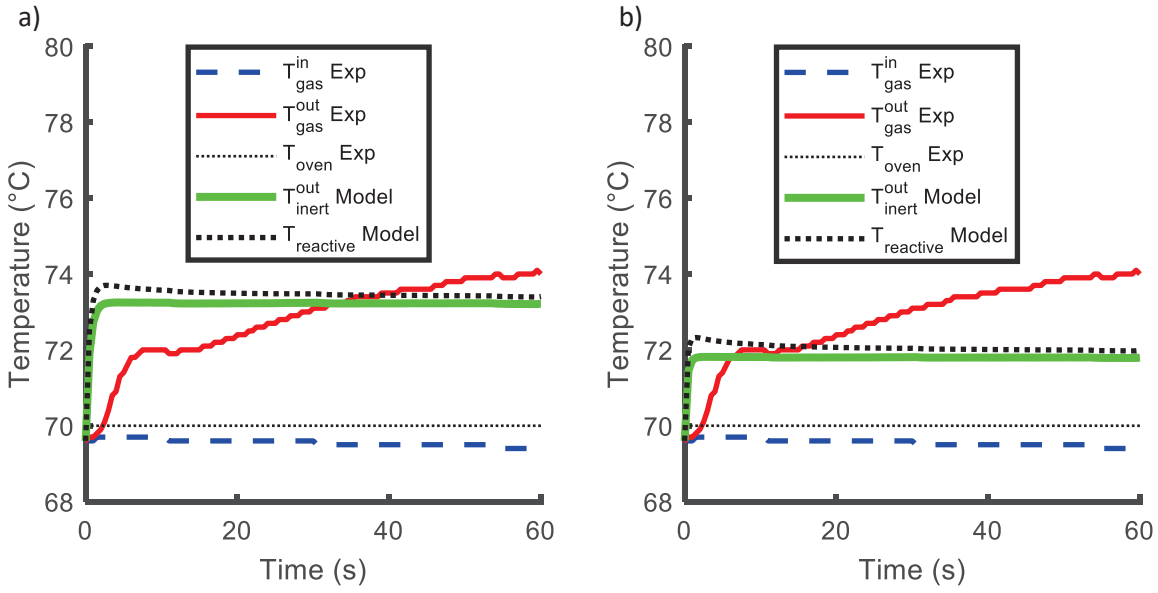

Figure 6: Assumption for reactor wall temperature equal to: a) $T_{\mathrm{w}} = (T_{\mathrm{oven}} + T_{\mathrm{g}})/2$, b) $T_{\mathrm{w}} = T_{\mathrm{oven}}$

4.3.2. *Catalyst particle heat transfer coefficient (h_{cat})*

The heat transfer coefficient for the catalyst particle were calculated using the correlation proposed by Kunii and Levenspiel[14], as previously described in section 3.6.1. We have assessed the importance of this parameter by reducing its value by 50%. As seen in Figure 7, reducing the value of this parameter affected the predicted temperatures of the reacting phase, indicating higher particle temperatures. Nonetheless, varying this parameter had no impact on the temperatures of the gas and inert phases. No impact was observed on the produced mass either, indicating that the difference observed in the temperature profiles had little impact on the reaction rate. These results are in agreement with what is expected in reality (lower values h_{cat} would lead to reduced heat transfer and thus hotter particles) and indicate good response of the reactor model.

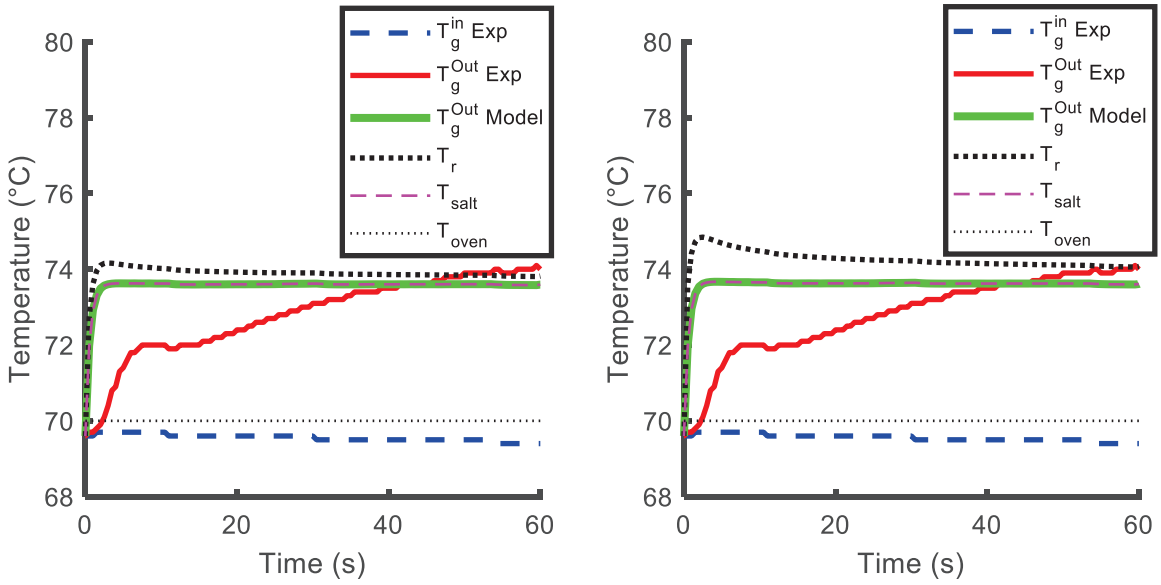

Figure 7: Assessing impact of h_{cat} on model prediction, a) h_{cat} calculated from correlation in literature[14], b) calculated value reduced by 50%

4.3.3. *Diameter of catalyst particles*

From this assessment, we observed that the catalyst particle diameter has a direct impact on the predicted temperatures of the reacting phase.

As shown in Figure 8, doubling the particle diameter (from 40 to 80 µm) led to significant increase in the predicted temperatures of the reacting phase, but had no effect on the gas and inert. The observed response is coherent with previous studies[19] on the impact of the particle sizes and indicates satisfactory sensitivity of the developed model.

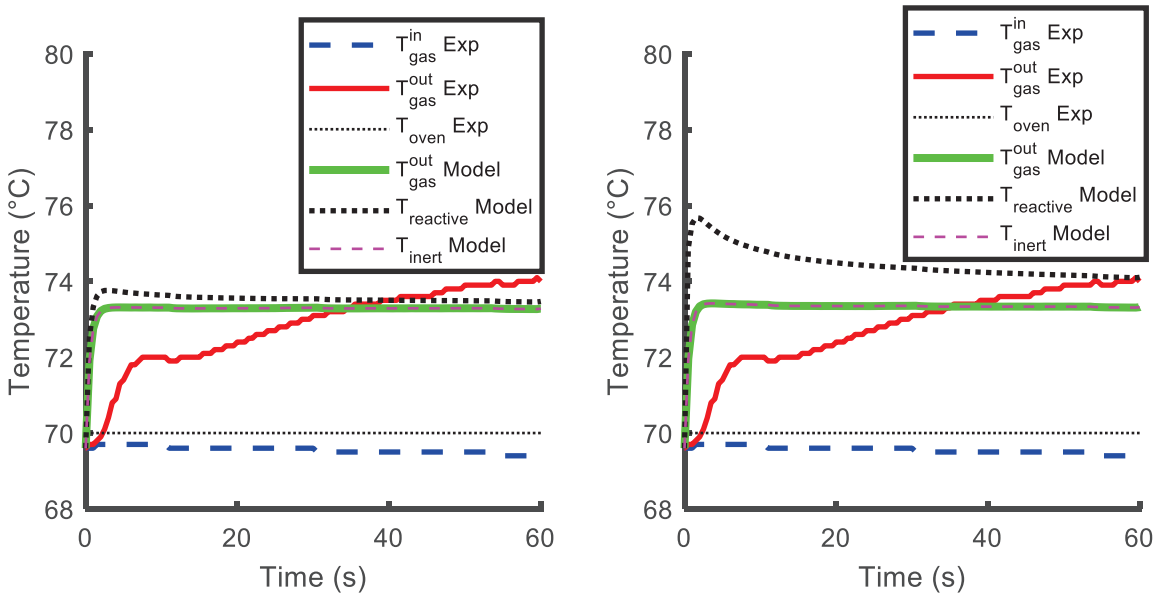

Figure 8: Assessing impact of catalyst particle diameter, a) 40 µm (value used in model calculation), b) 80 µm

4.3.4. *Conclusion*

A sensibility analysis was carried out for several terms and assumptions used in the development of the reactor model. For each term, we have imposed a variation margin to assess their influence on the estimated values.

The sensitivity analysis indicates that variabilities in the superficial temperature of the inner reactor wall have a direct impact on the predicted temperatures in the reaction zone. To avoid errors due to this assumption, we would ideally include experimental measurements of the reactor wall temperatures (from the reactor side, which could be difficult given the physical nature of the reactor contents) or propose a detailed model to describe it.

We estimated a moderate impact of the catalyst heat transfer coefficient of the reactor temperature and thus the produced mass, which validates the calculations based on the equation proposed by Kunii and Levenspiel[14]. Decreasing the value of the catalyst heat transfer coefficient led to higher temperatures of the reacting phase, but not on the gas and inert phases in the reactor. This observation is in agreement with what is expected in reality and indicates good sensitivity of the developed model.

Finally, we observed that increasing the catalyst diameters resulted in higher predicted temperatures for the reacting phase, but no impact on the predicted temperatures for the gas phase and only a negligible impact on the produced mass. This is in agreement with previous studies that indicated that catalysts with larger particle diameter can lead to transport limitations. [19]

The remaining evaluated parameters were judged to have unimportant impact on the model predictions. It is worth mentioning that we observed no effect of the effective thermal conductivity ($k_{e,z}$) on the model outcome (even when extrapolated to *1000), indicating that this term can be neglected from the energy balance.

The assessment of the parameters judged negligible can be found in the Appendix 2.

4.4. Conclusions on model validation

A dynamic 1-D model to describe the current stopped-flow reactor was developed and validated.

The model was validated for the assumptions of two and three phases in the reaction zone. The assessment indicated that the assumption of two phases was satisfactory for describing the system, in which gas and inert phases were considered jointly in the heat balance.

The predicted temperatures for the reacting phase (catalyst and polymer) only slightly exceed those of the gas and inert phases, which we took as an indication of satisfactory heat evacuation from the reactor. This is in agreement with the experimental observations assessed in chapter 2.

From the sensitivity study performed on the parameters and assumptions used in the reactor model, we concluded the main source of error in the model are the assumption for the surface temperature of the reactor wall. Imposing variations of the heating chamber temperature had a direct impact on the temperature profiles predicted by the model. To avoid this factor of uncertainty, ideally experimental measures of the reactor wall temperatures would be used instead of assuming constant values or a more detailed model could be proposed.

We observed that reducing the value of the catalyst heat transfer coefficient led to higher temperatures of the reacting phase, while the temperatures of the gas and inert phases were not affected. This indicated satisfactory sensitivity of the developed model, as the observed response was in agreement with what is expected in reality.

Moreover, we observed that increasing the particle diameter led to an increase in the predicted temperatures of the reacting phase but showed no impact on the gas and inert phases. This behavior is coherent with the potential transport resistances demonstrated by Bashir et al. [19] and indicate good sensitivity of the developed model.

As last, the sensitivity analysis indicated that the effective thermal conductivity ($k_{e,z}$) plays a negligible role in the energy balance.

From the simulation results and sensitivity analysis, we concluded the developed model provides satisfactory predictions for average temperature profiles for the current reactor under study.

5. Development of a High-Gain Observer

A High-Gain Observer was implemented to estimate values for unmeasured parameters, such as the heat produced by the reaction (Q_r) and the reaction rate (r_p).

The method consisted of minimizing the relative errors between the experimental and the calculated outlet temperature values by use of a tuning parameter θ.[20,21] The recorded experimental outlet temperatures are used as input data for the observer, as depicted in the block diagram in Figure 9. A detailed description of the development and application of non-linear observers can be found in the open literature. [20,22,23]

5.1. Introduction

As discussed in the introduction of this chapter, the main objective with the current modelling efforts were to interpret the experimental results and gain insights in terms of the catalyst kinetics. One of the approaches taken with this purpose was to use the reactor as a calorimeter.

In a broad definition given by Soares et al. [24], calorimetry is "the monitoring of heat balances in a reacting system, which allows inferring of the rates of exothermic (or endothermic) reactions and of some additional correlated variables, such as compositions. The technique is characterized by its simplicity, as it depends almost exclusively on the availability of temperature and flow-rate measurements of the main process streams...".

Calorimetry is perhaps the oldest analytical technique (see the ice calorimeter from Lavoisier and Laplace, 1780s [25]) which is still commonly used to investigate chemical reactions, often providing immediate access to characteristic quantities such as reaction kinetics or thermodynamics. Calorimetry is often used as a tool for on-line monitoring of industrial polymerization reactors and has also been successfully applied, in previous studies, to monitor reactions in the laboratory scale. [26]

This technique has been applied to study polymerization reactions in the lab scale at short reaction times. In these cases, estimation methods such as High-Gain Observers were applied to obtain polymerization rates from experimental temperature profiles.

One example is the work of Tisse et al. [27], who implemented a non-linear state observer to obtain precise reaction rates in short time slurry polymerizations with supported metallocene catalysts. Likewise, Browning et al. [5] adapted the approach from Tisse et al. to construct a 2-dimensional high gain observer to estimate kinetic parameters for short polymerization reactions in gas phase. In fact, the approach followed by Browning et al. to describe the earlier stopped-flow reactor (named SF 1, presented in chapter 2) was not too different from the one used in the present study.

In broad terms, an observer is a mathematical representation of a given system, which allows estimating internal states that usually cannot be directly accessed. The observer correlates the output values from a model (output data) with the available experimental (or input) data through a corrective term. This corrective term is proportional to the difference between the input and the output data times a gain (dependent of the structure of the system).[20]

The observer $\hat{\hat{x}}(t)$ for a given system can be written as follows: [20,22,23]

$$\hat{\hat{x}}(t) = \hat{x}(t) - f(x)(\hat{x}(t) - x(t)) \tag{3-37}$$

Where $\hat{x}(t)$ are the values estimated from the model, $x(t)$ are the available experimental measurements. The function $f(x)$, which includes the corrective term θ and the stablished gain, minimizes the difference between estimated and measured data.

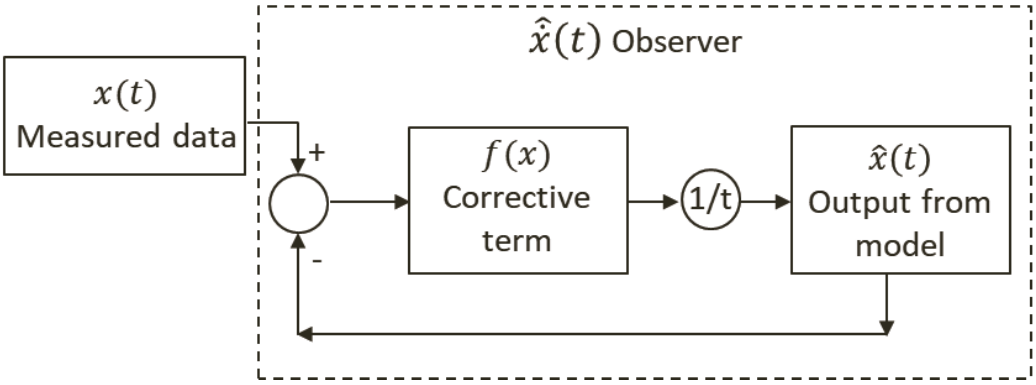

Figure 9: Diagram for High-Gain Observer

5.2. The novel reactor as a Calorimeter

According to Kammona et al. [28], an isothermal condition is primordial for monitoring polymerization reactions with a calorimeter.

The stopped-flow reactor currently under study does not fulfill this criterion, as it is strictly an isoperibolic system, in which the only temperature of the reactor external wall is kept constant by the heating chamber. The reaction temperature is not actively controlled and the heat evacuation from the reactor is done mainly by the outlet gas stream. In this case, the reaction kinetics are influenced by the temperature changes and must be determined by the model. Nonetheless, these effects are accounted for in the heat balances, which were described and validated in the previous sections.

5.3. Implementing a High-Gain Observer

The initial step in treating the reactor as a calorimeter is the definition of heat balances, as these are the link between the reaction rate and the outlet temperature.

In the current study, we have treated the reaction zone as one single compartment, which fundamentally means viewing the system as a CSTR. The single element observer is the simplest approach to overcome the lack of some experimental data, such as the temperature of the metal frit and that of the reactor walls (internal and external).

While this is clearly an approximation, it is a reasonable one consideration the geometry and small dimensions of the reactor. Besides, as demonstrated in chapter 2, the annular geometry provided a significant improvement in the heat evacuation, meaning that the measured outlet temperatures more closely reflect the real temperature of the reaction bed. At last, the single element observer remains the most straightforward method to gain direct access to the reaction rate.

The corrective term was determined by simulation and fixated at $\theta = 1$. This value allowed the simulations to converge quickly without losing sensitivity. The effect of the tuning parameter was assessed in the sensitivity analysis, in section 5.5. of this chapter.

Using the heat balances previously developed and validated for the reactor model (equation 3-21), we have implemented and validated a single element observer for the current set-up. These steps are described in the following sections.

5.3.1. *Heat balance and reaction rate*

The heat balance for the High-Gain Observer was based on the heat balance previously developed and validated for the reactor model, with the assumption of the reaction zone as a single compartment.

As for the heat balances developed for the reactor model, the temperature of the reactor wall was assumed equal to the temperature of the heating chamber, both assumed constant throughout the experiment.

The effective diffusivity thermal diffusivity was neglected, as the sensitivity analysis carried out for the reactor model indicated this term plays no role in the current system.

The heat balance for the single-element observer then becomes:

$$MC_p \frac{\mathrm{d}T}{\mathrm{d}t} = F_\mathrm{g}\rho_\mathrm{g}C_{p\mathrm{g}}\left(T_\mathrm{g}^\mathrm{in} - T\right) + S_\mathrm{w}U(T_\mathrm{w} - T) + Q_\mathrm{r} \tag{3-38}$$

With:

$$MC_p = \varepsilon V \rho_\mathrm{g} C_{p_\mathrm{g}} + V_\mathrm{s}\rho_\mathrm{s}C_{p_\mathrm{s}} + m_\mathrm{glassWool}C_{p_\mathrm{glassWool}} + m_\mathrm{PE}C_{p_\mathrm{PE}} + m_\mathrm{c}C_{p_\mathrm{c}} \tag{3-39}$$

The high-gain observer of the heat produced by the reaction is given by:

$$\frac{\mathrm{d}\hat{T}}{\mathrm{d}t} = \frac{1}{MC_p}\left(\hat{Q}_\mathrm{r} + F_\mathrm{g}\rho_\mathrm{g}C_{p\mathrm{g}}\left(T_\mathrm{g}^\mathrm{in} - T\right) + S_\mathrm{w}U(T_\mathrm{w} - T)\right) - 2\theta\left(\hat{T} - T\right) \tag{3-40}$$

With:

$$\frac{\mathrm{d}\hat{Q}_\mathrm{r}}{\mathrm{d}t} = -\theta^2 MC_p\left(\hat{T} - T\right) \tag{3-41}$$

The reaction rate $\left(R_p\right)$ for the propagation step, in terms of the heat produced by the reaction, remained as developed for the reactor model, as follows:

$$R_p = -\frac{Q_\mathrm{r}/V}{\Delta H_\mathrm{r} M_\mathrm{w}} \tag{3-42}$$

5.4. Validating the High-Gain Observer

The single element High-Gain Observer was applied for a 60 second experiment with the CGC catalyst, as for the reactor model.

The calculated outlet temperatures can be seen in Figure 10-a, together with the experimental temperature profiles. Figure 10-b shows the estimated results for the polymer mass formation overtime, together with the experimental result. Figure 11 shows the estimated dynamic reaction rates.

The obtained temperature profiles showed satisfactory fitting in relation to the experimental data and the nonlinear behavior of the polymerization process was captured. Moreover, the calculated mass of produced polymer provided insight on the catalyst activation and deactivation steps (effects not detected by the reactor model). At last, the predicted polymerization rates were in agreement with

the catalyst kinetics observed at full-time polymerization, which can be found in chapter 2 (section 5.5.1.).

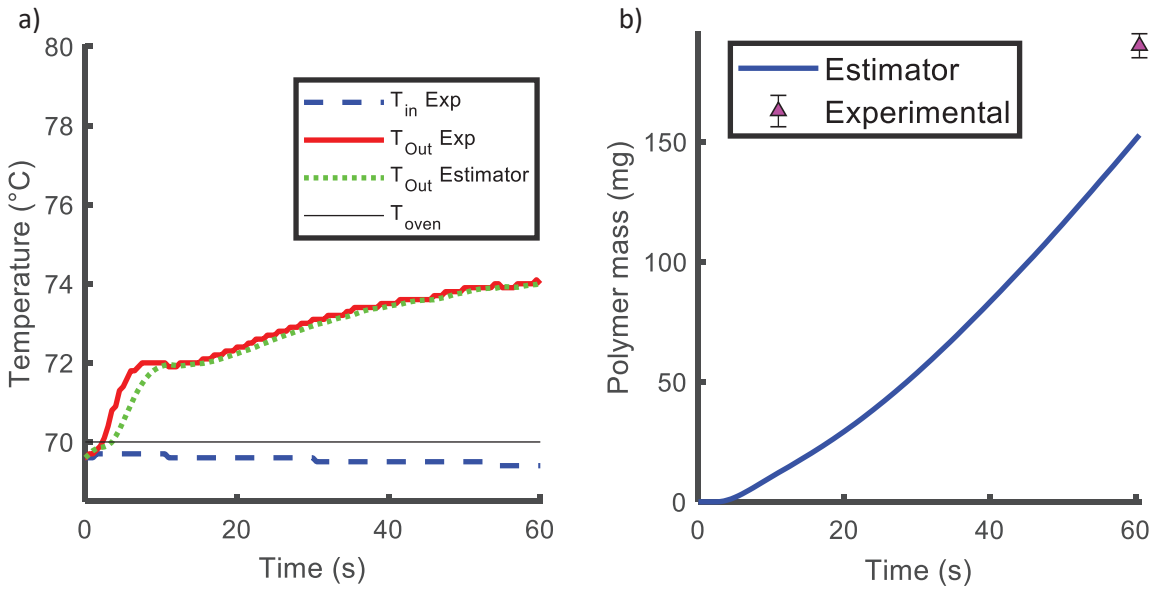

Figure 10: Estimated and experimental: a) outlet temperature profiles, b) mass of produced polymer

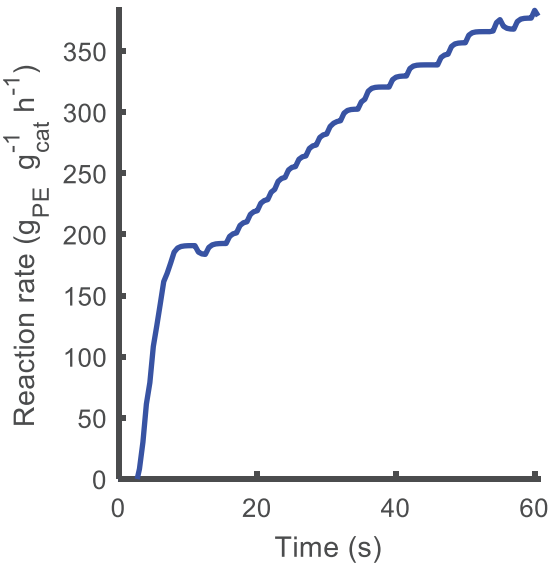

Figure 11: Estimated reaction rates

5.5. Sensitivity analysis

The tuning parameter for the Observer was determined by simulation. In this section, we have performed a sensitivity study on the effect of the tuning parameter on the temperature profiles estimated by the Observer.

5.5.1. *Effect of tuning parameter*

Figure 12 shows simulation results obtained with two values for the tuning parameter θ.

As seen in the following assessment, applying tuning parameters >1 provided very little improvement to the obtained estimations. Nonetheless, computational times were higher.

Therefore, we fixated the tuning parameter at $\theta = 1$. This value allowed obtaining satisfactory conversions at short computation times.

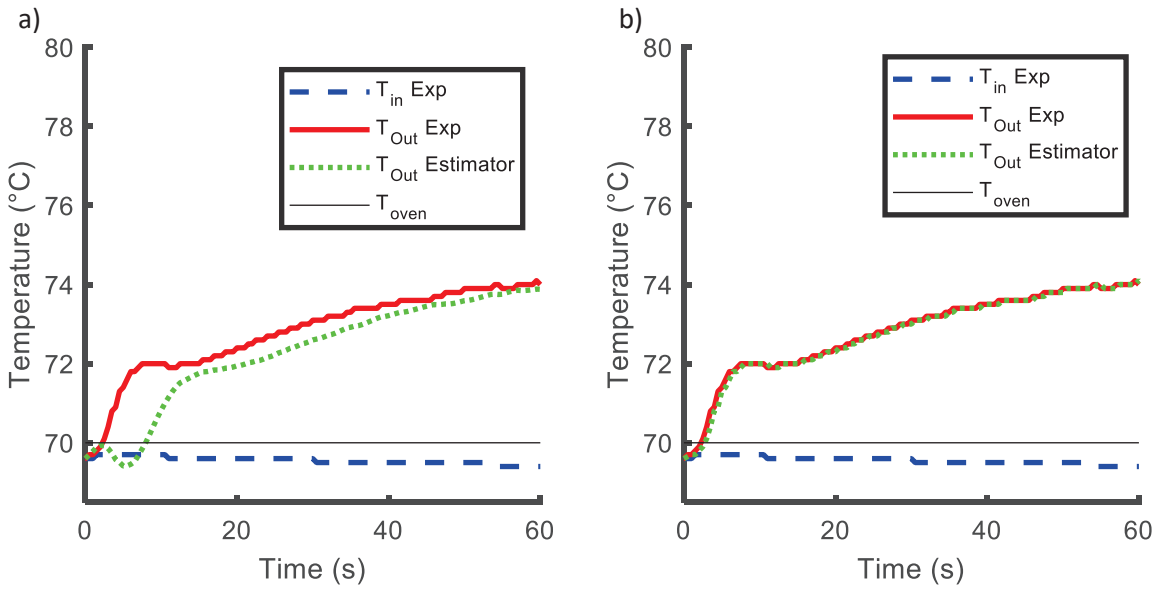

Figure 12: Effect of tuning parameter on predicted temperatures, a) θ=0.5, b) θ=10

5.6. Conclusion

A single element High-Gain Observer was implemented and provided robust results in relation to the experimental data. The observer allowed capturing the nonlinear behavior of the polymerization reaction and estimating the polymerization yields with acceptable accuracy.

The tuning parameter for the Observer was determined by simulation and assessed in the sensitivity analysis. The predicted polymerization rates were in agreement with those obtained in full-time polymerization conditions, previously carried out in chapter 2 (section 5.5.1.). At last, the implemented single element High-Gain Observer provided satisfactory estimates of the reaction temperature profiles, dynamic reaction rates and kinetic parameters.

We applied the estimated reaction rates to calculate the monomer conversion, for the catalyst used in this study – found in the Appendix 2. We obtained monomer conversions lower than 2%, which confirms our initial assumption of constant monomer concentration in the reactor.

6. Chapter conclusions

The development of a software component for a novel stopped-flow reactor was described and validated.

The software component consisted of a 1-D model of the reactor set-up, together with a High-Gain Observer, implemented to estimate reaction rates and kinetic parameters from the experimental temperature profiles.

Heat and mass transfer limitations at the reaction zone were assessed for the inter-particle and intraparticle levels. At this point, intraparticle gradients were neglected and the model did not include the description of a kinetic model.

Heat balances were described for the reactor in two approaches, assuming two or three components (or phases) in the reaction zone. The reactor model was validated with experimental data for both approaches and we confirmed our assumption of two phases in the reaction, for which we considered the reaction gas was in thermal equilibrium with the inert solids. The parameters and assumptions used for the model development were assessed as part of a sensitivity analysis, where the terms in the model were extrapolated to verify their effect on the model responses. This study indicated the developed model is robust and provides adequate estimates for average temperature profiles for the current reactor under study. Nonetheless, the model did not capture the nonlinear behavior of the reaction.

A High-Gain Observer was implemented to interpret the catalyst kinetic from the experimental data and provide insight on effects such as the catalyst activation and deactivation, which were not detected by the reactor model.

For the implementation of a High-Gain Observer, we assumed the reaction bed as a single-element and wrote the energy balance accordingly. The implemented Observer was validated with experimental data and provided access to unmeasurable states of the system, such as the heat produced by the reaction, the reaction rate and dynamic profiles of kinetic parameters. The estimated reaction rates for short reaction times were coherent with those obtained for full-time polymerization experiments, carried out with standard semi-batch reactors.

The implemented software allowed following the dynamic kinetic behavior of the ongoing polymerization, thus fulfilling our initial goal of properly interpreting the experimental data in terms of catalyst kinetics. The developed reactor model allowed to obtain mean values for the exponential kinetic constant, while the High-Gain Observed provided dynamic values for the reaction rate. Besides, the software component could be a useful tool to interpret temperature profiles at low productivities, where yields are too low to detect gravimetrically.

In this chapter, we have presented the development of the software component of the novel stopped-flow reactor. In the following chapter, the developed hardware and software components will be applied in specific case studies to interpret the kinetic behavior of different heterogeneous catalysts.

7. Nomenclature

Parameter	Definition	Unit
B	Deformation parameter	-
B_{iw}	Biot number ($B_{\mathrm{iw}} = h_w d_p / k_e$)	-
C_{p}	Specific heat capacity	$m^3.s^{-1}$
$C_{2,\mathrm{amorph}}$	Ethylene concentration in amorphous phase	
C_{Metal}	Metal concentration	$mol.L^{-1}$
C^*	Concentration of active sites	$mol.L^{-1}$
$d_{\mathrm{R}}^{\mathrm{in}}$	Diameter of porous frit	m
$d_{\mathrm{R}}^{\mathrm{out}}$	Diameter of reactor outer wall	m
$\mathrm{d_p}$	Diameter for nonspherical particles	m
E_{a}	Activation energy	$J.mol^{-1}$
F_{g}	Volumetric gas flowrate	$m^3.s^{-1}$
$h_{\mathrm{w}} = (h_{\mathrm{w}})_0 + (h_{\mathrm{w}})_{\mathrm{t}}$	Heat transfer coefficient at the reactor wall (inner, reaction side)	$W.m^{-2}.K^{-1}$
$(h_{\mathrm{w}})_0$	Stagnant/conductive contribution to h_i	$W.m^{-2}.K^{-1}$
h_p	Heat transfer coefficient between particles and gas	$W.m^{-2}.K^{-1}$
$(h_{\mathrm{w}})_{\mathrm{t}}$	Turbulent convective contribution to h_i	$W.m^{-2}.K^{-1}$
ΔH_{r}	Reaction enthalpy	$J.kg^{-1}$
k^*	Henry coefficient	$mol.L_{amorph}^{-1}\ atm^{-1}$
k	Heat conductivity	$W.m^{-1}.K^{-1}$
k_{e}	Effective heat conductivity of bed	$W.m^{-1}.K^{-1}$
$k_{p0}{}'$	Preexponential lumped kinetic coefficient $k_{p0}{}' = k_{\mathrm{p0}} \phi_{\mathrm{active}}$	$m^3.mol^{-1}.s^{-1}$
k_{p0}	Pre-exponential reaction rate constant	$m^3.mol^{-1}.s^{-1}$
k_s	Salt particle thermal conductivity	$W.m^{-1}.K^{-1}$
$k_{\mathrm{e,z,i}}$	Effective thermal conductivity	$W.m^{-1}.K^{-1}$
l_{s}	Thickness of a slab of solid material with the same resistance as one half spherical particle [15]	m

m	Mass	kg
M_{w}	Molecular weight of ethylene	kg.mol^{-1}
N	Number of particles	Scalar
P	Pressure	Pa
Q_{r}	Heat produced by the reaction	W
r	Radius	m
$R_{p,c}$	Reaction rate	g.g^{-1} catalyst.h^{-1}
R_{p}	Reaction rate	mol.m^{-3}.s^{-1}
R	Ideal gas constant	J.mol^{-1}.K^{-1}
S	Surface area	m^2
T	Temperature	K
U	Overall heat transfer coefficient	W.m^{-2}.K^{-1}
v	Superficial velocity	m.s^{-1}
V	Volume of reaction zone	m^3
V_{PE}	Volume of PE particle	m^3
ΔV	Fraction of reaction zone volume	m^3
y_w	$\mathrm{y}_w = l_{\mathrm{s}}/D_e^*$ [15]	-
ρ	Density	kg.m^{-3}
ε	Porosity of reaction bed i.e. the fraction of gas (the rest being salt, catalyst and polymer).	-
ϕ_{active}	Active fraction of active sites	wt%
φ_W	Heat transfer resistance between particles, fluid and wall	-
Suffixes		
c	Catalyst particle	
C2	Ethylene	
g	Monomer gas – Ethylene, or gas phase	
m	Measured from experiment	

i	Inert phase
inox	Stainless steel
r	Reacting phase
R	Reactor
p	Particle
PE	Polethylene - polymer
s	Salt particle
w	Reactor wall
Z	z axis of Reactor

8. References

(1) Olalla, B.; Broyer, J.-P.; McKenna, T. F. L. Heat Transfer and Nascent Polymerisation of Olefins on Supported Catalysts. *Macromol. Symp.* **2008**, *271* (1), 1–7. https://doi.org/10.1002/masy.200851101.

(2) Tioni, E.; Spitz, R.; Broyer, J. P.; Monteil, V.; McKenna, T. Packed-Bed Reactor for Short Time Gas Phase Olefin Polymerization: Heat Transfer Study and Reactor Optimization. *AIChE J.* **2012**, *58* (1), 256–267. https://doi.org/10.1002/aic.12576.

(3) Browning, B. Dynamic modelling of a fixed bed reactor - PhD Thesis https://tel.archives-ouvertes.fr/tel-01175971/document (accessed Dec 1, 2016).

(4) Browning, B.; Pitault, I.; Sheibat-Othman, N.; Tioni, E.; Monteil, V.; McKenna, T. F. L. Dynamic Modelling of a Stopped Flow Fixed Bed Reactor for Gas Phase Olefin Polymerisation. *Chem. Eng. J.* **2012**, *207–208*, 635–644. https://doi.org/10.1016/j.cej.2012.07.027.

(5) Browning, B.; Sheibat-Othman, N.; Pitault, I.; McKenna, T. F. L. A 2-D Observer to Estimate the Reaction Rate in a Stopped Flow Fixed Bed Reactor for Gas Phase Olefin Polymerization. *AIChE J.* **2014**, *60* (10), 3511–3523. https://doi.org/10.1002/aic.14538.

(6) Gaillard, C.; Despois, J. F.; Mortensen, A. Processing of NaCl Powders of Controlled Size and Shape for the Microstructural Tailoring of Aluminium Foams. *Mater. Sci. Eng. A* **2004**, *374* (1), 250–262. https://doi.org/10.1016/j.msea.2004.03.015.

(7) Soares, J. B. P.; McKenna, T. F. L. Polymerization Kinetics. In *Polyolefin Reaction Engineering*; John Wiley & Sons, Ltd, 2012; pp 131–185. https://doi.org/10.1002/9783527646944.ch5.

(8) Floyd, S.; Choi, K. Y.; Taylor, T. W.; Ray, W. H. Polymerization of Olefins through Heterogeneous Catalysis. III. Polymer Particle Modelling with an Analysis of Intraparticle Heat and Mass Transfer Effects. *J. Appl. Polym. Sci.* **1986**, *32* (1), 2935–2960. https://doi.org/10.1002/app.1986.070320108.

(9) Martinez, O. M.; Pereira Duarte, S. I.; Lemcoff, N. O. Modeling of Fixed Bed Catalytic Reactors. *Comput. Chem. Eng.* **1985**, *9* (5), 535–545. https://doi.org/10.1016/0098-1354(85)80028-4.

(10) Hutchinson, R. A.; Chen, C. M.; Ray, W. H. Polymerization of Olefins through Heterogeneous Catalysis X: Modeling of Particle Growth and Morphology. *J. Appl. Polym. Sci.* **1992**, *44* (8), 1389–1414. https://doi.org/10.1002/app.1992.070440811.

(11) Perego, C.; Peratello, S. Experimental Methods in Catalytic Kinetics. *Catal. Today* **1999**, *52* (2), 133–145. https://doi.org/10.1016/S0920-5861(99)00071-1.

(12) Groppi, G.; Ibashi, W.; Valentini, M.; Forzatti, P. High-Temperature Combustion of CH4 over PdO/Al2O3: Kinetic Measurements in a Structured Annular Reactor. *Chem. Eng. Sci.* **2001**, *56* (3), 831–839. https://doi.org/10.1016/S0009-2509(00)00295-5.

(13) Groppi, G.; Ibashi, W.; Tronconi, E.; Forzatti, P. Structured Reactors for Kinetic Measurements in Catalytic Combustion. *Chem. Eng. J.* **2001**, *82* (1), 57–71. https://doi.org/10.1016/S1385-8947(00)00342-9.

(14) Kunii, D.; Levenspiel, O. *Fluidization Engineering (Series in Chemical Engineering)*; 1991.

(15) Specchia, V.; Baldi, G.; Sicardi, S. Heat Transfer in Packed Bed Reactors with One Phase Flow. *Chem. Eng. Commun.* **1980**, *4* (1–3), 361–380. https://doi.org/10.1080/00986448008935916.

(16) van Antwerpen, W.; du Toit, C. G.; Rousseau, P. G. A Review of Correlations to Model the Packing Structure and Effective Thermal Conductivity in Packed Beds of Mono-Sized Spherical Particles. *Nucl. Eng. Des.* **2010**, *240* (7), 1803–1818. https://doi.org/10.1016/j.nucengdes.2010.03.009.

(17) Floyd, S.; Choi, K. Y.; Taylor, T. W.; Ray, W. H. Polymerization of Olefines through Heterogeneous Catalysis IV. Modeling of Heat and Mass Transfer Resistance in the Polymer Particle Boundary Layer. *J. Appl. Polym. Sci.* **1986**, *31* (7), 2231–2265. https://doi.org/10.1002/app.1986.070310724.

(18) Solve 1-D parabolic and elliptic PDEs - MATLAB pdepe - MathWorks France https://fr.mathworks.com/help/matlab/ref/pdepe.html (accessed Feb 12, 2020).

(19) Bashir, M. A.; Monteil, V.; Boisson, C.; McKenna, T. F. L. Experimental Proof of the Existence of Mass-Transfer Resistance during Early Stages of Ethylene Polymerization with Silica Supported Metallocene/MAO Catalysts. *AIChE J.* **2017**, *63* (10), 4476–4490. https://doi.org/10.1002/aic.15806.
(20) Sheibat-Othman, N. Advanced Strategies for Composition Control in Semi-Continuous Emulsion Polymerisation. phdthesis, Université Claude Bernard - Lyon I, 2000.
(21) Othman, N.; Mckenna, T. F.; Santos, A. M.; Févotte, G. Monitoring of Emulsion Polymerisations: A Study of Reaction Kinetics in the Presence of Secondary Nucleation. *Can. J. Chem. Eng.* **2002**, *80* (1), 88–104. https://doi.org/10.1002/cjce.5450800110.
(22) Gauthier, J.; Bornard, G. Observability for Any u(t) of a Class of Nonlinear Systems. *IEEE Trans. Autom. Control* **1981**, *26* (4), 922–926. https://doi.org/10.1109/TAC.1981.1102743.
(23) Gauthier, J. P.; Hammouri, H.; Othman, S. A Simple Observer for Nonlinear Systems Applications to Bioreactors. 1992.
(24) Soares, M.; Machado, F.; Guimarães, A.; Amaral, M. M.; Pinto, J. C. Real-Time Monitoring and Parameter Estimation of the Emulsion Polymerization of Carboxylated Styrene/Butadiene Latexes. *Polym. Eng. Sci.* **2011**, *51* (10), 1919–1932. https://doi.org/10.1002/pen.22002.
(25) Morris, R. J. Lavoisier and the Caloric Theory. *Br. J. Hist. Sci.* **1972**, *6* (1), 1–38. https://doi.org/10.1017/S000708740001195X.
(26) Guldbæk Karlsen, L.; Villadsen, J. Isothermal Reaction Calorimeters—I. A Literature Review. *Chem. Eng. Sci.* **1987**, *42* (5), 1153–1164. https://doi.org/10.1016/0009-2509(87)80065-9.
(27) Tisse, V. F.; Sheibat-Othman, N.; McKenna, T. F. L. A Lab-Scale Reaction Calorimeter for Olefin Polymerization. *Can. J. Chem. Eng.* **2010**, *88* (5), 783–792. https://doi.org/10.1002/cjce.20336.
(28) KAMMONA, O.; CHATZI, E. G.; KIPARISSIDES, C. Recent Developments in Hardware Sensors For the On-Line Monitoring of Polymerization Reactions. *J. Macromol. Sci. Part C* **1999**, *39* (1), 57–134. https://doi.org/10.1081/MC-100101417.

Chapter 4

Case studies: start-up behavior of supported catalysts in varying compositions of gas phase feed

Chapter 4: Content

1. Introduction 141

2. Impact of support structure on the behavior of classic metallocene catalysts 142
   - 2.1. Experimental Section 142
     - 2.1.1. Materials 142
     - 2.1.2. Polymerization procedure 143
     - 2.1.3. Catalyst synthesis procedure 144
     - 2.1.4. Silica and catalysts characterization 145
   - 2.2. Results and discussion 147
     - 2.2.1. Catalyst kinetics 148
     - 2.2.2. Reaction rates at early stages 150
     - 2.2.3. Polymer properties 151
     - 2.2.4. Particle morphology 152
   - 2.3. Conclusion 156

3. Comparing 2 families of metallocene catalysts at different gas-feed compositions 158
   - 3.1. Experimental Section 158
     - 3.1.1. Materials 158
     - 3.1.2. Polymerization procedures 158
     - 3.1.3. Design of Experiments (DOE) 159
   - 3.2. Variability assessment for catalysts in this study 160
     - 3.2.1. Results 161
     - 3.2.2. Conclusion 162
   - 3.3. Results and discussion 163
     - 3.3.1. Catalyst kinetics 163
     - 3.3.2. Reaction rates at early stages 166
     - 3.3.3. Polymer thermal properties 167
     - 3.3.4. Molecular weight 173
     - 3.3.5. Particle morphology 174
   - 3.4. Conclusion 181

4. Chapter conclusions 183

5. References 185

1. Introduction

As we have seen so far throughout this PhD dissertation, the main goal of the current project was to study the nascent phase of the polymerization under controlled and meaningful conditions representative of industrial scales.

As reviewed in chapter 1, one of the biggest challenges in the phenomena involved in the early stages of the polymerization is the lack of well-adapted apparatus. As previously stated, the principal goal of this project was to design and build a new tool that allows us to study the kinetics and morphology evolution of supported catalysts during gas phase polymerization under experimental conditions that are representative of those used in industrial scales.

In Chapter 2, we described the development of the hardware component of the new improved tool, which we name novel stopped-flow reactor (SF N). In Chapter 3, we described the development of the software component of the new tool that allows us to estimate overall polymerization rates directly from the temperature measurements (and overcome the one-point character of such experiments, which provide no real information on the evolution of the reaction kinetics).

In the current chapter, we will use this new tool to study the behavior of different supported catalysts under varying reaction conditions.

In the first case, we studied the impact of the physical structure of the support material on the catalyst behavior and particle morphology at early stages. For his purpose, we synthesized two metallocene catalysts using silica supports of different pore diameters and evaluated their behavior in terms of kinetics and morphology evolution.

On the second case study, we aimed to understand the impact of different components of the gas feed on the catalyst kinetics and polymer morphology for two different families of metallocene catalysts. For this, we followed a design of experiments to compare compare two families of metallocene catalysts, from which one classic metallocene and one commercial CGC catalyst in terms of their kinetics and polymer properties.

2. Impact of support structure on the behavior of classic metallocene catalysts

As discussed in the literature review in chapter 1, the physical structure of the support has a direct impact on the catalyst behavior, mainly in regards to the fragmentation of the polymerizing particles. Physical properties such as particle size and porosity play a significant role in the catalyst activity and quality of the obtained polymer.

In regards to particle size, it was observed in the works of Tisse et al.[1,2] that smaller silica particles led to higher catalyst activities than those observed for larger particles, for MAO activated metallocene catalysts. The same observation was made by Bashir et al., who attributed this phenomenon to higher mass transfer resistances encountered in bigger particles at early stages. [3,4]

In regards to the porosity of the support, Bashir observed faster catalyst activation in silica with smaller pores, which he attributed to faster particle fragmentation due to stress build-up in the porosity of the support. [3] On the other hand, the opposite effect was observed in the works of Tisse [5] (using silica supports) and Kumkaew et al. [6] (using molecular sieves). As we can see, the effect of the support porosity on the catalyst behavior is still unclear amongst the available sources in literature.

In the current section, we aimed to assess the impact of the support porosity on the catalyst kinetic behavior and morphology of the produced polymer. For this matter, the current study was performed using metallocene catalysts synthesized in our lab, using silica supports of different pore diameters, but very similar particle diameters (in order to control the effect of particle size) and pore volumes.

2.1. Experimental Section

The materials used in the current study, as well as full-time and short-time polymerization procedures are described below.

The full-time and short-time experiments presented in this case study, as well as the catalysts synthesis and material characterizations, were performed in collaboration with Bs. Felipe Morais Bolner, as part of his MSc research project performed under my direction.

2.1.1. *Materials*

The catalysts used in this study were synthesized using silica supports provided by AGC Si-Tech Company Ldt. The physical properties of the two silicas used in this study are described in Table 1, with analysis done via nitrogen porosimetry and Thermogravimetry Differencial Thermal Analysis (TG-DTA) by the provider.

Rac-ethylenebis(4,5,6,7-tetrahydro-1-indenyl)zirconium dichloride (THI) from by Strem Chemicals Inc was used used for catalyst synthesis.

MAO solution by Grace Davidson in 29.4 %wt of toluene with the following characteristics: 13.3 %wt Al, 4.94 %wt TMA was used as co-catalyst.

Triisobutylaluminum (TIBA) purchased from Witco GmbH was used as scavenger in a 1 M solution in dry heptane.

Ethylene with 99.95% purity purchased from Air Liquide – France was used as monomer gas throughout this study. The gas was purified by flowing through tree purification columns. The first was filled with reduced BASF R3-16 catalyst (CuO supported on alumina), the second with molecular sieves (13X, 3A, Sigma-Aldrich), and finally a column of Selexsorb COS (Alcoa). For short-time reactions with the novel stopped-flow reactor, a cartridge filled with 10 g of Alumina grafted with TEA was added in the feed line as an additional purification measure for ethylene. The procedure for the preparation of the grafted Alumina is described in Appendix 1.

Nitrogen gas with 99.999% purity purchased from Air Liquide France was used as inert gas in the short-time polymerization reactions for plugging in the reactors, purging the set-up and pressurizing the reactor before polymerization.

Carbon dioxide with 99.995% purity purchased from Air Liquide France was used as quenching agent for the short-time polymerization reactions.

Silica code	Silica trade name	Specific superficial area (m^2/g)	Pore volume (mL/g)	Pore diameter (nm)	Mean particle size (µm)	TG-DTA (%) Loss on Drying (180 °C)	TG-DTA (%) Loss on Ignition (850 °C)
S2	AGC SUNSPERA® DM-H-302	618	1,7	11	37	4,9	9,7
S4	AGC SUNSPERA® DM-L-403	363	2.11	23.3	42.7	3.7	7.1

Tableau 1: Silica physical properties, given by the provider

2.1.2. *Polymerization procedure*

The experimental conditions applied for the metallocene catalysts used in this section are described below.

Full-time polymerization

Full-time polymerization reactions of 60 minutes duration were carried out in a spherical 2.5L lab-scale semi-batch reactor, also referred to as Turbosphere reactor. Details on the reactor set-up and operation procedure were described in Chapter 2 (Ch. 2, section 2.1.1.).

For the metallocene catalyst used in this study (C06 and C25), 25-40 mg catalyst were dispersed in approximately 100 g of coarse NaCl (previously dried at 400 °C for 4 hours. 1.4 mL of a 1 M solution of Triisobutylaluminum (TIBA) were used as scavenger for the reactor environment.

Reactions were performed in homopolymerization with Ethylene under constant pressure of 11 barg, reaction temperature of 75°C and constant agitation at 200 rpm. The experiments of 60 minutes duration were repeated at least twice in order to confirm reproducibility of results.

Short-time polymerization

Short-time polymerization reactions were carried out with the novel Stopped-flow reactor (SF N). Details on the reactor set-up and operation procedure were described in Chapter 2 (Ch. 2, section 5.3.2.).

For the catalysts used in this study 25-35 mg catalyst were dispersed in approximately 1200 mg fine NaCl seedbed (preparation of seedbed described elsewhere).[7,8]

The reaction temperature was set to 75 °C. Polymerizations were carried out in reaction times of 15 to 90 seconds under ethylene flow of 986 g/h and 11 barg pressure, keeping a superficial gas velocity of 20 cm/s.

2.1.3. *Catalyst synthesis procedure*

Two-step incipient wetness method was used to prepare the catalysts used in this study. The two-step method was selected as a way to avoid possible catalyst deactivation by interaction with the functional groups on the silica surface.

Initially, each silica was dehydroxylated at 600°C under dynamic vacuum of 10^{-3} to 10^{-5} mbar. The silica was heated to 200 °C at a heating rate of 5 °C/min and left open for 2 hours to remove moisture, followed by overnight dehydroxylation at 600 °C under vacuum.

The initial step consisted of the passivation of MAO onto the silica support, resulting in a solid hereafter referred to as SMAO. For the SMAO preparation, a volume of 3.5 mL of MAO solution (aiming for 13 wt% Al in the final catalyst) was diluted in 150 % of the pore volume of each silica in pure dry toluene and added dropwise to 2 g of silica in a Schlenk flask inside of an Argon-atmosphere glovebox. The resulting slurry was heated at 80 °C for 4 hours under argon atmosphere without stirring. Afterwards, we performed one washing step with Heptane. The supernatant solution over the slurry was removed with a syringe and the same volume of dry Heptane was added, followed by gently stirring by hand. After decantation, the supernatant Heptane was removed with a syringe and the slurry was dried under dynamic vacuum at 80 °C for 2 hours. The resulting free-flowing white powder, hereafter called SMAO, was stored in the glovebox.

Next, the metallocene complex was impregnated dropwise onto the SMAO support. For the catalyst preparation, rac-ethylene bis(4,5,6,7-tetrahydro-1-indenyl)zirconium dichloride, hereafter referred to as THI, was grafted onto the surface of SMAO targeting an Al/Zr ratio of 150. For 500 mg SMAO, 9.3 mg of THI were dissolved in 1.7 mL of pure dry toluene in a glass vial under magnetic stirring for 1 hour, forming a white cloudy solution. Following, in a Schlenk flask, the THI/Toluene solution was added dropwise onto 500 mg of SMAO, resulting in a yellow slurry. The slurry was heated at 50 °C for 1 hour under argon atmosphere with no stirring. One washing step was performed with Heptane and the slurry was dried under vacuum at 50 °C for 2 hours. The resulting supported catalyst was a free-flowing yellow powder, which was stocked inside of a glovebox away from light exposure.

The THI metallocene catalyst was selected since transfer to monomer is not its main chain termination mechanism. Therefore, variations of the monomer pressure during the reaction should reflect on to the molar mass of the obtained polymer.[3]

To facilitate referencing, the names of the silica supports used in this study were abbreviated, as described in Table 2. Catalysts C14 and C25 are two different batches of the same catalyst.

Catalyst ID#	Silica abbreviation code	Silica trade name
C06	S2	AGC SUNSPERA® DM-L-303
C14	S4	AGC SUNSPERA® DM-L-403
C25	S4	AGC SUNSPERA® DM-L-403

Tableau 2: Synthesized catalysts and their corresponding silica supports. C14 and C25 two of the same catalyst

2.1.4. *Silica and catalysts characterization*

The analytical techniques used to characterize the silica, SMAO and catalysts synthesized in this study are described as follows. More details on the used analytical techniques can be found in the Appendix 1.

The dehydroxylated silica, SMAO and catalysts were characterized by Diffuse Reflectance Fourier Transform Infrared Spectroscopy (FT-IR-DRIFT) to follow their surface composition. As seen in Figure 1, the silica dehydroxylated at 600°C contains essentially isolated silanol groups on its surface, characterized by a sharp peak at around 3745 cm^{-1}. As seen in the SMAO profiles, the silanol groups are no longer visible, signaling effective grafting of MAO, which is characterized by the C-H stretching in the region of 3000 to 2840 cm^{-1}. [9–12]

The dehydroxylated silica and catalysts were evaluated with nitrogen porosimetry to measure the porosity of the samples. Specific surface areas were obtained from the Brunauer-Emmett-Teller (BET) and pore size distribution was determined by Barrett-Joyner-Halenda (BJH) equation. Figure 2 shows the obtained pore sizes for the silica supports dehydroxylated at 600 °C (S2 600 and S4 600), together with the corresponding catalysts (C06 and C25). We observed a shift to the left in the pore size profile of the catalysts in relation to their silica supports, indicating reduction of the average pore diameters. This, which was also observed for other types of silica by Bashir [3], suggests that the porosity of the supports was partially occupied during the grafting process, most likely by the bulky MAO molecules.

The aluminum and zirconium mass content in the catalysts was measured by Inductively Coupled Plasma-Atomic Emission Spectroscopy (ICP-AES) analysis, performed by the Mikroanalytisches Labor Pascher, in Remagen-Bandorf, Germany. As seen in Table 3, the synthesized catalysts C06 and C25 possess Al/Zr ratios slightly superior to the aim of 150. On the other hand, catalyst C14 possess Al/Zr ratio slightly lower than aimed. Nonetheless, we these results confirm the successful incorporation of the necessary active species.

The synthesized catalysts were observed with SEM and SEM-EDX analysis. As observed in Figure 3, the SEM images show catalyst particles are spherical and the particle size seems quite uniform. This suggests the impregnation method employed during preparation was efficient in preserving the original morphology of the silica supports.

The SEM-EDX analysis results show the distribution of Aluminum (orange) and Silicon (green) inside the catalyst particles. The Aluminum atoms, originated from the grafting with MAO, indicate uniformity of the catalyst impregnation/activation procedure throughout the catalyst.

As observed in Figure 4, particles of catalyst C06 presented a uniform Aluminum distribution on the majority of particles, with few particles showing core-shell Aluminum distribution. For catalyst C25, seen in Figure 5, Aluminum seems to be uniformly distributed throughout the totality of the particles. These results suggest that the impregnation of the support with MAO molecules was more effective for the silica support of bigger pore sizes (catalyst C25) than for small pore sizes (catalyst C06). Nonetheless, given that the surface cuts for the EDX analysis are subjected to variability, it is possible that particles of the same sample are not cut in exactly the same way. Therefore, it is not unusual to observe different Al distributions within the same sample.

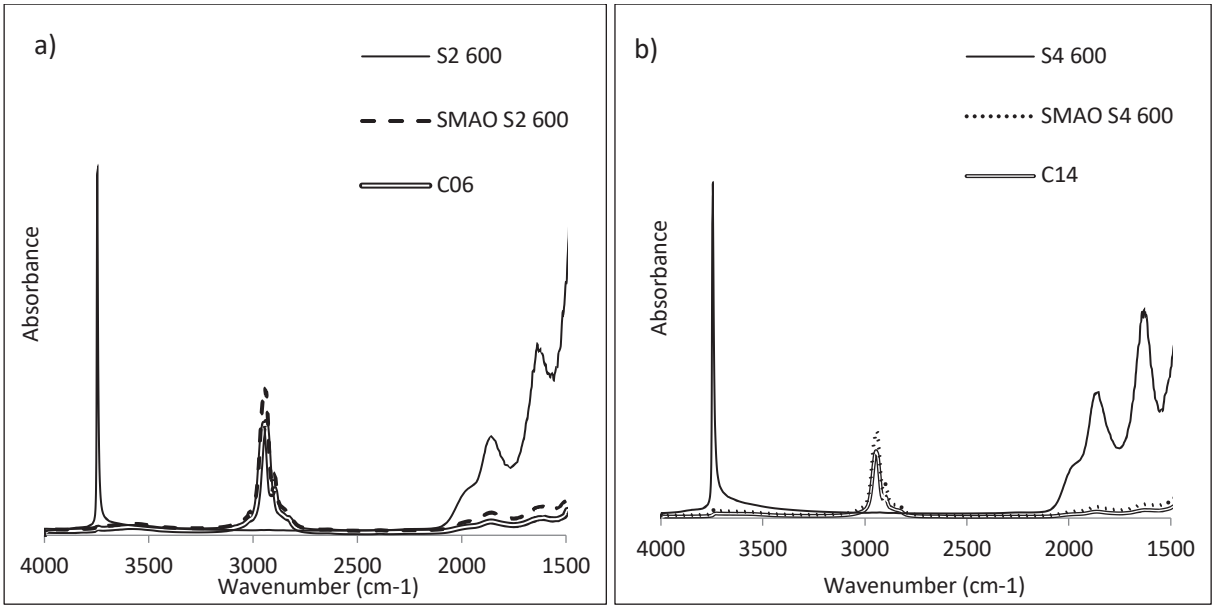

Figure 1: DRIFT analysis for dehydroxylated silica, corresponding SMAO and supported catalysts

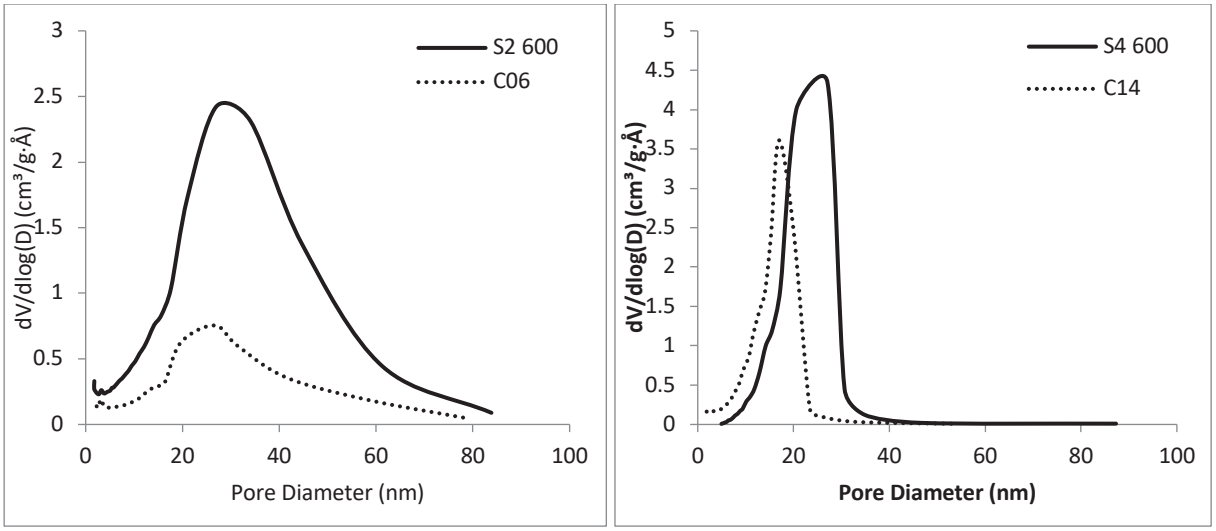

Figure 2: Pore diameter distributions for dehydroxylated silicas and their corresponding supported catalysts

Catalyst ID#	Respective silica	Al (wt%)	Zr (wt%)	Al (mol%)	Zr (mol%)	Al/Zr
C06	S2 600	15.1	0.26	0.5597	0.0029	196.37
C14	S4 600	14.5	0.40	0.5374	0.0044	122.57
C25	S4 600	16.9	0.26	0.6264	0.0029	219.78

Tableau 3: ICP analysis results for the synthesized catalysts

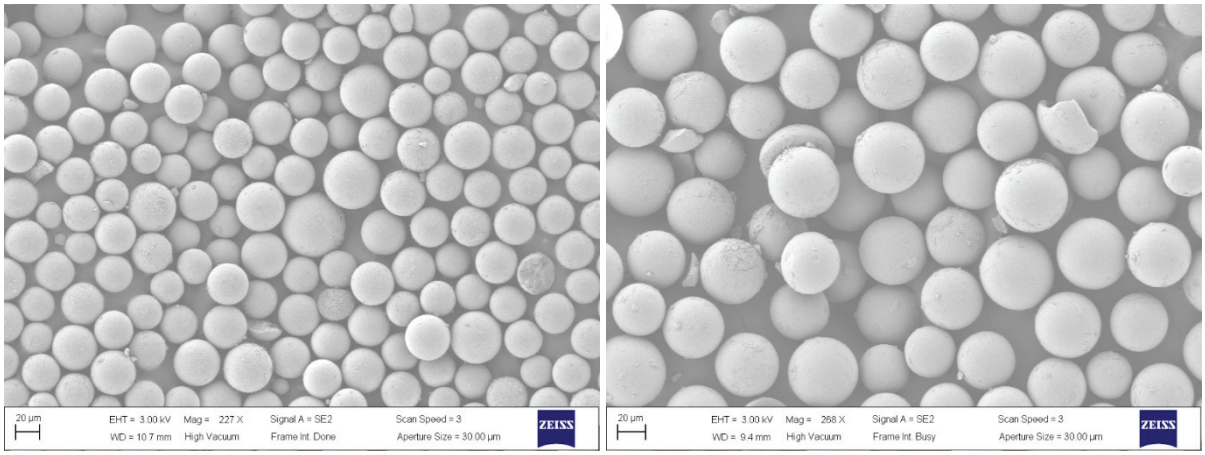

Figure 3: SEM imaging for catalysts a) C06 (11 nm support), b) C25 (23.3 nm support)

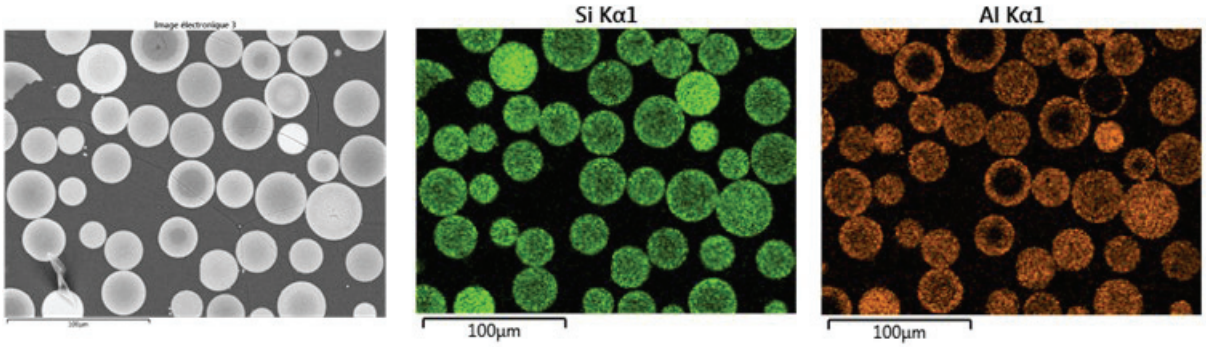

Figure 4: SEM-EDX for catalyst C06 (support with 11 nm pore diameter)

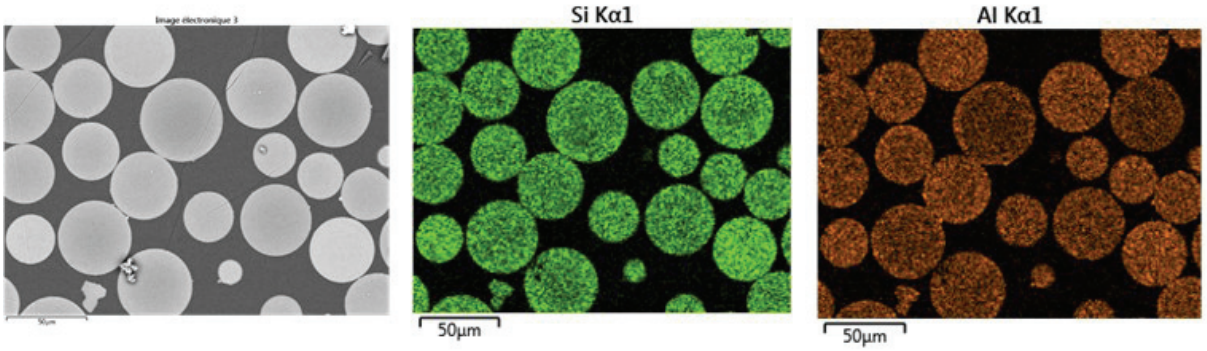

Figure 5: SEM-EDX for catalyst C25 (support with 23.3 nm pore diameter)

2.2. Results and discussion

The impact of the pore size of the support on the kinetic behavior of the catalysts was evaluated through full-time and short-time polymerization reactions with ethylene. The produced polymers were evaluated in terms of their physical properties by thermal analysis (DSC) and particle morphology by SEM and SEM-EDX microscopy. At last, the experimental data from short-time experiments were evaluated with the developed software component developed in chapter 3.

From the different characterization techniques assessed in the previous section, we have concluded that the 2-step synthesis method employed during catalyst preparation was satisfactory in impregnating the desired active species (Al and Zr).

As indicated by the SEM-EDX analysis performed on surface cuttings of the catalysts, the silica support with larger pore diameters (23.3 nm) led to catalyst particles with homogeneous distribution of aluminum on the totality of the support (catalyst C25). On the other hand, this analysis indicated that, for smaller pore diameters (11 nm), a portion of the resulting catalysts presented core-shell distribution of aluminum, grafted mainly on the outer surface of the support particle (catalyst C06).

2.2.1. *Catalyst kinetics*

The activity profiles obtained from full-time polymerizations with ethylene are found in Figure 6.

The catalysts made from different silica supports showed different activity profiles. The sharp peak observed for the catalyst made with bigger pore diameters (pores of 23.3 nm, catalyst C14) indicated fast catalyst activation followed by its quick deactivation. This behavior could be explained if we assume that larger pores led to less initial mass transfer resistance and thus rapid polymer formation. The pores might rapidly be blocked by the new polymer leading to a decrease in the rate.

A different behavior was observed for the catalyst made with smaller pore diameters (pores of 11 nm, catalyst C06). The activity profile showed slower and gradual catalyst activation (in relation to C25), the absence of sharp activation / deactivation peaks and overall low polymerization rates. Considering the SEM-EDX analysis performed on this catalyst, the observed core-shell distribution of aluminum throughout the catalyst would certainly lead to parts of the particle that had no active sites (if the catalyst precursor is not activated by MAO it will exhibit very poor activity). This could certainly explain the low reaction rates observed.

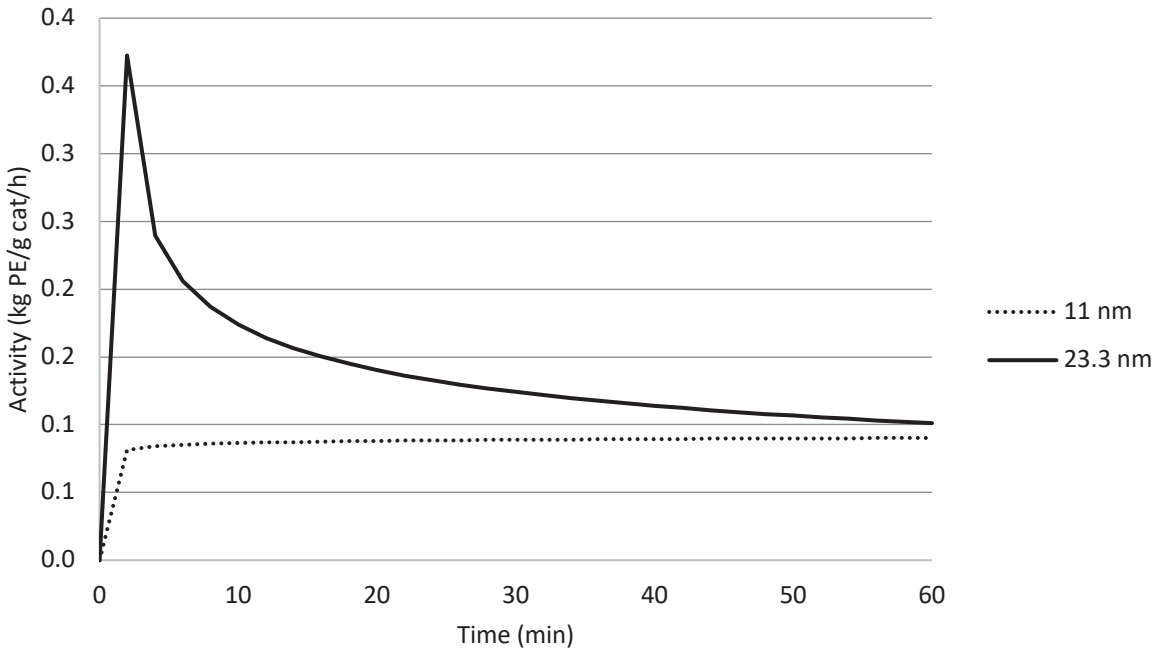

Figure 13: Full-time polymerization kinetics for support of 11 nm (catalyst C06) and 23.3 nm (catalyst C14)

The outlet temperature profiles for short-time polymerization reactions performed with the studied catalysts between 15 and 90 seconds can be seen in Figures 7 and 8.

Similar conclusions can be drawn from the polymerization tests done at short reaction times as those observed at longer reaction times.

For the silica support with bigger pores (Figure 7), high temperature gradients were observed at the reaction start-up, with considerable increase from 15 seconds of reaction. This behavior was reproduced in both the 15 s and the 90 s reactions. The evolution of the polymerization yield, shown in Figure 9, followed the same trend with much higher yields observed for the catalyst prepared on bigger pores.

Likewise, very mild temperature gradients were observed for the silica support with smaller pores (Figure 8). This behavior, together with the yields observed in Figure 9, are in agreement with the kinetic observations for the full-time polymerization kinetics.

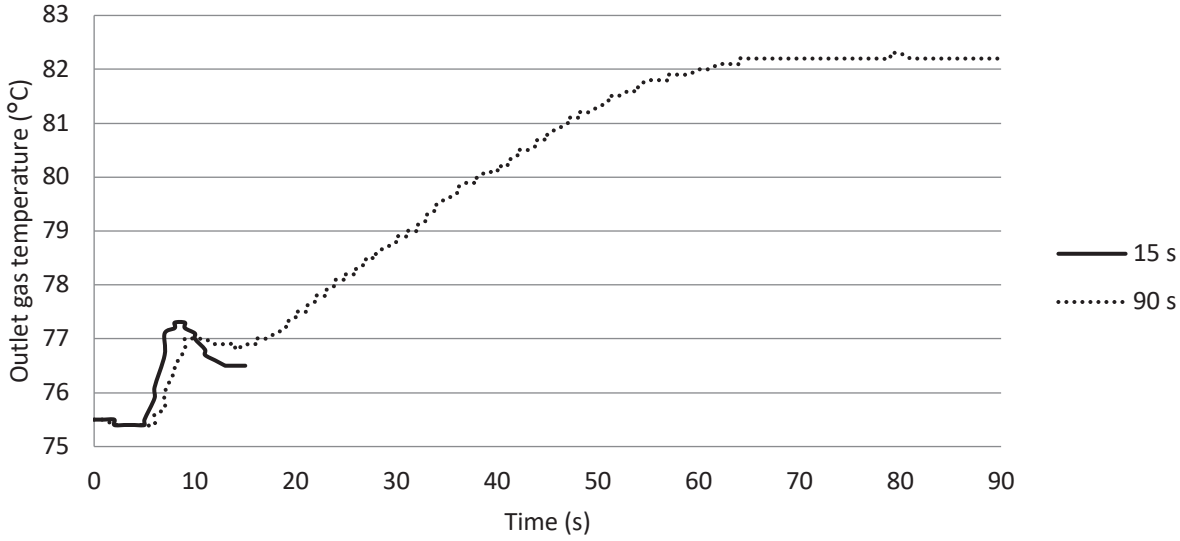

Figure 7: Temperature profiles with 23.3 nm support (catalyst C25)

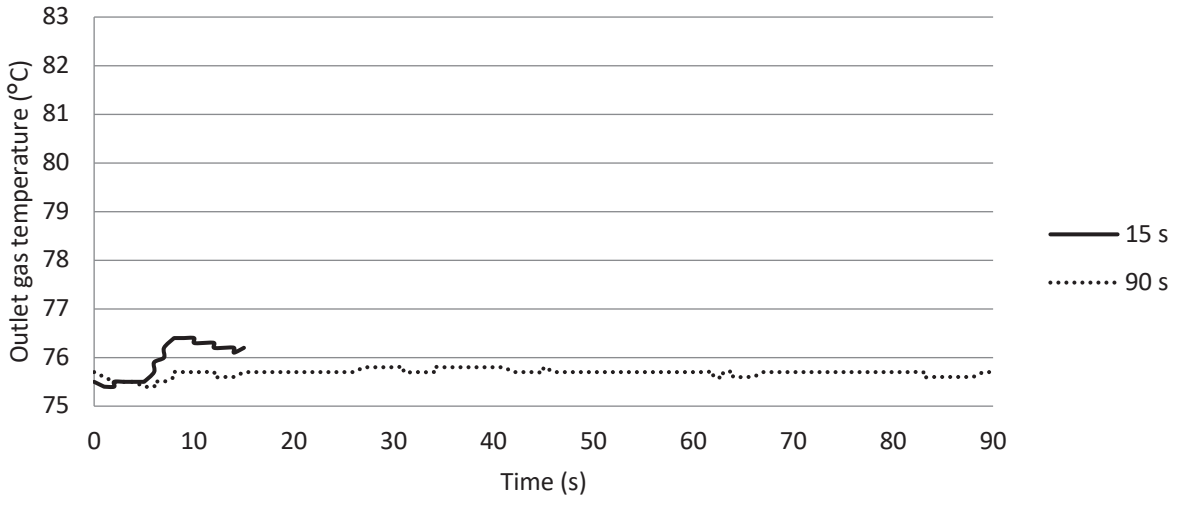

Figure 8: Temperature profiles with 11 nm support (catalyst C06)

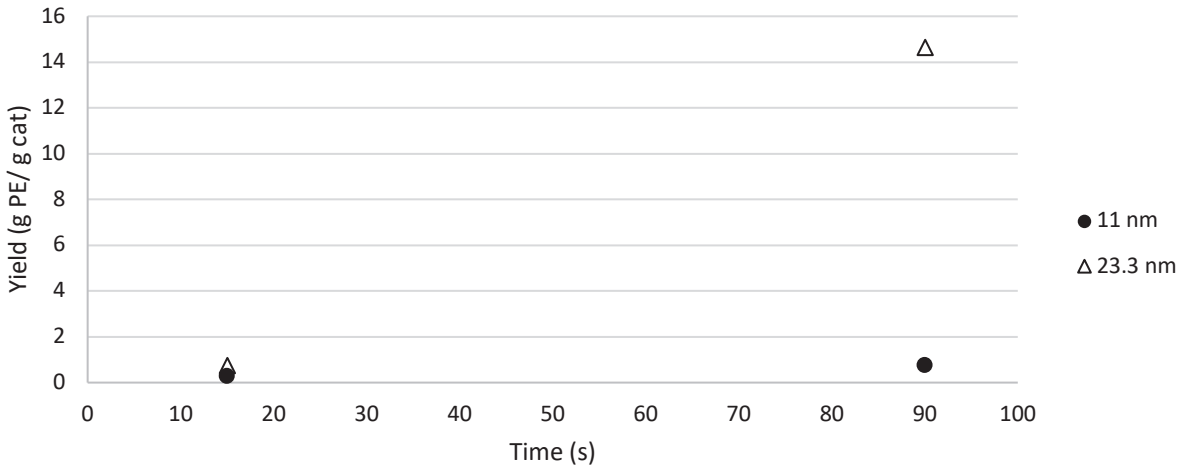

Figure 9: Polymerization yields at increasing reaction times for catalysts C06 (11 nm) and C25 (23.3 nm)

2.2.2. *Reaction rates at early stages*

Here, we have applied the previously developed software (reactor model and estimator) to interpret the catalyst kinetics at short reaction times.

From the experimental data (recorded temperatures and polymer yields), we have estimated the dynamic rates of polymerization, seen in the Figure 10.

The estimated reaction rates for both catalysts are coherent with those observed in the assessment of full-time polymerization kinetics, shown in Figure 6. The obtained results show the contrast the activity of catalysts prepared with different silica supports. At the beginning of the reaction, the catalyst with bigger pore sized (23.3 nm, C25) presents reaction rates that are about 10 times higher than for the catalyst with smaller pores (11 nm, C06). At longer reaction times (Figure 6), this is precisely what we observed for these catalysts; initial activity profiles that are very distinct and then reach a similar plateau as the reaction progresses.

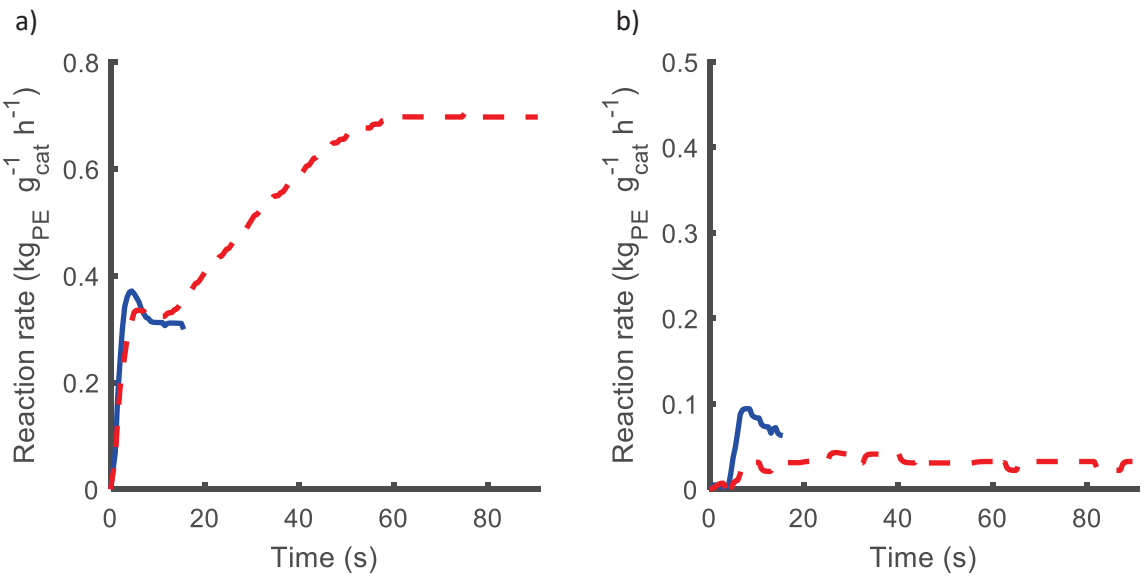

Figure 10: Estimated reaction rates for: a) C25 (23.3 nm support), b) C06 (11 nm support) estimated values for: a) reaction rates, b) polymer mass production + exp. Values

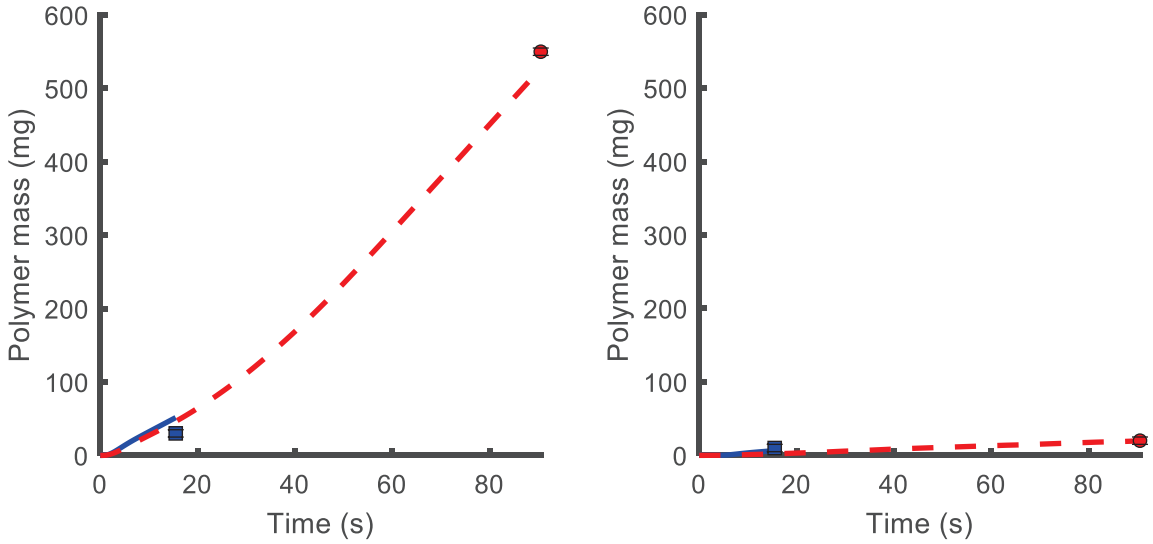

Figure 11: Estimated polymer production and experimental values for a) C25 (23.3 nm support, b) Catalyst C06 (11 nm support)

2.2.3. *Polymer properties*

The properties of the obtained homopolymers for full-time (60 minutes) and short-time (15 to 90 seconds) polymerization reactions were evaluated in terms of thermal properties of the produced polymer. Moreover, we followed the average molecular weights for polymer produced in full-time coditions.

As seen in table 4, the polymer crystallinities increase with the time of reaction for both catalysts, as previously observed by Tioni et al. and Di Martino et al.[13,14] We observed no effect of the support porosity on the polymer thermal properties and average MW at full-time polymerization reactions (60

minutes). This suggests that the active sites on each support produced the same polymer (in other words, the nature of the active sites was not compromised by using one support or the other). If this is the case, this appears to be more evidence that the lower polymerization rate observed (per gram of support) with C06 is due to a diminished quantity of "active" active sites per particle because. The obtained Polydispersity Index were slightly higher for the silica with smaller pores (catalyst C06), but this can just as easily be attributed to variations in the SEC measurements as anything else.

The crystallinity for the silica support with bigger pores -23.3 nm, catalysts C14 and C25) at 90s reaction approached values obtained for full-time polymerization conditions. This behavior is coherent with the kinetic behavior observed for this catalyst at full-time polymerization profiles (high polymerization rates observed at the reaction start), as well as the high temperature gradients observed at short-time reactions and estimated reaction rates.

For reactions lasting less than 90 seconds for catalyst C25, the low crystallinity values obtained reflect the amorphous character of the polymer at early stages, perhaps not yet free from the constraint of the support, as previously observed in works of Tioni et al.[13]

We observed low crystallinities for the polymers obtained at short reaction times with the silica of smaller pore diameters (11 nm, catalyst C06). Given the low polymerization rates and slow activation observed for this catalyst, this could be explained by a high content of solid support, which could lower the measured crystallinities.

Pore diameter (nm)	Silica name	Catalyst ID#	Reaction duration	Yield (gPE/gcata)	Tm (°C)	Crystallinity %	MW (Dalton)	PDI
23.3	DM-L-403	C25	15s	0,74	128,5	29,8	-	-
		C25	90s	14,65	127,4	53,4	-	-
		C14	60 min	117,95	131,7	63,6	102 173	3,283
11	DM-H-302	C06	15s	0,29	125,1	12,4	-	-
			90s	0,76	130,4	18	-	-
			60 min	79,82	132,4	61,76	100 333	4,639

Tableau 4: Polymerization yields and polymer properties for polymers made with catalysts C14 and C25.

2.2.4. *Particle morphology*

The particle morphology of the homopolymers obtained in short reaction times (15 to 90 seconds) were evaluated using SEM and SEM-EDX .

For the SEM-EDX analysis, we have chosen to display the element detection charts for Silicon (green) (silica support) and Carbon (red), aiming to correlate changes in the silica support (Silicon) with the polymer formation (Carbon). Given the analysis were prepared with a carbon metallization, the red contrasts are subtle, but one can follow the progressive polymer formation on the support.

The impact of the different kinetics can be observed in the SEM images for both studied catalysts.

In Figure 12, the SEM images for polymers obtained with silica with higher pore sizes (23.3 nm, catalyst C25) showed a more pronounced degree of fracture as early as 15 seconds of reaction, due to the hydraulic stress caused by polymer accumulation at the high initial rates, in relation to smaller pores (catalyst C06). After 90 seconds, it appears that at least some of the C25-based particles are expanding with the inert silica layer being carried by the polymer made in the center of the particles. Moreover, we observed noticeable particle growth and widespread irregularity in the overall morphology. We could suggest that the high polymerization rates observed at the beginning of the reaction led to heat transfer resistances that could have resulted in polymer softening. Another interesting feature seen in these short time SEM images is that not all of the particles polymerize at the same rate.

SEM-EDX analysis results seen in Figure 13 show a well-defined portion of the support that is separated from the core. This behavior is not observed at 90 s of reaction. The SEM and EDX images suggest that the catalyst surface is inactive, but not the core.

These observations are in agreement with the kinetic behavior of this catalyst discussed in the previous section, with the larger silica pores catalyst (C25) having higher activities than the catalyst from silica with smaller pores (C06) at short reaction times.

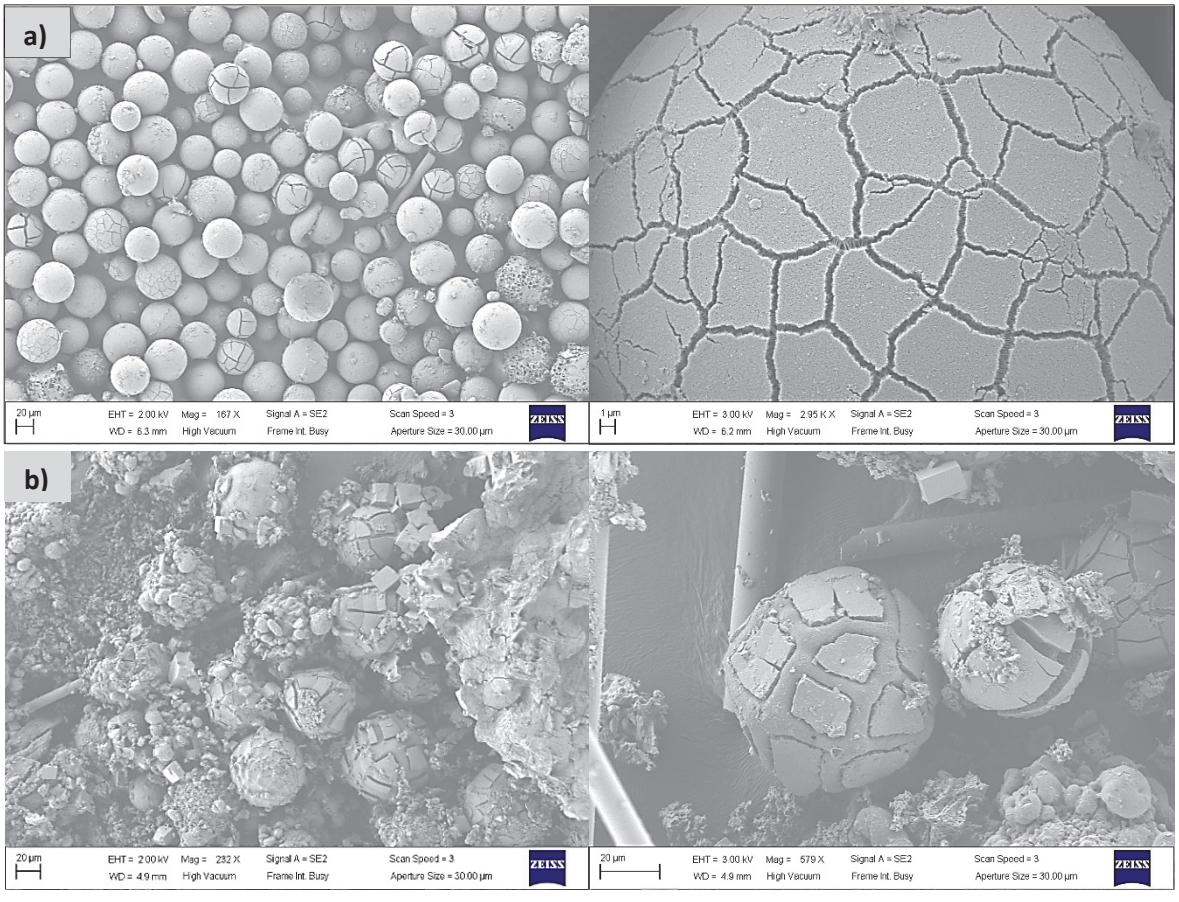

Figure 12: SEM analysis of polymers done with catalyst C25 at: a) 15s, b) 90s

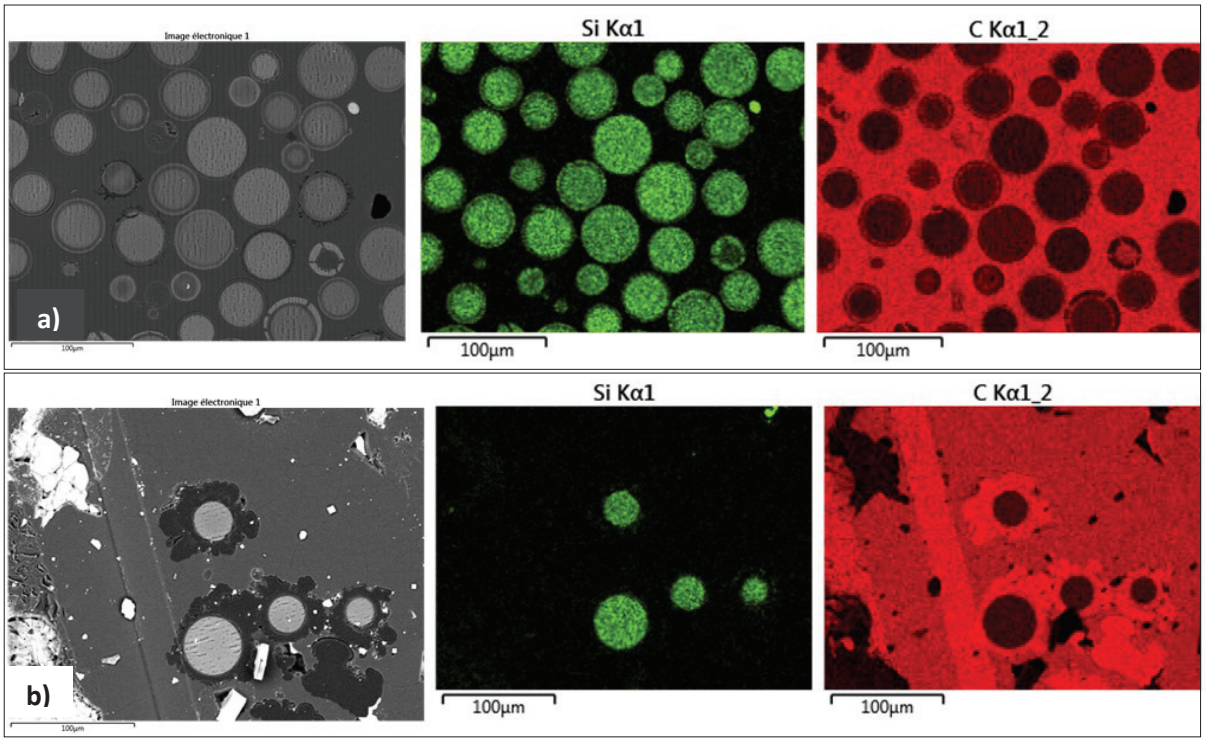

Figure 13: SEM-EDX for polymers formed with catalyst C25 at: a) 15s, b) 90s.

In the SEM images for catalyst C06 (smaller silica pore volume), in Figure 14, we observed no visible fracturing on the particle surface at 15 seconds of reaction. At 90 seconds of polymerization, some whole (possibly unreacted) particles are present, but the polymer formation and particle growth become more pronounced. Nonetheless, a smooth morphology is kept and no polymer melting was observed.

SEM-EDX analysis results seen in Figure 15 allowed similar observations. At 15 seconds, the polyethylene formation is very subtle, seen only at the center of the larger particles. After 90 seconds, a layer-by-layer polymerization mechanism can be observed, as a sheet of support is separated from its core and a layer of polymer (red) can be seen in the corresponding image. These observations are in agreement with the kinetic behavior of this catalyst discussed in the previous section, the overall low activities achieved with this catalyst, as well as the core-shell aluminum distribution observed for this catalyst.

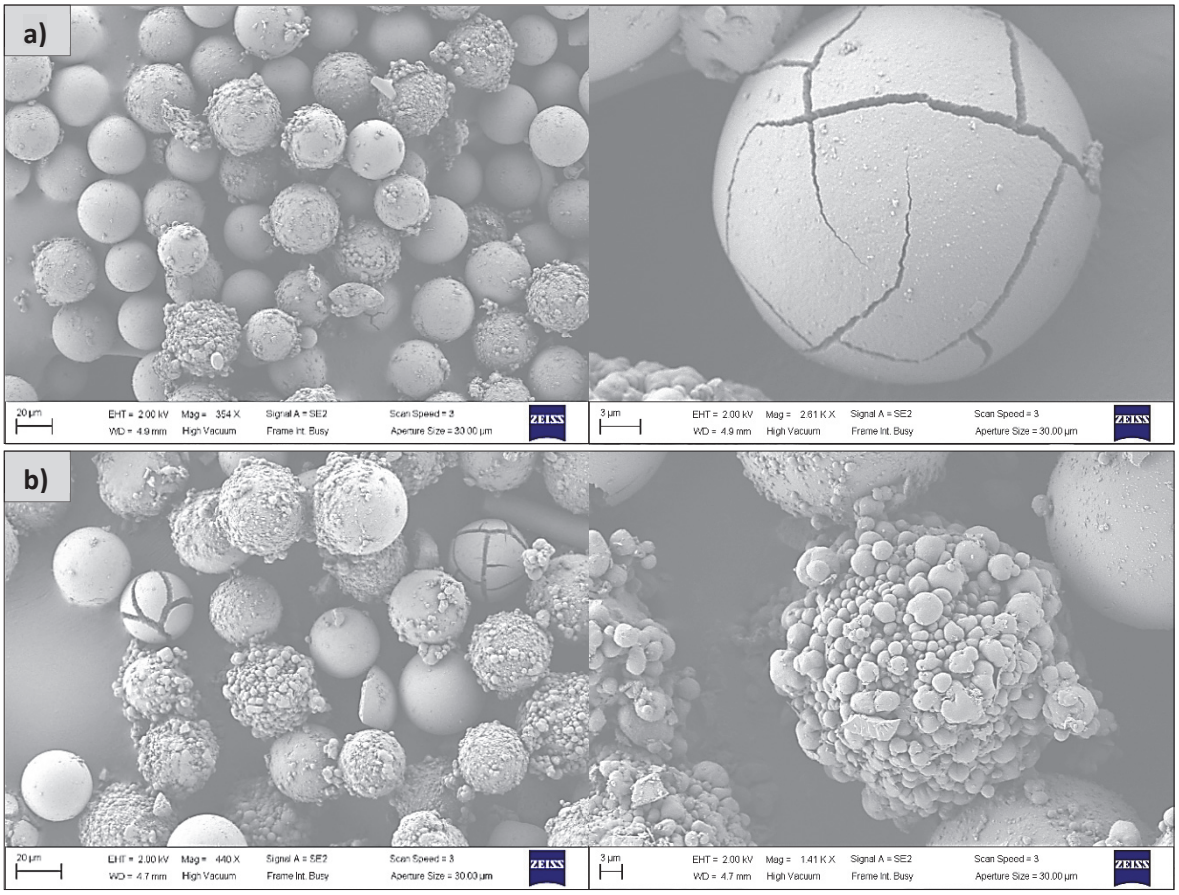

Figure 14: SEM analysis of polymers done with catalyst C06 at: a) 15s, b) 90s

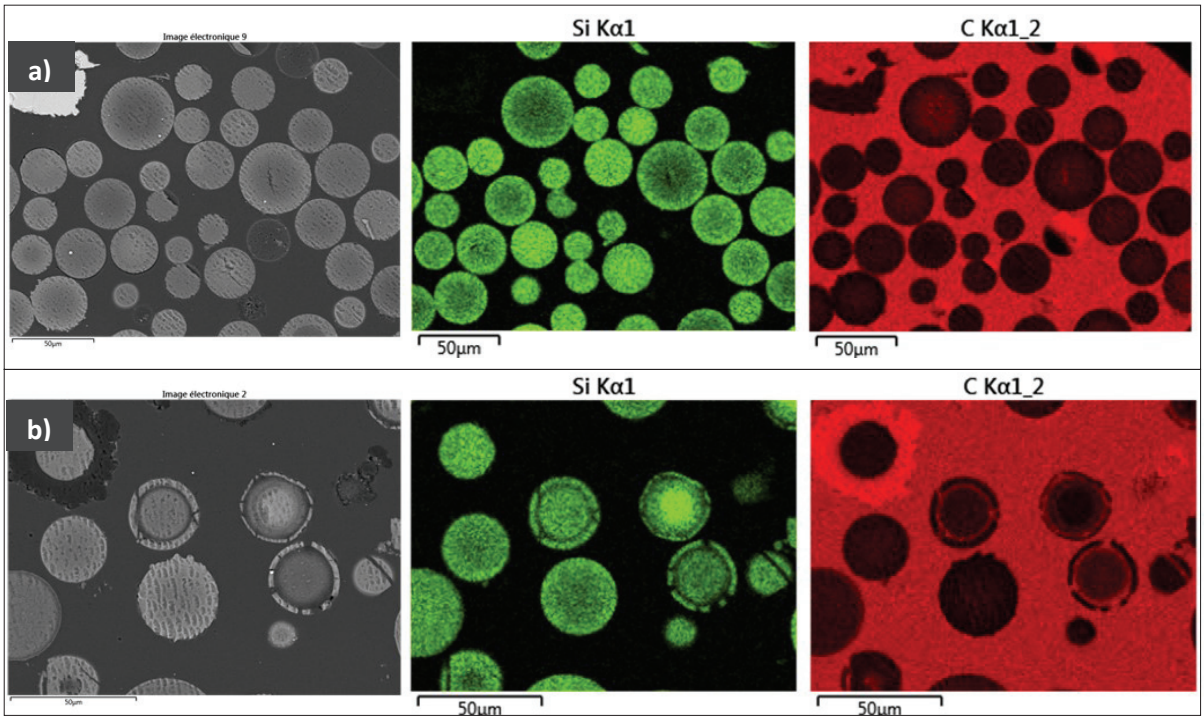

Figure 15: SEM-EDX for polymers formed with catalyst C06 at: a) 15s, b) 90s.

2.3. Conclusion

Classic metallocene catalysts were synthesized with different silica supports, aiming to evaluate their impact on the catalyst behavior at early stages. Results from the analytical techniques showed that the method employed for catalyst preparation was effective in incorporating the desired aluminum and zirconium amounts while maintaining the original structure of the silica supports.

SEM-EDX analysis performed on the synthesized catalysts indicated homogeneous distribution of aluminum atoms throughout the support particles for silica with larger pore sizes (23.3 nm). For the support with smaller pore sizes (11 nm), this analysis showed core-shell distribution of aluminum on a portion of the observed particles. Nevertheless, the surface cuts performed for the EDX analysis are done by hand and not all particles are necessarily cut in the same way. Some slices go through the middle of the particles (or at the equator), and some cuts might happen closer to the poles. In that sense, it is natural to see different aluminum distributions for the same catalyst. Considering the non-negligible possibility of mass transfer resistances to the bulky MAO molecule (reported values between 7.5 and 12.5 Å)[15–17], then the molecule does not penetrate into the heart of the catalyst particles, but only a certain distance toward the center.

From the kinetic assessment at full-time polymerization reactions with ethylene, bigger pores seemed to lead to a much higher initial polymerization rate, followed by quick deactivation; while smaller pores led to gradual activation. We linked the observed behaviors to the rapidity of particle fragmentation during the reaction. We hypothesized bigger pores (shown to have more homogeneous Al distribution) led to the catalyst particle being more homogeneously activated, which led to faster particle fragmentation due to quick polymer build-up in the porosity of the support. On the other hand, smaller pores (shown to have core-shell Al distribution) could have resulted in activation on the catalyst surface, leading to lower reaction rates, thus slower particle growth. The estimated reaction rates were in agreement with the observed kinetics at longer times and reflected the same trend, activities for the catalyst with bigger pores was about 10 times higher than the counterpart at early stages of the reaction ($\leq$90s).

From the assessment of the polymer properties, the support porosity seemed to have no significant effect on the polymer thermal properties and average MW at full-time polymerization reactions (60 minutes), suggesting that the active sites in both catalysts are similar, so any observed differences are more likely of a physical nature. For short-time reactions, the polymer crystallinities seemed to increase, which we linked to the constraint effect of the support porosity, a phenomena observed in a previous study from our group. [13]

Evaluations at short reaction times from 15 to 90 seconds, performed with the novel stopped-flow reactor, indicated a similar behavior. High temperature gradients were observed at early stages for silica with bigger pores, while very mild gradients were observed for the smaller pores. The observed kinetic effects were reflected on the morphology of the polymer particles obtained at short reaction times.

Morphology observations by SEM, coupled with the fact that the EDX images all show a well-defined layer of support separated from the core, the surface of the catalyst particles is inactive (a behavior previously observed by Tisse [5]), but behaves normally below the surface. We still cannot underlie the the reasons for this behavior. After 90 seconds of reaction, it seems like some particles are expanding

with silica fragments being carried by the polymer being formed at the particle center. The higher level of fractures observed on the particle surface suggest faster particle fragmentation. [18] Moreover, we observed a noticeable loss of control of the particle morphology after 90 seconds, which we correlated with possible heat transfer resistances. For silica with smaller pores, we observed less flagrant fracturation on the particle surface and no particle agglomeration, which were in agreement with the low reaction rates observed for this catalyst. In all cases, the microscopy analysis showed different article morphologies for the same sample, which suggest that not all of the particles polymerize at the same rate. Given the aforementioned conclusions, the assessed silica supports are perhaps not suited for utilization in polyolefin applications.

To conclude, this case study demonstrated how the novel stopped-flow reactor can satisfactorily be used to provide information on the morphology development at early reaction times under meaningful reaction conditions.

3. Comparing 2 families of metallocene catalysts at different gas-feed compositions

Given the complex nature of supported catalysts and polymerization processes, it is often challenging to determine the impact of each reaction condition parameter, as well as possible interaction between these parameters, on the reaction behavior and quality of the obtained polymer. In such cases, experimental design can provide some useful insights. Besides allowing to reduce the number of experimental runs necessary for such evaluations.

In the current case study, we have applied a Design of Experiments (DOE) to assess the impact of different reaction conditions (i.e. reaction time, hydrogen content and comonomer content) on the kinetic behavior and polymer morphology for two families of metallocene catalysts.

3.1. Experimental Section

The current case study was performed with two different catalysts, one classic Zirconocene catalyst, hereafter referred to as **CpZ 2**, and one constrained geometry catalyst, hereafter referred to as **CGC M**. These catalysts were evaluated under varying reaction times and compositions of the gas phase feed, which were followed according to an Experimental Design.

The materials used in the current study, procedures for full-time and short-time polymerization, as well as the description of the applied Design of Experiments (DOE) are described as follows.

3.1.1. *Materials*

The classic metallocene catalyst used in this study (CpZ 2) consists of a classic supported Zirconocene. It's worth mentioning that this catalyst produces hydrogen in-situ as part of its chain termination mechanism.

The constrained geometry catalyst used in this study (CGC M) is a proprietary catalyst, supplied by INEOS.

The feed gases (Ethylene, Nitrogen and carbon dioxide) used for the full-time and short-time polymerization reactions were the same as previously described in section 2.1.1 of this chapter.

Anhydrous 1-Hexene (minimum purity 99%, purchase from Sigma-Aldrich ICN - Germany) was dried with Magnesium Chloride overnight, followed by distillation and freeze pumping to remove an oxygen traces. The dry and purified 1-Hexene was then stored in the freezer.

3.1.2. *Polymerization procedures*

The experimental conditions applied for the catalysts used in this section are described below.

Full-time polymerization

Full-time polymerization reactions were carried out in a spherical 2.5L lab-scale semi-batch reactor commonly called the *Turbosphere* reactor. The detailed reactor set-up and operation procedure can be found in Chapter 2 (Ch. 2, section 2.1.1.).

For the classic Zirconocene catalyst used in this study (CpZ 2), 50 mg catalyst were employed. As scavenger for the reactor environment, 0.8 mL of a 1 M solution of Triisobutylaluminum (TIBA) were used. The reactions were performed in homopolymerization with Ethylene under constant pressure of 7.5 barg and reaction temperature of 84°C.

For the constrained geometry metallocene catalyst used in this study (CGC M 2), 100 mg catalyst were employed. As scavenger for the reactor environment, 0.5 mL of a 1 M solution of Triisobutylaluminum (TIBA) were used. The reactions were performed in homopolymerization with Ethylene under constant pressure of 7.5 barg and reaction temperature of 70°C.

The experiments were performed with 60 minutes duration and constant agitation at 200 rpm.

Short-time polymerization

Short-time polymerization reactions were carried out with the novel Stopped-flow reactor (SF N), with set-up description and operation procedures previously described in chapter 2 (Ch. 2, section 2.1.1.).

For the classic Zirconocene catalyst used in this study (CpZ 2), the reaction bed was composed of 30-50 mg catalyst in approximately 1200 mg fine NaCl seedbed. The reaction temperature was 84 °C and ethylene pressure was 7.5 barg, keeping a gas velocity of 50 cm/s.

For the commercial CGC catalyst used in this section (CGC M), the reaction bed was composed of 40-60 mg catalyst in roughly 1200 mg fine NaCl seedbed. The reaction temperature was 70 °C and ethylene pressure was 7.5 barg, keeping a gas velocity of 50 cm/s.

3.1.3. *Design of Experiments (DOE)*

We have applied Experimental design in the assessment of catalysts CpZ 2 and CGC M in order to tackle the effects of the process variables on the reaction outcomes (polymerization yield and polymer properties).

We have proposed orthogonal factorial designs for both catalysts evaluated in the current case study by following the approach sequence proposed by Box et al.[19,20], in which experimental data are obtained at every combination of the varying experimental parameters.

The initial step was the choice of the factors (independent variables, x_n) and levels of variation for each factor (-1, 0, +1). Following, we fixated the variables to be measured as experimental results (dependent variables).

Finally, we performed the multiple regression of the obtained results in relation to the variable factors with the software Statistica 10, to better understand the relationship between the independent and dependent variables. More details on the data treatment can be found in the Appendix 1.

For catalyst CpZ 2, the varying factors were the reaction time and comonomer content in the gas feed. The experiments were performed in random order and the ethylene pressure (7.5 barg) and reactor temperature (84 °C) were kept constant for all experimental runs. For this catalyst, the full factorial composition of two factors varying at three levels (3^2 factorial design) results in a total of 9 experiments.

For catalyst CGC M, the varying factors were the reaction time, the comonomer content in the gas feed and the hydrogen content in the gas feed. The experiments were performed in random order and the ethylene pressure (7.5 barg) and reactor temperature (70 °C) were kept constant for all experimental runs. For this catalyst, the full factorial composition of three factors varying at three levels (3^3 factorial design) results in a total of 27 experiments. In this case, we opted for a fractional factorial design, where experiments in which two of the varying conditions are of the same level were excluded from the analysis, thus resulting in 9 experiments.

For both catalysts, we performed three repetitions of the experiment on the central point (0, 0, 0), in order to estimate the experimental error. Moreover some extra points to be interpreted qualitatively were added as extrapolations to the central point

The experimental limits for the independent variables were defined based on indications from the catalyst suppliers. The chosen factors and levels of variation can be found in Tables 5 and 6.

The responses (dependent variables) for the experimental evaluation were the polymerization yield and polymer thermal properties including polymer crystallinity and melting temperature (Tm).

The experimental matrix for the catalysts used in this study, as well as the full list of experiments used for the experimental design can be found in the Appendix 3.

Variable factor		Level			
		-1	0	1	Extra
		Low	Middle	High	
X1	[1-C6] (wt%)	0	8	16	20
X2	Time (s)	5	30	55	---

Tableau 5: Factors and levels of variation for catalyst CpZ 2

Variable factor		Level			
		-1	0	1	Extra
		Low	Middle	High	
x1	[H2] (mol%)	0	0.3	0.6	1.5
x2	[1-C6] (wt%)	0	8	16	20
x3	Time (s)	5	12.5	20	60

Tableau 6: Factors and levels of variation for catalyst CGC M

3.2. Variability assessment for catalysts in this study

The variability of the performed polymerization reactions was assessed for the catalysts used in this study in terms of their polymerization yields. For this purpose, the standard deviation (or dispersion) was calculated for a series of polymerization tests performed at increasing reaction times under the same reaction conditions. Calculations were based on a minimum of three experiments performed at each reaction time. The full list of experiments can be found in Appendix 3.

Calculations followed the following formula for the uncorrected sample standard deviation:

$$\sigma = \sqrt{\frac{1}{N}\sum_{i=1}^{N}(x_i - \bar{x})^2} \quad (4\text{-}1)$$

Where σ is the uncorrected standard deviation, N is the number samples used for the calculation, x_i are the observed sample values and $\bar{x}$ is the average value of the sample population.

Moreover, Dixon's Q test was applied to determine if the results furthest from the average were outliers that should not be included in the variability assessment.[21,22] The results included in the variability assessment were not considered as outliers.

3.2.1. *Results*

The following reaction conditions were applied for the variability assessment:

For the classic metallocene catalyst CpZ 2, reactions were performed with 30-50 mg catalyst at 84°C, 7.5 bars Ethylene with gas velocity of 50 cm/s.

For the CGC catalyst CGC M, reactions were performed with 35-60 mg catalyst at 70°C, 7.5 bars Ethylene with gas velocity of 50 cm/s.

Yield variability assessment for classic metallocene catalyst (CpZ 2)

Figure 16 displays the average polymerization yields obtained from the variability assessment for catalyst CpZ 2, with details for the plot described in Table 7.

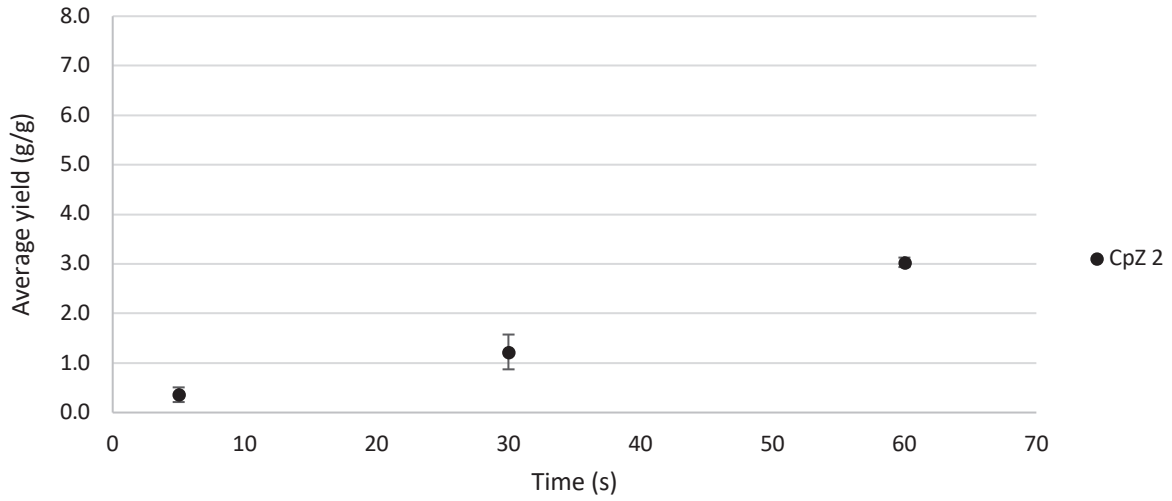

Figure 16: Average yields and standard deviations with increasing reaction time for classic metallocene catalyst CpZ 2

Catalyst used	Reaction time (s)	Average Yield (g/g)	Standard deviation (σ)
CpZ 2	60	3.0	0.1
	30	1.2	0.4
	5	0.4	0.1

Tableau 7: Assessment of average yield evolution with reaction time using a classic metallocene catalyst. Reactions performed with 30-50 mg catalyst at 84°C, 7.5 bars Ethylene with gas velocity of 50 cm/s.

Yield variability assessment for CGC metallocene catalyst (CGC M)

Figure 17 displays the average polymerization yields obtained from the variability assessment for catalyst CpZ 2, with details for the plot described in Table 8.

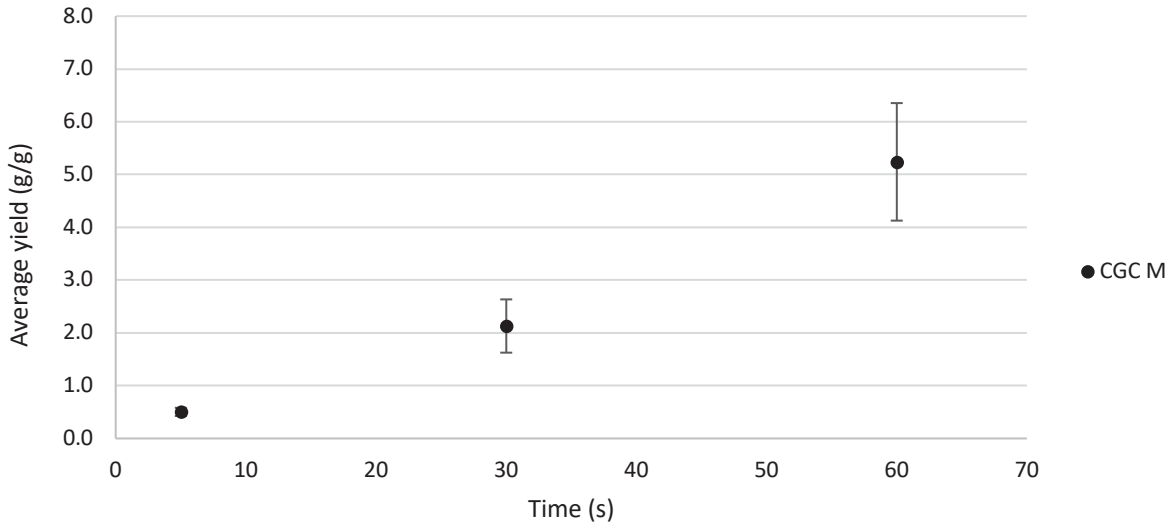

Figure 17: Average yields and standard deviations with increasing reaction time for classic metallocene catalyst CpZ 2

Catalyst used	Reaction time (s)	Average Yield (g/g)	Standard deviation (σ)
CGC M	60	5.2	1.1
	30	2.1	0.5
	5	0.5	0.1

Tableau 8: Assessment of average yield evolution with reaction time using a classic metallocene catalyst. Reactions performed with 30-50 mg catalyst at 84°C, 7.5 bars Ethylene with gas velocity of 50 cm/s.

3.2.2. *Conclusion*

A variability assessment was performed for the catalysts used in this study based on the calculation of the uncorrected standard deviations for the polymerization yields obtained at increasing reaction times.

For both assessed catalysts, linear trends between the average yields and reaction times were observed, indicating coherence in the evolution of polymer production with time.

We observed overall lower polymerization yields for the classic metallocene catalyst (CpZ 2) in relation to the CGC catalyst during the evaluated time frame (5 to 60 seconds).

This behavior is in agreement with the full-time polymerization kinetics observed for these catalysts, in which the classic metallocene catalyst (CpZ 2) reaches its maximum activities at about 30 minutes of reaction.

We observed overall lower dispersion of results for the classic metallocene catalyst (CpZ 2), in relation to the CGC catalyst (CGC M). Moreover, the dispersion of the polymerization yield results for the CGC catalyst was more significant for increasing reaction times.

Upon discussion with the catalyst provider, it appears that the method used for its production is in fact susceptible to inhomogeneity in its performance. This actually shows another useful application for the SF N: rapid evaluation of catalyst performance. It would be quite easy at a production site or elsewhere to use this device to test catalyst before its use in order to detect any batch-to-batch variations.

3.3. Results and discussion

The experimental results obtained following the proposed design of experiments were interpreted with the software Statistica 10. The full list of experiments used for the statistical assessment can be found in the Appendix 3.

The Pareto charts were interpreted to determine the statistical value the variable factors have on the experimental responses, in which parameters with a p value higher than .05 are considered to have significant statistical value. We have applied the ANOVA (analysis of variance) method to detect the main interaction effects between the factors and obtain the value of R-square, which indicates the discrepancy of the results in relation to the predicted data. Finally, the response surfaces were obtained considering linear main effects only and the plots were interpreted to gain insight on how the variable factors impact the responses and identify potential relationships between the parameters.

The obtained results were interpreted in terms of catalyst kinetics and polymer properties. Moreover, the kinetic behavior at the reaction start-up was interpreted with the software component developed in chapter 3.

At last, morphology observations of the obtained polymers were used for qualitative evaluation of the polymer properties.

3.3.1. *Catalyst kinetics*

The obtained Pareto diagrams and response surfaces were interpreted to investigate the kinetics of the metallocene catalysts used in the current study, correlating the independent experimental factors (reaction time, 1-Hexene content and Hydrogen content) with the obtained polymerization yields.

The kinetic profiles obtained at full-time polymerization conditions are found in Figure 18.

From the obtained full-time polymerization kinetics for both catalysts, the classic metallocene CpZ 2 presents a slower activation profile in which the reaction rates gradually increase until reaching its peak at about 35 minutes of reaction. On the other hand, the CGC catalyst presents very fast activation early in the reaction, reaching the maximum activity at about 5 minutes and then gradually decaying.

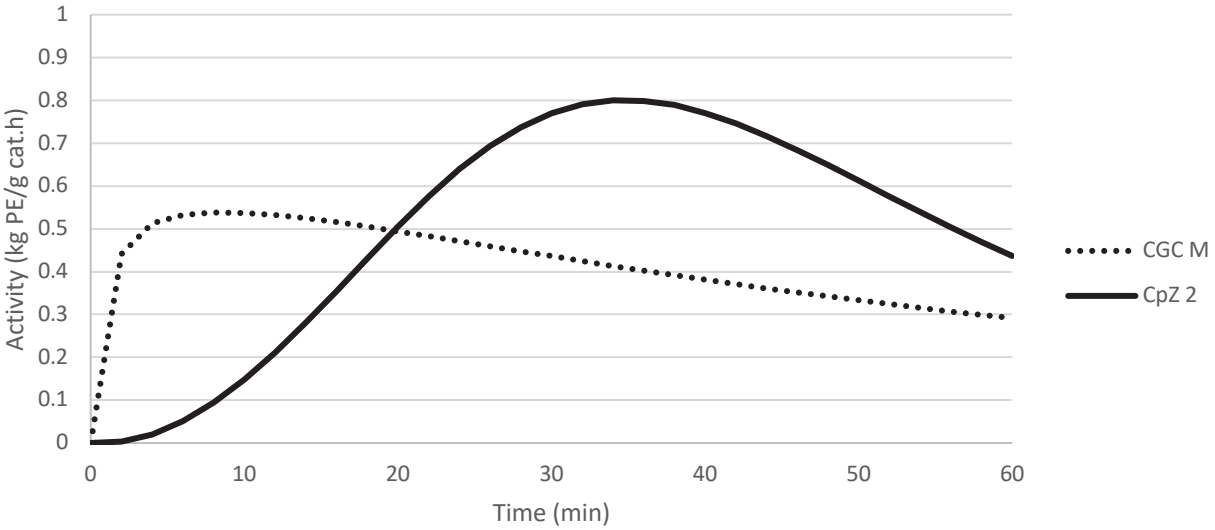

Figure 18: Full polymerization kinetics for 60 minute homopolymerization reactions with ethylene

The results obtained from short-time reactions with the novel stopped-flow reactor are described as follows.

For both catalysts assessed in this section (CpZ 2 and CGC M), the Pareto diagrams seen in Figure 19 indicated that the duration of the reaction was the main factor influencing the polymerization yields at short reaction times. This is of course expected in and of itself, but has been included to show that changing 1-hexene levels within the suggested range does not appear to have a statistically significant impact on the yield over the time frame of interest.

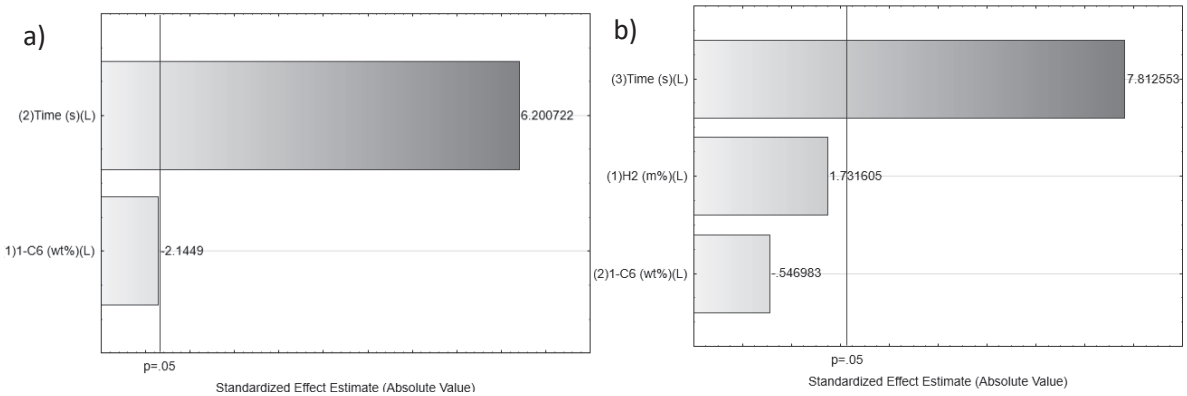

Figure 19: Pareto diagrams for polymerization yield for catalysts: a) classic metallocene CpZ2 (R^2=0.71947), b) CGC catalyst CGC M (R^2=0.64438)

This effect is also visible at the obtained response surfaces, seen in Figures 20 and 21.

The effect of reaction time and 1-hexene content on the polymerization yields for both catalysts can be seen in Figure 20. These projections indicated that the yields for catalyst CpZ 2 were slightly improved by the comonomer content in the gas feed at short reaction times. For this catalyst, the highest yields were observed at higher reaction times (>50 s) and high concentration of 1-hexene (>8 wt%). For the assessed CGC catalyst, the content of 1-hexene did not seem to have an impact on the reaction yields at the analyzed reaction times.

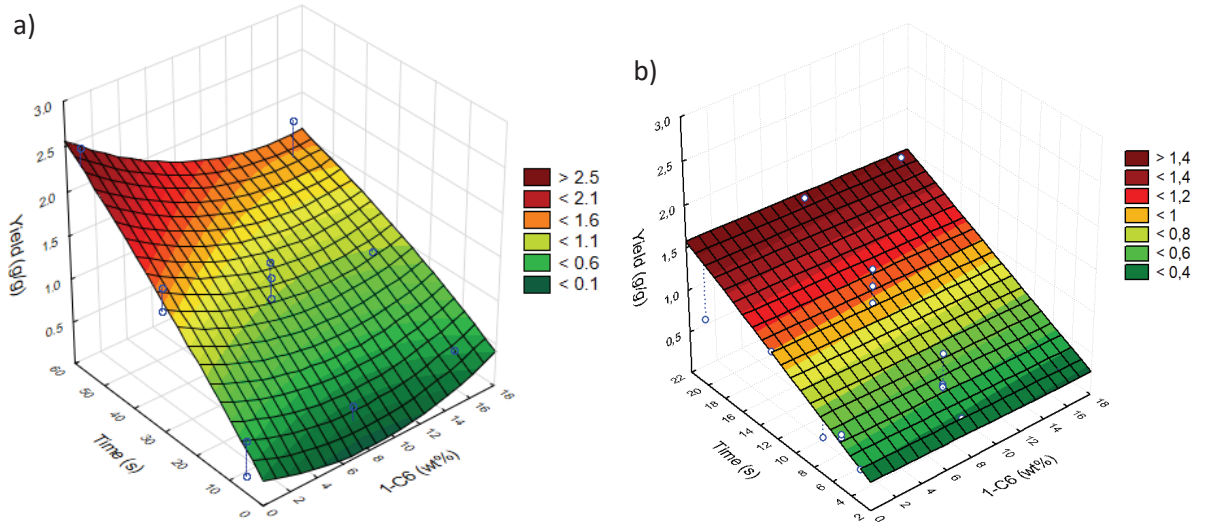

Figure 20: Response surfaces for yield for catalysts: a) classic metallocene CpZ2 (R^2=0.71947), b) CGC catalyst CGC M (R^2=0.64438)

The effects of reaction time, 1-Hexene content and Hydrogen content for the CGC M catalyst can be seen in Figure 21. These results suggested that hydrogen does not have a significant statistical impact on the polymerization yield for the evaluated concentrations (0 to 0.6 molar %) and time frame. Likewise, the surface plot shown in Figure 21-b suggests that the interaction between hydrogen and 1-hexene is not of statistical interest.

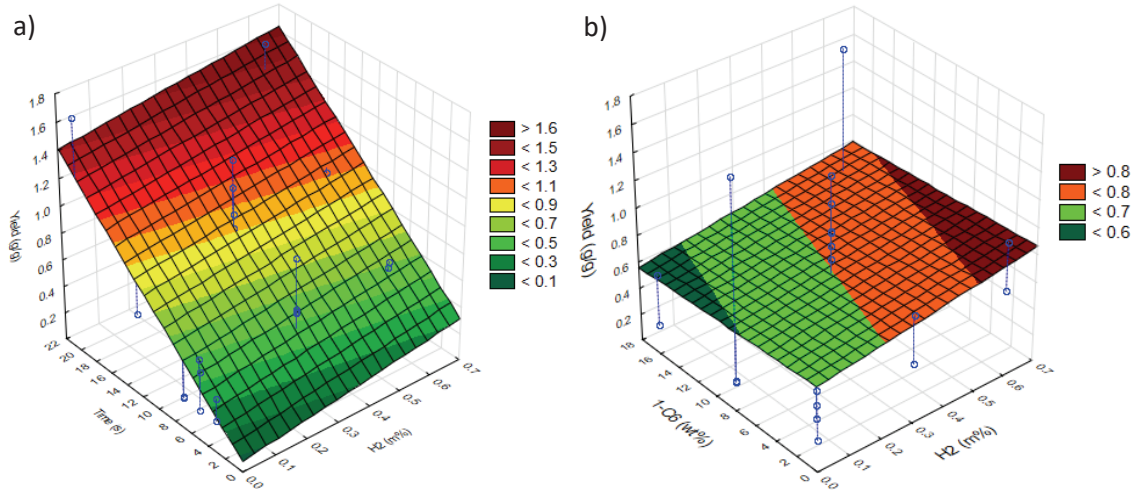

Figure 21: Response surface for Yield for CGC M catalyst in relation to: a) time and H2 content, b) interaction between H2 and 1-C6 content.

3.3.2. *Reaction rates at early stages*

The software component developed in Chapter 3 was applied to the experimental data in order to evaluate the kinetic behavior of the catalysts in homopolymerization conditions at early stages.

The High-Gain Observer was applied on experiments performed at increasing reaction times to evaluate the evolution of reaction rates at early stages.

The estimated reaction rates for the catalysts used in this study can be found in Figure 22. The estimated reaction rates for catalyst CGC M at short reaction times were coherent with the kinetic profiles obtained for full-polymerization times, seen in Figure 18. Figure 23 shows the estimated reaction outlet temperature profiles and dynamic estimates of produced polymer mass, together with the experimental values.

For the classic metallocene CpZ 2, we observed a pronounced activation peak in the first seconds, which then subsided and the reaction seemed to progress in a slower increasing rate. The slower activation of this catalyst was visible on the full-time polymerization profile, but the activation peak was only detected in the reactions performed in the stopped-flow reactor. Given each curve in the plot derives from an individual experiment, this behavior seems to happen in a reproducible manner independently of the reaction duration, which suggests a particularity of the catalyst.

This behavior is contrasted with what is observed for the CGC catalyst. In this case, the estimated rates at different reaction times indicate that the catalyst activation happened quite fast from early and then slows down. These predictions are in agreement with the kinetic behavior observed for this catalyst in full polymerization times (60 minutes).

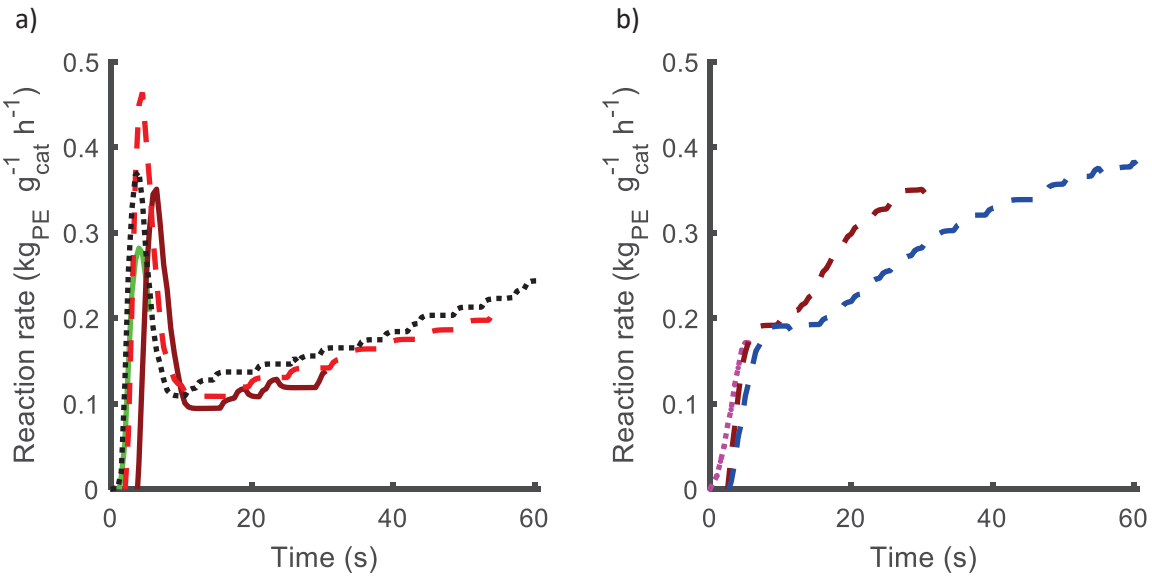

Figure 22: Estimated reaction rates for catalysts: a) CpZ2, b) CGC M

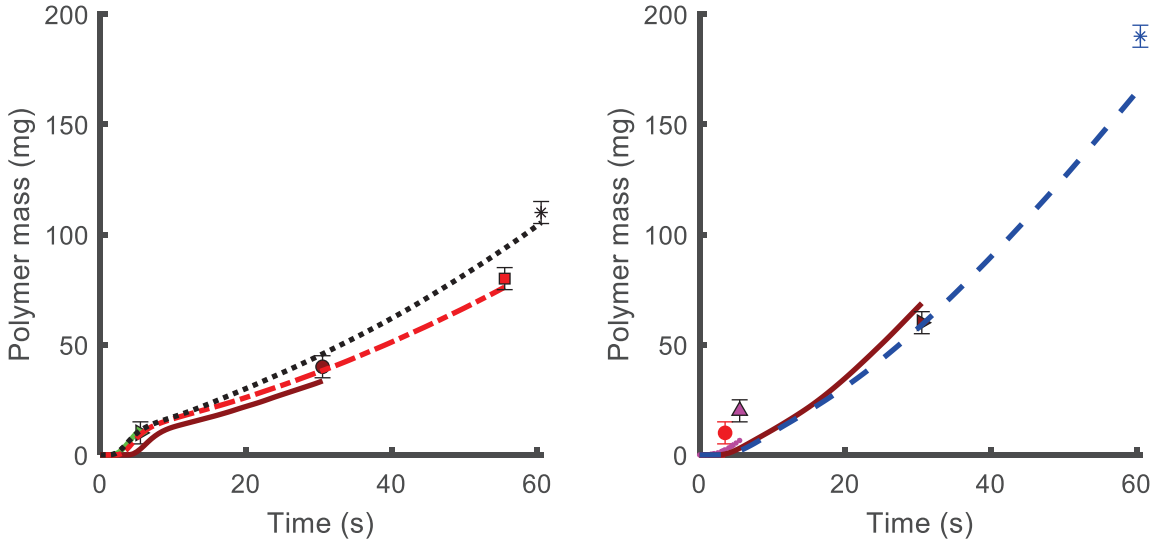

Figure 23: Estimated mass of produced polymer for catalysts: a) CpZ2, b) CGC M

3.3.3. *Polymer thermal properties*

The Pareto diagrams and response surfaces were interpreted to investigate the effect of the independent experimental factors (reaction time, 1-Hexene content and Hydrogen content) on the melting temperatures of the obtained polymer.

The Pareto diagrams seen in Figure 24 indicated the main experimental factors influencing the melting temperature of the obtained polymers, for both catalysts.

For the classic metallocene catalyst CpZ 2, the duration of the reaction was the main factor influencing the melting temperatures at short reaction times, followed by a secondary effect of the 1-Hexene content in the gas feed. For the CGC M catalyst, the 1-Hexene content has the highest effect on the polymer melting temperatures, followed subsequently by the hydrogen content and reaction time.

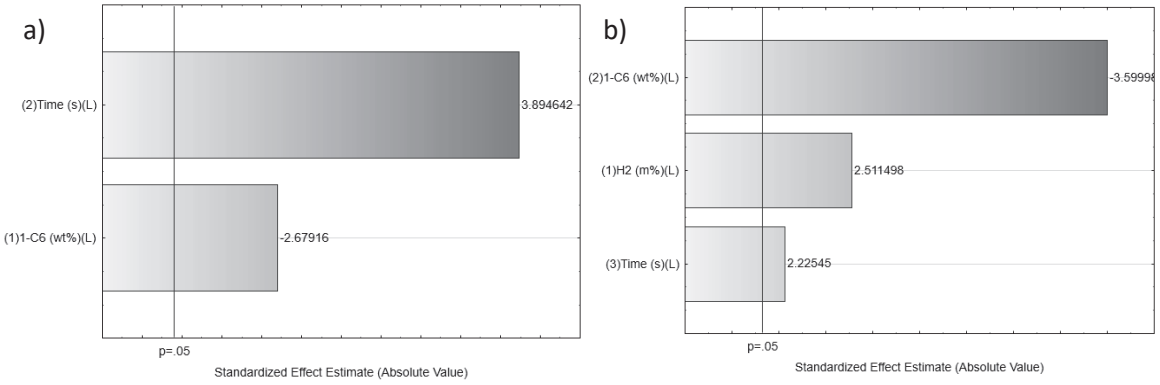

Figure 24: Pareto diagrams for polymer melting temperatures (Tm) for catalysts: a) classic metallocene CpZ 2 (R^2=0.60796), b) CGC catalyst CGC M (R^2=0.46942)

These effects were also remarked from the obtained response surfaces seen in Figures 25 and 26.

These observations are coherent with the particularities of the studied catalysts. Given that the CGC catalyst is known for its the higher capacity to incorporate lower alpha olefins and produce polymers with higher amorphous character (and thus with lower melting temperatures), this could explain the more pronounced effect of 1-Hexene content for the CGC catalyst than for the classic metallocene CpZ 2. Moreover, the fact that hydrogen is the main chain termination agent could explain its effect for the studied CGC catalyst, as seen in Figure 26. We could assume that higher hydrogen concentrations in the gas feed lead to polymer containing shorter chains, and thus higher melting temperatures.

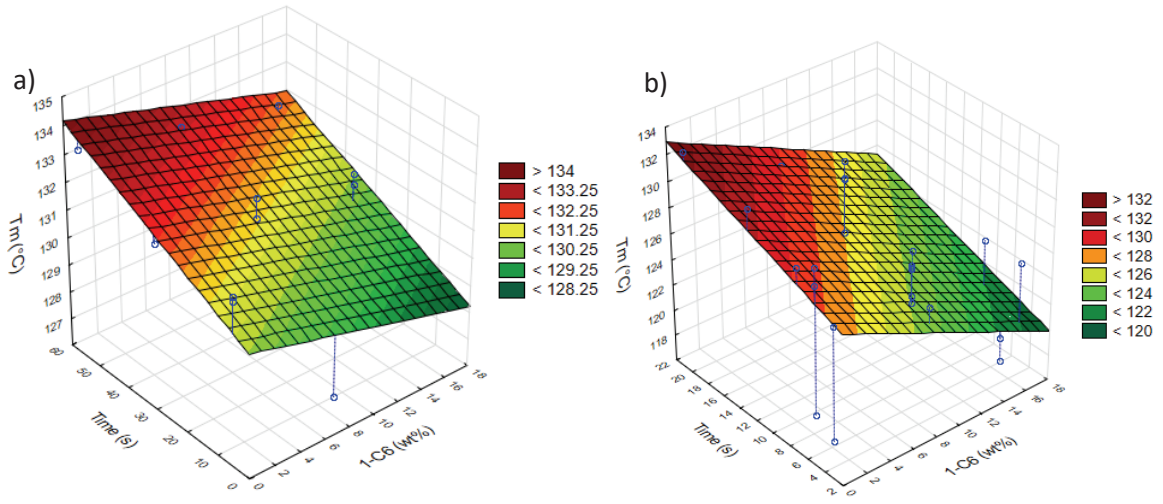

Figure 25: Response surfaces for Tm (°C) for catalysts: a) classic metallocene CpZ 2 (R^2=0.60796), b) CGC catalyst CGC M (R^2=0. 46942)

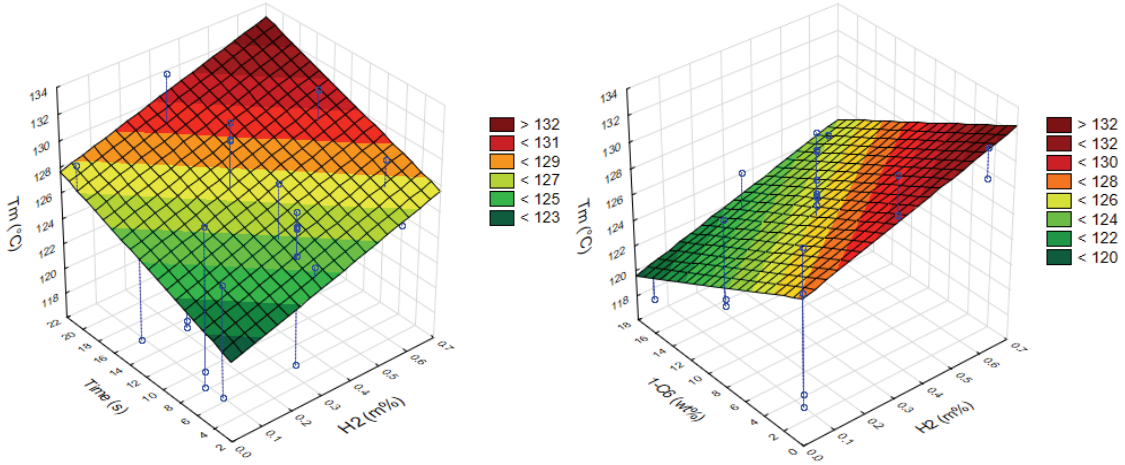

Figure 26: Response surface for Tm against time and hydrogen content for the CGC catalyst (R^2=0. 46942)

In terms of polymer crystallinity, the Pareto diagrams seen in Figure 27 indicated that the reaction duration was the main experimental factor influencing the polymer crystallinities for both catalysts. For the CGC catalyst, the hydrogen content had a secondary effect on the polymer crystallinity, followed by the 1-Hexene content. The fact time is most influential in the current evaluation can be explained by the evolution of the particle morphology. As has been suggested in previous studies by Di Martino et al.[14] and Tioni et al.[13], low polymer crystallinities at early stages of the reaction might

very well be related to the confinement effect of the polymer inside the porosity of the support, which is overcome as the reaction progresses and the particle grows.

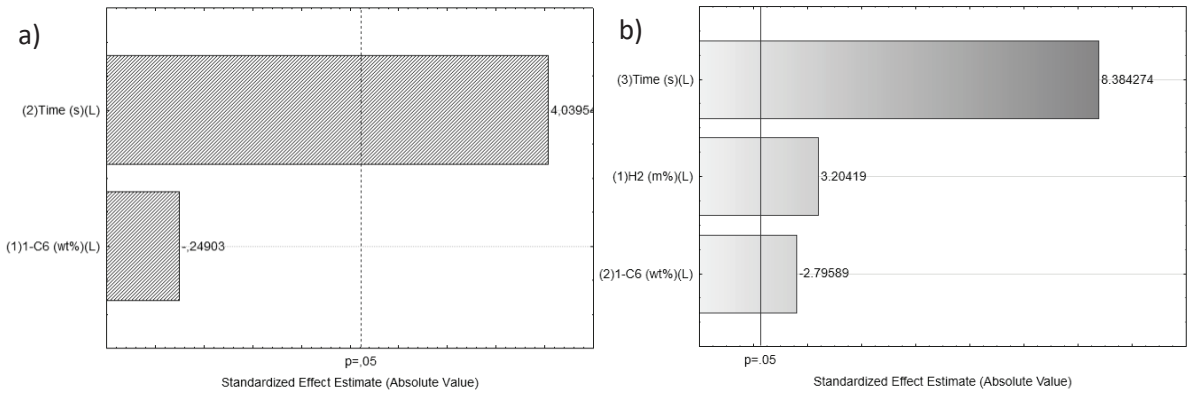

Figure 27: Pareto diagrams for polymer crystallinities for catalysts: a) classic metallocene CpZ2 (R2=0.4232), b) CGC catalyst CGC M (R2=0.66765)

The observations were also visible in the obtained response surfaces seen in Figures 28 and 29. Moreover, as shown in Figure 29, the highest observed polymer crystallinities were obtained at higher (0.6 molar %) hydrogen contents and no 1-Hexene in the gas feed. Following the same line of thought as proposed for the melting temperatures, we could assume that higher hydrogen concentrations (chain termination agent) lead to shorter polymer chains and, thus polymers with higher crystalline content.

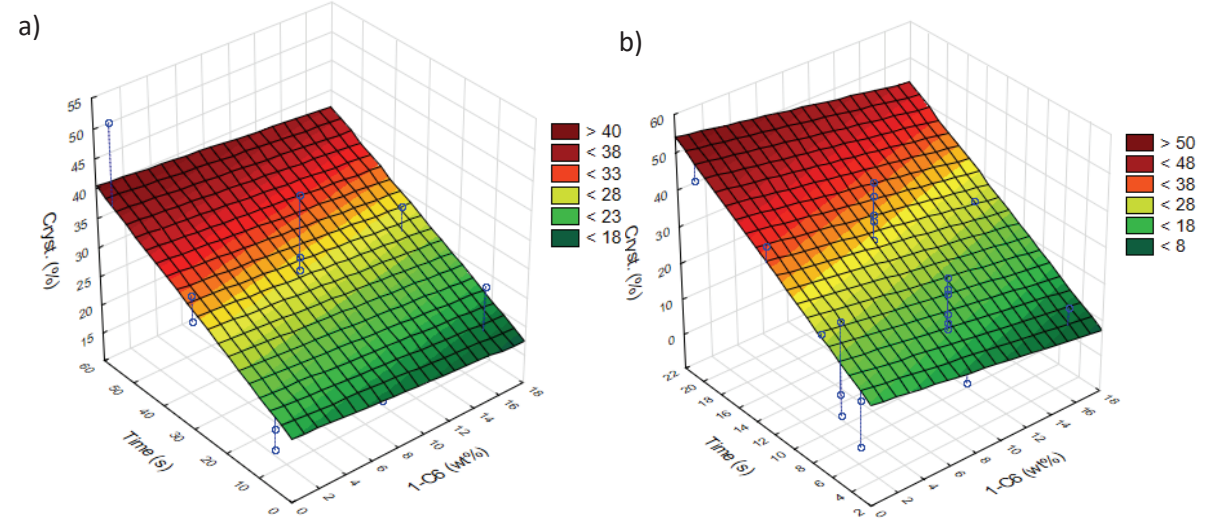

Figure 28: Response surfaces for polymer crystallinity for catalysts: a) classic metallocene CpZ2 (R2=0.4232), b) CGC catalyst CGC M (R2=0. 66765)

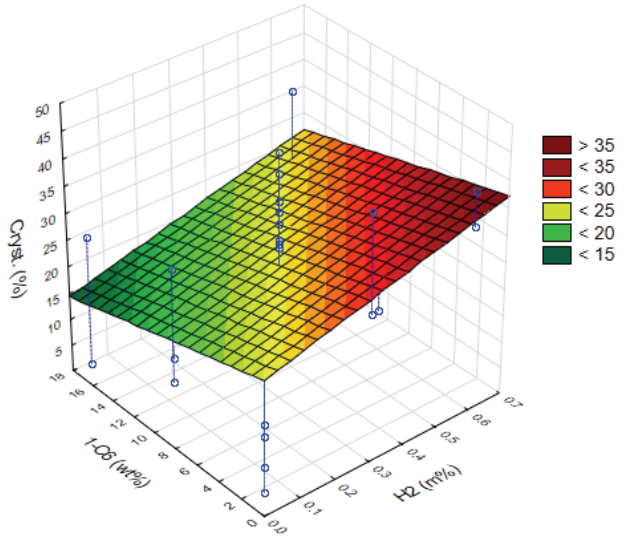

Figure 29: Response surface for polymer crystallinity in terms of 1-C6 and H2 content for the CGC catalyst

Besides the statistical evaluation, we have assessed the evolution of polymer thermal properties by following the melting and crystallization temperature profiles obtained from DSC analysis. Details on the experiments used for this assessment can be found in the Appendix 3.

In Figures 30 and 31, we have assessed the effect of comonomer during the melting and crystallization of the obtained polymers, measured without removing the support fragments. The following reactions were performed with 8 wt% 1-Hexene as comonomer.

As we can see, both catalysts presented bimodal crystallization peaks at short reaction times (5 seconds), which are no longer visible from 30 seconds of reaction. As discussed above, this behavior has been previously observed and linked to the confinement of nascent polymer chains in the porosity of the inorganic support. As the polymerization progresses, more chains grow free from the containment effect that perturbs the polymer crystallinity. The observed bimodality is most likely due to the presence of remaining inorganic support in the particles. Moreover, these observations suggest that, for both metalocene and CGC catalysts assessed in this study, the particle fragmentation is completed in a time frame between 5 and 30 seconds of reaction. Similar observations were made from the assessment performed with higher 1-hexene content in the gas feed (16 wt%). These plots can be found in the Appendix 3, together with the list of experiments used in this section.

The same assessment was performed for catalyst CGC M with 8 wt 1-Hexene and 0.3 m% hydrogen in the gas feed. The evolution of thermal profiles is seen in Figure 32, in which the same behavior as previously discussed was again observed, with a dual crystallinity peak observed at 5 seconds of

reaction, suggesting that the amounts of hydrogen used in these experiments had no remarkable effect on the observed crystallization and melting profiles.

These observations point out that, indeed, reaction time is the most influential factor on the polymer thermal properties at short reaction times; an observation that is in agreement with those from the statistical study.

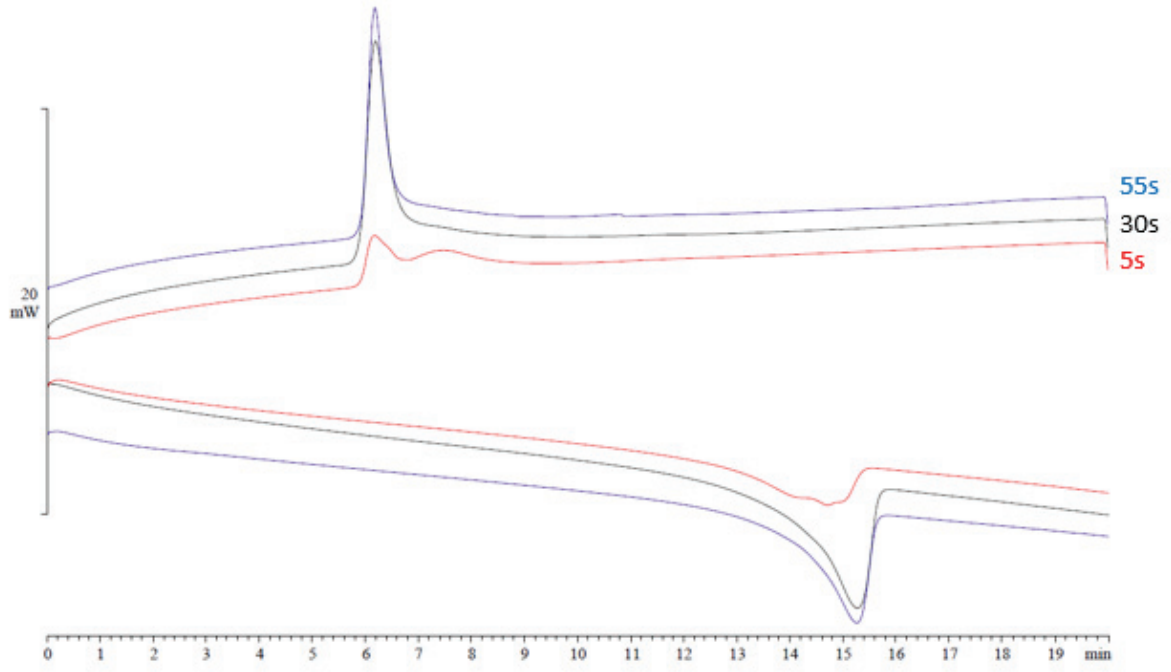

Figure 30: Evolution of thermal properties for classic metallocene CpZ2. Reaction conditions: C2 + 8 wt% 1-C6 in gas feed

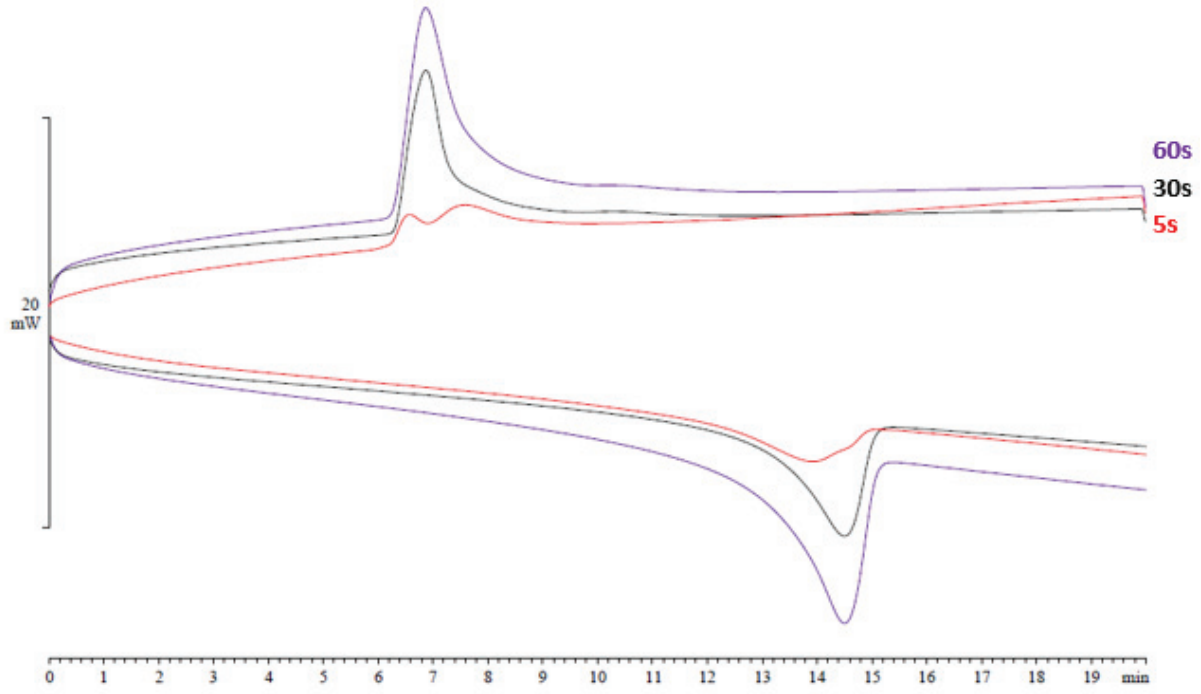

Figure 31: Evolution of thermal properties for catalyst CGC M. Reaction conditions: C2 + 8 wt% 1-C6 in gas feed

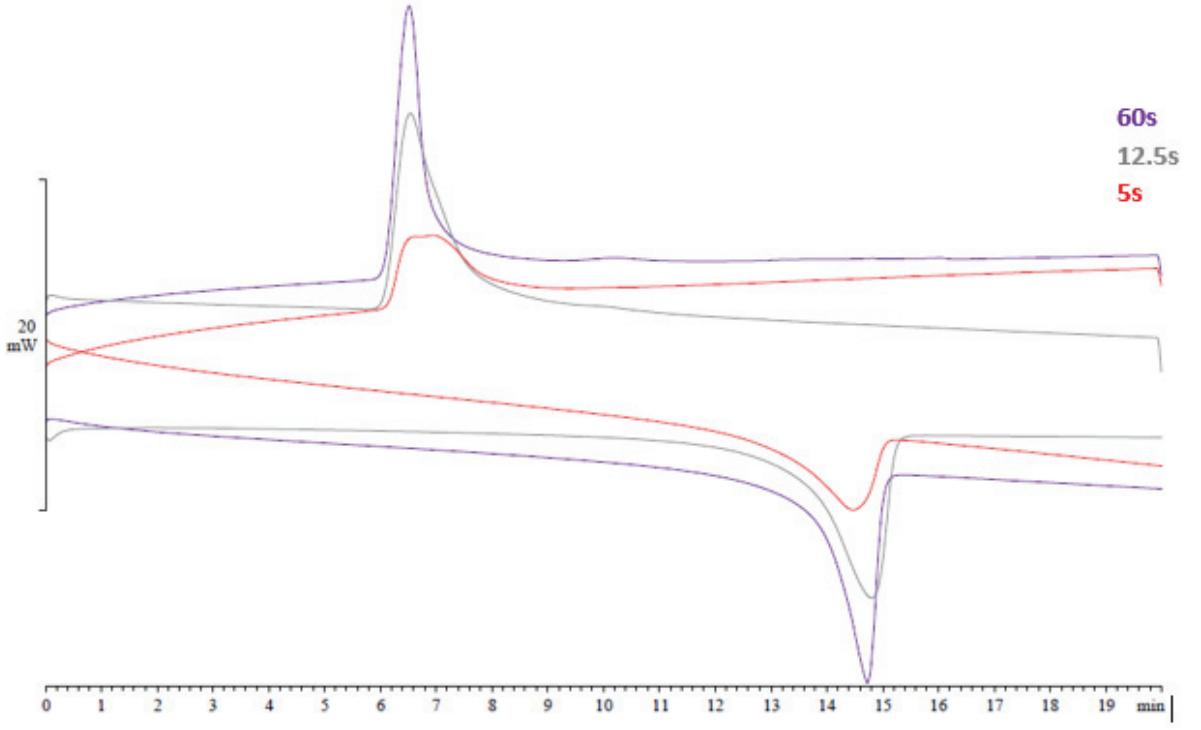

Figure 32: Evolution of thermal properties for catalyst CGC M. Reaction conditions: C2 + 8 wt% 1-C6 + 0.3m% H2 in gas feed

3.3.4. *Molecular weight*

The Pareto diagram seen in Figure 33 indicates that, for the classic metallocene CpZ 2, the main experimental element influencing the measured average molecular weights is the reaction duration.

These observations are coherent when we consider the previous indications that reaction time is the main factor impacting the polymerization yields for this catalyst. We could infer, in this case, that higher polymerization yields lead to bigger polymer macroparticles and, therefore, higher molecular weight averages. The same observations can be drawn from the surface plot shown in Figure 34.

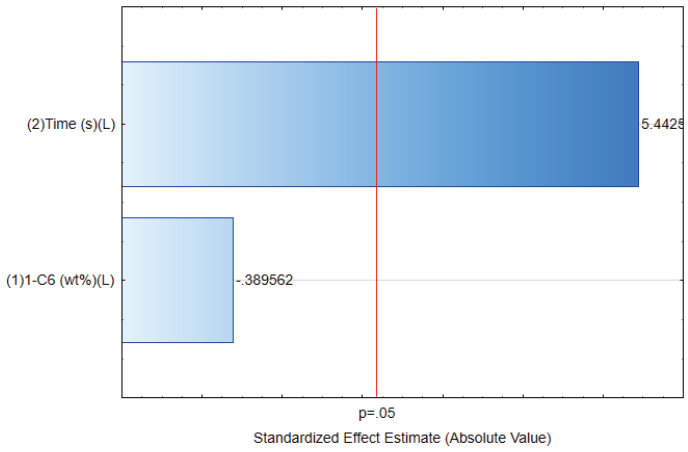

Figure 33: Pareto diagrams for Mw for classic metallocene CpZ2 (R2=0.71233)

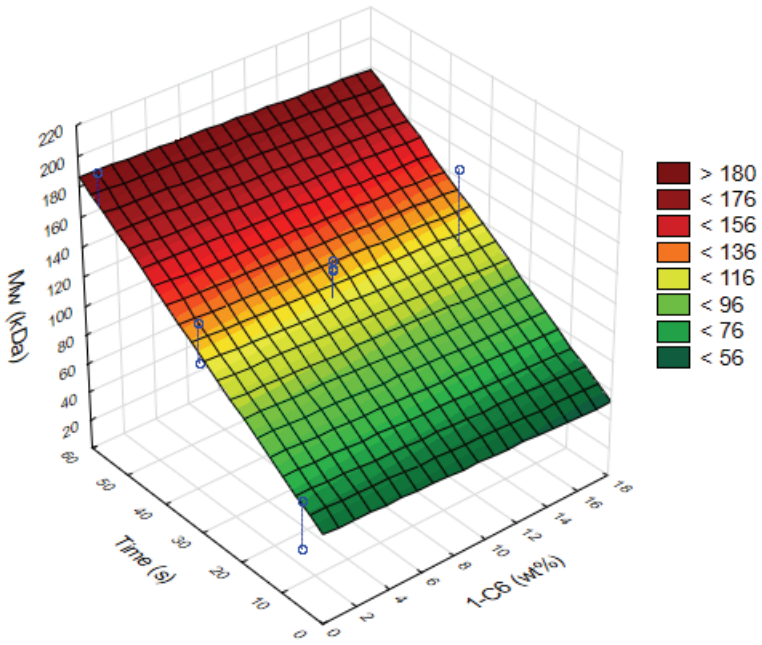

Figure 34: Response surfaces for Mw for classic metallocene CpZ2 (R2=0.71233)

The evaluation of molecular weights for the CGC catalyst used for the current set of experiments was delayed due to malfunction of the SEC equipment in our lab.

3.3.5. *Particle morphology*

In this section, the polymer properties were qualitatively evaluated in terms of polymer morphology obtained from SEM and SEM-EDX analysis. We aimed to evaluate the impact of varying reaction conditions on the particle growth for different families of supported metallocene catalysts.

The particle morphology was assessed for the varying compositions of gas feed at increasing reaction times.

- **Classic metalocene - CpZ 2**

For the classic metallocene catalyst CpZ 2, SEM analysis in polymerization reactions performed with ethylene only as feed gas, seen in Figures 35 to 37, indicated a coherent progression of the particle sizes with reaction time. At 5 seconds reaction, we observed some fractures on the particle surfaces and modest polymer formation (Figure 35). Moreover, we see imprints of the cubic salt particles used as seedbed, which suggest that, at this timeframe, the polymer is still quite amorphous. At 30 seconds reaction (Figure 36), the polymer formation is clearly more pronounced and the particles are bigger, which indicates that fragmentation has already taken place. At 60 seconds of reaction (Figure 37), the particles are bigger and the particle growth seems more even. The morphological observations are in agreement with the previous discussion on the evolution of polymer crystallinity with time.

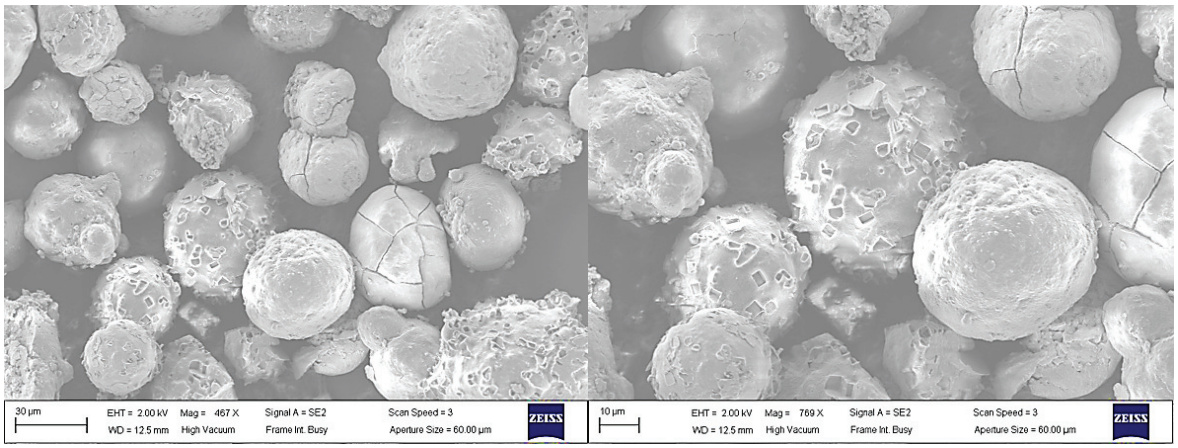

Figure 35: SEM analysis of polymer from 5 s reaction with CpZ 2. Gas feed: C2 only.

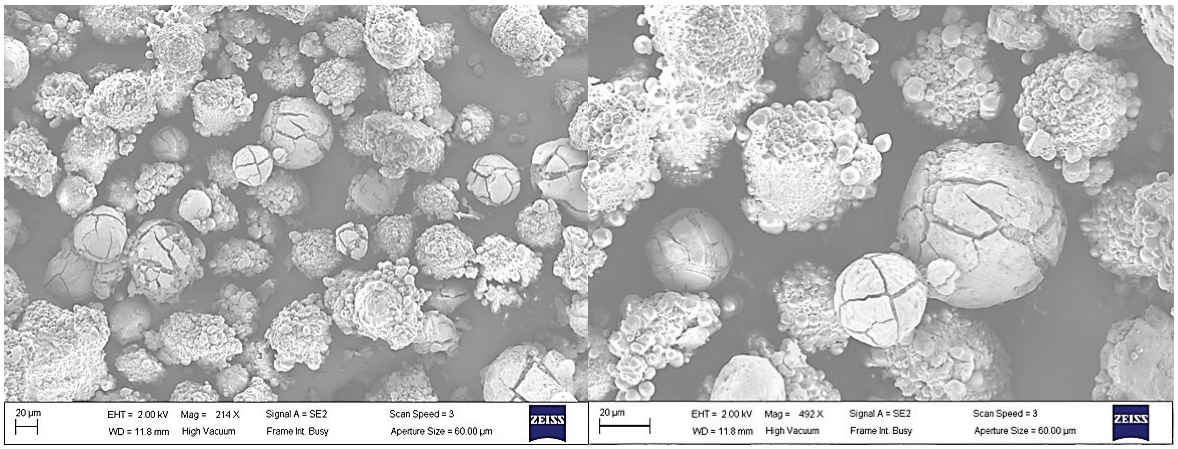

Figure 36: SEM analysis of polymer from 30 s reaction with CpZ 2. Gas feed: C2 only.

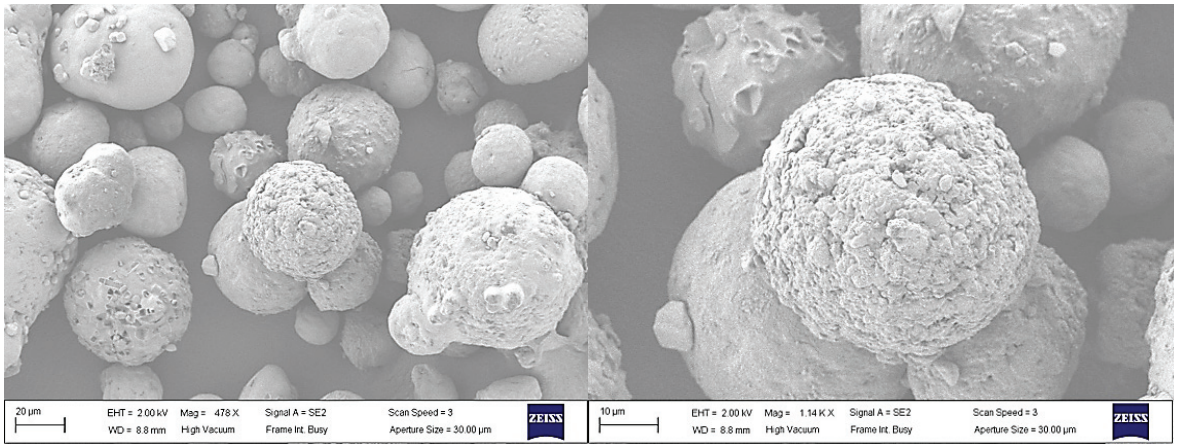

Figure 37: SEM analysis of polymer from 55 s reaction with CpZ 2. Gas feed: C2 only.

In Figures 38 to 40, we performed the same assessment with of 8 wt% 1-hexene in the gas feed, which is the central point in the DOE, for this catalyst. Between 5 and 30 seconds, the observed overall morphology and average particle size have not drastically changed in relation to those obtained without copolymer at the same time frame. At 55 seconds of reaction, the particle growth seems more even, which is coherent with the fact that the polymer, at this stage, is more ductile.

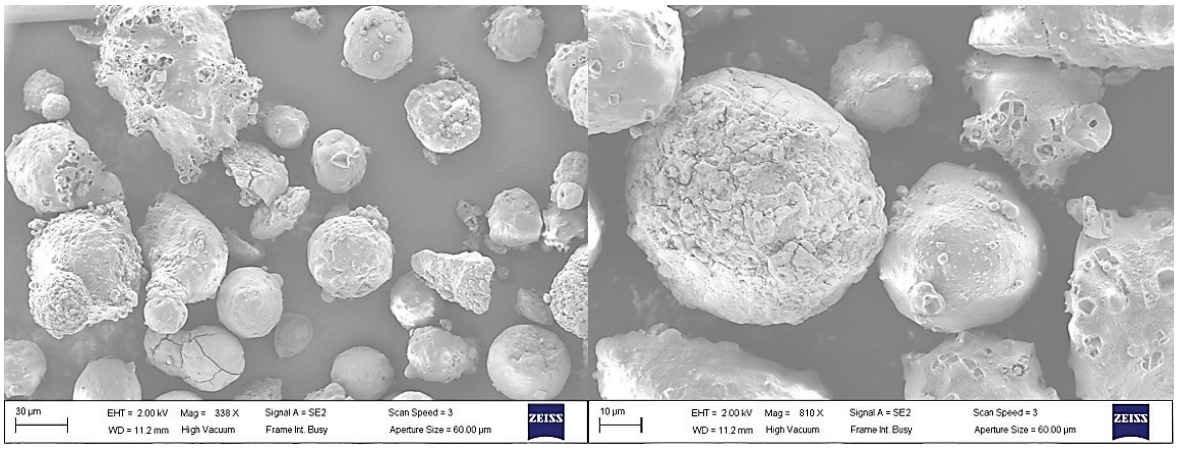

Figure 38: SEM analysis of polymer from 5 s reaction with CpZ 2. Gas feed: C2, 8 wt% 1-C6

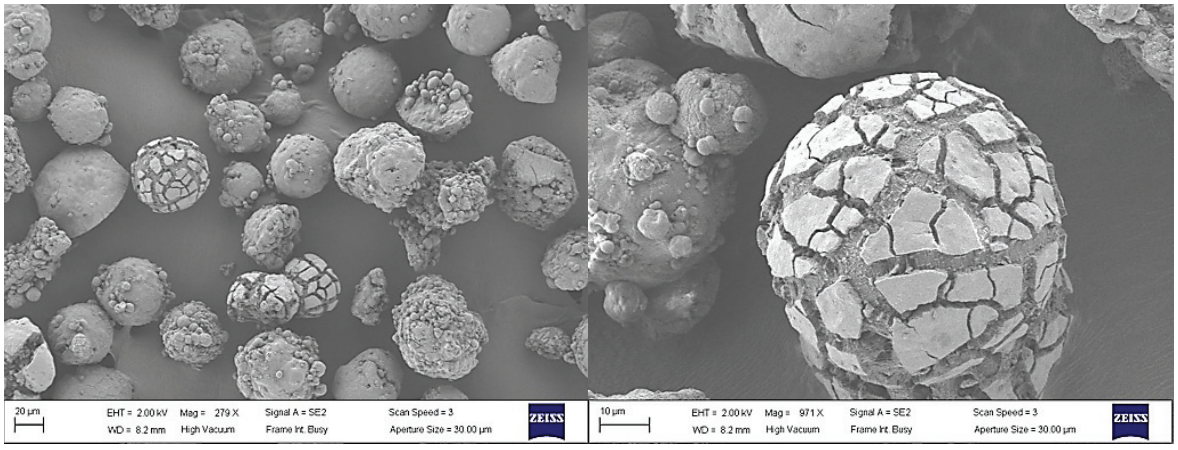

Figure 39: SEM analysis of polymer from 30 s reaction with CpZ 2. Gas feed: C2, 8 wt% 1-C6

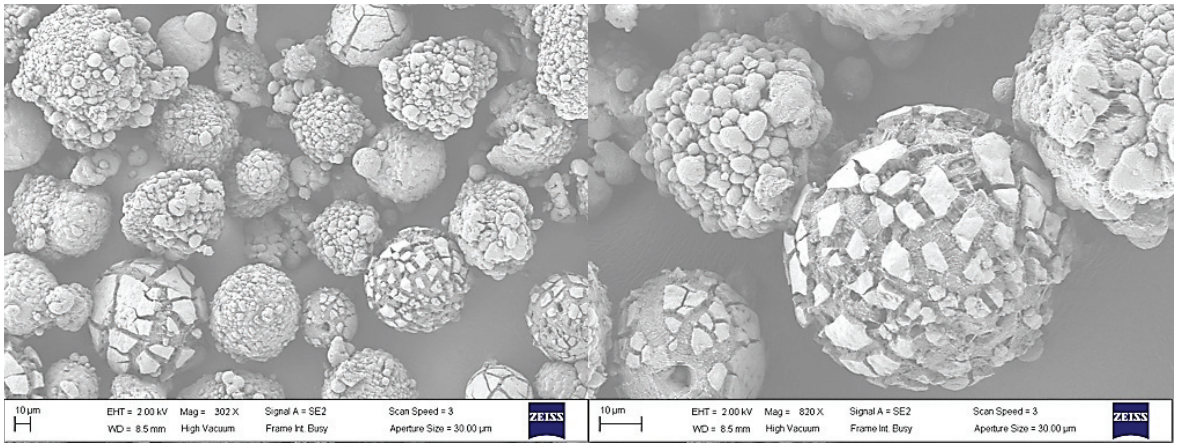

Figure 40: SEM analysis of polymer from 55 s reaction with CpZ 2. Gas feed: C2, 8 wt% 1-C6

As seen in the figures bellow, increasing the amount of 1-hexene to 16 w% in the gas feed does not generate a flagrant change in the particle morphology. In Figure 41, we see a particle growth pattern that seems different to those previously observed. The observed web structure can be related to the plasticized character of the formed polymer due to the higher amounts of comonomer. Nonetheless, still in Figure 41, the particles on the left the particles do not look particularly different to those obtained with lower amounts of comonomer.

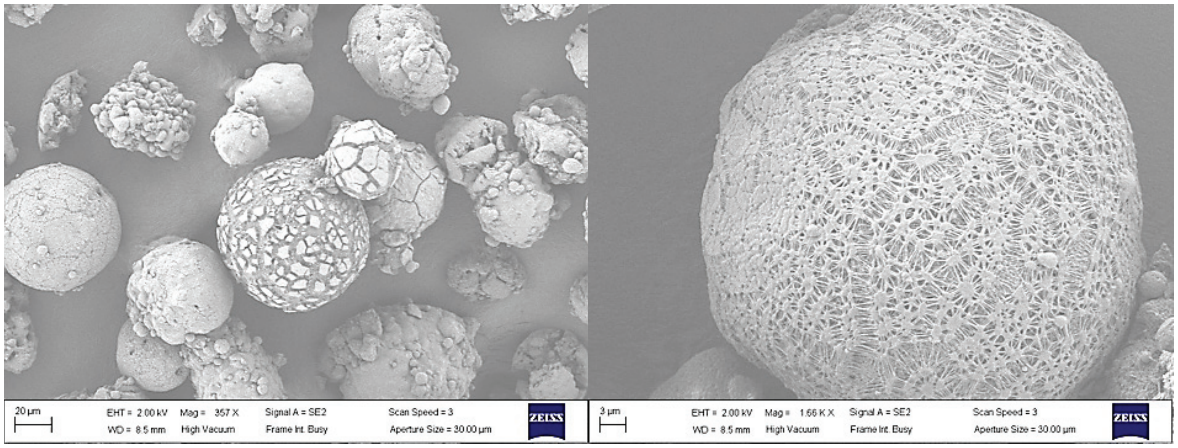

Figure 41: SEM analysis of polymer from 55 s reaction with CpZ 2. Gas feed: C2, 16 wt% 1-C6

SEM-EDX analysis results for samples obtained at the central point (ethylene and 8 wt% 1-hexene) with the classic metallocene catalyst are seen in Figures 42 and 43. At 5 seconds, we can see a layer of support is separated from its core, which suggests a layer-by-layer particle growth at very early stages. At 55 seconds, however, we observed (when comparing silica and carbon detections), that polymer formation in present at the particle core. This observation is coherent with the idea that the catalyst surface is inactive and polymer growth in the middle will cause fractures on the surface.

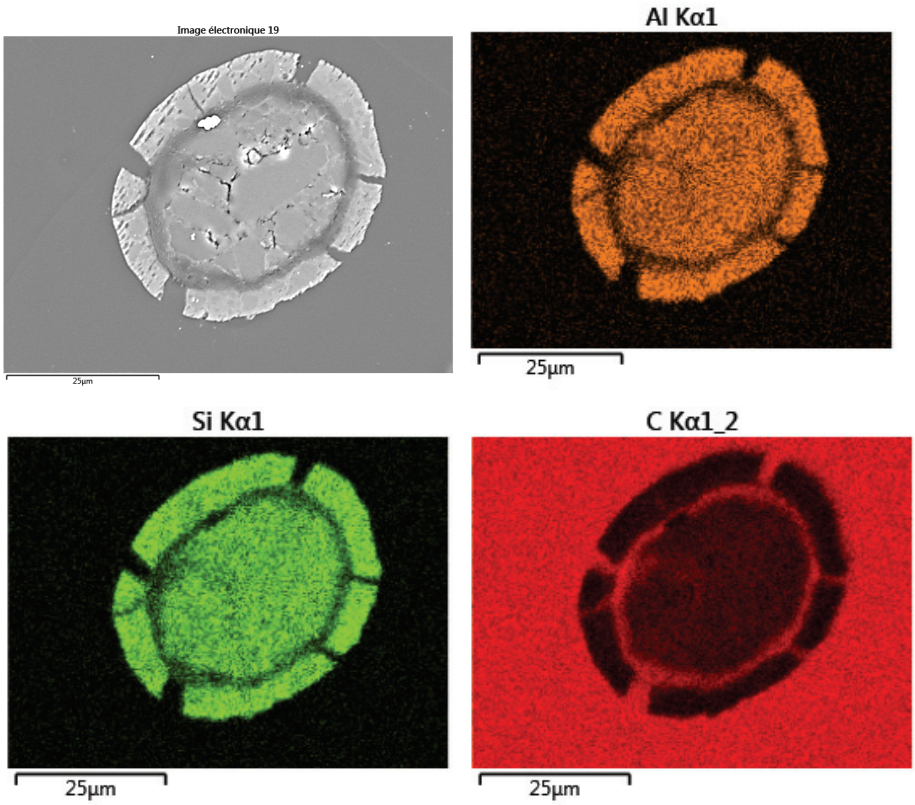

Figure 42: SEM-EDX of polymer from 5 s reaction with CpZ 2. Gas feed: C2, 8 wt% 1-C6

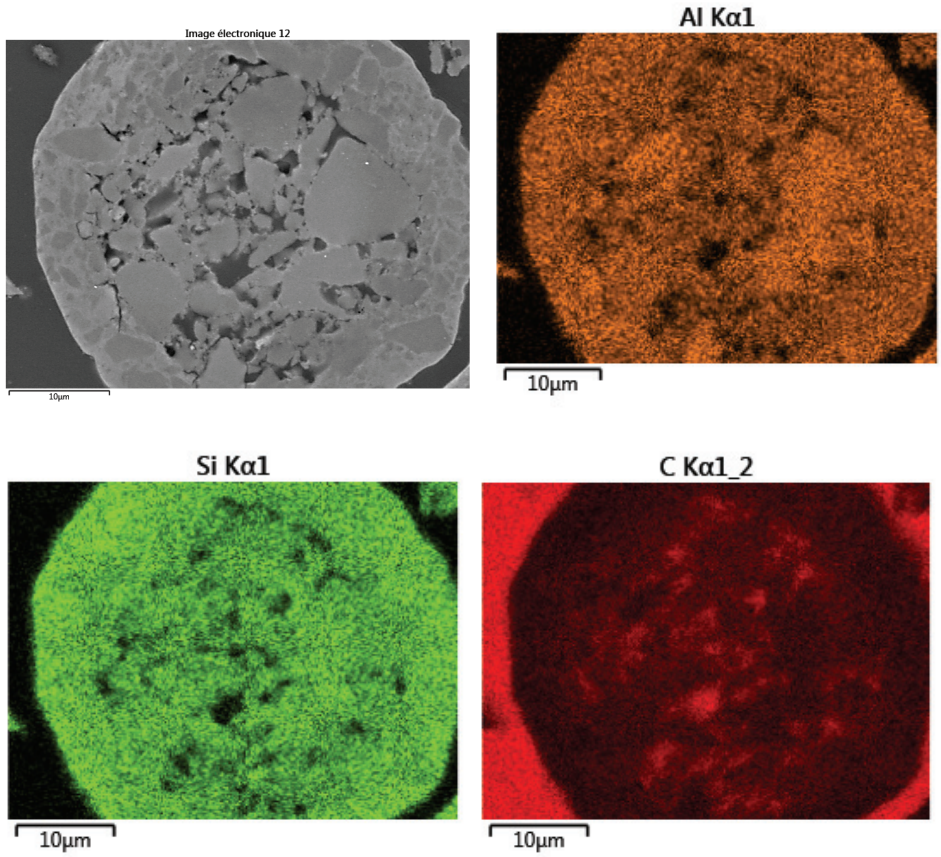

Figure 43: SEM-EDX of polymer from 55 s reaction with CpZ 2. Gas feed: C2, 8 wt% 1-C6

- **Constrained geometry - CGC M**

For the CGC catalyst used in this study, Figures 44 and 45 show the SEM images performed on polymers from homopolymerization reactions. At 5 seconds (Figure 44), no fractures can be seen on the particle surfaces and the overall particle diameter is pretty much equal to that of the original catalyst (d_{50}=40µm). At 60 seconds (Figure 45, the particle growth is noticeable and uniform and inactive silica surfaces are not visible.

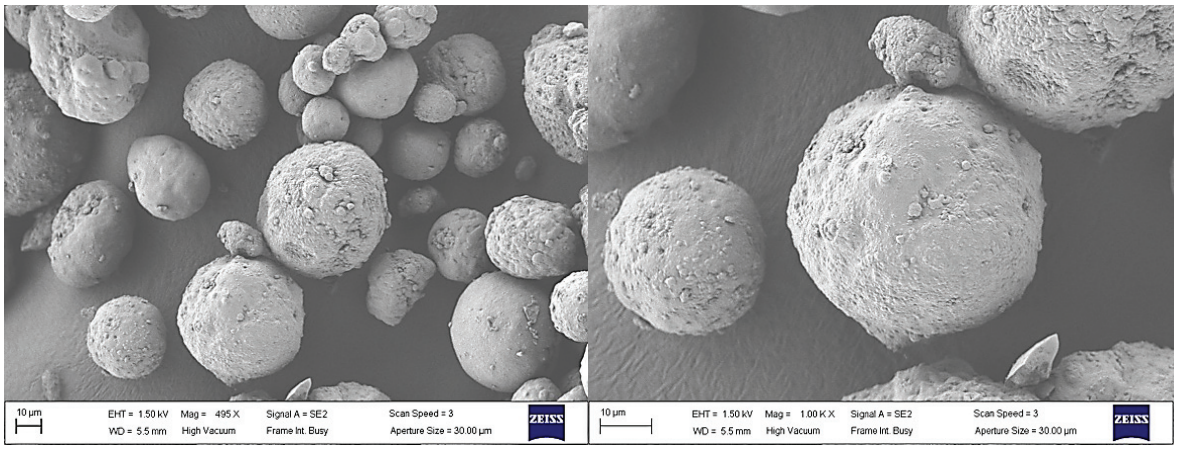

Figure 44: SEM analysis of polymer from 5 s reaction with CGC M. Gas feed: C2 only.

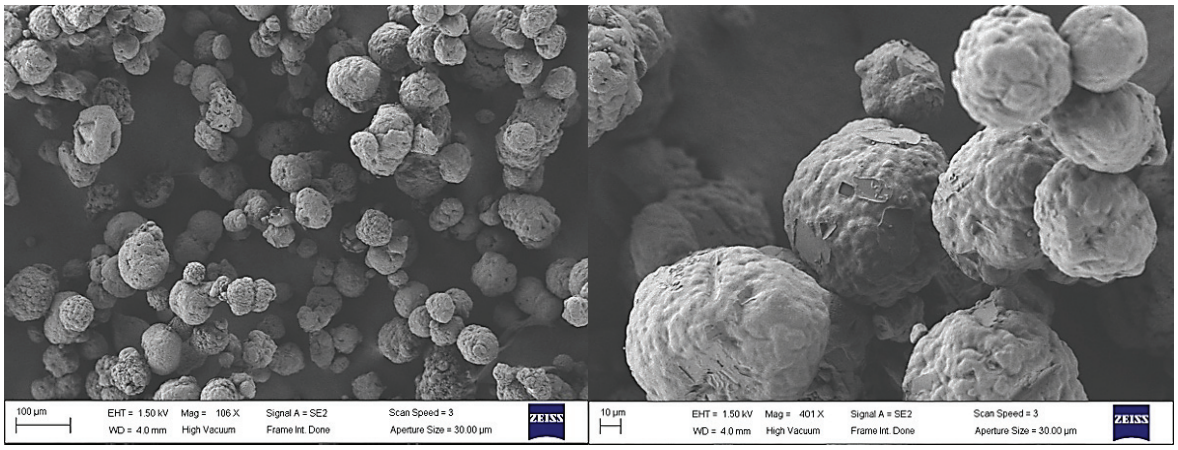

Figure 45: SEM analysis of polymer from 60 s reaction with CGC M. Gas feed: C2 only.

In Figures 46 to 48, we see polymer particles obtained at the central point of the DOE for this catalyst, which consists of ethylene, 8 wt% 1-hexene and 0.3 m% hydrogen in the gas feed. At 5 seconds (Figure 46), we see a few cracks on the particle surface but very little polymer formation. At 12.5 seconds, the fragments on the surface are visible and widespread. This can be related to the fast activation profile observed for this catalyst. At 60 seconds (Figure 48), the particles have grown significantly, but we observe different shapes (as well as imprint from the salt particles) that could suggest variable crystallization rates for different particles. In all cases, we can see how a given batch of catalysts have particles that behave in very different ways.

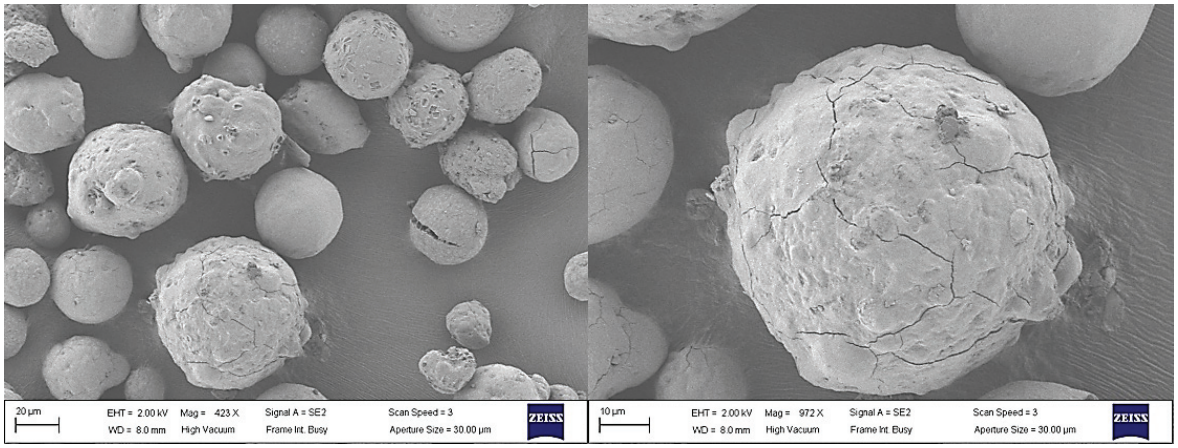

Figure 46: SEM analysis of polymer from 5 s reaction with CGC M. Gas feed: C2, 8 wt% 1-C6, 0.3 m% H2.

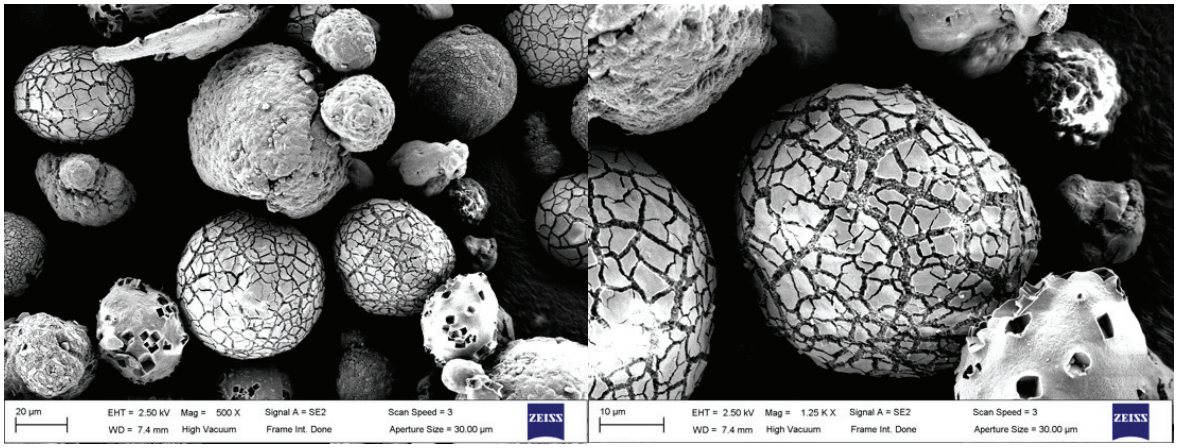

Figure 47: SEM analysis of polymer from 12.5 s reaction with CGC M. Gas feed: C2, 8 wt% 1-C6, 0.3 m% H2.

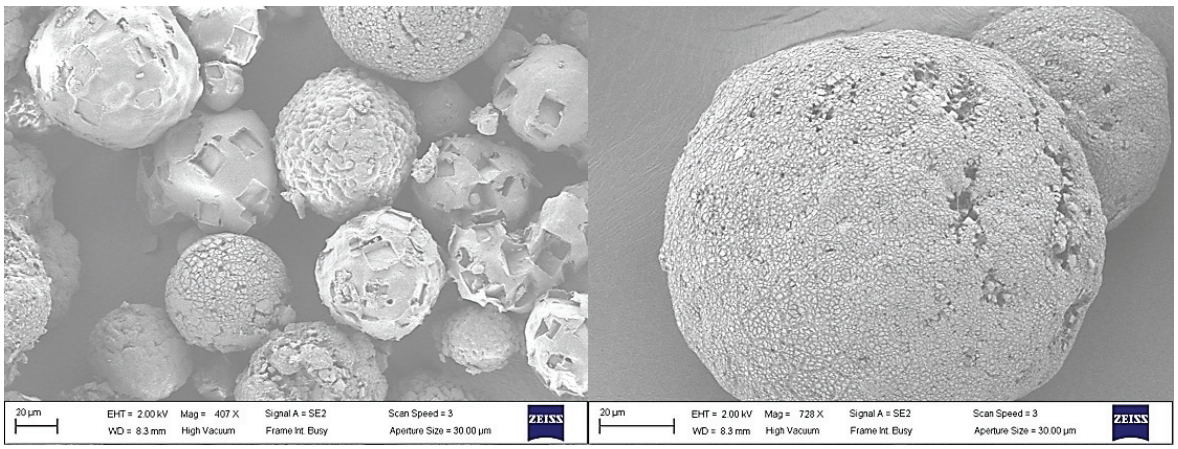

Figure 48: SEM analysis of polymer from 60 s reaction with CGC M. Gas feed: C2, 8 wt% 1-C6, 0.3 m% H2.

Variations on the central point experimental conditions can be seen in Figure 49 and 50. When increasing the hydrogen concentration in the feed to 1.5 m% at a 12.5 second reaction, the observed particles seem to behave in the same way as those obtained at the central point of the DOE (8 wt% 1-hexene and 0.3 m% hydrogen), with similar cracking patterns on the surface and comparable particle size. When increasing the amount of comonomer to 16 wt% in the feed at a 12.5 second reaction, the

obtained particles are comparable to those obtained at the central point conditions. These observations are coherent with the effects detected in the statistical interpretations of the polymer thermal properties, in which the reaction time was the main factor influencing the crystallinity of the polymers.

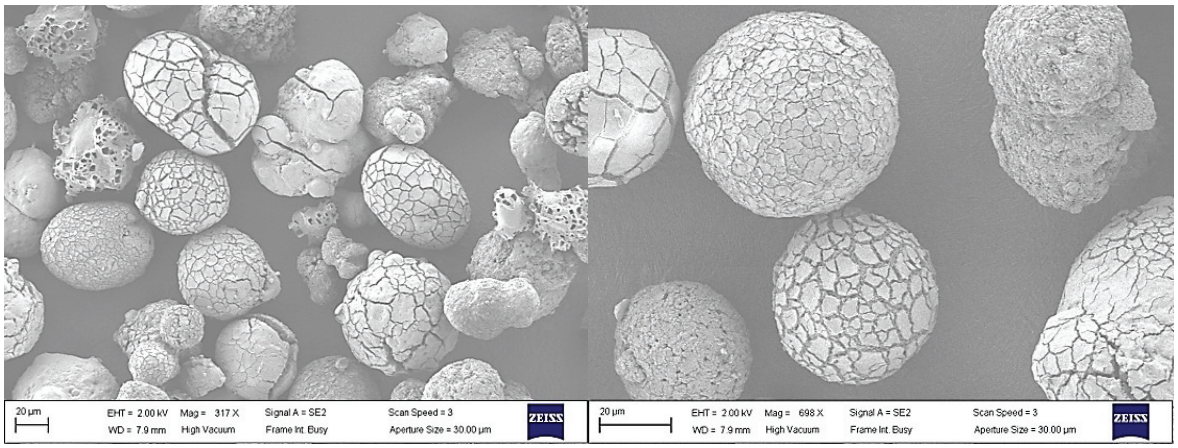

Figure 49: SEM analysis of polymer from 12.5 s reaction with CGC M. Gas feed: C2, 8 wt% 1-C6, 1.5 m% H2.

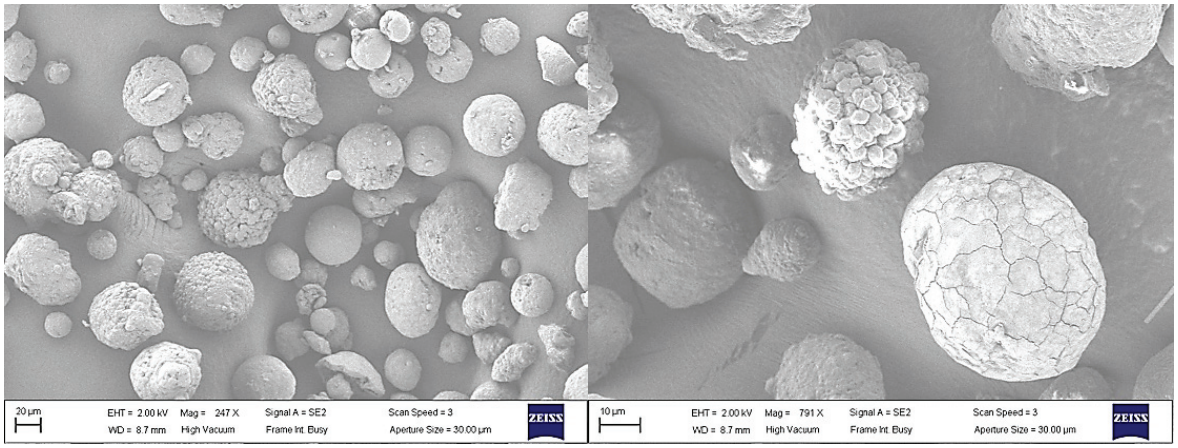

Figure 50: SEM analysis of polymer from 12.5 s reaction with CGC M. Gas feed: C2, 16 wt% 1-C6, 0.3 m% H2

SEM-EDX analysis results for samples obtained at the central point (ethylene, 8 wt% 1-hexene and 0.3 m% hydrogen), are seen in Figure 51. At 5 seconds, we can see that polymer formation in already visible at the particle core. This observation is coherent with what was observed for the classic metallocene catalyst, as well as the fact that the CGC catalyst presented higher activities at the reaction start.

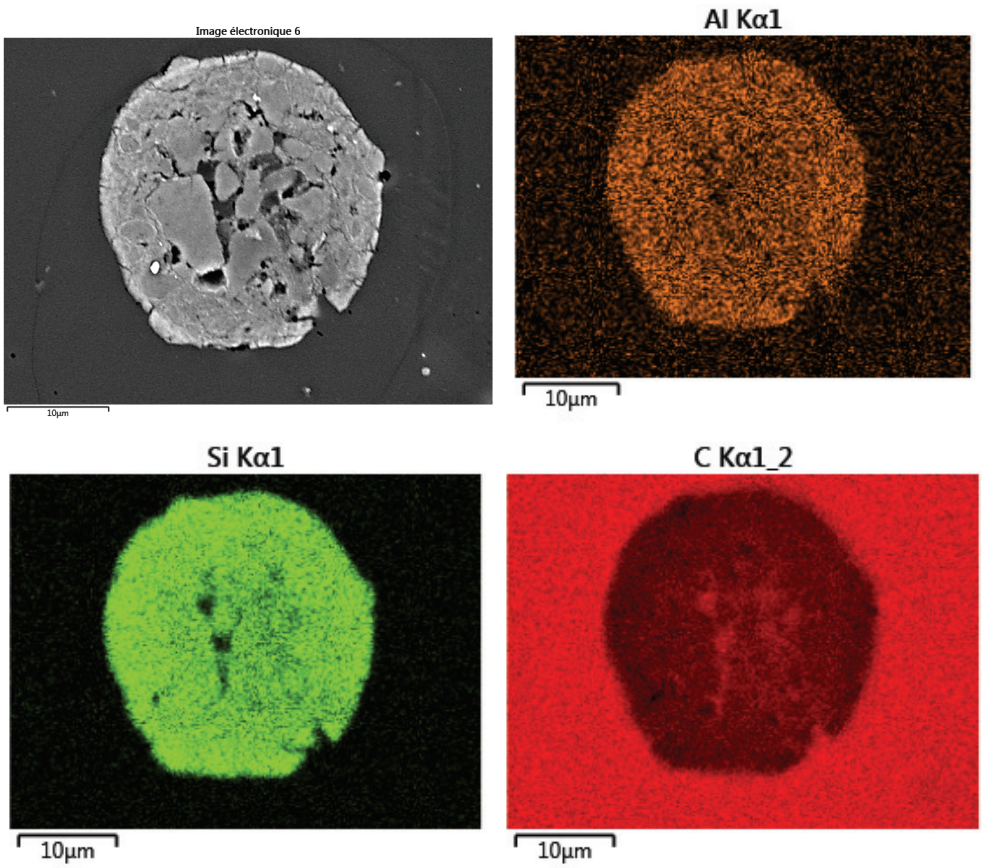

Figure 51: SEM-EDX of polymer from 5 s reaction with CGC M. Gas feed: C2, 8 wt% 1-C6, 0.3 m% H2

3.4. Conclusion

With the novel stopped-flow reactor, we have compared two different families of metallocene catalysts in terms of their kinetics, polymer properties and particle morphologies at short reaction times. For this purpose, we have followed an Experimental Design to assess the impact of different reaction conditions (reaction time and composition of the gas feed) on the catalyst behavior.

The classic metallocene catalyst used in this study (CpZ 2), which is known to produce H2 in situ, was assessed in terms of reaction duration and comonomer content (1-Hexene) in the continuous gas feed. For this catalyst, the performed statistical evaluation indicated that the reaction time is the main influencer on the polymerization yield, as well as on the development of polymer properties (average molecular weights, crystallinities and melting temperatures).

The constrained geometry metallocene catalyst used in this study (CGC M) was assessed in terms of reaction duration, comonomer content (1-Hexene) and hydrogen content in the continuous gas feed. For this catalyst, the statistical interpretation of results indicated that polymer melting temperatures are mainly influenced by the comonomer content in the gas feed, which is in agreement with the higher capacity of this catalyst for incorporation of α-olefins.

For both studied catalysts, the polymer crystallinity was primarily affected by the reaction time. This was confirmed by the DSC analysis performed at increasing reaction times.

In addition, we performed a qualitative study on the evolution of polymer morphology in the different studies reaction conditions. The SEM observations allowed a similar conclusion as the statistical analysis, and the reaction time seems to be the main factor contributing to the reaction yield and thus, to the size of the observed particles. In the assessed timeframes, we observed the presence of inert support fragments at the exterior of the particles. Moreover, SEM-EDX analysis results for both catalysts suggested that the polymer formation begins at the center of the particle and 'pushes' outwards in the growth process.

The predictions from the regression model were evaluated with precaution, given the low values obtained for R squared reflecting the discrepancy of measured and estimated results. Even so, the observed results were in agreement with inputs from the catalyst provider.

Nonetheless, our aim with the statistical analysis of results was to interpret the relation between cause and effect of different parameters varied simultaneously while reducing the number of experiments. If the goal is to perform a statistical evaluation for prediction purposes, more experiments are needed to account for the variability that is inherent to the experimental preparation.

At last, this case study demonstrated how the novel stopped-flow reactor is a useful tool for gaining insights on aspects such as catalyst kinetics, evolution of polymer properties and particle fragmentation at early reaction times.

4. Chapter conclusions

In this chapter, we have demonstrated how the novel stopped-flow reactor is a useful tool in studying different aspects related to the nascent phase of the polymerization.

In the first application, we have synthesized two metallocene catalysts using different silica supports to evaluate the impact of the pore size on the catalyst behavior. The catalysts were evaluated in terms of kinetics and morphology evolution at full-time and short-time polymerization reactions with ethylene. The kinetic studies indicated that the silica with bigger pores led to fast catalyst activation, higher initial followed by quick deactivation. On the other hand, smaller pores led pores led to a more mild activation profile. In both cases, the overall polymerization rates were quite low. Morphology observations by SEM and SEM-EDX of polymers obtained with the stopped-flow reactor indicated similar conclusions. The silica with bigger pores led to faster particle growth and loss of morphology control at 90 seconds of reaction, which we linked to possible heat transfer resistance at the particle level. Likewise, the silica with smaller pores generated polymers with much less visible polymer, a reflection of the low reaction rates. From these assessments, we concluded that the tested silica supports are perhaps not suited for applications in olefin polymerization. This case study demonstrated how the novel reactor is a useful tool in studying catalyst kinetics and morphology development at early stages.

In the second application, we studied the effect of different reaction conditions on two families of supported metallocene catalysts. We followed a design of experiments and combined the statistical evaluation of results with experimental data on thermal properties and qualitative interpretation of the particle morphologies. The statistical approach indicated that the main factor of influence in the reaction kinetics and polymer properties at early reaction times (<60s) is the duration of the reaction. For the CGC catalyst, the comonomer content in the continuous gas feed was detected as a factor of influence for the polymer thermal properties, which is coherent given the higher capacity of such catalysts in incorporating α-olefins. Moreover, we systematically followed the crystallization and melting temperature profiles for different compositions of the gas-phase at increasing reaction times. The thermal profiles suggested an effect of confinement of the growing polymer in the porosity of the support for short reaction times. We interpreted these observations as another indication that the reaction time is the main factor controlling particle growth and, therefore, the crystallization process (when the same experimental conditions are kept). At last, morphological observations with SEM indicated a similar trend, which we judged by the particles average size and general observation of polymer formation on the surfaces. These microscopy analysis showed the presence of inert support fragments at the exterior of the polymer particles in reactions shorter than 60 seconds. Moreover, SEM-EDX analysis provided similar results for both catalysts, indicating the polymer formation begins at the core of the particle and proceeds outwards, an observation that suggests the catalyst surface is, indeed, inactive.

At last, the predicted reaction rates at early stages (<60 seconds) captured similar trends as those observed for longer reaction times (60 minutes), for all catalysts used in this chapter. This is yet another indication that the novel set-up (hardware and software components) can be used to provide clues on the catalyst kinetic behavior under industrially representative conditions.

To conclude, in this chapter we presented a few examples that demonstrate the capability of the novel stopped-flow reactor in the studying catalyst kinetics, polymer properties, morphology evolution and

the potential of using this tool for catalyst screening purposes, all in industrially meaningful experimental conditions. As we have seen throughout this project, the conclusion of this work provides an extensive ray of possibilities for advances in the study of the nascent phase of the polymerization. On the following chapter, we will discourse on the main conclusions of this PhD research project and a few perspectives for future works.

5. References

(1) Tisse, V. F.; Boisson, C.; Prades, F.; McKenna, T. F. L. A systematic study of the kinetics of polymerisation of ethylene using supported metallocene catalysts - ScienceDirect https://www-sciencedirect-com.docelec.univ-lyon1.fr/science/article/pii/S1385894709008407 (accessed Jan 11, 2020).

(2) Tisse, V. F.; Briquel, R. M.; McKenna, T. F. L. Influence of Silica Support Size on the Polymerisation of Ethylene Using a Supported Metallocene Catalyst. *Macromol. Symp.* **2009**, *285* (1), 45–51. https://doi.org/10.1002/masy.200951106.

(3) Bashir, M. A. Impact of Physical Properties of Silica on the Reaction Kinetics of Silica Supported Metallocenes and Polyethylene Morphology. phdthesis, Université de Lyon, 2016.

(4) Bashir, M. A.; Monteil, V.; Boisson, C.; McKenna, T. F. L. Experimental Proof of the Existence of Mass-Transfer Resistance during Early Stages of Ethylene Polymerization with Silica Supported Metallocene/MAO Catalysts. *AIChE J.* **2017**, *63* (10), 4476–4490. https://doi.org/10.1002/aic.15806.

(5) Tisse, V. F. Kinetics and Morphology of Metallocene Catalysts Used in Ethylene Polymerisation, PhD. 2006.

(6) Kumkaew, P.; Wu, L.; Praserthdam, P.; Wanke, S. E. Rates and Product Properties of Polyethylene Produced by Copolymerization of 1-Hexene and Ethylene in the Gas Phase with (n-BuCp)2ZrCl2 on Supports with Different Pore Sizes. *Polymer* **2003**, *44* (17), 4791–4803. https://doi.org/10.1016/S0032-3861(03)00473-7.

(7) Tioni, E.; Spitz, R.; Broyer, J. P.; Monteil, V.; McKenna, T. Packed-Bed Reactor for Short Time Gas Phase Olefin Polymerization: Heat Transfer Study and Reactor Optimization. *AIChE J.* **2012**, *58* (1), 256–267. https://doi.org/10.1002/aic.12576.

(8) Gaillard, C.; Despois, J. F.; Mortensen, A. Processing of NaCl Powders of Controlled Size and Shape for the Microstructural Tailoring of Aluminium Foams. *Mater. Sci. Eng. A* **2004**, *374* (1), 250–262. https://doi.org/10.1016/j.msea.2004.03.015.

(9) Bashir, M. A.; Vancompernolle, T.; Gauvin, R. M.; Delevoye, L.; Merle, N.; Monteil, V.; Taoufik, M.; McKenna, T. F. L.; Boisson, C. Silica/MAO/(n-BuCp)2ZrCl2 Catalyst: Effect of Support Dehydroxylation Temperature on the Grafting of MAO and Ethylene Polymerization. *Catal. Sci. Technol.* **2016**, *6* (9), 2962–2974. https://doi.org/10.1039/C5CY01285F.

(10) Van Grieken, R.; Carrero, A.; Suarez, I.; Paredes, B. Ethylene Polymerization over Supported MAO/(NBuCp)2ZrCl2 Catalysts: Influence of Support Properties. *Eur. Polym. J.* **2007**, *43* (4), 1267–1277. https://doi.org/10.1016/j.eurpolymj.2007.01.008.

(11) Bianchini, D.; dos Santos, J. H. Z.; Uozumi, T.; Sano, T. Characterization of MAO-Modified Silicas. *J. Mol. Catal. Chem.* **2002**, *185* (1), 223–235. https://doi.org/10.1016/S1381-1169(02)00047-X.

(12) Panchenko, V. N.; Semikolenova, N. V.; Danilova, I. G.; Paukshtis, E. A.; Zakharov, V. A. IRS Study of Ethylene Polymerization Catalyst SiO2/Methylaluminoxane/Zirconocene. *J. Mol. Catal. Chem.* **1999**, *142* (1), 27–37. https://doi.org/10.1016/S1381-1169(98)00275-1.

(13) Tioni, E.; Monteil, V.; McKenna, T. Morphological Interpretation of the Evolution of the Thermal Properties of Polyethylene during the Fragmentation of Silica Supported Metallocene Catalysts. *Macromolecules* **2013**, *46* (2), 335–343. https://doi.org/10.1021/ma302150v.

(14) Martino, A. D.; Weickert, G.; McKenna, T. F. L. Contributions to the Experimental Investigation of the Nascent Polymerisation of Ethylene on Supported Catalysts, 1. *Macromol. React. Eng.* **2007**, *1* (1), 165–184. https://doi.org/10.1002/mren.200600013.

(15) Trefz, T. K.; Henderson, M. A.; Wang, M. Y.; Collins, S.; McIndoe, J. S. Mass Spectrometric Characterization of Methylaluminoxane. *Organometallics* **2013**, *32* (11), 3149–3152. https://doi.org/10.1021/om400256f.

(16) Babushkin, D. E.; Semikolenova, N. V.; Panchenko, V. N.; Sobolev, A. P.; Zakharov, V. A.; Talsi, E. P. Multinuclear NMR Investigation of Methylaluminoxane. *Macromol. Chem. Phys.* **1997**, *198* (12), 3845–3854. https://doi.org/10.1002/macp.1997.021981206.

(17) Babushkin, D. E.; Brintzinger, H.-H. Activation of Dimethyl Zirconocene by Methylaluminoxane (MAO)Size Estimate for Me-MAO- Anions by Pulsed Field-Gradient NMR. *J. Am. Chem. Soc.* **2002**, *124* (43), 12869–12873. https://doi.org/10.1021/ja020646m.
(18) Modelling Induced Tension in a Growing Catalyst/Polyolefin Particle: A Multi-Scale Approach for Simplified Morphology Modelling - Di Martino - 2007 - Macromolecular Reaction Engineering - Wiley Online Library https://onlinelibrary-wiley-com.docelec.univ-lyon1.fr/doi/full/10.1002/mren.200600036?casa_token=LEzEycpyGh4AAAAA%3AR81GE617e0lf5YRcAkBfqVYit_gWTX-bAAILtGUs3gIeZ80Q6Fs1zkKR6TIo7NUWKvGAOf0YlWvs1u0 (accessed Mar 28, 2020).
(19) Box, G. E. P. *Statistics for Experimenters : An Introduction to Design, Data Analysis, and Model Building*; Wiley, 1978.
(20) E. P. Box, G.; Hunter, J. S.; Hunter, W. G. Statistics for Experimenters: Design, Innovation, and Discovery, 2nd Edition https://www.wiley.com/en-az/Statistics+for+Experimenters%3A+Design%2C+Innovation%2C+and+Discovery%2C+2nd+Edition-p-9780471718130 (accessed Jan 17, 2019).
(21) Dean, R. B.; Dixon, W. J. Simplified Statistics for Small Numbers of Observations. *Anal. Chem.* **1951**, *23* (4), 636–638. https://doi.org/10.1021/ac60052a025.
(22) Rorabacher, D. B. Statistical Treatment for Rejection of Deviant Values: Critical Values of Dixon's "Q" Parameter and Related Subrange Ratios at the 95% Confidence Level. *Anal. Chem.* **1991**, *63* (2), 139–146. https://doi.org/10.1021/ac00002a010.

Chapter 5

Conclusions and perspectives

Chapter 5: Content

1. Conclusions 189
2. Perspectives 193
3. References 194

1. Conclusions

In this PhD research work, we developed a novel state-of-the-art stopped-flow reactor that successfully allows one to study early stages of gas phase olefin polymerization in industrially representative conditions. The central focus of this project was to provide a tool that improved on the existing methods originally developed for this purpose (mainly in regards to heat evacuation limitations), and expand the array of possible experimental conditions to permit working with different gas mixtures at moderate temperatures, pressures and superficial gas velocities. The novel stopped-flow reactor developed during this work was a product of our innovative approach towards the reactor geometry and the tailored execution from a specialized engineering firm. In this PhD thesis, we demonstrated that the novel tool effectively satisfied our initial goals and represents an important achievement in the investigation of the nascent phase.

The principal motivations for this PhD project were reviewed in chapter 1, where we highlighted the importance of studying early stages of the polymerization in order to better understand the factors that govern catalyst kinetics and optimum control of the polymerization reaction outcomes. As we have seen, working with heterogeneous catalysts entails several complexities that are particularly prominent at the very beginning of the reaction, when the risk of potential heat and mass transfer resistances is most pronounced. The particle growth and morphology evolution are governed by the particle break-up process. The fragmentation step is, in its turn, dependent on the catalyst kinetics and the physical and mechanical properties of the support and forming polymer. The reaction kinetics itself is subjected to the temperature and concentration profiles inside the particles, all of which will also affect the qualities of the final product. For instance, non-negligible mass transfer limitations at the particle level can lead to inhomogeneous particle growth that can compromise the quality of the polymer and the functioning of the reactor. Moreover, heat transfer limitations can lead to particle overheating followed by polymer softening, diffusion limitations due to pore clogging and, finally, catalyst deactivation. As we can see, the phenomena governing the polymerization reaction in its earliest stages form an interconnected web of cause and effect that require precise control to ensure the quality of the entire process. At this point, it is clear that understanding such phenomena is of major economic interest, given the importance of the polyolefin market.

Nonetheless, experimentally studying such short timeframes requires adapted tools that can capture the rapidity of the changes taking place and, ideally, to follow the catalyst kinetics and evolution of the polymer properties, all while maintaining reaction conditions that are representative of heat and mass transfer phenomena present in industrial scales. As we saw in chapter 1, a number of different techniques have been employed in the attempt of studying the early stages of the polymerization. Nonetheless, none seems as promising as the stopped-flow technique in maintaining the *realistic* nature of the experiment. Important advances have been achieved in the understanding of catalyst kinetics and evolution of particle morphology for heterogeneous catalysts during the nascent phase while using the stopped-flow technique. Nonetheless, most of the works found in the open literature were performed in the slurry phase and the options for studying such phenomena in gas-phase conditions were modest; in fact, to the best of our knowledge, this has only been attempted in our research group. Previous works showed the potential of the stopped-flow technique for studying the impact of reaction conditions on heat transfer and particle fragmentation in gas-phase. [1–4] Nonetheless, the existing tools presented a number of practical limitations, mainly related to poor heat evacuation and overall lack of equipment robustness. Besides, the experimental conditions allowed with such tools were limited as the system was not adapted for injecting liquids in a controlled manner in the reaction zone. Moreover, the construction of the reactor itself led to imprecise measurements of the reaction temperature, which was detrimental to the correct interpretation of the reaction kinetics. Given the promising applications of this technology in the study of early stages, the focus of the current project was on the improvement of such tools.

In chapter 2, we described the development of a novel stopped-flow reactor that aimed to tackle issues observed with the previous tools, mainly related to poor heat evacuation and the presence of non-negligible temperature gradients in the reaction bed. Our first step was to propose a reactor prototype with an annular geometry in order to improve the gas distribution in the reactor and thus, tackle the main issues of poor heat evacuation and imprecise temperature measurements observed with the previous tools. From the assessment of the reactor prototype, we confirmed the positive impact of the annular geometry from lower temperature excursions observed during the polymerization reactions, as well as similar polymerization yields obtained from the use of different types of inert seedbed for catalyst dispersion. We concluded the novel geometry had great potential for studying the nascent phase in gas-phase under controlled conditions. However, several limitations were still encountered, mainly due to the 'do-it-yourself' character of the set-up construction. The reactor prototype was built from available marketed parts and the dimensions made handling and maintaining inertness in the bed a real challenge. The set-up provided poor thermal response, as the heating bath was often not efficient in ensuring stable reaction temperatures. Besides, the set-up was not adapted for a wide range of experimental conditions, such as working with different gas mixtures or in condensed mode. It became clear to us that the professional engineering of this reactor tool would overcome most of the observed limitations. We worked in collaboration with a specialized company focused on providing tailored technical solutions (ILS, Berlin). We presented ILS with the reactor design (annular geometry), the main constraints related to the operation of stopped-flow reactors (mainly proper sealing, ease in handling and precise control of the reaction conditions), as well as the possibility of injecting different process gases (some of which are liquids at room temperature) at a range of temperatures, pressures and gas superficial velocities that are representative of industrial reactors.

The hardware component developed with ILS was validated through a thorough experimental assessment, described in chapter 2. The new set-up included a number of improvements. One of the biggest advances with the new set-up was the fact that the reactors were custom made. While keeping the same annular design as the reactor prototype, the dimensions of the novel reactors were optimized to facilitate handling, reduce potential pressure drops and, most importantly, to allow sealing the reactors with crimp caps inside the glove box. The experimental capacity was highly improved with the new set-up by the possibility of injecting several gases (e.g. different monomers, hydrogen) and the incorporation of an CEM evaporator that permits injecting components that are liquid at room temperature (e.g. 1-hexene, n-pentane). The new set-up allowed the operation of three stopped-flow reactors in a sealed heating chamber, which showed to significantly improve the thermal response of the system in relation to the previous versions. The use of Coriolis mass-flow controllers adapted to a wide range of operation conditions allowed the accurate control of pressures and flowrates during the reaction, in gas superficial velocities as high as 50 cm/s. The successful completion of the novel professionally engineered stopped-flow reactor represented an important milestone in the current project, as the new tool fulfilled our end-goal of obtaining an improved tool to perform gas-phase polymerizations at short reaction times with accurate control of reaction conditions, all while working in an inert environment.

The new stopped-flow tool included both a hardware and a software components to be used together in order to optimize the extraction and interpretation of the experimental data. In chapter 3, we have reviewed the development of the software component, which consisted of a reactor model and state-observer for the novel set-up. The software component was developed in order to estimate the overall polymerization rates from the temperature measurements and, thus, overcome the one-point character of such experiments (which provide no real information on the catalyst kinetics). For this purpose, a simplified one-dimensional model at the macromolecular level was selected to estimate the rate of polymerization at each moment of the reaction. The implemented model was validated with experimental data and the accuracy of the simplifying assumptions was assessed with a sensitivity

study. We observed that the estimated temperatures of the reacting phase (comprised of catalyst and polymer as a pseudo-homogeneous phase) were only slightly higher than those estimated for the inert and gas components of the reaction bed. These observations were in agreement with the experimental assessment carried out in chapter 2, where we concluded on a significant improvement in the evacuation of the heat of reaction with the annular reactor geometry. At last, we implemented a single-element High-Gain Observer to allow access to unmeasured states of the system, mainly the evolution of the reaction rates. The state estimator was validated with experimental data and the calculated reaction rates for short reaction times (<60 seconds) were coherent with those observed experimentally in full-time polymerization conditions (60 minutes).

In chapter 4, after satisfactory conclusion of the hardware and software components for the novel stopped-flow reactor, we demonstrated the usefulness of the new tool in specific case studies with different silica supported metallocene catalysts.

In the first application, we investigated the role of the physical properties of the silica support on the kinetic behavior and polymer properties for MAO-activated metallocene catalysts. As previously discussed, the properties of the inorganic support play a crucial role in the process of particle fragmentation and, therefore, growth process. Understanding how different physical and mechanical properties impact the catalyst behavior is crucial for the improvement of existing processes, as well as for the design of tailored catalysts. The effect of different aspects of the support properties (e.g. particle size, pore structure) have been previously investigated in a number of works.[5–10] Nonetheless, a clear picture of the effect of the support porosity on the catalyst behavior is still not available as different studies derived diverging conclusions. We synthesized two metallocene catalysts with silica supports of different pore sizes and evaluated the outcome in terms of catalyst kinetics, polymer properties and particle morphology by SEM and EDX. The trend observed was quite clear; the silica support with bigger pores (23.3 nm) led to faster polymerization rates, followed by quick catalyst deactivation. The same was observed on the morphology assessment with SEM, in which we saw a loss of control in the particle morphology from 90 seconds of the reaction. On the contrary, smaller silica pores (11 nm) led to a gradual activation profile, which was reflected on little polymer formation on the catalyst particles. We observed no clear impact of the pore structure on the polymer thermal properties and molecular weights. At last, the overall activities for both catalysts were quite low; indicating that perhaps the used silica are not appropriate for applications in olefin polymerization.

In the second case study, we compared the effect of various reaction conditions (i.e. reaction time, 1-hexene and hydrogen contents in the gas feed) on two different families of metallocene catalysts: one classic zirconocene and one CGC. We applied an experimental design to assess the impact of the different reaction conditions on the catalysts kinetic behavior and polymer properties. Despite the low values of R-squared obtained from the statistical evaluation (discussed in the Perspectives section), the predicted behavior trends were coherent with those observed by the catalyst supplier. For both catalysts, the statistical evaluation indicated that the reaction duration is the main factor of impact on the polymerization yield. For the CGC catalyst, the content of 1-hexene was detected as the main factor of impact on the polymer thermal properties, which is somewhat expected given the higher capacity for this family of metallocenes to incorporate α-olefins. Moreover, we combined the statistical evaluation of results with experimental data on the evolution of the polymer thermal properties. This assessment showed a gradual increase of the polymer crystallinity that seemed to be more dependent on the reaction duration than the composition of the gas feed.

Finally, the qualitative interpretation of SEM and EDX observations for all supported metallocene catalysts studied in this chapter indicated the presence of polymer at the particle core, from early stages of the reaction. We took this as sign that the particle growth begins at the center of the particle and proceeds outwards, an observation that suggests the catalyst surface is, indeed, inactive. In addition, the application of the developed software component estimated reaction rates at early stages (<60 seconds) that followed a comparable trend as those observed for full-polymerization conditions. This was another indication as to how the novel set-up can be used for the rapid evaluation of catalyst performance.

To conclude, we consider to have successfully achieved the initial goal of this PhD project as to provide an optimized experimental tool for studying early stages of gas phase olefin polymerization. As we have seen throughout this work, the novel tool allows for a multitude of interesting applications; some of which will be proposed in the following section.

2. Perspectives

Concerning the software component developed in chapter 3, we proposed a simplified one-dimensional model to describe the reactor and predict reaction rates from the experimental data. In the development of the software proposed in this work, we neglected the possibility of concentration and temperature gradients at the particle level. Nonetheless, as indicated by a number of MGM-based modeling works, the risk of mass and heat transfer resistances is more pronounced at the beginning of the polymerization reaction. [50,51,67,69] Therefore, accounting for such phenomena with a more detailed modelling effort would be a valuable addition to the current work. Moreover, in the current work, the model was developed for ethylene as the only reaction gas but extending it for multiple components should be relatively straightforward. Given the novel stopped-flow reactor allows a wide range of operation conditions, such as injection of hydrogen and liquid components in the feed stream; it would be interesting that the software component is adapted to interpret the reaction kinetics in cases of condensed mode operation and copolymerization reactions.

In chapter 4, we performed an investigation on the impact of silica pore structure on the behavior of supported metallocene catalysts. The observed trends were clear for the two catalysts synthesized for the study. Nonetheless, a more thorough assessment with different probes could confirm (or refute) our observations. In all cases, performing systematic SEM-EDX analysis from polymers obtained at short reaction times with different silica supports would be beneficial.

In chapter 4, the impact of different reaction conditions on catalyst behavior was assessed through a statistical evaluation of the experimental results. Nonetheless, mainly due to time constraints, we did not complete a full assessment of the polymer properties. The completion of such as assessment for the polymer average molecular weights, polydispersity indexes and comonomer contents could be an interesting suggestion for future works and could lead to interesting insights on chain development and comonomer incorporation at early stages. Concerning the statistical evaluation of the results, we obtained low values for the R-squared coefficient, which reflects the discrepancy between measured and estimated results. Given that our aim with the statistical evaluation was not quantitative and that the observed trends were confirmed by the catalyst provider, we took this with a grain of salt. If one wishes to perform a statistical assessment for prediction purposes with the novel set-up, more repetitions of the experiments are needed in order to account for the variability that is inherent to the experimental preparation and, in many cases, to the fact that catalysts of the same batch might react differently.

At last, the current work provided experimental data mainly on the behavior of supported metallocene catalysts. Expanding this investigation to other types of heterogeneous catalysts (Phillips or Ziegler-Natta) could provide a rich set of reliable data for insights on the catalyst kinetics and morphology evolution. In case of applications with Ziegler-Natta catalysts, the current set-up is not adapted for the injection of alkylated agents. This means that the catalysts must be pre-activated and suffer a long pre-contact period that could impair the validity of any conclusions. Ideally, the set-up should allow the injection of aluminum-alkyls in order to activate the catalysts in-situ. This is not an easy task, but perhaps the installation of traps for alkyl agents could be a possible solution to the problem.

3. References

(1) Tioni, E.; Broyer, J. P.; Spitz, R.; Monteil, V.; McKenna, T. F. L. Heat Transfer in Gas Phase Olefin Polymerisation. *Macromol. Symp.* **2009**, *285* (1), 58–63. https://doi.org/10.1002/masy.200951108.

(2) Tioni, E.; Spitz, R.; Broyer, J. P.; Monteil, V.; McKenna, T. Packed-Bed Reactor for Short Time Gas Phase Olefin Polymerization: Heat Transfer Study and Reactor Optimization. *AIChE J.* **2012**, *58* (1), 256–267. https://doi.org/10.1002/aic.12576.

(3) Tioni, E.; Monteil, V.; McKenna, T. Morphological Interpretation of the Evolution of the Thermal Properties of Polyethylene during the Fragmentation of Silica Supported Metallocene Catalysts. *Macromolecules* **2013**, *46* (2), 335–343. https://doi.org/10.1021/ma302150v.

(4) McKenna, T. F. L.; Tioni, E.; Ranieri, M. M.; Alizadeh, A.; Boisson, C.; Monteil, V. Catalytic Olefin Polymerisation at Short Times: Studies Using Specially Adapted Reactors. *Can. J. Chem. Eng.* **2013**, *91* (4), 669–686. https://doi.org/10.1002/cjce.21684.

(5) Tisse, V. F.; Boisson, C.; Prades, F.; McKenna, T. F. L. A systematic study of the kinetics of polymerisation of ethylene using supported metallocene catalysts - ScienceDirect https://www-sciencedirect-com.docelec.univ-lyon1.fr/science/article/pii/S1385894709008407 (accessed Jan 11, 2020).

(6) Tisse, V. F.; Briquel, R. M.; McKenna, T. F. L. Influence of Silica Support Size on the Polymerisation of Ethylene Using a Supported Metallocene Catalyst. *Macromol. Symp.* **2009**, *285* (1), 45–51. https://doi.org/10.1002/masy.200951106.

(7) Tisse, V. F. Kinetics and Morphology of Metallocene Catalysts Used in Ethylene Polymerisation, PhD. 2006.

(8) Bashir, M. A. Impact of Physical Properties of Silica on the Reaction Kinetics of Silica Supported Metallocenes and Polyethylene Morphology. phdthesis, Université de Lyon, 2016.

(9) Bashir, M. A.; Monteil, V.; Boisson, C.; McKenna, T. F. L. Experimental Proof of the Existence of Mass-Transfer Resistance during Early Stages of Ethylene Polymerization with Silica Supported Metallocene/MAO Catalysts. *AIChE J.* **2017**, *63* (10), 4476–4490. https://doi.org/10.1002/aic.15806.

(10) Kumkaew, P.; Wu, L.; Praserthdam, P.; Wanke, S. E. Rates and Product Properties of Polyethylene Produced by Copolymerization of 1-Hexene and Ethylene in the Gas Phase with (n-BuCp)2ZrCl2 on Supports with Different Pore Sizes. *Polymer* **2003**, *44* (17), 4791–4803. https://doi.org/10.1016/S0032-3861(03)00473-7.

Appendix 1

Experimental Section

1. Calculating the linear gas velocity – reactors SF 1 and SF 2

To convert the volumetric flowrates measured during the experiments to gas velocities inside the reactor, we applied the equation of state for ideal gases supposing mass conservation between the reactor bed and the flowmeter.

The linear gas velocity (u) was calculated as a function of the volumetric flow rate (Q_{room}), as follows:

$$u = \frac{P_{room} T_r}{P_r T_{room}} Q_{room} \frac{1}{\pi(\frac{D_t}{2}^2)\varepsilon}$$

Where P_{room} and T_{room} are the pressure and temperature of rotameter used during the experiments (i.e. 1 atm and 25°C). P_r and T_r are the reaction conditions. Q_{room} is the volumetric flowrate measured by a rotameter at the reactor exit. D_t is the reactor diameter and ε is the bed porosity.

2. Professional engineering of novel stopped-flow reactor (SF N)

This section was done in collaboration with the ILS (Integrated Lab Solutions) engineers involved in the current project and entails the steps followed in the development and construction of the novel stopped-flow unit.

The unit development followed a general timeline, divided into the following milestones:

1. Sales and customer
2. Basic Engineering
3. Detailed Engineering
4. Construction
5. Testing and validating

1) Sales and customer

This initial meeting consisted of the communication of our goals, wants and needs to the commercial engineers at ILS. At this point, we presented the concept of our project, the goals with the stopped-flow reactor, the evolution of the set-up up to date and the challenges we would like to overcome with the novel set-up.

We provided ILS with the reactor design (annular geometry), the desired reaction volume (6.5 cm^3) and the need for a minimum gap of 3 mm to allow filing the reactor with the catalyst and seedbed. We communicated the main constraints related to the functioning in stopped-flow reactions, mainly the necessity of proper reactor sealing, ease in operation in the glove-box and the ability to allow a wider range of experimental conditions, including the ability to inject different process gases, some of which are liquids at room temperature. Likewise, we provided the desired range of operations in terms of

reaction temperature, pressures, gas velocities, amounts for hydrogen and liquids (e.g. 1-Hexene, n-pentane) in the continuous gas feed. These requirements were based on reaction conditions commonly observed in industrial settings.

At this point, the commercial engineers draft an initial version of the unit P&ID, to be further refined in the following steps.

2) Basic Engineering

At this stage, the responsible engineers verified the feasibility of our requirements and modified the initial P&ID accordingly. A list of components was provided and the initial P&ID was refined. The Hazard and Operation (HazOp) procedure was performed and an alarm matrix was set-up for the system, producing a standardized diagram that correlates cause and effect for the possible dangerous events.

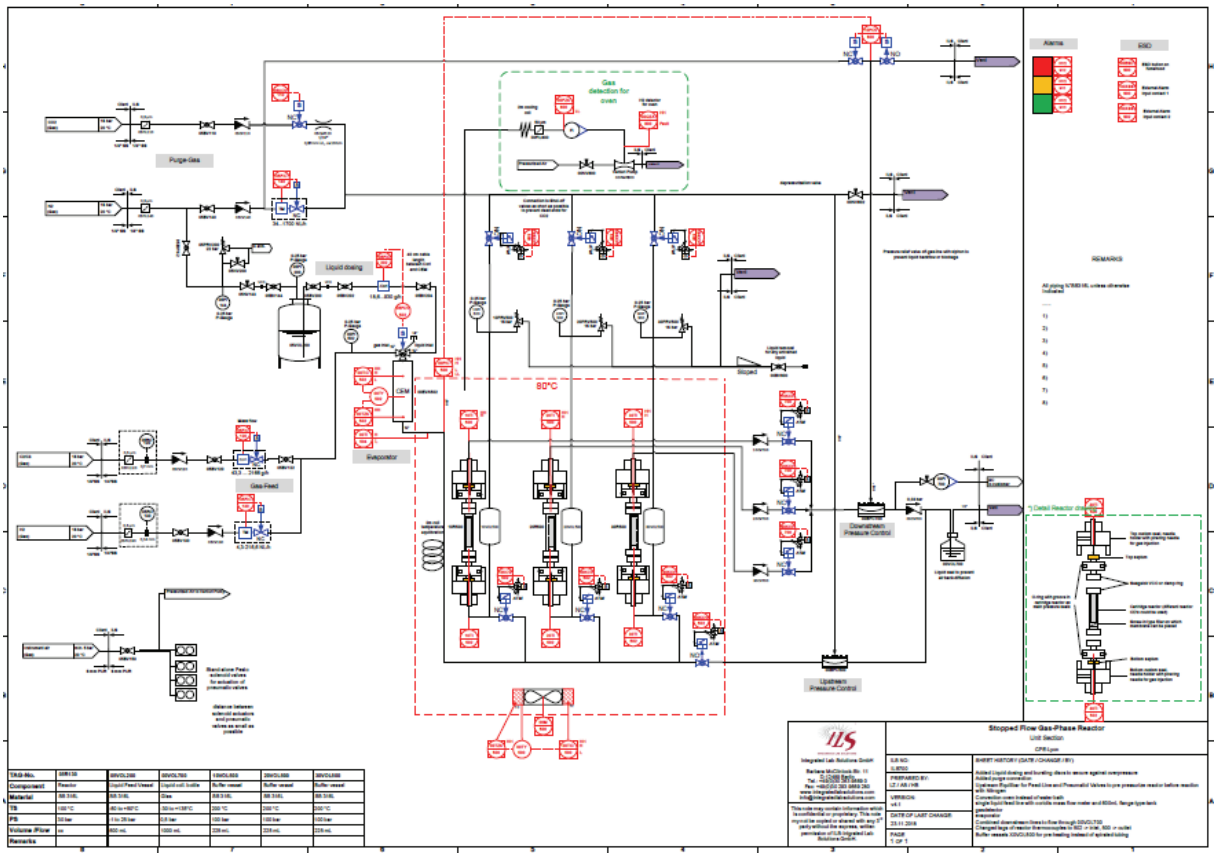

Figure 1: Refined (final) P&ID of the reactor set-up

3) Basic Engineering calculations

From the reaction conditions requirements (mainly temperature, pressures and gas velocities) and the requirements for the reactor design (reaction volume of 6.5 cm^3 and minimum gap of 3 mm), the reactor dimensions were determined in order to minimize the pressure drop in the reactor.

A mass balance for the reaction components was described in order to determine the operational ranges for the mass flow controllers in the set-up.

Moreover, a similar mass balance (shown in Figure 2) was described to estimate the nitrogen flowrates needed to create the same pressure drop over the reactor as the ethylene flow, in order to minimize the pressure drop when switching the gases.

	A	B	C	D
1		value	unit	SI
2		Nitrogen		
3	superficial flow velocity	50	cm/s	0,5
4	Reference pressure	7,5	barg	850000
5	liquid fraction		wt%	
6	reaction volume	6,5	cm^3	0,0000065
7	Reference temperature	70	°C	343,15
8				
9	annular gap:			
10	d1	15,748	mm	0,015748
11	d2	10	mm	0,01
12				
13	calc:			
14	A	116,24	mm^2	0,00011624
15	h	55,92	mm	0,05591949
16				
17	flow reaction conditions:			
18	dV/dt	**209,23**	L/h	5,8119E-05
19		**58,12**	ml/s	
20	flow normalized conditions:	**1415,66**	NL/h	0,00039324
21		**23,59**	NL/min	
22				

Figure 2: Mass balance for Nitrogen gas

4) Detailed Engineering

At this step, the detailed engineering of the set-up took place with the modeling with a CFD software (Autodesk) of the custom-made reactors (Figures 3-5), the overall set-up and the electric cabinet.

Likewise, the automation of the set-up was carried out, as well as the programming of the software interface (Siemens) shown in Figure 6. Finally, the necessary parts for construction were confirmed and purchased.

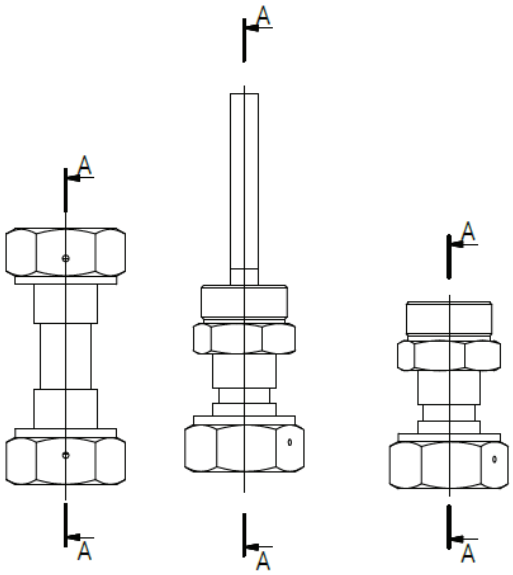

Figure 3: Engineering of custom made reactors

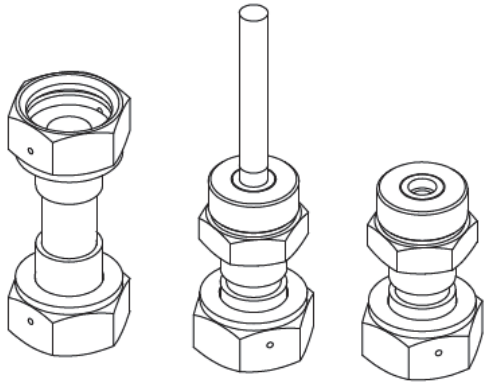

Figure 4: Engineering of custom made reactors

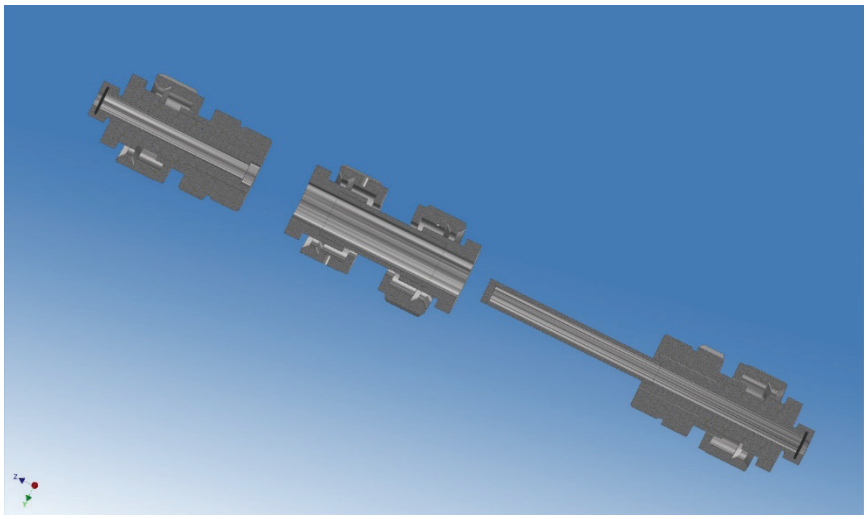

Figure 5: Unassembled reactor model work

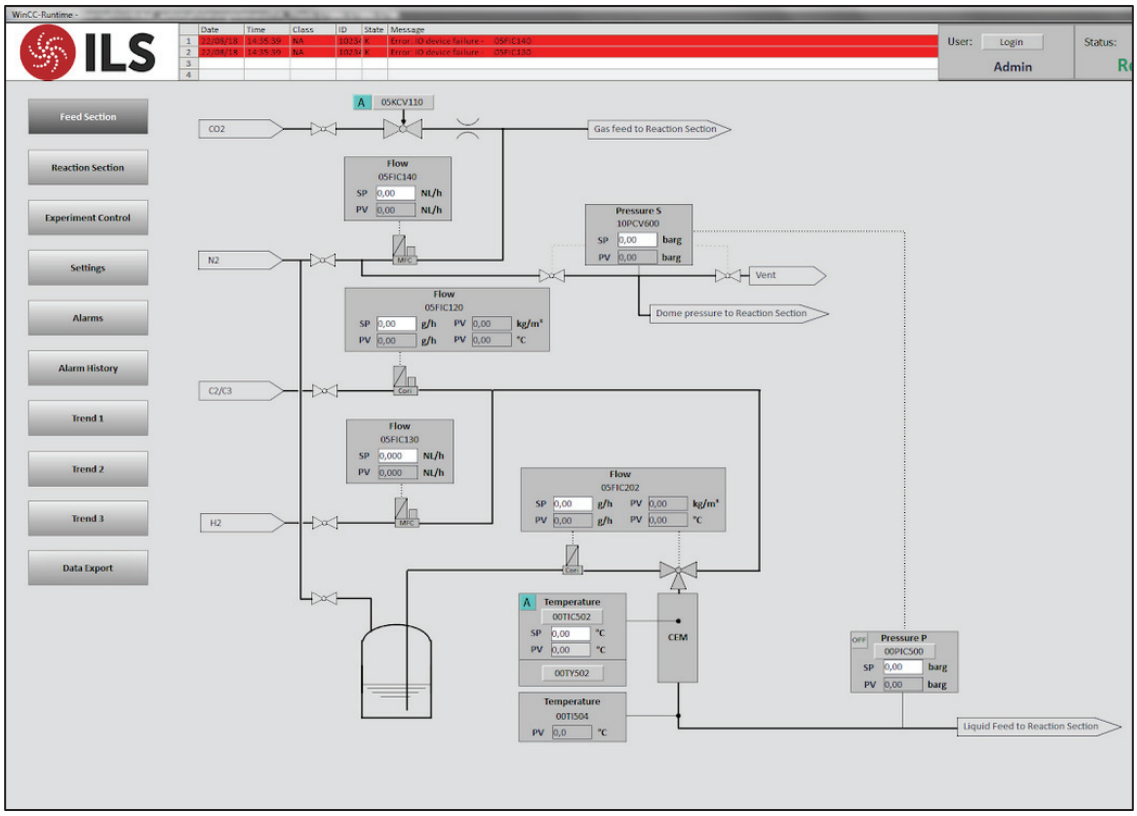

Figure 6: Automated and user-friendly control interface of novel reactor set-up

5) Construction, Testing and validating

At this stage, the construction and assembly of all reactor parts was done by the execution team at ILS. The system was tested in the ILS faciliies for pressure resistance, leaks and correct response of all automated valves and software.

The Factory Acceptance Testing (FAT) was carried out in the ILS facilities in Berlin. Together with the responsible engineers at ILS, we performed the unit commissioning in which all functions of the novel set-up were tested in cold mode (without catalyst) and using water in the liquid vessel, to inspect the functioning of the unit as a whole. We performed functional tests to verify the stability of pressures, temperatures and flows; as well as to become familiar with the user interface and the procedure for loading and unloading of the reactors. We comprehensively went through the alarm matrix and the actions to be taken in case of various sources of malfunction (e.g. gas leaks, temperature overshoots, required minimum pressures).

The Site Acceptance Testing (SAT) was carried out in our facilities in the C2P2 lab in Lyon. Together with the responsible engineers from ILS, we performed the same sequence of tests as in the FAT, in order to verify correct functionality of the unit after transportation and installation.

Figure 7: Novel Stopped-Flow reactor, ready for delivery.

Figure 8: Novel Stopped-Flow reactor, upon delivery at the C2P2 lab, in Lyon

3. Synthesis of Alumina grafted with TEA

The procedure hereby described was used for the preparation of alumina grafted with TEA, which served as a supplementary scavenger for the monomer gas during short-time polymerization reactions. This procedure is based on 30 g of γ –Alumina (Al2O3) of 1/16'' from STREM (CAS: 1344.28.1), for which we assumed a density of about 2.0 OH groups per nm^2 (650 $mmolg^{-1}$).[1]

The Alumina was first calcined at 500°C under air flow overnight, followed by dehydroxylation at 500 °C under high vacuum overnight. The amount of TEA to be applied was based on the OH concentration of the used support, with 10% excess. The used TEA was in a 1M solution in Heptane.

In a recipient, sufficient Heptane (22 mL, in our case) was added to completely wet the Alumina, creating a suspension. Next, the TEA solution (18 mL, in our case) was added dropwise to the suspension. The recipient was left slightly open, under argon flow, until bubbling ceased. Afterwards, the recipient was closed and left under room temperature overnight. Then, the supernatant was removed and we performed three washing steps with pure Heptane, using the same volume as the removed supernatant. Finally, the grafted Alumina was dried under vacuum, at room temperature, for at least 2 hours and stocked in the glovebox.

We performed infrared analysis of the calcined and dehydroxylated Alumina prior and after the grafting with TEA, seen in Figure 9. The grafting process is independent of the type of OH group on the Alumina surface and the presence of alkyl groups is confirmed by apparition of C–H-characteristic bands at 3000–2800 and 1460–1320 cm^{-1}., as indicated by Mazoyer et al.[1]

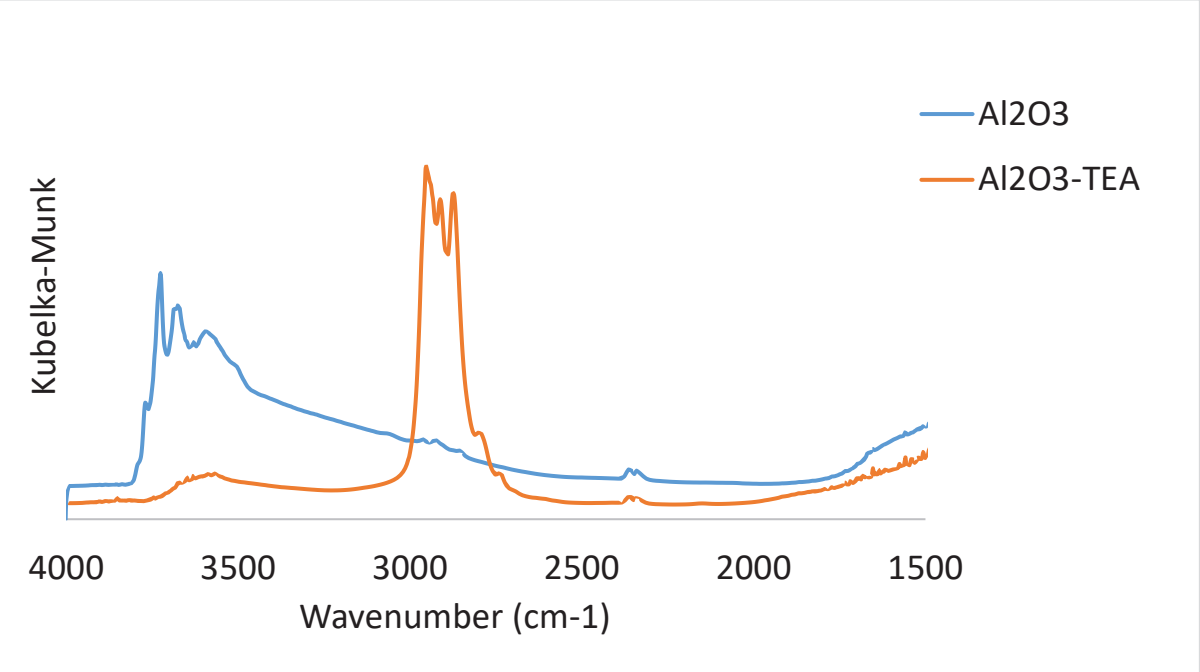

Figure 9: Infrared spectra of thermally treated Al_2O_3 and TEA impregnated Al_2O_3.

4. Analytical Techniques

Differential Scanning Calorimetry (DSC)

Characterization of thermal properties was performed with differential scanning calorimetry (DSC), using Mettler Toledo DSC 3, with autosample function and a 120 thermocouple sensor.

Al samples were accurately weighed (between 5 and 10 mg) and sealed in 40 µm aluminum pans.

The analysis were performed in four heating steps. The samples were initially heated from -20°C to 180°C at heating rate of 10 K/min. Next, the samples were cooled from 180°C to -20°C at a heating rate of 10K/min and remained isothermal at -20°C for 5 minutes. Finally, a second heating step was performed from -20°C to 180°C at a rate of 10K/min.

We consider data obtained during the second heating step. Crystallinity of the samples was calculated using a value of 293 J/g for a full crystalline polyethylene.

The melting temperatures (Tm) were measured at the peak of the endothermic peak of the second heating, and crystallization temperatures (Tc) at the exothermic peak of the cooling step. The degree of crystallinity (χ_c) of the analyzed samples was calculated using the software STAR^e Mettler by:

$$\chi_c = \Delta H_f / \Delta H_{f0}$$

Where ΔH_f (J.g^{-1}) is the melting heat of the sample and ΔH_{f0} (=293 J.g^{-1}) is the melting heat of 100% crystalline polyethylene.

Nitrogen porosimetry

The dehydroxylated silica and catalysts used in Chapter 4 were evaluated with nitrogen porosimetry analyses to follow the surface porosity of the samples. Analysis were done with a Micromeritics ASAP 2020 V3.04 H.

Samples were degassed before the adsorption and desorption measurements at 77 K with no thermal treatment during the analysis. Specific surface areas were obtained from the Brunauer-Emmett-Teller (BET) and pore size distribution was determined by Barrett-Joyner-Halenda (BJH) equation.

FT-IR-DRIFT

The dehydroxylated silica, SMAO and catalysts were characterized by Diffuse Reflectance Fourier Transform Infrared Spectroscopy (FT-IR-DRIFT) to follow their surface composition.

The DRIFT cell was filled with approximately 20 mg of sample inside an argon-filled glove box. The signals were collected in a Nicolet 6700 FT-IR spectrometer using OMNIC software 8.1 version and peaks were obtained by Kubelka-Munk equation, with 64 scans accumulated for each analysis in a resolution of 4 cm^{-1}.

Size Exclusion Chromatography (SEC)

The molecular weight distributions of polymer samples were characterized by SEC by Waters, Alliance GPCV 2000. The system was equipped with two detectors (a refractometer and a viscometer) and three columns (PL gel Olexis 7*300 mm from Varian). Analyses were performed in trichlorobenzene (TCB) at

a flow rate of 1 mL/min. The molecular weight distributions were calculated by a calibration based on polyethylenes of different weight average molecular weights and only the RI signal was used for calculations in order to erase any possible artifact coming from experimental errors during the determination of the polymer mass. The original samples were in fact support/polymer particles that had been separated from the NaCl seedbed by washing at ambient temperature with demineralized water. The exact polymer quantity (varying between 1 and 10 mg depending on yield) was calculated using the total sample weight and reaction yield value. The particles were then dissolved in trichlorobenzene at 150°C for 3 hours and filtered before injection into the chromatography columns in order to remove the inorganic support particles. Heterogeneities in the original samples or incomplete removal of the inorganic support could lead to errors in the molecular weight calculations if the viscometer signal was taken as reference. The morphology of the polymer particles was observed by Scanning electron microscope (SEM). The microscope used was a MEB QUANTA 250, with samples under high vacuum. Previously, a coat of Cu of 10 nm was deposited over the samples, under rotation.

SEM and SEM-EDX

Particle morphologies were observed by Scanning Electron Microscopy (SEM) technique at the "Centre technologique des microstructures" (CTμ) at the Lyon 1 University with a MEB ZEISS Merlin Compact microscope.

Samples were observed under high vacuum with accelerating voltages of 5 to 10 keV, depending on each individual case. Prior to observation, samples were fixed to a standard aluminum slotted head covered with carbon adhesive tab. A coat of Cu of 10 nm was deposited over the rotating samples by sputtering under vacuum.

The SEM-EDX were observed after surface cutting of the samples. Samples were fixated into an EpoFix resin and surface cutting was performed with a 'Diatome Ultra 45' diamond knife on a Reichert Ultracut S ultramicrotome.

5. Design of Experiments (DOE)

For the treatment of the data with the software Statistica 10, the choice of Industrial Statistics & Six Sigma was selected, followed by choice of Experimental Design (DOE). Next, we selected the treatment option 'Central Composite, non-factorial, surface designs' with 3 factors and 1 block, in which we chose to evaluate linear main effects only.

As described in the works of Andrade[2], the general model used to estimate the main interactions between the independent and dependent variables can be expressed as the second-order linear regression model:

$$Y = \beta_0 + \sum_{i=1}^{k} \beta_i x_i \quad _1 + \sum_{i=1}^{k} \sum_{j=1}^{k} \beta_{ij} x_1 x_j + \varepsilon$$

In which Y is de dependent variable, $\beta_i(\,0,1,\ldots,k)$ are the linear regression coefficients, $x_i$are the independent variables and ε is the unobserved random error associated with the experimental data.

The linear regression coefficient β is obtained from the least square model solution, assuming the least square function ($\Im$) to be minimized as follows:

$$\Im = \sum_{i=1}^{n} \varepsilon^2 = \sum_{i=1}^{n} \left[Y - \left(\beta_0 + \sum_{i=1}^{k} \beta_i x_i \; + \sum_{i=1}^{k} \sum_{j=1}^{k} \beta_{ij_{i \leq j}} x_1 \, x_j \right) \right]^2$$

The experimental matrix that described the current systems is described as:

$$\wp = \beta_0 + \beta_1 x_1 + \beta_2 x_2 + \; + \beta_3 x_3 + \; \beta_{11} {x_1}^2 + \beta_{22} {x_2}^2 + \; \beta_{33} {x_3}^2 + \beta_{12} x_1 x_2 + \beta_{13} x_1 x_3 + \beta_{23} x_1 x_3 + \epsilon$$

In which, for catalyst CpZ 2 (3^2) is described by terms including $i = 1, 2$ and catalyst CGC M (3^3) is described by terms including $i = 1, 2, 3$.

The main effects correspond to the observed change in the average response results when a factor is varied while others remain unchanged. To determine the impact of each of the variables in the obtained responses, we have interpreted the Pareto diagram, in which parameters with a p value higher than .05 are considered to have significant statistical value. The evaluation of results can also be done by observing the graph of predicted values versus observed values with a confidence interval of 95%, in which the observed value is the dependent variable and the predicted value is estimated by the regression equation.

We have applied the ANOVA (analysis of variance) technique, shown in Table 1, to interpret the main interaction effects between the factors. The columns in the ANOVA table indicate the sources of variation, the sum of squares (SS), the degrees of freedom (df), the mean squares (MS), the F statistical test and the parameter p. The statistical parameter p allows to interpret the interaction between the effects without needing a table of critical values of the distribution F. If the value of p is smaller than the level of significance chosen α, the null hypothesis is rejected. The effect highlighted in red in the table is the one with considerable influence on the analyzed system. The value of 'R-square' shows the discrepancy of results in relation to the predicted data.

	ANOVA; Var.:Yield (g/g); R-sqr=.64438; Adj:.60759 (Spreadsheet5) 3 factors, 1 Blocks, 33 Runs; MS Pure Error=.0490189 DV: Yield (g/g)				
Factor	SS	df	MS	F	p
(1)H2 (m%)(L)	0.146981	1	0.146981	2.99846	0.103852
(2)1-C6 (wt%)(L)	0.014666	1	0.014666	0.29919	0.592435
(3)Time (s)(L)	2.991916	1	2.991916	61.03598	0.000001
Lack of Fit	1.079321	14	0.077094	1.57275	0.197201
Pure Error	0.735283	15	0.049019		
Total SS	5.102669	32			

Tableau 1: Example of ANOVA table obtained from the software Statistica 10

We have employed the use of the response surface methodology (RSM) in the software in order to observe how the tested variables affect the test responses, identify the relationship between the parameters, as well as the combined effect between them. Generally, the plot results are derived from the first order polynomials previously defined as $\wp$. The resulting plot provides a three-dimensional view of the response surface, with the importance of each factor indicated by the color coding.

6. References

(1) Mazoyer, E.; Trébosc, J.; Baudouin, A.; Boyron, O.; Pelletier, J.; Basset, J.-M.; Vitorino, M. J.; Nicholas, C. P.; Gauvin, R. M.; Taoufik, M.; Delevoye, L. Heteronuclear NMR Correlations To Probe the Local Structure of Catalytically Active Surface Aluminum Hydride Species on γ-Alumina. *Angew. Chem. Int. Ed.* **2010**, *49* (51), 9854–9858. https://doi.org/10.1002/anie.201004310.

(2) Andrade, F. N. de. Effect of Condensable Materials during the Gas Phase Polymerization of Ethylene on Supported Catalysts. phdthesis, Université de Lyon, 2019.

Appendix 2

Reactor model sensitivity analysis

1. Sensitivity analysis

Parameters evaluated in terms of their contribution to the developed reactor model in chapter 3.

1.1. Treatment of the metal frit in the heat balance

In the current model, we assumed the metal frit does not affect the reaction zone and, therefore, was not included in the description of heat balances. To test this assumption, we have programmed an alternative approach, assuming that the metal frit is in the same temperature of the inlet gas.

In this case, the frit was accounted for as an insert in the reactor, thus contributing to the total heat capacity of the system. The metal frit was then included in the *inert* phase of the model for the reaction zone. For this case, we assumed the inner heat transfer coefficient of the metal frit (U_{Frit}) to be 43% of that of stainless steel, given the porosity of the material.

The heat capacity term for the inert phase, in this case, becomes:

Inert phase: $\left(MC_p\right)_i = V_s\rho_s C_{p_s} + m_{\text{glassWool}} C_{p_{\text{glassWool}}} + m_{\text{frit}} C_{p_{\text{frit}}}$

In Figure 1, we find the resulting plots for both studied cases.

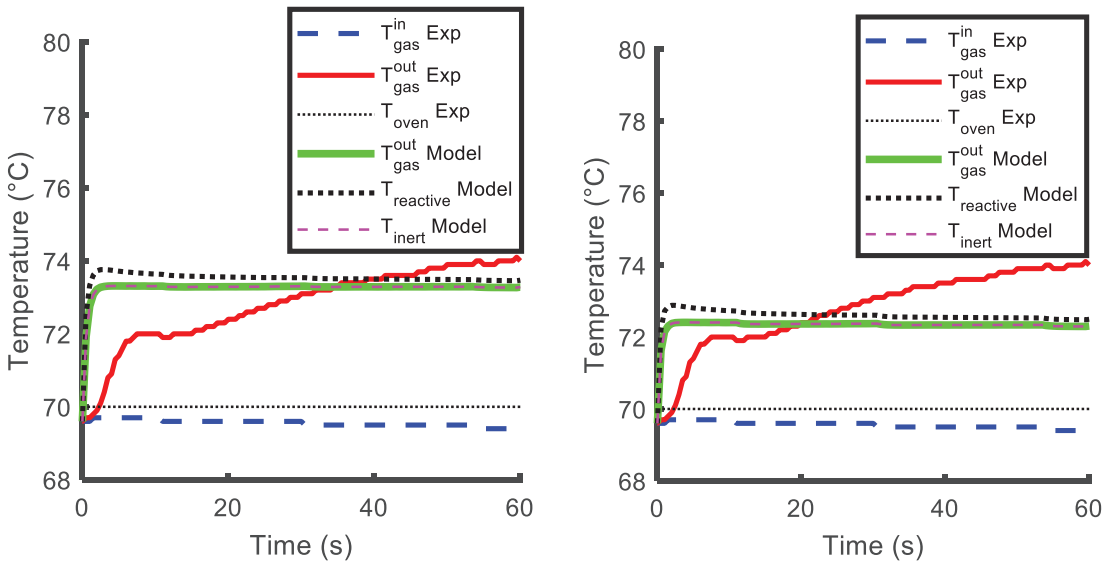

Figure 1: Assumptions for treatment of the metal frit: a) no influence on reaction zone, b) an insert in the reactor with U_{frit} =836 W.m^{-2}.K^{-1}

Accounting for the metal frit as an insert in the reactor seems absorb part of the heat generated early in the reaction, thus slowing down the temperature increase. Nonetheless, for both cases evaluated, the plotted temperatures reach the same values.

Given that the frit is continually filled with monomer gas coming in the opposite direction as the heat generated by the reaction, we have confirmed our hypothesis that the frit should not be accounted for as part of the reaction zone.

1.2. Catalyst activation period

For the model development, we assumed the catalyst activation happens sufficiently fast to neglect a period of activation.

Here, we have imposed an arbitrary activation period of 3 seconds to evaluate the impact on the model predictions. In this case, the value of k_{p0} was set to zero for the 'activation period', then kept constant at $k_{p0} = 130$ for the remaining time of reaction.

In Figure 2, we find the resulting plots for both studied cases.

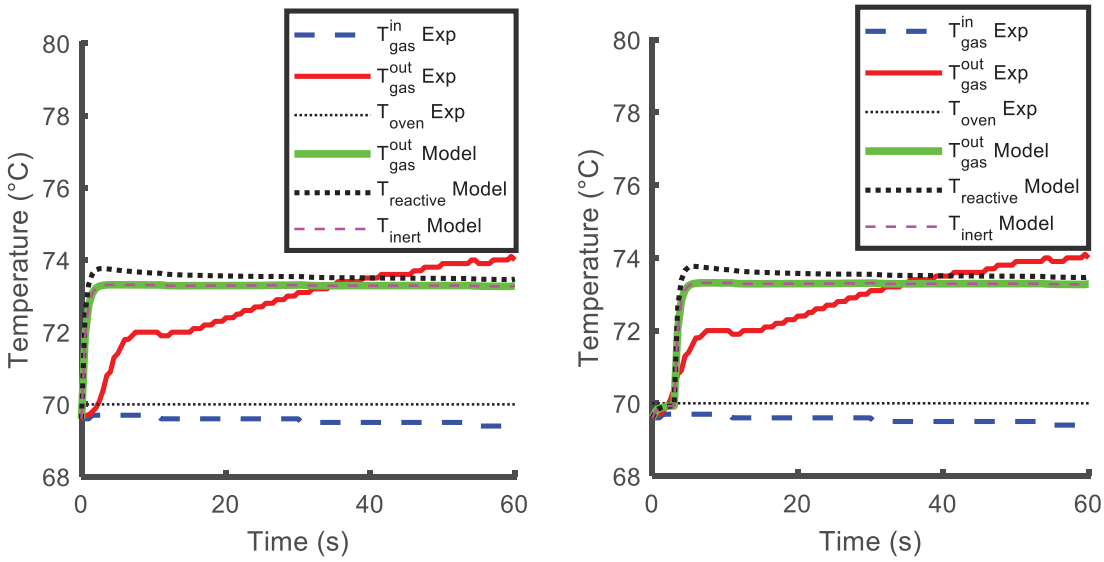

Figure 2: Assumptions for catalyst activation period: a) no activation period, b) activation period of 3 seconds

Imposing an activation period of 3 seconds shifted the predicted temperatures but had no impact on the profiles. We have, therefore, neglected an activation period for the catalyst in the reactor model.

1.3. Heat transfer coefficient at the reactor wall (hi)

The effect of varying the heat transfer coefficient at the reactor wall was assessed.

As shown in Figure 3, increasing the value of h_i by a factor of 1.5 had negligible effect on the estimated temperature profiles.

From this assessment, we were confident in our calculations for h_i, described in in chapter 3.

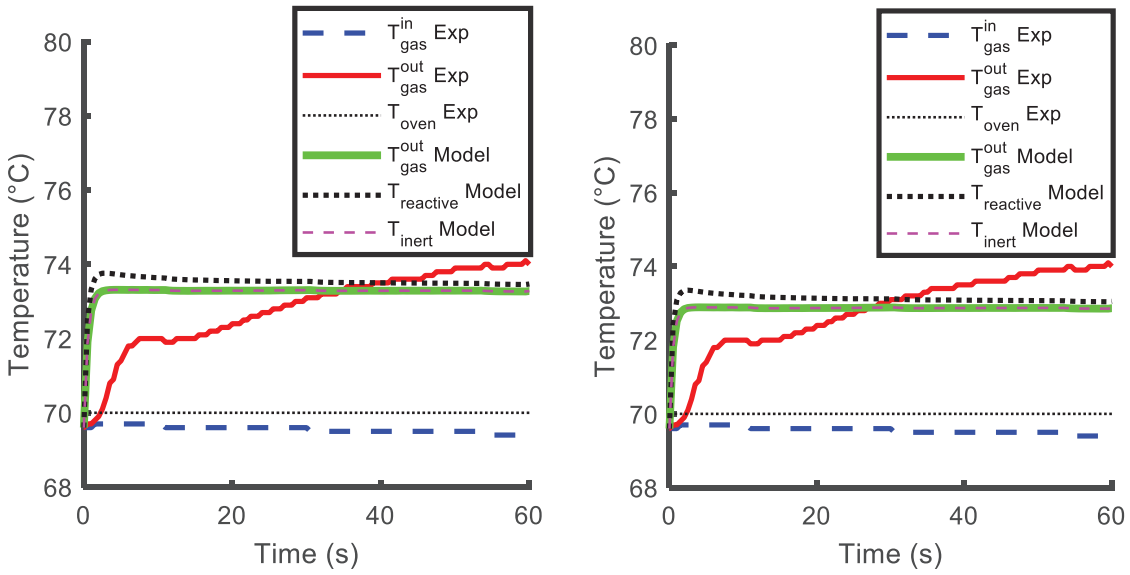

Figure 3: Effect of h_i on model estimation, a) h_i as calculated in chapter 3, b) value of h_i*1.5

1.4. Salt particle heat transfer coefficient (h_{salt})

We have assessed the impact of h_{salt} , calculated in chapter 3 with the correlation proposed by Kunii and Levenspiel.[1]

We concluded the value of h_{salt} must be reduced by a factor of 100 in order to produce significant changes in the estimated temperature profiles, which gives us confidence in the calculations used for h_{salt}.

Results of the assessment are seen in Figure 4.

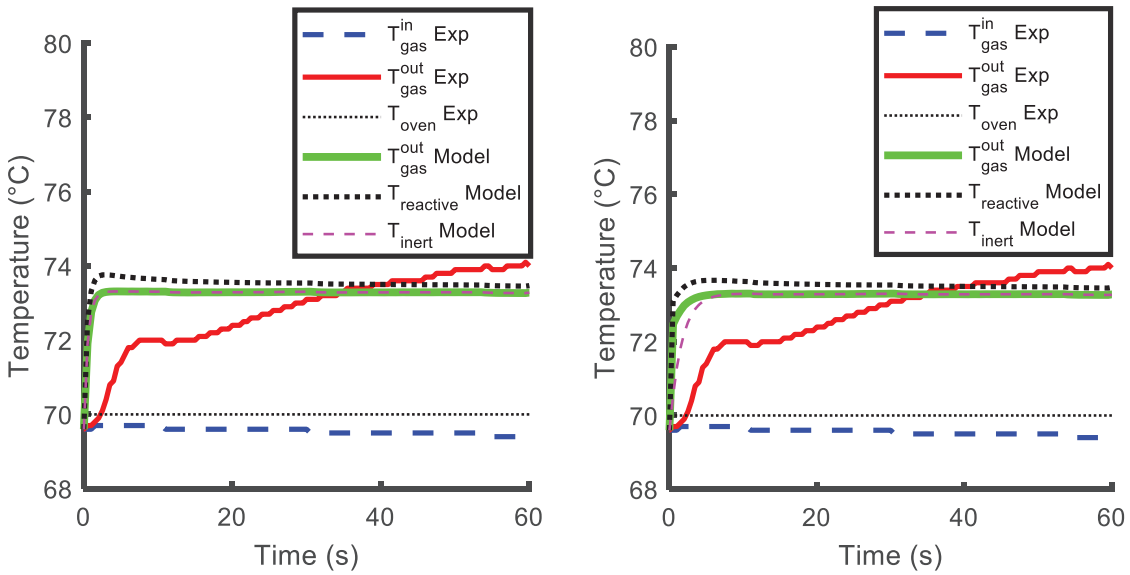

Figure 4: Effect of hsalt on model estimation, a) hsalt as calculated in chapter 3, b) value of hsalt/100

1.5. Diameter of salt

The inert seedbed used for the model developed was composed of salt crystals agglomerated into particles of average diameter of 50 µm.

As part of the sensitivity analysis of the reactor model, we have assessed the impact of increasing the size of the particles used as seedbed while maintaining the same mass of salt.

As seen in Figure 5, increasing the diameter of the salt particles led to a significant increase of all predicted temperatures. This effect is coherent and has been previously observed in the works of Tioni et al.[2]

For the current model, the main effect of increasing the salt particle diameter was an increase in the Reynolds number in the reactor and, therefore, reduction of the heat transfer coefficient at the reactor wall (h_i). The obtained values of the estimated parameters can be found in Table 1.

Salt particle diameter (µm)	Reynolds number (-)	Overall heat transfer coefficient (U) (W.m^{-2}.K^{-1})
45	22.5	854
300	125	447

Tableau 1: Calculated Reynolds number and overall heat transfer coefficient, in relation to salt particle diameter

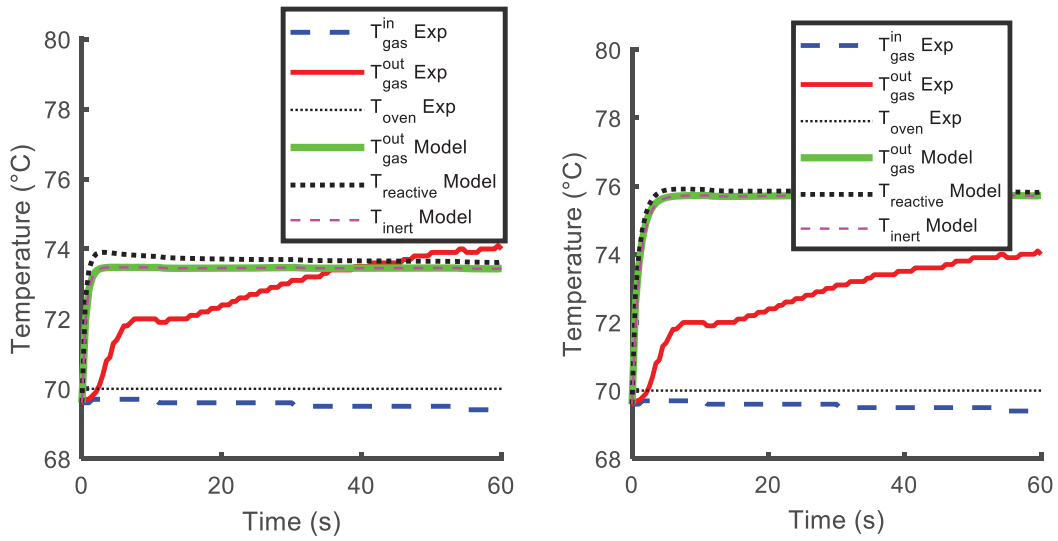

Figure 5: Effect of diameter of salt particle, a) 50 µm, b) 300 µm

1.6. Effective thermal conductivity

We observed no effect of the effective thermal conductivity ($k_{\mathrm{e,z}}$) on the model outcome (even when extrapolated to *1000), indicating that this term can be neglected from the energy balance.

The thermal conductivity is known for the gas and salt. The effective thermal conductivity was calculated precisely in chapter 3 and can be used for the inert phase when the two phases model is employed. However, the axial conductivity is calculated in a different way.[3] It is concluded here that there is no need for big precision regarding this parameter as the whole term ($k_{\mathrm{e,z}}\frac{\partial^2 T}{\partial z^2}$) is negligible – the estimated values can be seen in the following section.

2. Numerical assessment of reactor model

The estimated values for all terms of the reactor model can be found bellow:

$$\begin{bmatrix} \frac{\partial T_{\mathrm{i}}}{\partial t} + \underbrace{v_{\mathrm{z}}\frac{\partial T_{\mathrm{i}}}{\partial z}}_{-9.78e-10} \\ \frac{\partial T_{\mathrm{r}}}{\partial t} + \underbrace{v_{\mathrm{z}}\frac{\partial T_{\mathrm{r}}}{\partial z}}_{-3.4e-10} \end{bmatrix} = \begin{bmatrix} \underbrace{\frac{k_{\mathrm{e,z,i}}V_i\frac{\partial^2 T_i}{\partial z^2}}{(mC_p)_{\mathrm{i}}}}_{-1.7e-16} \\ \underbrace{\frac{k_{\mathrm{e,z,r}}V_r\frac{\partial^2 T_r}{\partial z^2}}{(mC_p)_{\mathrm{r}}}}_{3.41e-16} \end{bmatrix} + \begin{bmatrix} \underbrace{\frac{F_{\mathrm{g}}\rho_{\mathrm{g}}C_{\mathrm{pg}}(T_{\mathrm{g}}^{\mathrm{in}}-T_{\mathrm{i}})}{(mC_p)_{\mathrm{i}}}}_{-2.18} + \underbrace{\frac{F_{\mathrm{g}}\rho_{\mathrm{g}}C_{\mathrm{pg}}(T_{\mathrm{r}}-T_{\mathrm{i}})}{(mC_p)_{\mathrm{i}}}}_{+0.128} \\ \underbrace{-\frac{F_{\mathrm{g}}\rho_{\mathrm{g}}C_{\mathrm{pg}}(T_{\mathrm{r}}-T_{\mathrm{i}})}{(mC_p)_{\mathrm{r}}}}_{-0.15} \end{bmatrix}$$

$$+ \begin{bmatrix} \underbrace{\frac{S_{\mathrm{r}}h_{\mathrm{r}}(T_{\mathrm{r}}-T_{\mathrm{i}})}{(mC_p)_{\mathrm{i}}}}_{9.06} + \underbrace{\frac{S_{\mathrm{w}}h_{\mathrm{w}}(T_{\mathrm{w}}-T_{\mathrm{i}})}{(mC_p)_{\mathrm{i}}}}_{-6.78} \\ \underbrace{-\frac{S_{\mathrm{r}}h_{\mathrm{r}}(T_{\mathrm{r}}-T_{\mathrm{i}})}{(mC_p)_{\mathrm{r}}}}_{-11.15} \end{bmatrix} + \begin{bmatrix} 0 \\ \underbrace{\frac{Q_{\mathrm{r}}}{(mC_p)_{\mathrm{i}}}}_{11} \end{bmatrix}$$

From this assessment, we neglected the convection terms that include the gas velocity (v_{z}).

3. Monomer conversion

We estimated the ethylene conversion from the reaction rates obtained from the High-Gain Observer and the monomer flow rates, in order to validate hypothesis of constant monomer concentration in the reactor, as follows:

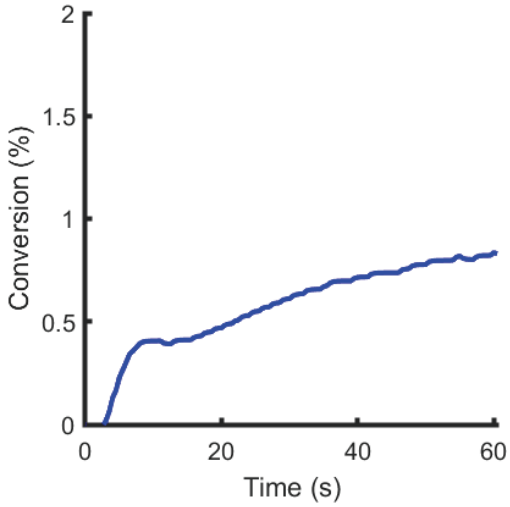

Figure 6: Estimated monomer conversion

4. References

(1) Kunii, D.; Levenspiel, O. *Fluidization Engineering (Series in Chemical Engineering)*; 1991.

(2) Tioni, E.; Spitz, R.; Broyer, J. P.; Monteil, V.; McKenna, T. Packed-Bed Reactor for Short Time Gas Phase Olefin Polymerization: Heat Transfer Study and Reactor Optimization. *AIChE J.* **2012**, *58* (1), 256–267. https://doi.org/10.1002/aic.12576.

(3) Tiemersma, T. P.; Patil, C. S.; Sint Annaland, M. van; Kuipers, J. A. M. Modelling of Packed Bed Membrane Reactors for Autothermal Production of Ultrapure Hydrogen. *Chem. Eng. Sci.* **2006**, *61* (5), 1602–1616. https://doi.org/10.1016/j.ces.2005.10.004.

Appendix 3

List of experiments

1. Variability assessment

The list of experiments used for assessing the yield variability for catalyst CpZ 2 and CGC M in chapter 4 is found below.

The experiment ID# is defined as the date of reaction, followed by the number indicating the number of tests performed in the day and, finally, by the reactor that was used for the experiment, such as:

YY.MM.DD (date) - # (n experiment set performed that day R# reactor number)

- **List of experiments with catalyst CpZ 2 (classic metallocene)**

Catalyst used	Experiment ID#	Reaction time (s)	Catalyst mass (mg)	Yield (g/g)
CpZ 2	190826 R2	60	36	3,1
	190828 R2	60	31	3,0
	191002-2 R4	55	31	2,6
	191002 R5	30	30	1,7
	1911121 R2	30	25	0,8
	1911121 R3	30	33	1,2
	190826 R3	5	51	0,2
	190828 R3	5	30,5	0,3
	191002 R6	5	32	0,3
	191016 R5	5	33	0,6

- **List of experiments with catalyst CGC M (CGC metallocene)**

Catalyst used	Date and reactor #	Reaction time (s)	Catalyst mass (mg)	Yield (g/g)
CGC M	190710-2 R2	60	62,0	3,4
	190718 R2	60	38,0	5,0
	190809 R2	60	49,0	4,0
	190619 R3	60	55,0	6,7
	190909 R3	30	50,6	2,6
	191121-2 R4	30	35	1,4
	191121-2 R6	30	50,9	2,4
	190620-2 R2	5	40,7	0,5
	190624-2 R2	5	52	0,6
	190916 R1	5	49	0,4

2. Design of Experiments (DOE)

A list of the experiments used for the statistical analysis performed in chapter 4 is here presented.

Experimental matrix for catalyst CGC M and CpZ 2:

Experimental runs	Factors		
	H2 (%mol)	1-C6 (wt.%)	Time (sec)
1	-	-	-
2	-	0	+
3	-	+	0
4	0	-	+
5	0	0	0
6	0	+	-
7	+	-	0
8	+	0	-
9	+	+	+
10	0	0	0
11	0	0	0
12	0	0	0

Experimental runs	Factors	
	1-C6 (wt.%)	Time (sec)
1	-	-
2	0	-
3	+	-
4	-	0
5	0	0
6	+	0
7	-	+
8	0	+
9	+	+
10	0	0
11	0	0
12	0	0

It is worth mentioning that two separate DOE analysis were performed for catalyst CGC M for different time intervals (shown in Tables 2 and 3). Nonetheless, the data was merged into the statistical analysis, using function xxx in the software Statistica 10.

Moreover, given to malfunction in the SEC equipment at our lab and time constraints, the analysis of the molecular weight was not included in the DOE analysis.

Date and reactor #	Experimental run	H2 (%mol)	1-C6 (wt.%)	Time (sec)	Yield (g/g)	Tm (°C)	Crystallinity %	Mw (Daltons)	Mw/Mn
190624-2 R2	1	0	0	5	0,6	131	14,8	722 469	3,0
190923 R5	2	0	8	20	1,7	129	33,57	392 673	2,1
190813-2 R2	3	0	16	12,5	0,6	118,8	28,2	336 746	3,5
190923 R6	4	0,3	0	20	0,8	133	45,7	71 374	2,7
190814 R3	5	0,3	8	12,5	0,9	127	37	77 671	2,4
190823 R2	6	0,3	16	5	0,4	117	9	107 465	2,5
190822 R2	7	0,6	0	12,5	1,0	132	41	37 686	3,9
190823 R3	8	0,6	8	5	0,6	125	23	56 447	2,0
190822-2 R2	9	0,6	16	20	1,7	124	39	43 466	3,8
190904-2 R1	10	0,3	8	12,5	1,4	131	42		
190904 R6	10	0,3	8	12,5	0,8	131,1	29,3		
190904-2 R3	10	0,3	8	12,5	1,2	132,4	42		
190821-2 R2	11	0,3	8	12,5	1,2	127	37		
190822-2 R3	12	0,3	8	12,5	1,0	125	35	76 051	2,3

Figure 1: Experiments used for DOE - catalyst CGC M

Date and reactor #	Experimental run	H2 (%mol)	1-C6 (wt.%)	Time (sec)	Yield (g/g)	Tm (°C)	Crystallinity %	Mw (Daltons)	Mw/Mn
190909-2 R3	1	0	0	3	0,4	127,6	17	280020	2,13
191009 R4	2	0	8	7	0.22	123	17.2	128451	2.065
191009 R5	3	0	16	5	0,22	118,8	4,34		
191009 R6	4	0,3	0	7	0,44	130,1	27,6	87457	2,09
191009-2 R4	5	0,3	8	5	0,41	128,9	19	128451	2,07
191009-2 R5	6	0,3	16	3	0,2	125,6	15,11	109020	2,1
191009-2 R6	7	0,6	0	5	0,64	129,7	34,4		
191010-2 R6	8	0,6	8	3	0,38	125,6	7,72		
191010 R5	9	0,6	16	7	0,44	125,6	8,8		
191010 R6	10	0,3	8	5	0,62	127,7	20,6		
190812-2 R2	10	0,3	8	5	0,6	124,1	29,9		
190812-2 R3	10	0,3	8	5	0,4	125,5	28,5		
191010-2 R4	11	0,3	8	5	0,59	127,8	15,7	132616	3,16
190625-2 R2	12	0,3	8	5	0,99	123,9	28,5		

Figure 2: Experiments used for DOE - catalyst CGC M

Experiment date/reactor	Experimental run	1-C6 (wt.%)	Time (sec)	Yield (g/g)	Tm (°C)	Crystallinity %	Mw (Daltons)	Mw/Mn
190826 R3	1	0	5	0,2	132,1	17	40 808	2,17
190828 R3	1	0	5	0,33	122	11,2		
191002 R6	1	0	5	0,31	122	14,22		
191016 R5	1	0	5	0,6	131,9	20,6	72 953	2,45
191002-2 R5	2	8	5	0,39	126,7	16,3	47 196	3,9
191002-2 R6	3	16	5	0,43	128,4	27,3	55 262	2,8
191002 R4	4	0	30	1,39	132	33	143 157	2,14
191002 R5	4	0	30	1,66	132	28,73	116 807	4,44
1911121 R2	4	0	30	0,80	132,9	35		
1911121 R3	4	0	30	1,21	132,9	24,9		
191003-2 R5	5	8	30	1,22	132	29	145 341	2,99
191003-2 R6	6	16	30	0,96	131,3	24	167 924	2,43
191003 R5	6	16	30	0,60	130,9	31,8	126 833	4,37
191002-2 R4	7	0	55	2,6	133,5	52,8	197 721	2,1
191003-2 R4	8	8	55	1,61	132	25,5	146 132	3,21
191003 R4	8	8	55	1,17	132,8	32,7	157 262	2,11
191007 R5	9	16	55	1,91	132,1	33,7	130 779	4,17
191016 R4	10	8	30	1,4	131,3	41,7	109 131	4,22
191004 R5	11	8	30	0,98	132	31,3	139 602	2,1
191007 R4	12	8	30	0,92	131,3	23	137 797	3,1

Tableau 3: Experiments used for DOE - catalyst CpZ 2

3. DSC crystallinity evolution

List of experiments used to assess the evolution of polymer thermal properties at increasing times. Performed in homopolymerization conditions with ethylene.

Catalyst	Conditions	Experiment ID #	Reaction time (s)	Tm (°C)	Crystallinity %
CpZ 2	8 wt% 1-C6	191002-2 R5	5	126,7	16,26
		191003-2 R5	30	132	29
		191003-2 R4	55	132	25,52
	16wt% 1-C6	191002-2 R6	5	128,5	27,3
		191003-2 R6	30	131,3	24
		191007 R5	55	132	33,7

Tableau 4: Experiments used assessment of thermal properties evolution – CpZ 2

Catalyst	Conditions	Experiment ID #	Reaction time (s)	Tm (°C)	Crystallinity %
SRAC 270	8 wt% 1-C6	190708 R3	5	120,2	17,2
		191009 R4	7	123	17,2
		190923 R5	20	129,0	33,6
		190813 R3	30	124,4	33,6
		190711 R2	60		
	16wt% 1-C6	191009 R5	5	118,8	4,52
		190813-2 R2	12,5	118,8	28,2
	8 wt% 1-C6 0,3m% H2	190812-2 R2	5	124,1	29,9
		190821-2 R2	12,5	127,5	37
		190718 R3	60	126,5	45
	8 wt% 1-C6 0,6m% H2	191015 R5	3	125,6	7,72
		190823 R3	5	125,2	24
	16 wt% 1-C6 0,3m% H2	191009-2 R5	3	125,6	15,11
		190823 R2	5	117	10,7
	16 wt% 1-C6 0,6m% H2	191010 R5	7	125,6	8,8
		191001 R1	20	130,85	53,1
		190822-2 R2	30	124,9	39

Tableau 5: Experiments used assessment of thermal properties evolution – CGC M

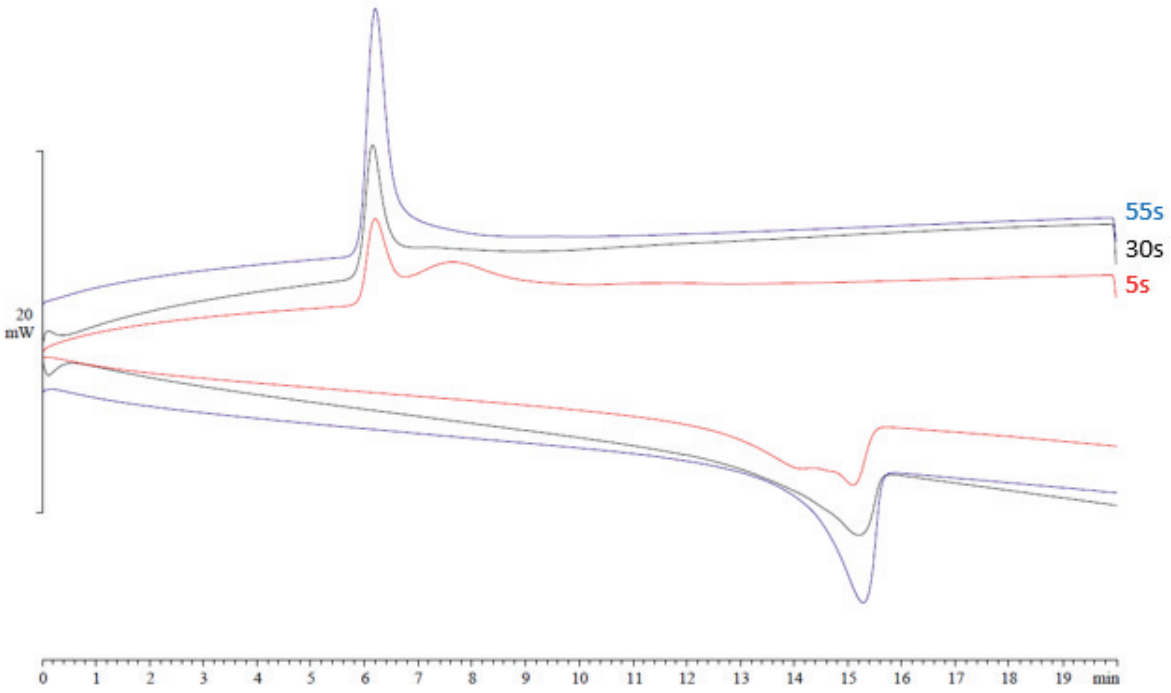

Figure 1: DSC plots - classic metallocene CpZ2. Reaction conditions: C2 + 16 wt% 1-C6 in gas feed

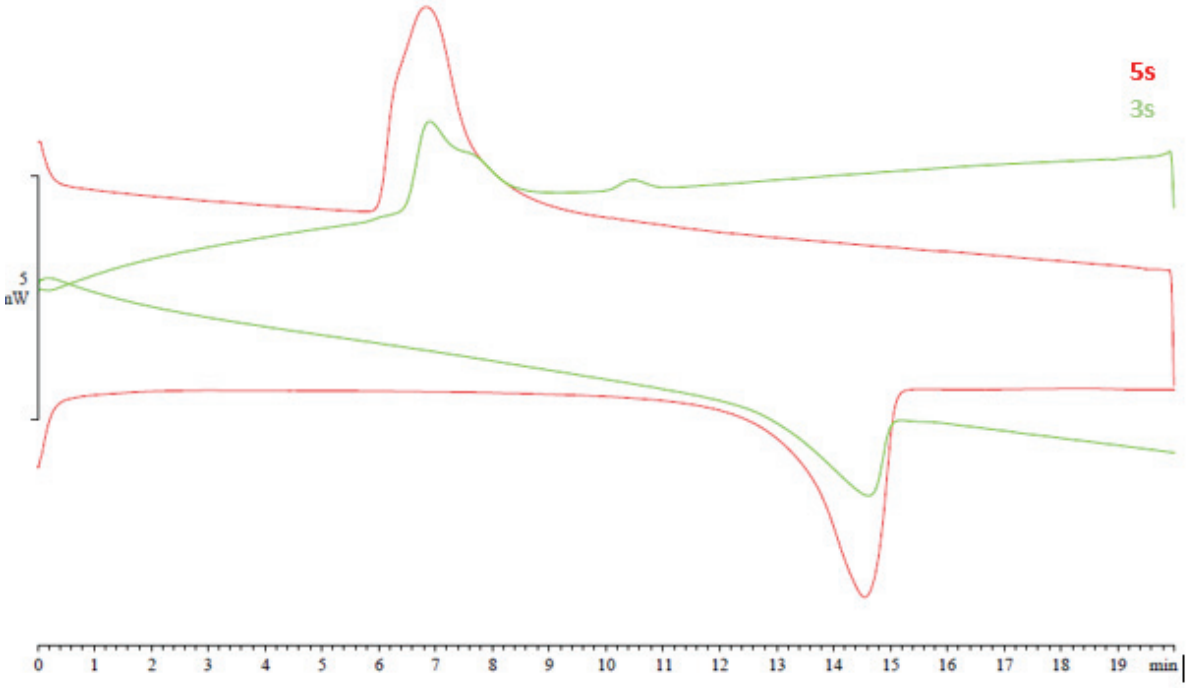

Figure 2: DSC plots - catalyst CGC M. Reaction conditions: C2 + 8 wt% 1-C6 + 0.3m% H2 in gas feed

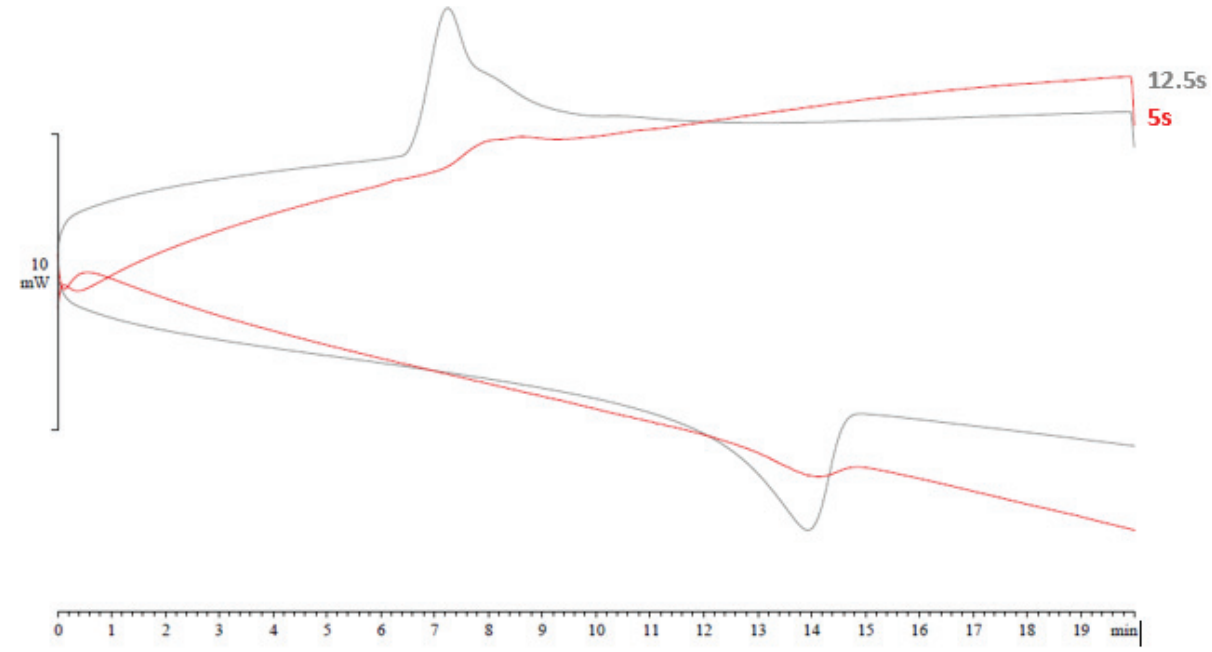

Figure 3: DSC plots - catalyst CGC M. Reaction conditions: C2 + 16 wt% 1-C6 in gas feed

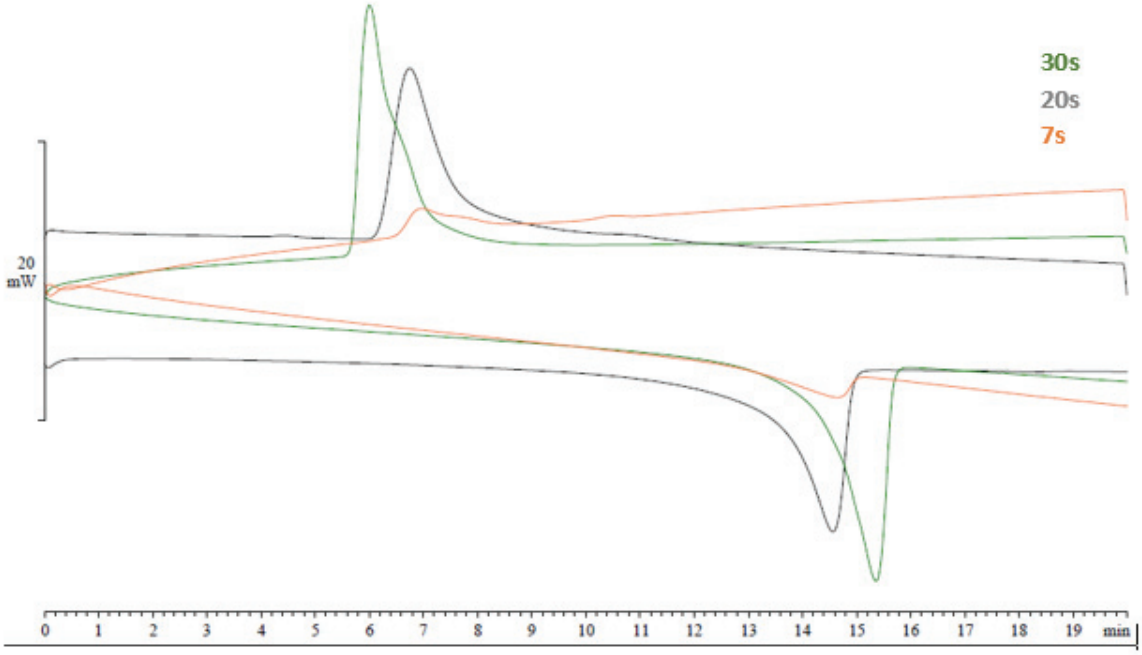

Figure 4: DSC plots - catalyst CGC M. Reaction conditions: C2 + 16 wt% 1-C6 + 0.6m% H2 in gas feed